COMPUTATION OF FORCES EXERTED ON A MICROPARTICLE BY A LASER BEAM

RETO RODOLFO DORIZZI

A thesis submitted in partial fulfilment of the
requirements of the University of Hertfordshire
for the degree of Doctor of Philosophy

This programme of research was carried out in the
Department of Physics, Astronomy and Mathematics,
Faculty of Engineering and Information Sciences,
University of Hertfordshire

October 2004

Acknowledgements

I would especially like to thank my supervisors Dr Z. J. Ulanowski and Dr I. K. Ludlow for their constructive discussions, helpful criticism and encouragements throughout this work.

Abstract

A mathematical description of the electromagnetic fields of non-paraxial laser beams is derived and used to calculate the trapping forces on spherical particles. The fields are exact solutions to the wave equation. A set of closed-form expressions for the scalar field of such a beam is presented first. The solution for the order 00 is equivalent to the wave of a combined complex-point source and sink. In the far field the two lowest order solutions, 00 and 01, closely match the energy density produced by a high-numerical aperture lens illuminated by a paraxial Gaussian beam. At the large beam waist limit these two solutions reduce to the paraxial beam form. However, it is found that only the 01 order solution is physically realizable, since the total energy flux through the transverse section of the 00 order beam is infinite. The scalar solutions of arbitrary order are then used to derive solutions to the vector wave equation. Next, the electric and magnetic fields that closely fit the far-field boundary conditions for a focusing lens are constructed from the solutions for the orders 00 and 01. These fields are in general elliptically polarized at the beam waist. However at the large beam waist (paraxial) limit and in the far field limit the fields become linearly polarized. The electromagnetic field due to order 01 is used to calculate the Maxwell stress tensor, and hence the trapping forces exerted on a dielectric microsphere in a single beam laser tweezers setup. It is demonstrated that the electromagnetic theory model based on the 5th order Gaussian beam approximation due to Barton is accurate for almost paraxial beams (numerical aperture NA<0.25), when compared to the model derived here. However, for strongly focused beams (NA>1) the 5th order approximation breaks down. Trapping forces on water droplets suspended in air and on polystyrene spheres suspended in water, exerted by a Gaussian laser beam focused with lenses of various numerical apertures are calculated. It is established that a model accurate for a strongly focused beam is vital, since in order to trap a particle effectively a focusing lens with NA>1 is required.

Index

1. Background

1. 1. Introduction

The laser beam of light is generated inside the resonator cavity of the laser by the process of spontaneous emission, stimulated emission and absorption. These processes are triggered by an electromagnetic (E.M.) wave interacting with a material. Lasers generate or amplify coherent radiation at frequencies in the infrared, visible and ultraviolet regions of the E.M. spectrum. Many different laser materials and many different atomic systems are used to produce laser cavities. The main types include: semiconductor based lasers such as the GaAs laser, gas based lasers such as the HeNe laser and solid state lasers such as the ruby or neodymium yttrium aluminium garnet (Nd:YAG) laser. The resonator cavity of the laser can be viewed in analogy with the quantum mechanical particle in a box problem. Hence the resonator cavity gives rise to transverse E.M. modes (TEM modes) and longitudinal modes (standing wave modes). Since the lowest order transverse oscillation mode (TEM_{00}) of the laser cavity gives rise to a light beam with a Gaussian irradiance profile, it is referred to as a Gaussian beam. Pioneering work describing the laser resonator, based on diffraction theory, was presented by Schawlow and Towns [1]. Fox and Lie [2] were the first researches to calculate the modes of the laser cavity using scalar diffraction theory. A laser beam, like any other form of light, is based on an E.M. wave propagating in space and carrying momentum. In addition the laser beam has some very specific properties such as very high directionality, monochromaticity, coherence and radiance [3]. These properties lead to an enormous variety of applications. Each area of application makes use of one or more of these characteristic properties of the beam. It is possible to separate the areas of applications of laser beams into two categories; weakly or unfocused and strongly focused laser beams.

Unfocused and weakly focused Gaussian beams:

The laser beam is not focused in applications such as laser pointers, lidar speed guns, telecommunication and light interference based applications, since use is made of the high directionality, monochromaticity, coherence and radiance of the laser beam. If for example in a laser pointer or lidar speed gun the beam would be strongly focused, then the laser pointer would shine a large faint spot onto the screen it is pointed at, since the beam would lose its property of high directionality and hence would be strongly divergent. Similarly a lidar gun would not function properly, since only a small amount of the laser light would be reflected back off the body work of the vehicle it is pointed at and the greatest part of the light would shine into the space surrounding the vehicle. In a lidar gun [4], a battery

powers the laser diode. This diode emits infrared laser pulses every five milliseconds. Filters receive pulses reflected off a target object and focus them onto an avalanche diode, which converts them to electronic signals. High-speed timing circuitry tracks the time it takes for a pulse to reflect and return from the target, and algorithms use the data to determine the object's distance. The algorithm calculates the distance again for subsequent pulses and then computes the velocity by dividing the change in distance by the change in time. In a laser pointer a laser diode emits a beam of light in the visible region of the E.M. spectrum. This low power laser light beam can then be pointed onto any screen. In telecommunication the laser beam is internally reflected when propagating along optical fibers. In this application use is made of the properties of directionality and coherence of the laser light. In interference based applications, such as holography use is made of the high coherence of the laser light.

Strongly focused Gaussian beams

Tightly focused Gaussian laser beams are used in applications such as laser printers, metal cutting instruments, surgical instruments, burning of wafers for microchips, microscopy, optical information storage (CD and DVD players), light scattering from particles and entrapment and manipulation of particles. In light scattering applications, a laser beam is shone on an object, and the scattered field is investigated in order to determine the size, structure and refractive index of the particle. In this application use is made of the high degree of monochromaticity of the laser beam. In applications such as CD/DVD players, use is made of the high directionality and radiance of the laser beam. In order to read a CD a laser beam scans the surface of the disc, if the surface of the disc reflects the light, it is regarded in binary terms as a one and if it is not reflected, then the signal is regarded as a zero. Therefore a sequence of ones and zeros can be obtained. The same principle is used in DVD players. The data density of DVD's is much greater than that of CD's. So in order to store more data it is useful to focus a laser beam as strongly as possible. In applications such as metal cutting, surgical instruments and laser printers, use is mainly made of the property of radiance. In some of these applications the laser in effect burns a hole. The more focused the beam is, the more heat is produced at the focus. Furthermore in applications such as surgical instruments and metal cutting it can be said that the tighter the beam is focused, the less damage is inflicted to the regions in the proximity of the focus, since the focal spot becomes smaller. In the case of a laser printer, where the laser beam is used to charge the drum, the resolution can be increased by decreasing the focal spot

radius. In this work the attention is concentrated on the manipulation of microparticles. Atoms can be trapped by laser light since light carries momentum, and thus exerts radiation forces. If an atom is bombarded with a beam of light of a particular frequency, it will continuously absorb and re-emit photons. As the atom absorbs each photon, it receives a momentum kick in the direction of the light beam propagation. These kicks add up to produce a scattering force, which is proportional to the momentum of each photon and the number of photons that the atom scatters per second. For each photon, which is absorbed by the atom, one is emitted. Since the photons are released with no preferred direction, the changes in momentum caused by the emission, average to zero. Absorption and emission have the net effect of pushing the atom in the direction of the light propagation. It is impossible to construct a light trap out of any configuration of light beams if the scattering force is proportional to the light intensity. The problem is that the beams cannot be arranged to generate only inward directed forces. Any light that enters a trapping region must eventually escape and must therefore carry outward directed forces as well. Atoms can be trapped due to the dipole force. An E.M. field with a local maximum can be achieved in a dynamic system. Since light is made up of a rapidly oscillating E.M. field, a focused laser beam can produce an alternating E.M. field with a local maximum. When this field interacts with an atom, it alters the distribution of electrons within the atom, thereby inducing an electric dipole moment. As the field changes polarity, the dipole moment of the atom also switches around. As long as the field changes at a rate slower than the natural oscillation frequencies of the atom, the dipole moment remains aligned with the field. Thus the atom continues to move towards the local maximum. In the 1980's and early 1990's work on atom trapping has stimulated renewed interest in manipulating neutral particles. Not only atoms, but also micron-size particles, such as polystyrene spheres, can be optically trapped. The steep gradient of the irradiance profile at the centre of a focused laser beam gives rise to trapping forces. As long as the light is tuned away from absorption frequencies of the particle, it will be drawn into the region of highest light intensity. In 1970 Ashkin [5] trapped micron-size latex spheres suspended in water between two focused, counter propagating beams of light. It was later realised that if a single beam is focused tightly enough, the gradient force would suffice to overcome the scattering force that pushes the particle in the direction of propagation of the laser beam [5, 6, 7].

Today, a commonly used technique to manipulate microparticles is "optical trapping". An optical trap is also known as a "laser tweezers". Laser tweezers use a strongly focused laser

beam, with wavelength in the near infrared region of the E.M. spectrum, to hold in place or to move a microparticle. Laser tweezers can also be used to hold and move organelles inside of cells without puncturing the intervening membranes. Thus laser tweezers are a non-contact method. The optical tweezers can easily be integrated with a conventional microscope by introducing the laser light into the body of the microscope and focusing it with the viewing objective. Observation of the trapped particles is made possible by a CCD camera attached to the microscope [7, 8]. Ashkin and Dziedzic [9] found that laser tweezers are able to handle live bacteria and other organisms without apparently damaging them. The ability to trap live organisms without harming them is surprising, since the intensity at the focal point is about 10^{11} Wm^{-2} [7]. It turns out, that as long as the organism is very nearly transparent at the frequency of the trapping light, the beam passes through the object without significant energy being absorbed and converted into destructive heat or even generating damaging photochemistry. Furthermore, the organism is effectively cooled by the surrounding water. This ability has captured the imagination of biologists. Berns [6] has managed to manipulate chromosomes inside a cell nucleus. On an even smaller scale Chu [7] and colleagues have managed to manipulate a single DNA molecule by attaching polystyrene spheres to the ends of a strand of DNA and holding the spheres with two optical tweezers. But a tightly focused laser beam can also act as scalpel or scissors in medical applications in order to perform minimally invasive surgery on organs. Laser scissors consist of a tightly focused beam of light with wavelength in the near ultraviolet region of the E.M. spectrum, which ablates the material at the focus of the beam. The beams of scissors and tweezers differ significantly in duration and intensity. Whereas the scissors employ short pulses of high irradiance, tweezers make use of continuous, low-irradiance beams. In biological applications the cell membrane can be incised, i.e. the laser cutting a micron-size hole that seals within a fraction of a second. Through this technique, called optoporation (pore production through optical means), molecules can be inserted into a cell when the pores are open without permanently damaging the membrane. Furthermore using laser scissors, particular changes in a chromosome, deep within the cell, can be produced, which persists in the cloned progeny of those cells. In Europe, laser-scissors have been used for the manipulation of human gametes (sperm and egg) as part of a procedure called assisted hatching. The scissors thin or remove a small area of the protective zona pellucida of eggs that have been fertilised in a laboratory dish. The very early embryos are then placed in the womb, where the thinning of the zona appears to abet implantation. By using these techniques it was found that the pregnancy rate can be increased by more than 50 percent [6]. Berns [6] and his colleagues have used laser

scissors to open a single cell in order to analyse its chemical components at any given moment. If a laser is focused on or above the glass microscope slide on which the cell rests, a minuscule cloud of ionised gas, called microplasma, is formed. The expansion and contraction of this micro plasma generates mechanical stresses that can rupture the cell. By placing a tiny glass capillary tube just above the cell, it is possible to collect its contents and to analyse them, producing a snapshot of the cell's biochemistry at that moment. This technique has the potential for applications in single-cell analytical chemistry. One particular goal is to determine the exact identities and concentrations of proteins important in cancer at the single-cell level. In all applications of laser tweezers and scissors precision and selectivity is very important. Precision refers to the targeting of the laser beam exactly to the correct point, selectivity pertains to the controlled alteration of the target while leaving the surrounding unaffected. In this area of application, use is made of the fact that the irradiance profile of a TEM_{00} mode Gaussian laser beam has cylindrical symmetry along the axes of propagation and the irradiance profile is of Gaussian form. This implies that the irradiance profile is clearly defined and hence the E.M. field accurately calculable. The advantage of using a laser which produces a Gaussian distribution of energy is that the energy forming the focal spot can be characterised by a bell shaped curve. Because only the peak of this curve may have sufficient energy to alter a particular target organelle, the effective spot can be significantly smaller than the diameter of the measured focal spot. For example a neodymium yttrium aluminium garnet (Nd:YAG) laser operating at a wavelength of 532 nm can produce a beam spot radius of 499 nm when focused with a state-of-the-art, oil-immersion microscope objective at 100 × magnification [6]. It could intuitively be assumed that a laser beam would behave in accordance with the ray optics approximation but, as will be demonstrated, this is not the case. In order to make advances in many of these areas, it is advantageous to have an accurate, mathematical description of the laser beam. The first aim of the present research is to derive a model which describes the E.M. field of a tightly focused Gaussian laser beam. The second aim is to use the derived E.M. field in order to calculate the Maxwell stress tensor and hence to determine the optical trapping forces exerted on a dielectric spherical particle. The principle of the generation of such a beam will be examined. The most common approximation models such as the paraxial beam approximation, the fifth order Gaussian beam approximation, a model based on the complex source point model and a numerical method based on Fourier transform theory will be discussed. It will be demonstrated that the paraxial Gaussian beam approximation is accurate for weakly focused beams. However for strongly focused beams this model is not accurate enough. Some of the new developments require the half angle

divergence to be as close to 90° as possible. In order to improve precision, a good understanding of the physical properties of a strongly focused Gaussian beam is required. Thus without precise models describing the tightly focused Gaussian beam the forces acting on an optically trapped object cannot be calculated with reasonable accuracy. Recent studies have shown the necessity of a better description of such a beam in order to make further developments in all areas of applications discussed above. The aim of this chapter is to discuss the generation of laser beams and their properties. In the chapters 2, 3 and 4 a new model is derived which leads to a closed form description of a tightly focused laser beam of arbitrary order. Since many applications are based on the E.M. field produced by a laser, there is a need for an exact E.M. model; therefore the presented model is an exact vector description of a tightly focused laser beam. Using this new E.M. model, the forces exerted by a strongly focused Gaussian beam on a dielectric microsphere are calculated in chapter 5.

Since the laser light is an E.M. wave, the most basic equations any closed form description of a Gaussian beam has to satisfy are Maxwell's equations and the wave equation, that can be derived form the four Maxwell equations:

$$\nabla \bullet \mathbf{E}(\mathbf{r},t) = \frac{\rho(\mathbf{r})}{\varepsilon} \tag{1.1}$$

$$\nabla \bullet \mathbf{B}(\mathbf{r},t) = 0 \tag{1.2}$$

$$\nabla \times \mathbf{B}(\mathbf{r},t) = \mu \mathbf{J}(\mathbf{r},t) + \varepsilon\mu \frac{\partial \mathbf{E}(\mathbf{r},t)}{\partial t} \tag{1.3}$$

$$\nabla \times \mathbf{E}(\mathbf{r},t) = -\frac{\partial \mathbf{B}(\mathbf{r},t)}{\partial t} \quad . \tag{1.4}$$

Where $\mathbf{E}(\mathbf{r}, t)$ is the electric field intensity at position $\mathbf{r} = x\hat{\mathbf{i}} + y\hat{\mathbf{j}} + z\hat{\mathbf{k}}$, $\hat{\mathbf{i}}, \hat{\mathbf{j}}$ and $\hat{\mathbf{k}}$ being the Cartesian unit vectors, and time t. $\mathbf{B}(\mathbf{r}, t)$ is the flux density at position $\mathbf{r}$ and time t, $\mathbf{J}(\mathbf{r}, t)$ is the electric current density, $\rho(\mathbf{r})$ is the charge density, $\mu=\mu_0\mu_r$ is the absolute permeability, μ_0 is the vacuum permeability of free space and μ_r is the permeability of the material, $\varepsilon=\varepsilon_0\varepsilon_r$ is the absolute permittivity, ε_0 is the permittivity of free space and ε_r is the permittivity of the material

In the case of a physical realisable time-harmonic E.M. field, in regions remote from any sources, such as the field produced by a propagating laser beam, in a linear, isotropic, homogeneous, non magnetic medium, the absence of free charge and current, i.e. $\rho(\mathbf{r})=0$ and $\mathbf{J}(\mathbf{r}, t) =0$ is implied. Thus Eqs.(1.1 – 1.4) reduce to

$$\nabla \bullet \mathbf{E}(\mathbf{r},t) = 0 \tag{1.5}$$

$$\nabla \bullet \mathbf{B}(\mathbf{r},t) = 0 \tag{1.6}$$

$$\nabla \times \mathbf{B}(\mathbf{r},t) = \varepsilon\mu_0 \frac{\partial \mathbf{E}(\mathbf{r},t)}{\partial t} \tag{1.7}$$

$$\nabla \times \mathbf{E}(\mathbf{r},t) = -\frac{\partial \mathbf{B}(\mathbf{r},t)}{\partial t} \quad . \tag{1.8}$$

Taking the curl of Eq. (1.8)

$$\nabla \times (\nabla \times \mathbf{E}(\mathbf{r},t)) = -\frac{\partial (\nabla \times \mathbf{B}(\mathbf{r},t))}{\partial t} \quad , \tag{1.9}$$

using the vector identity: $\nabla \times (\nabla \times \mathbf{E}(\mathbf{r},t)) = \nabla(\nabla \bullet \mathbf{E}(\mathbf{r},t)) - \nabla^2 \mathbf{E}(\mathbf{r},t)$ and substituting Eq. (1.7) into Eq. (1.9) yields with the help of Eq. (1.5)

$$\nabla^2 \mathbf{E}(\mathbf{r},t) - \varepsilon\mu_0 \frac{\partial^2 \mathbf{E}(\mathbf{r},t)}{\partial t^2} = 0 \quad , \tag{1.10}$$

where ∇^2 is the Laplacian operator, given in Cartesian coordinates by

$$\nabla^2 = \frac{\partial^2}{\partial x^2} + \frac{\partial^2}{\partial y^2} + \frac{\partial^2}{\partial z^2} \quad .$$

Remembering that the speed of light in vacuum can be expressed as

$$c = \frac{1}{\sqrt{\varepsilon_0 \mu_0}} ,$$

It follows that

$$\varepsilon\mu_0 = \frac{1}{v^2} .$$

Therefore Eq. (1.10) can be rewritten as

$$\nabla^2 \mathbf{E}(\mathbf{r},t) - \frac{1}{v^2} \frac{\partial^2 \mathbf{E}(\mathbf{r},t)}{\partial t^2} = 0 \quad , \tag{1.11}$$

where v is the velocity of light in a medium. Assuming a time harmonic factor $e^{-i\omega t}$, with ω being the angular frequency, and defining the propagation constant of light in a medium, k, as $k = \omega\sqrt{\varepsilon\mu_0} = \frac{\omega}{v}$, Eq. (1.11) becomes

$$\left(\nabla^2 + k^2\right)\mathbf{E}(\mathbf{r},t) = 0\,. \tag{1.12}$$

Further, in the considered case, it can be shown from Eqs. (1.7) and (1.8), that there is the following dependence between $\mathbf{E}(\mathbf{r},t)$ and the magnetic field intensity $\mathbf{H}(\mathbf{r},t)$,

$$\nabla \times \mathbf{E}(\mathbf{r},t) = i\omega\mu_0\mathbf{H}(\mathbf{r},t)$$

$$\nabla \times \mathbf{H}(\mathbf{r},t) = -i\omega\varepsilon\mathbf{E}(\mathbf{r},t),$$

where in the considered case $\mathbf{H}(\mathbf{r},t) = \frac{\mathbf{B}(\mathbf{r},t)}{\mu_0}$.

Thus for the magnetic field intensity Eq. (1.12) can be written as

$$\left(\nabla^2 + k^2\right)\mathbf{H}(\mathbf{r},t) = 0\,. \tag{1.13}$$

In order to derive the E.M. field of a laser beam, it is easier to first discuss the form of the exact solution to the scalar wave equation

$$\nabla^2 u(r,t) = \frac{1}{v^2}\frac{\partial^2 u(r,t)}{\partial t^2} \quad , \tag{1.14}$$

and subsequently derive the solution in chapter 2. Referring to Eq. (1.14), $u(r, t)$ is a scalar field and $r = \sqrt{x^2 + y^2 + z^2}$ is the location of a point P with respect to the origin of the coordinate system. It will be demonstrated in chapter 3 how a vector solution to the wave equation can be obtained based on the scalar solution to the wave equation. Consider a light disturbance at a position P and time t represented by a scalar function $u(r, t)$; for the case of linearly polarised waves, this function may be regarded as a representation of the electric or the magnetic field strength. It is also assumed here, that the wave considered is monochromatic. The field of such a monochromatic wave may be written as [10]

$$u(r,t) = U(r)\cos\left(\phi(r) - \omega t\right) \quad . \tag{1.15}$$

Where $U(r)$ and $\phi(r)$ are the amplitude and phase, respectively, of the wave at position P. Since $u(r, t)$ is generally complex, and only the real part of $u(r, t)$ has physical meaning, Eq. (1.15) can be rewritten, using complex notation, as

$$u(r,t) = \mathrm{Re}\left[U(r)e^{i(\phi(r)-\omega t)}\right] \quad , \tag{1.16}$$

where Re means "*the real part of*".

$u(r)$, is given by the following complex function of position (sometimes called phasor)

$$u(r) = U(r)e^{i\phi(r)} \quad . \tag{1.17}$$

In the case where $u(r, t)$ represents an optical wave, it must satisfy the scalar wave equation Eq. (1.14) at each source free point. However, since the time dependence $e^{-i\omega t}$ is known, the complex function $u(r)$ is an adequate description of the disturbance. Substituting Eq. (1.16) into Eq. (1.14) leads to

$$\mathrm{Re}\left[\nabla^2 u(r)e^{-i\omega t}\right] = \mathrm{Re}\left[-\frac{\omega^2}{v^2}u(r)e^{-i\omega t}\right]$$

or

$$\mathrm{Re}\left[\nabla^2 u(r)\right] = \mathrm{Re}\left[-k^2 u(r)\right]. \tag{1.18}$$

It thus follows from Eq. (1.18) that the complex disturbance $u(r)$ must satisfy the time-independent equation

$$\left(\nabla^2 + k^2\right)u(r) = 0 \quad , \tag{1.19}$$

known as the Helmholtz equation. Where the function $u(r)$ represents the spatial part (that is the time-independent part) of the solution of the wave equation.

Another important aspect to consider is, that E.M. waves carry energy. The instantaneous energy flux through a particular area is given by the instantaneous Poynting vector

$$\mathbf{S}_{inst}(\mathbf{r},t) = \mathbf{E}(\mathbf{r},t)\times\mathbf{H}(\mathbf{r},t). \tag{1.20.a}$$

However, since the irradiance is a measurable quantity it is necessary in order to obtain the physical quantity of interest, to again only consider the real part of $\mathbf{E}(\mathbf{r}, t)$ and $\mathbf{H}(\mathbf{r}, t)$. Thus Eq. (1.20.a) is re-expressed according to Wangsness [11] as

$$\mathbf{S}(\mathbf{r},t) = \mathrm{Re}[\mathbf{E}(\mathbf{r},t)] \times \mathrm{Re}[\mathbf{H}(\mathbf{r},t)]. \tag{1.20.b}$$

Since the electric and magnetic field intensities of the E.M. waves oscillate in time, so does the Poynting vector. Hence the quantity of interest is the time averaged Poynting vector $\langle \mathbf{S} \rangle$. In order to calculate the time averaged Poynting vector [11], the electric and magnetic field intensities are written as

$$\mathbf{E}(\mathbf{r},t) = \mathbf{E}_0 e^{i(\mathbf{k}\cdot\mathbf{r}-\omega t)} \tag{1.21}$$

and

$$\mathbf{H}(\mathbf{r},t) = \mathbf{H}_0 e^{i(\mathbf{k}\cdot\mathbf{r}-\omega t)}, \tag{1.22}$$

where the propagation vector $\mathbf{k}=k\hat{\mathbf{k}}$, $\mathbf{E}_0$ and $\mathbf{H}_0$ are arbitrary constant vectors. In order to simplify the expressions, the following substitution is made:

$$\mathbf{E}(\mathbf{r},0) = \mathbf{E}_0 e^{i\mathbf{k}\cdot\mathbf{r}} \tag{1.23}$$

and

$$\mathbf{H}(\mathbf{r},0) = \mathbf{H}_0 e^{i\mathbf{k}\cdot\mathbf{r}}. \tag{1.24}$$

The real part of $\mathbf{E}(\mathbf{r},0)$ and $\mathbf{H}(\mathbf{r},0)$ are abbreviated in the derivations below as $\mathbf{E}_R(\mathbf{r},0)$ and $\mathbf{H}_R(\mathbf{r},0)$. Similarly the imaginary parts are abbreviated as $\mathbf{E}_I(\mathbf{r},0)$ and $\mathbf{H}_I(\mathbf{r},0)$.

Thus Eqs. (1.21) and (1.22) can be written as

$$\mathbf{E}(\mathbf{r},t) = \left(\mathbf{E}_R(\mathbf{r},0) + i\mathbf{E}_I(\mathbf{r},0)\right)\left(\cos\omega t - i\sin\omega t\right) \tag{1.25}$$

and

$$\mathbf{H}(\mathbf{r},t) = \left(\mathbf{H}_R(\mathbf{r},0) + i\mathbf{H}_I(\mathbf{r},0)\right)\left(\cos\omega t - i\sin\omega t\right). \tag{1.26}$$

Hence

$$\mathrm{Re}[\mathbf{E}(\mathbf{r},t)] = \mathbf{E}_R(\mathbf{r},0)\cos\omega t + \mathbf{E}_I(\mathbf{r},0)\sin\omega t \tag{1.27}$$

and

$$\mathrm{Re}[\mathbf{H}(\mathbf{r},t)] = \mathbf{H}_R(\mathbf{r},0)\cos\omega t + \mathbf{H}_I(\mathbf{r},0)\sin\omega t\,. \tag{1.28}$$

On substitution of Eqs. (1.27) and (1.28) into Eq. (1.20.b), the Poynting vector can be rewritten as

$$\mathbf{S}(\mathbf{r},t) = (\mathbf{E}_R(\mathbf{r},0)\times\mathbf{H}_R(\mathbf{r},0))\cos^2\omega t + (\mathbf{E}_R(\mathbf{r},0)\times\mathbf{H}_I(\mathbf{r},0)+\mathbf{E}_I(\mathbf{r},0)\times\mathbf{H}_R(\mathbf{r},0))\cos\omega t\sin\omega t + (\mathbf{E}_I(\mathbf{r},0)\times\mathbf{H}_I(\mathbf{r},0))\sin^2\omega t \tag{1.29}$$

Now averaging the Poynting vector over one cycle of oscillation leads to

$$\langle\mathbf{S}(\mathbf{r})\rangle = \frac{1}{2}[(\mathbf{E}_R(\mathbf{r},0)\times\mathbf{H}_R(\mathbf{r},0))+(\mathbf{E}_I(\mathbf{r},0)\times\mathbf{H}_I(\mathbf{r},0))], \tag{1.30}$$

since $\langle\cos^2\omega t\rangle = \langle\sin^2\omega t\rangle = \frac{1}{2}$ and $\langle\cos\omega t\sin\omega t\rangle = 0$.

It is now interesting to demonstrate, that Eq. (1.30) can be obtained in a different way. Taking the complex conjugate of Eq. (1.26) leads to

$$\mathbf{H}^*(\mathbf{r},t) = (\mathbf{H}_R(\mathbf{r},0)-i\mathbf{H}_I(\mathbf{r},0))(\cos\omega t + i\sin\omega t) = (\mathbf{H}_R(\mathbf{r},0)-i\mathbf{H}_I(\mathbf{r},0))e^{i\omega t}\,, \tag{1.31}$$

where asterisk represents complex conjugation. Similarly Eq. (1.25) can be rewritten as

$$\mathbf{E}(\mathbf{r},t) = (\mathbf{E}_R(\mathbf{r},0)+i\mathbf{E}_I(\mathbf{r},0))e^{-i\omega t}\,. \tag{1.32}$$

Thus

$$\mathbf{E}(\mathbf{r},t)\times\mathbf{H}^*(\mathbf{r},t) = \mathbf{E}_R(\mathbf{r},0)\times\mathbf{H}_R(\mathbf{r},0)+\mathbf{E}_I(\mathbf{r},0)\times\mathbf{H}_I(\mathbf{r},0)+ i(\mathbf{E}_I(\mathbf{r},0)\times\mathbf{H}_R(\mathbf{r},0)-\mathbf{E}_R(\mathbf{r},0)\times\mathbf{H}_I(\mathbf{r},0)) \tag{1.33}$$

By taking the real part of Eq. (1.33) and comparing the result with Eq. (1.30) it follows that the time averaged Poynting vector is given by

$$\langle\mathbf{S}(\mathbf{r})\rangle = \frac{1}{2}\mathrm{Re}[\mathbf{E}(\mathbf{r},t)\times\mathbf{H}^*(\mathbf{r},t)]. \tag{1.34}$$

Two closely related quantities to the time averaged Poynting vector, are the time averaged electric and magnetic energy densities given by Pedrotti and Pedrotti [12] as

$$\langle u_E(\mathbf{r})\rangle = \frac{1}{4}\varepsilon \mathbf{E}(\mathbf{r},t)\bullet \mathbf{E}^*(\mathbf{r},t) \tag{1.35}$$

and

$$\langle u_H(\mathbf{r})\rangle = \frac{1}{4}\mu_0 \mathbf{H}(\mathbf{r},t)\bullet \mathbf{H}^*(\mathbf{r},t) \quad , \tag{1.36}$$

which can be obtained using similar calculations as above. Additionally $\langle u_E(\mathbf{r})\rangle = \langle u_H(\mathbf{r})\rangle$.

The total time average energy density is given by $\langle u_E(\mathbf{r})\rangle + \langle u_H(\mathbf{r})\rangle$.

Thus

$$\langle u(\mathbf{r})\rangle = \frac{1}{2}\varepsilon \mathbf{E}(\mathbf{r},t)\bullet \mathbf{E}^*(\mathbf{r},t) = \frac{1}{2}\mu_0 \mathbf{H}(\mathbf{r},t)\bullet \mathbf{H}^*(\mathbf{r},t)$$

Especially in optics the irradiance at a position **r** [12]

$$I(\mathbf{r}) = \langle |\mathbf{S}(\mathbf{r})| \rangle = \frac{1}{2}\sqrt{\frac{\varepsilon}{\mu_0}}\mathbf{E}(\mathbf{r},t)\bullet \mathbf{E}^*(\mathbf{r},t) = \frac{1}{2}\sqrt{\frac{\mu_0}{\varepsilon}}\mathbf{H}(\mathbf{r},t)\bullet \mathbf{H}^*(\mathbf{r},t) \tag{1.37}$$

of a plane E.M. wave is of interest.

Since a laser beam of light is generated in an optical resonator, it is necessary to discuss the optical resonator first.

1.2. The optical resonator

Fox and Lie [2] were the first researchers to calculate the oscillations modes of the plane parallel resonator using scalar diffraction theory. However their treatment did not lead to an analytical solution describing the resonator modes. Boyd and Gordon [13] however found an analytical solution for the resonator modes, by considering a confocal resonator cavity instead of a plane parallel resonator. The field treated by Fox and Li [2] can be described by a scalar quantity $u(\mathbf{r})$ representing, for instance, the magnitude of the electric field. $u_1(\mathbf{r}_1)$ is an arbitrary field distribution at a point P_1 on mirror 1. This distribution will, due to diffraction, produce a field distribution $u_2(\mathbf{r}_2)$ at a point P_2 on mirror 2.
(See Fig. 1.1.) , n is the normal to mirror 1 and 2:

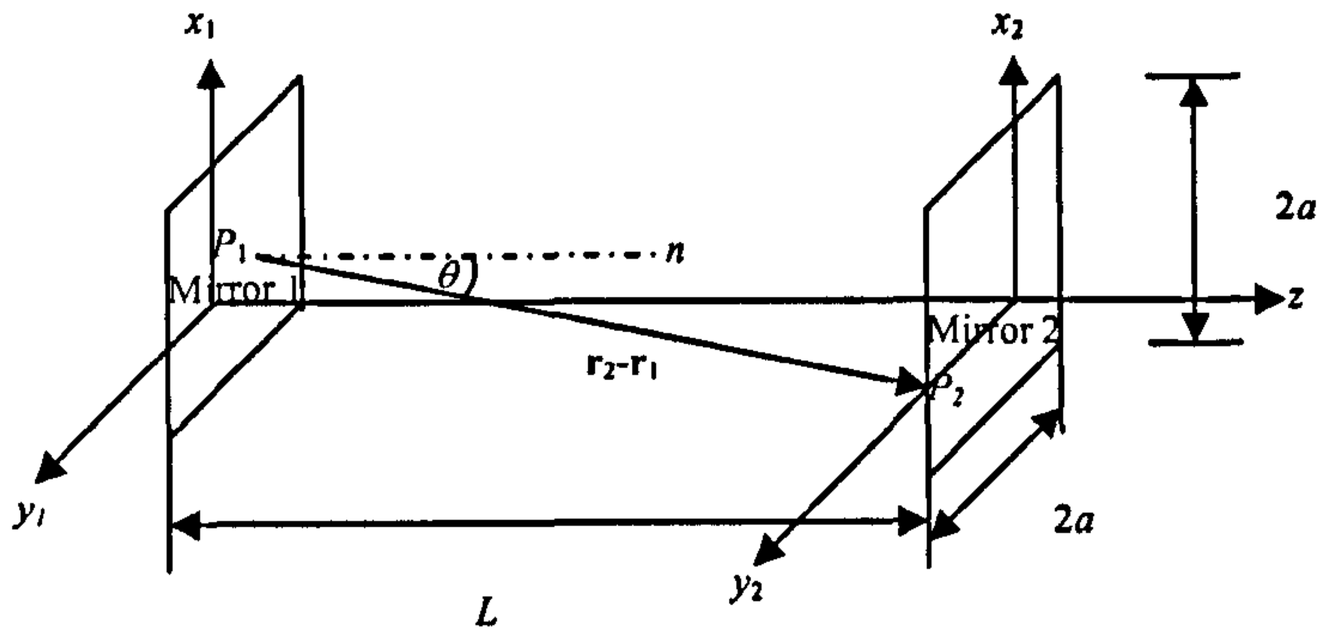

Fig. 1.1. Mode calculation for a plane parallel resonator by use of Kirchhoff diffraction integral (adapted from Svelto [3]).

Fox and Li [2] found that the field $u_2(\mathbf{r}_2)$ at a general point P_2 on mirror 2 can be expressed in terms of the field $u_1(\mathbf{r}_1)$ at a general point P_1 on mirror 1, using the Fresnel-Kirchhoff diffraction integral, as

$$u_2(\mathbf{r}_2) = -\frac{i}{2\lambda}\int\frac{u_1(\mathbf{r}_1)e^{ik|\mathbf{r}_2-\mathbf{r}_1|}(1+\cos\theta)}{|\mathbf{r}_2-\mathbf{r}_1|}\mathrm{d}S_1 \quad . \tag{1.38}$$

Where $|\mathbf{r}_2-\mathbf{r}_1| = \sqrt{(x_2-x_1)^2+(y_2-y_1)^2+(z_2-z_1)^2}$ is the distance between the points P_1 and P_2, θ is the angle that $|\mathbf{r}_2-\mathbf{r}_1|$ makes with the normal to mirror 1, n, at P_1, $\mathrm{d}S_1$ is the surface element around P_1, $k=\frac{2\pi}{\lambda}$, λ being the wavelength. The integral must be evaluated over the entire surface S_1. A distribution $u(\mathbf{r})$ corresponding to a cavity mode is considered instead of a general distribution $u_1(\mathbf{r}_1)$. If the two mirrors are identical, then the field distribution on mirror 2, as calculated by Eq. (1.38) must again be equal to $u(\mathbf{r})$ apart from some constant factor σ. Thus the following equation is obtained

$$\sigma u(\mathbf{r}_2) = -\frac{i}{2\lambda}\int\frac{u(\mathbf{r}_1)e^{ik|\mathbf{r}_2-\mathbf{r}_1|}(1+\cos\theta)}{|\mathbf{r}_2-\mathbf{r}_1|}\mathrm{d}S_1 \quad . \tag{1.39}$$

Eq. (1.39) is a Fredholm homogeneous integral equation of the second kind [3]. Its eigensolutions $u(\mathbf{r})$ give the cavity-mode field distribution over the mirrors. Once the field distribution $u(\mathbf{r})$ on the mirrors is known, it is possible, through Eq. (1.38), to calculate the field distribution at any point inside (standing wave) or outside (travelling wave) the resonator [3]. Fox and Li [2] made the approximation that the propagating wave inside the cavity is a purely transverse spherical wave; i.e. the wave has no longitudinal component. Fox and Li [2] considered the case where the cavity length L is much greater than its transverse dimension a, i.e. $L>>a$, Thus Eq. (1.39) was considerably simplified as

$\cos\theta \cong 1$ and $|\mathbf{r}_2 - \mathbf{r}_1| \cong L$ can be substituted in the amplitude factor appearing under the integral sign. In order to get a suitable approximate expression for the phase factor $k|\mathbf{r}_2 - \mathbf{r}_1|$, $|\mathbf{r}_2 - \mathbf{r}_1|$ is written as

$$|\mathbf{r}_2 - \mathbf{r}_1| = \left[L^2 + (x_1 - x_2)^2 + (y_1 - y_2)^2\right]^{\frac{1}{2}}$$

$$= L + \frac{1}{2L}\left[(x_1 - x_2)^2 + (y_1 - y_2)^2\right] + \varepsilon, \tag{1.40}$$

where a binomial expansion was used and it is apparent that $L = z_2 - z_1$. The remainder of the power series, ε, can be neglected provided that $k\varepsilon << 2\pi$ [3]. As ε consists of a converging series having terms of alternating signs, it follows that its value is smaller than the magnitude of the first term.

Boyd and Gordon [13] considered the confocal resonator, assuming for simplicity reasons, that the two mirrors have square cross sections of dimensions $2a$ (Fig. 1.2.), and have the same radius of curvature. Thus the foci of the two mirrors coincide at the centre of the cavity. It is thus implied that the length of the cavity is equal to the radius of curvature.

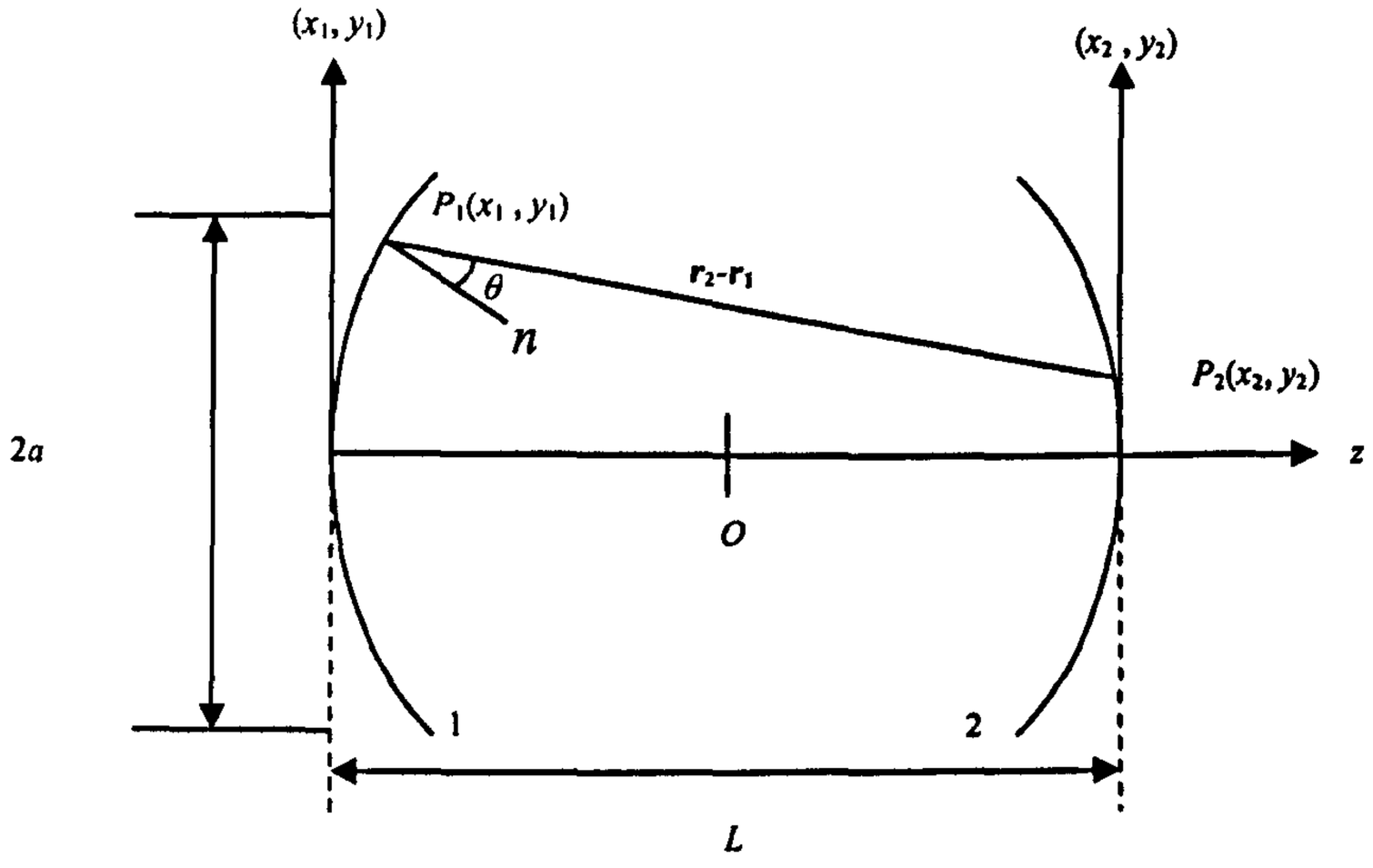

Fig. 1.2. Mode calculation for a confocal resonator using Kirchhoff diffraction integral (adapted from Svelto [3])

In their derivation it was also assumed that $L >> a, \cos\theta \cong 1$ and $|\mathbf{r}_2 - \mathbf{r}_1| \cong L$ can be substituted in the amplitude factor appearing under the integral sign in Eq.(1.39). However the net result of this assumption is, that the analytic solutions presented by Boyd and Gordon [13] are not exact solutions to the scalar Helmholtz equation. Instead they are solutions to the paraxial wave equation.

1.3. The paraxial wave equation

E.M. fields in free space or in any uniform isotropic medium are governed in general by the scalar wave equation. Thus by only considering the electric field, Eq. (1.19) can be rewritten as

$$\left[\nabla^2 + k^2\right]E(x,y,z) = 0 \quad , \tag{1.41}$$

where $E(x,y,z)$ is the phasor amplitude of a field distribution that varies with time as $e^{-i\omega t}$. Fox and Li [2] made the approximation that the propagating wave inside the cavity is a purely transverse spherical wave. As the optical beam propagates along the cavity axes, the primarily spatial dependence of $E(x,y,z)$ is an e^{ikz} variation. Since the transverse profile of the beam changes slowly with distance z due to diffraction and propagation effects, $E(x,y,z)$ is redefined as:

$$E(x,y,z) \equiv E_0 u(x,y,z) e^{ikz} \quad , \tag{1.42}$$

where $u(x,y,z)$ is a complex scalar wave amplitude which describes the transverse profile of the beam. Substituting Eq. (1.42) into Eq (1.41) yields in Cartesian coordinates

$$\frac{\partial^2 u(x,y,z)}{\partial x^2} + \frac{\partial^2 u(x,y,z)}{\partial y^2} + \frac{\partial^2 u(x,y,z)}{\partial z^2} + 2ik\frac{\partial u(x,y,z)}{\partial z} = 0 \,. \tag{1.43}$$

However Eqs. (1.42) and (1.43) can also be expressed in cylindrical coordinates as

$$E(\rho,\theta,z) \equiv E_0 u_c(\rho,\theta,z) e^{ikz} \tag{1.44}$$

and

$$\frac{1}{\rho}\frac{\partial}{\partial\rho}\left(\rho\frac{\partial u_c(\rho,\theta,z)}{\partial\rho}\right) + \frac{1}{\rho^2}\frac{\partial^2 u_c(\rho,\theta,z)}{\partial\theta^2} + \frac{\partial^2 u_c(\rho,\theta,z)}{\partial z^2} + 2ik\frac{\partial u_c(\rho,\theta,z)}{\partial z} = 0 \tag{1.45}$$

respectively, where $\rho = \sqrt{x^2 + y^2}$. It has to be emphasized that with the e^{ikz} dependence factored out, the remaining z dependence of the wave amplitude $u(x,y,z)$ or $u_c(\rho,\theta,z)$, is basically caused by diffraction effects, and this z dependence will in general be slow compared not only to one optical wavelength, as in e^{ikz}, but also in the transverse variations due to the finite width of the beam. The slowly varying dependence of $u(x,y,z)$ or $u_c(\rho,\theta,z)$

respectively on z is mathematically expressed by the *paraxial approximation* [14] in Cartesian coordinates as

$$\left|\frac{\partial^2 u(x,y,z)}{\partial z^2}\right| << \left|2k\frac{\partial u(x,y,z)}{\partial z}\right| \quad \text{or} \quad \left|\frac{\partial^2 u(x,y,z)}{\partial x^2}\right| \quad \text{or} \quad \left|\frac{\partial^2 u(x,y,z)}{\partial y^2}\right| \quad , \tag{1.46}$$

and in cylindrical coordinates as

$$\left|\frac{\partial^2 u_c(\rho,\theta,z)}{\partial z^2}\right| << \left|2k\frac{\partial u_c(\rho,\theta,z)}{\partial z}\right| \quad \text{or} \quad \left|\frac{\partial^2 u_c(\rho,\theta,z)}{\partial \rho^2}\right| \quad \text{or} \quad \left|\frac{\partial^2 u_c(\rho,\theta,z)}{\partial \theta^2}\right| \quad . \tag{1.47}$$

Thus the *paraxial wave equation* can be written in Cartesian coordinates as

$$\nabla_t^2 u(x,y,z) + 2ik\frac{\partial u(x,y,z)}{\partial z} = 0 \tag{1.48}$$

and in cylindrical coordinates as

$$\nabla_t^2 u_c(\rho,\theta,z) + 2ik\frac{\partial u_c(\rho,\theta,z)}{\partial z} = 0 \quad . \tag{1.49}$$

where ∇_t^2 is the Laplacian operator on the coordinates in the transverse plane.

1.3.1. Solutions to the paraxial wave equation

Boyd and Gordon [13] found the following eigenfunctions for the resonator modes in Cartesian coordinates

$$u_{mn}(x,y,z) = \frac{w_0}{w(z)} H_m\left(\frac{x\sqrt{2}}{w(z)}\right) H_n\left(\frac{y\sqrt{2}}{w(z)}\right) e^{-\frac{x^2+y^2}{w^2(z)}} e^{-i\left[k\frac{\left(x^2+y^2\right)}{2R(z)}+kz-(n+m+1)\phi(z)\right]} \quad , \tag{1.50.a}$$

in the literature referred to as the Hermite-Gaussian beam modes (TEM_{mn}). Since it is known from section 1.2. that $u(\mathbf{r})$ represents the magnitude of the electric field say, it is possible to write

$$E_{mn}(x,y,z) = E_0 u_{mn}(x,y,z) \quad . \tag{1.50.b}$$

The functions $H_m(s)$ and $H_n(s)$ in Eq. (1.50.a) are the Hermite polynomials of the m^{th} and n^{th} order (n=0, 1, 2, … and m=0, 1, 2, …). The Hermite polynomials are given by Boas [15] as

$$H_n(s) = (-1)^n e^{s^2} \frac{d^n}{ds^n} e^{-s^2} \quad . \tag{1.51}$$

On solving Eq. (1.51) it is found that

$$\begin{aligned} H_0(s) &= 1 \\ H_1(s) &= 2s \\ H_2(s) &= 4s^2 - 2 \end{aligned} \quad . \tag{1.52}$$

Since the beam is focused at the centre of the confocal resonator, it is convenient to choose the origin of the Cartesian coordinate system to be at the centre of the resonator.

The beam spot radius *w(z)* which appears in Eq. (1.50.a) is given by Svelto [3] as

$$w(z) = w_0 \sqrt{1 + \left(\frac{2z}{L}\right)^2} \quad , \tag{1.53}$$

where

$$w_0 = \sqrt{\frac{L\lambda}{2\pi}} \text{ or } w_0^2 k = L \tag{1.54}$$

is the spot radius at the centre of the resonator. The smallest spot radius occurs at the origin, z=0. The quantity w_0 is therefore usually referred to as the spot radius at the beam waist, or the beam waist radius, and the z coordinate is measured along the propagation direction with its origin at the waist. For $z = \pm\frac{L}{2}$ (i.e. on the mirrors) Eq. (1.53) gives $w\left(z = \pm\frac{L}{2}\right) = \sqrt{2} w_0$. Thus the spot radius at the mirrors is $\sqrt{2}$ larger than that at the centre of the resonator. This is readily understood from the fact that the mirrors tend to focus the

beam at the resonator centre. The functions $R(z)$ and $\phi(z)$, which appear in the phase term, the last exponential factor of Eq. (1.50.a), are given by Svelto [3] as

$$R(z) = z\left[1+\left(\frac{L}{2z}\right)^2\right] \qquad \phi(z) = \tan^{-1}\frac{2z}{L} \qquad (1.55)$$

From Eq. (1.50.a) it can be shown that the equiphase surfaces are, to a good approximation, spherical with radius of curvature equal to $R(z)$. ($R(z)$ is +ve when the centre of curvature is to the left of the wavefront.) For z=0 (centre of the resonator) R=∞ and the wavefront is plane, as expected from symmetry considerations. For $z=\pm\frac{L}{2}$ (i.e. on the mirrors) R=L. This shows that, as expected, the two mirror surfaces are also equiphase surfaces. If a laser beam is focused by a lens, then the minimum spot radius is at the focus (focal spot), referred to as the beam waist. Also in this case, the coordinate system has its origin at the beam waist. However Eqs. (1.53 and 1.55) are written with the help of Eq. (1.54) in a different form, by expressing the terms $\frac{2z}{L}$ and $\frac{L}{2z}$ in terms of w_0. Thus Eq. (1.53) becomes

$$w(z) = w_0\sqrt{1+\left(\frac{\lambda z}{\pi\omega_0^2}\right)^2}\quad , \qquad (1.56)$$

and Eqs. (1.55) become

$$R(z) = z\left[1+\left(\frac{\pi w_0^2}{\lambda z}\right)^2\right] \qquad \phi(z) = \tan^{-1}\left(\frac{\lambda z}{\pi\omega_0^2}\right) \qquad (1.57)$$

In cylindrical coordinates the eigenfunctions for the resonator modes can obtained from [16] and written in a form consistent with [13] as

$$u_{mn}(\rho,\theta,z) = \frac{w_0}{w(z)}\left(\frac{\rho\sqrt{2}}{w(z)}\right)^n \cos(n\theta)L_m^n\left(\frac{2\rho^2}{w(z)^2}\right)e^{-\frac{\rho^2}{w^2(z)}}e^{i\left[\frac{k\rho^2}{2R(z)}+kz-(2m+n+1)\phi(z)\right]}, \qquad (1.58.a)$$

or in terms of the magnitude of the electric field

$$E_{mn}(\rho,\theta,z) = E_0 u_{mn}(\rho,\theta,z). \qquad (1.58.b)$$

In the literature, these eigenfunctions are referred to as the Laguerre-Gaussian beam modes (TEM^*_{mn}). Where $L_m^n(s)$ are the associated Laguerre polynomials (m=0, 1, 2, ... and n is not restricted to be an integer. The only restriction is that n>-1) [15]

$$L_m^n(s) = \frac{s^{-n}e^s}{m!}\frac{d^m}{ds^m}\left(s^{n+m}e^{-s}\right) \quad . \tag{1.59}$$

On solving Eq. (1.59) it is found that

$$\begin{aligned} L_0^n(s) &= 1 \\ L_1^n(s) &= n+1-s \\ L_2^n(s) &= \frac{1}{2}(n+1)(n+2)-(n+2)s+\frac{1}{2}s^2 \end{aligned} \quad . \tag{1.60}$$

Substituting n=m=0 into Eq. (1.50.a) or Eq. (1.58.a) and only considering the amplitude part of these equations, it can be seen that the amplitude $A(x,y,z)$ or $A(\rho,\theta,z)$ respectively of the E.M. wave is proportional to

$$A(x,y,z) \propto e^{-\left(\frac{x^2+y^2}{w(z)^2}\right)} \tag{1.61}$$

or

$$A(\rho,\theta,z) \propto e^{-\left(\frac{\rho^2}{w(z)^2}\right)}. \tag{1.62}$$

From Eq. (1.62) it is apparent that the amplitude profile is gaussian in form. At the beam waist, $w(z)$=w_0 and it can be seen from Eq. (1.62) that if ρ=w_0, then A∝1/e. Thus $w(z)$ is the distance at which the amplitude is 1/e times that on axis.

1.3.2. Validity of the paraxial wave equation

An optical beam can be made up of a superposition of plane wave components travelling in directions making various angles with the z axis. Thus the axial and transverse variation of a plane wave component $E(x,z)$ (considering for simplicity reasons only one transverse coordinate) travelling at an angle θ to the z axis, in the xz plane can be written according to Siegman [14] as

$$E(x,z) = E_0 e^{ikx\sin\theta + ikz\cos\theta} = E_0 u(x,z) e^{ikz} \quad . \tag{1.63}$$

Then the exact form of the reduced complex scalar wave amplitude $u(x,z)$, and its approximate form in the paraxial approximation, becomes (using the small angle approximation given by Boas [15])

$$u(x,z) = e^{ikx\sin\theta - ikz(1-\cos\theta)} \approx e^{ik\left(\theta x - \frac{\theta^2 z}{2}\right)} \quad . \tag{1.64}$$

By using the small angle approximation, the normalized first and second derivatives of $u(x,z)$ in the transverse direction take the values

$$\begin{aligned} i\frac{2k}{u(x,z)}\frac{\partial u(x,z)}{\partial z} &= -2k^2(1-\cos\theta) \approx +k^2\theta^2 \\ \frac{1}{u(x,z)}\frac{\partial^2 u(x,z)}{\partial x^2} &= -k^2\sin^2\theta \approx -k^2\theta^2 \end{aligned} \quad . \tag{1.65}$$

However the second derivative in the z direction takes on the form

$$\frac{1}{u(x,z)}\frac{\partial^2 u(x,z)}{\partial z^2} = -k^2(1-\cos\theta)^2 \approx -\frac{k^2\theta^4}{4} \quad . \tag{1.66}$$

This is smaller than either of the preceding terms by the ratio $\frac{\theta^2}{4}$ (θ measured in radians).

This ratio will be very much less than 1 as long as $\theta \le \frac{1}{2}$ radian. Thus paraxial optical beams can be focused or can diverge at cone angles up to approximately 30 degrees, before significant corrections to the paraxial wave equation become necessary [14]. Therefore even though the paraxial wave approximation is not an exact solution to Maxwell's equations, it is a simple representation of a weakly focused Gaussian beam. As the paraxial Gaussian beam description was the first description of the laser beam, all the nomenclature is based on it. Furthermore the paraxial approximation can be used as a benchmark for any other model, which describes a Gaussian beam. As in the so-called paraxial limit, i.e. for a weakly focused beam, any such model should produce the same results as the paraxial approximation.

1.4. Description of a Gaussian laser beam.

The Gaussian laser beam is produced inside the resonator cavity of the laser. The adjective Gaussian is given since TEM_{mn} modes are defined to be the product of a Hermite polynomial and a Gaussian function. Since in the case of the TEM_{00} mode the Hermite polynomials of zero-order, $H_0(s)=1$, are multiplied with a Gaussian function, the radial profile of a beam propagating along the z axis is thus Gaussian along the x and y directions. Hermite–Gaussian laser beams are used in rectangular coordinates, as they are produced by rectangular laser cavities. Semiconductor based lasers normally have such cavities. However it is also possible to obtain Laguerre-Gaussian beams from a single longitudinal mode HeNe laser that operates in a stationary TEM^{*}_{01} hybrid mode configuration [17]. The Gaussian function here is multiplied by the generalized Laguerre polynomials. Since the Laguerre polynomial of zero-order $L_0^0(s)=1$, the radial profile of a lowest order beam propagating along the z axis is Gaussian, and is symmetric, with the axes of symmetry being the z axis. These modes are thus called the "Laguerre-Gaussian modes. Since both the Hermite-Gaussian and Laguerre-Gaussian functions each form a complete basis sets of orthogonal functions, it is possible to expand any Hermite solution in terms of Laguerre functions and vice versa. The normalised Gaussian irradiance profile at the beam waist of the few lowest order TEM_{mn}, which are obtained by substituting Eq. (1.50.b) into Eq. (1.37) and normalising the functions to 1, with $w_0=\sqrt{2}$, can be seen from Figs. 1.3.a), 1.4. a) 1.5.a) and 1.7.a). Fig. 1.6. a) represents the mode produced by a linear superposition of the TEM_{01} and the TEM_{10} modes. These modes are sometimes in the literature shown as density plots. The density plots for these modes can be seen in Figs. 1.3.b), 1.4.b) 1.5.b) and 1.7.b). Fig. 1.6.b) represents the density plot of the mode produced by a linear superposition of the TEM_{01} and the TEM_{10} modes. It is clearly visible from these plots that the normalised irradiance profile is Gaussian only for the lowest order TEM_{00}.

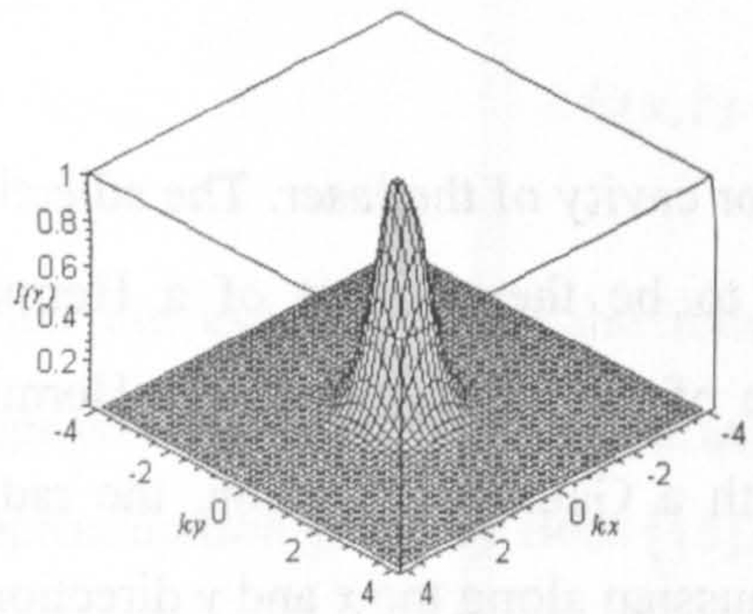

Fig. 1.3.a) TEM_{00} Hermite-Gaussian beam mode

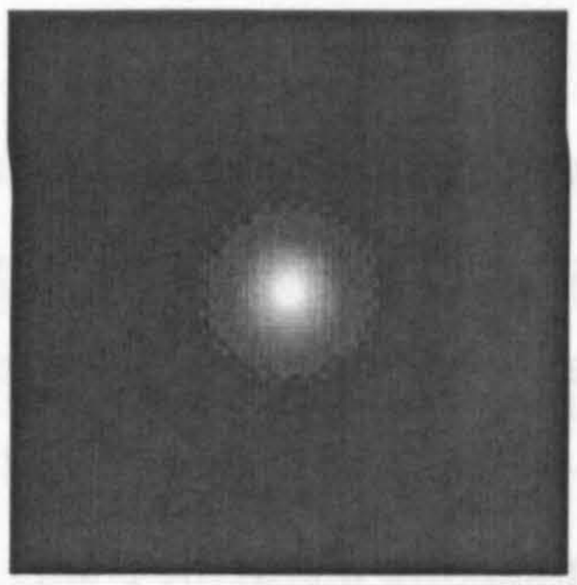

Fig. 1.3.b) Density plot TEM_{00} Hermite-Gaussian beam mode

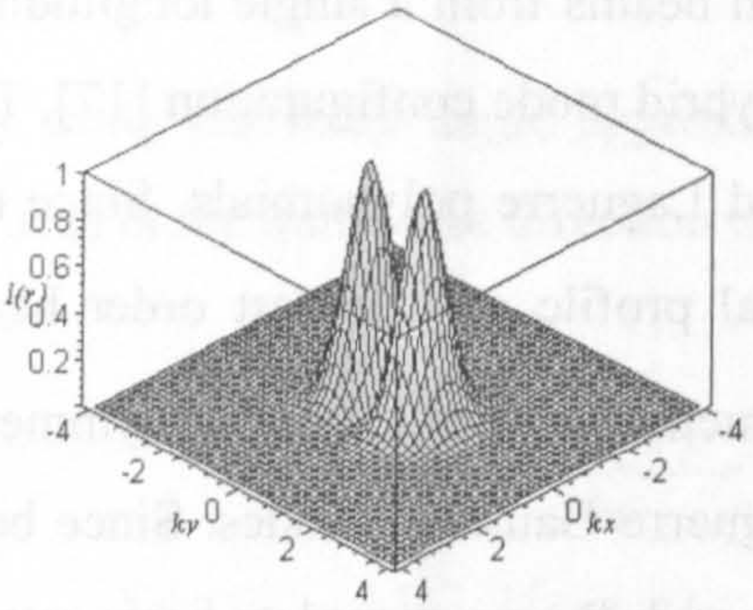

Fig. 1.4.a) TEM_{01} Hermite-Gaussian beam mode

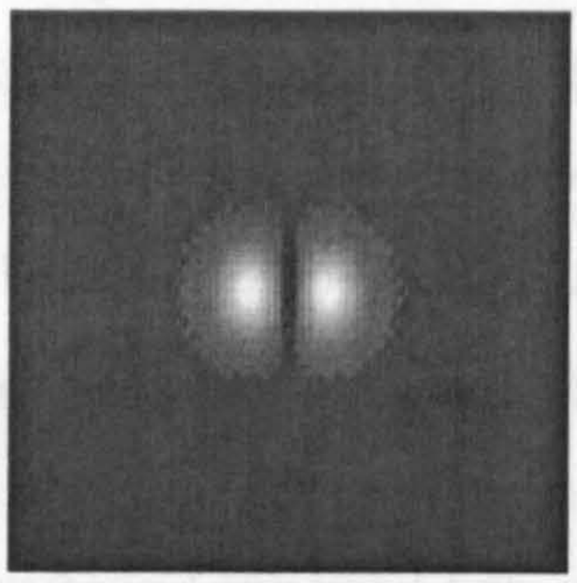

Fig. 1.4.b) Density plot TEM_{01} Hermite- Gaussian beam mode

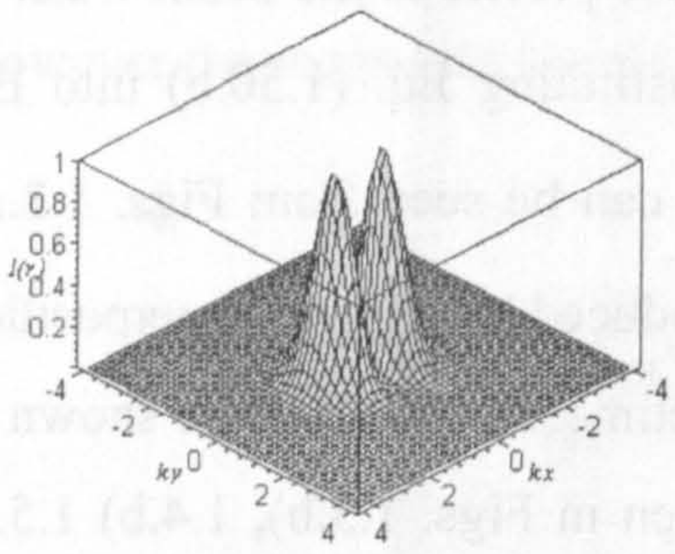

Fig. 1.5.a) TEM_{10} Hermite-Gaussian beam mode

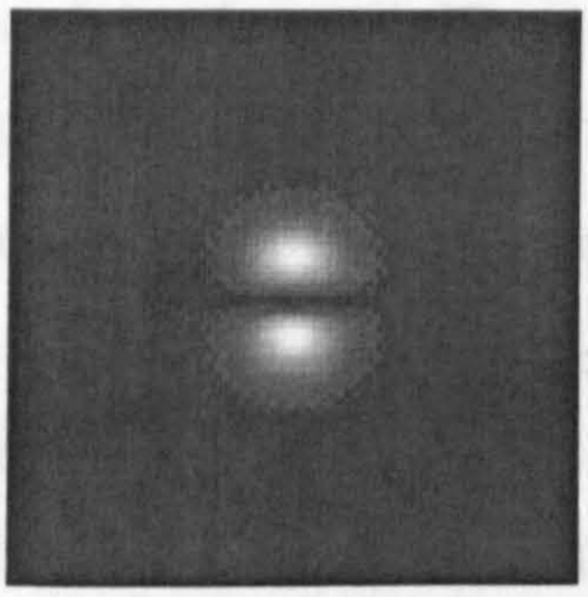

Fig. 1.5.b) Density plot TEM_{10} Hermite-Gaussian beam mode

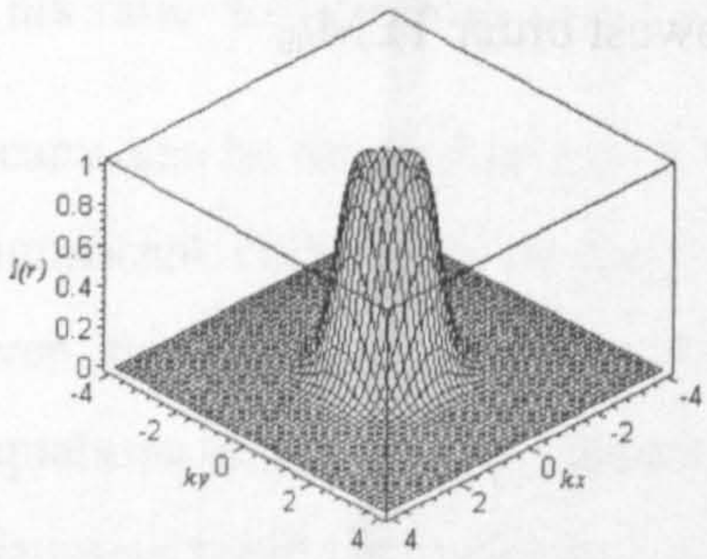

Fig. 1.6.a) Linear superposition of TEM_{10} and TEM_{01} Hermite-Gaussian beam mode

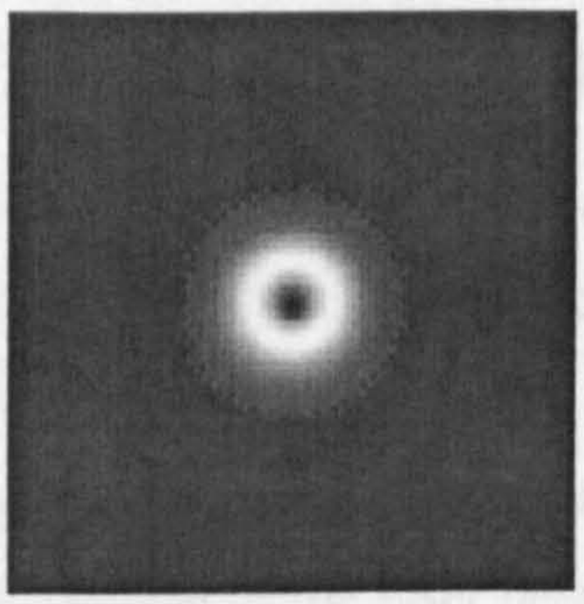

Fig. 1.6.b) Density plot of linear superposition TEM_{10} and TEM_{01} Hermite-Gaussian beam modes

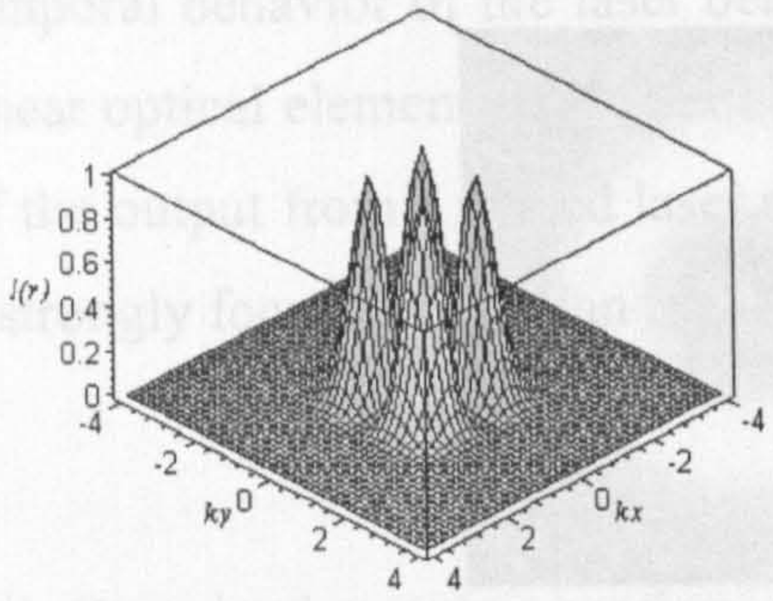

Fig. 1.7.a) TEM_{11} Hermite-Gaussian beam mode

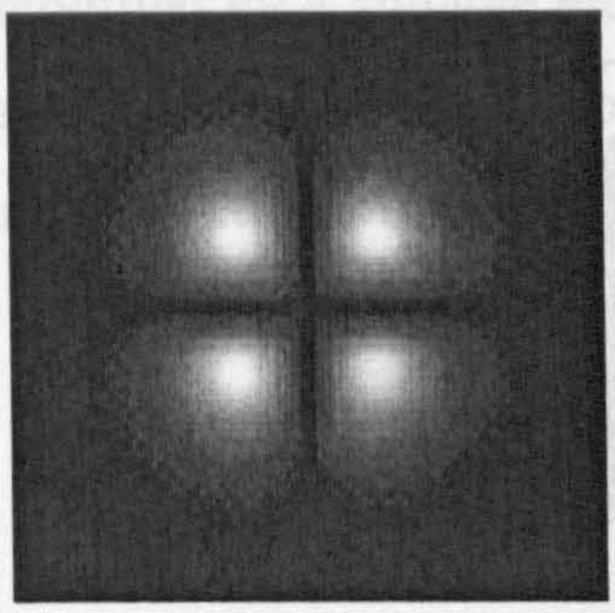

Fig. 1.7.b) Density plot TEM_{11} Hermite - Gaussian beam mode

Figs. 1.8.a), 1.9.a) and 1.10.a) shows the normalised irradiance profile at the beam waist, which are obtained by substituting Eq. (1.58.b) into Eq. (1.37) and normalising the functions to 1, with $w_0 = \sqrt{2}$, for the few lowest order TEM^*_{mn} Laguerre-Gaussian beam modes. Again only the lowest order mode TEM^*_{00} has a Gaussian irradiance profile. The density plots for these modes can be seen in Figs. 1.8.b), 1.9.b) 1.10.b). From Figs. 1.9.a) and b) it is apparent why the TEM^*_{01} mode is referred to in the literature as the donut mode. This mode can also be constructed by a linear superposition of a TEM_{10} and TEM_{01} Hermite-Gaussian beam mode [14], which is apparent by comparing Fig. 1.6.a) with Fig 1.9.a) and Fig. 1.6.b) with Fig. 1.9.b). Siegman [14] claims that this linear superposition of the Hermite-Gaussian modes oscillating separately and independently, with slightly different oscillating frequencies, due to the astigmatism introduced by the Brewster window in the laser, are more likely to be responsible for the donut mode, than the TEM^*_{01} Laguerre-Gaussian beam mode. He further claims that an $m = 0$ Laguerre-Gaussian mode cannot exist, since a Laguerre-Gaussian mode can never have a null on axis.

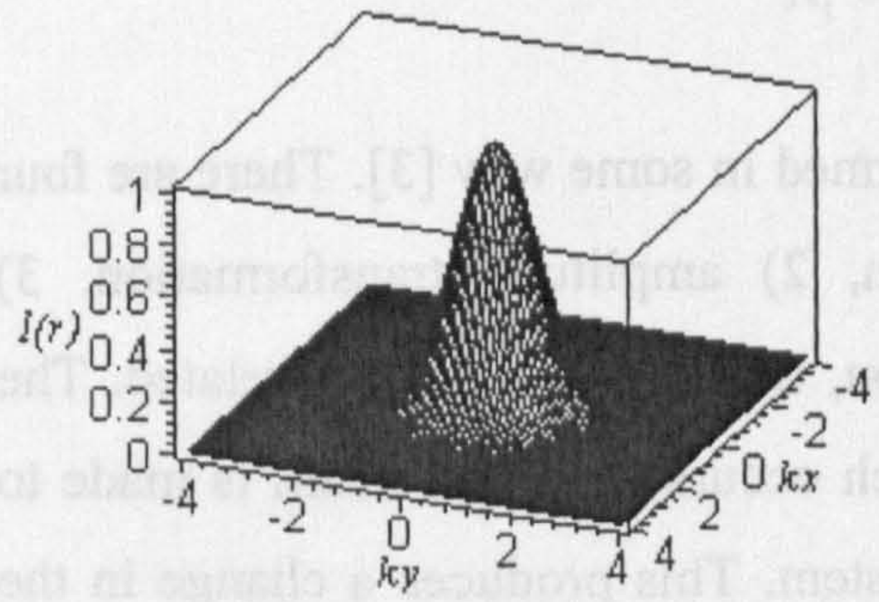

Fig. 1.8.a) TEM^*_{00} Laguerre-gaussian beam mode

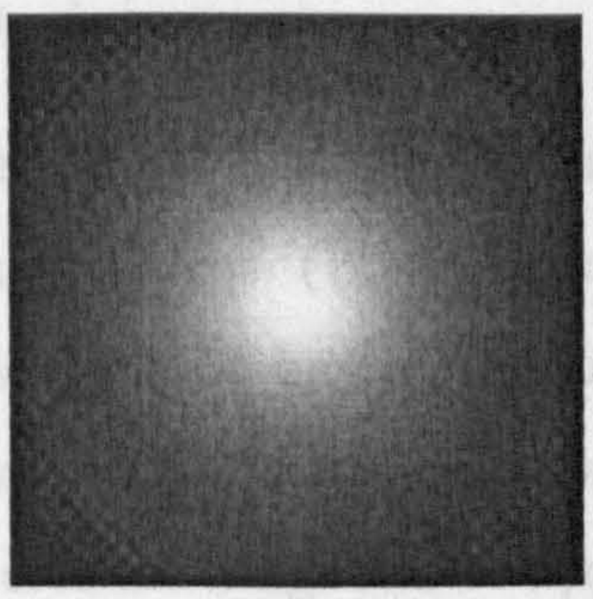

Fig. 1.8.b) Density plot TEM^*_{00} Laguerre-gaussian beam mode

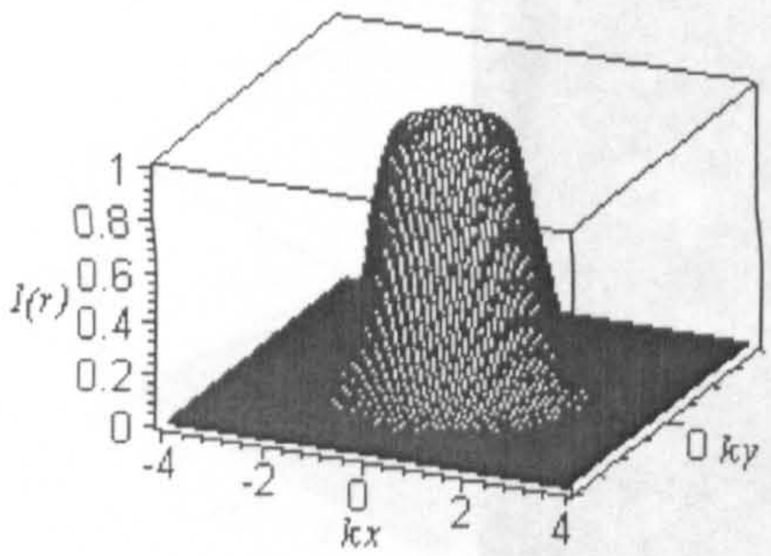

Fig. 1.9.a) TEM^{*}_{01} Laguerre-gaussian beam mode

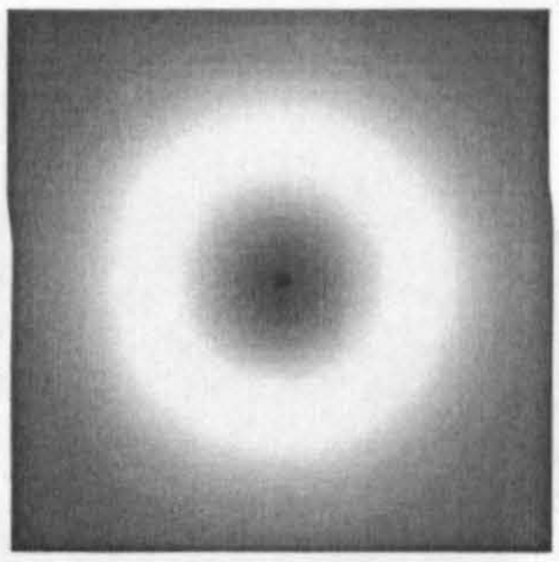

Fig. 1.9.b) Density plot TEM^{*}_{01} Laguerre-gaussian beam mode

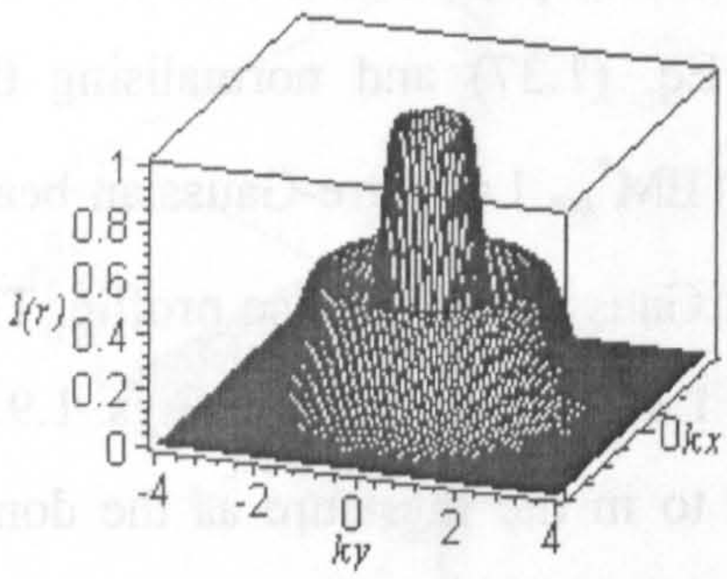

Fig. 1.10. a) TEM^{*}_{11} Laguerre-gaussian beam mode

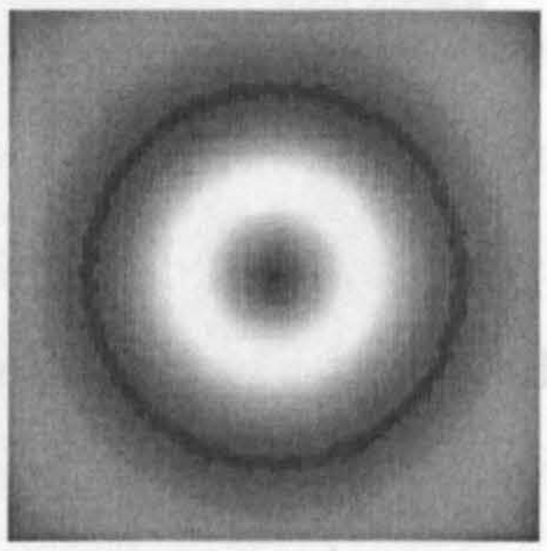

Fig. 1.10.b) Density plot TEM^{*}_{11} Laguerre-gaussian beam mode

In real lasers the Brewster windows and any other tilted surfaces or distorted elements usually provide a small but inherent rectangular symmetry to the laser cavity. Thus real lasers elect to oscillate in near-Hermite-Gaussian modes rather than near-Laguerre-Gaussian modes.

1.5. Laser beam transformation

Before a laser beam is put to use, it is usually transformed in some way [3]. There are four types of transformations; 1) spatial transformation, 2) amplitude transformation, 3) wavelength transformation and 4) time transformation, which are often interrelated. The most common type of transformation is the one which occurs when the beam is made to propagate in free space through a suitable optical system. This produces a change in the spatial distribution of the beam. Thus this is called "spatial transformation" of the laser beam. Amplitude transformation occurs when a beam is passed through an optical amplifier or attenuator. Wavelength transformation occurs when the wavelength of the beam is changed as a result of propagation through a suitable non-linear material. The

temporal behavior of the laser beam can be modified by a suitable electro-optical or non-linear optical element. This is called "time transformation". For example the time variation of the output from a pulsed laser may be changed. As this work deals with the behavior of a strongly focused Gaussian laser beam, only the spatial transformation will be considered.

1.6. Gaussian beam propagation

The expressions for the beam spot radius w and radius of curvature R of the equiphase are given by Eq. (1.56) and the first equation in Eqs. (1.57). The propagation properties of this beam depend only on the wavelength and the value of w_0 of the spot radius at the beam waist. Once w_0 is known, both the amplitude and phase are known at the waist. It has to be emphasised that the wavefront is plane at the waist. Eq. (1.56) shows that the square of the beam spot radius at a distance z from the waist is given by the sum of the squares of the spot radius at the waist, w_0^2, and the contribution $\left[\frac{\lambda z}{\pi w_0}\right]^2$ arises from diffraction.

If a TEM_{00} Gaussian beam is focused by a lens of focal length f (See Fig. 1.11.), then just before the lens, the spot radius w_1 and the radius of curvature R_1 of the beam can, according to Eqs. (1.56) and the first equation in Eqs.(1.57) be written as

$$w_1 = w_{01}\sqrt{1+\left(\frac{\lambda L_1}{\pi w_{01}^2}\right)^2} \tag{1.67}$$

$$R_1 = L_1\left[1+\left(\frac{\pi w_{01}^2}{\lambda L_1}\right)^2\right] \quad . \tag{1.68}$$

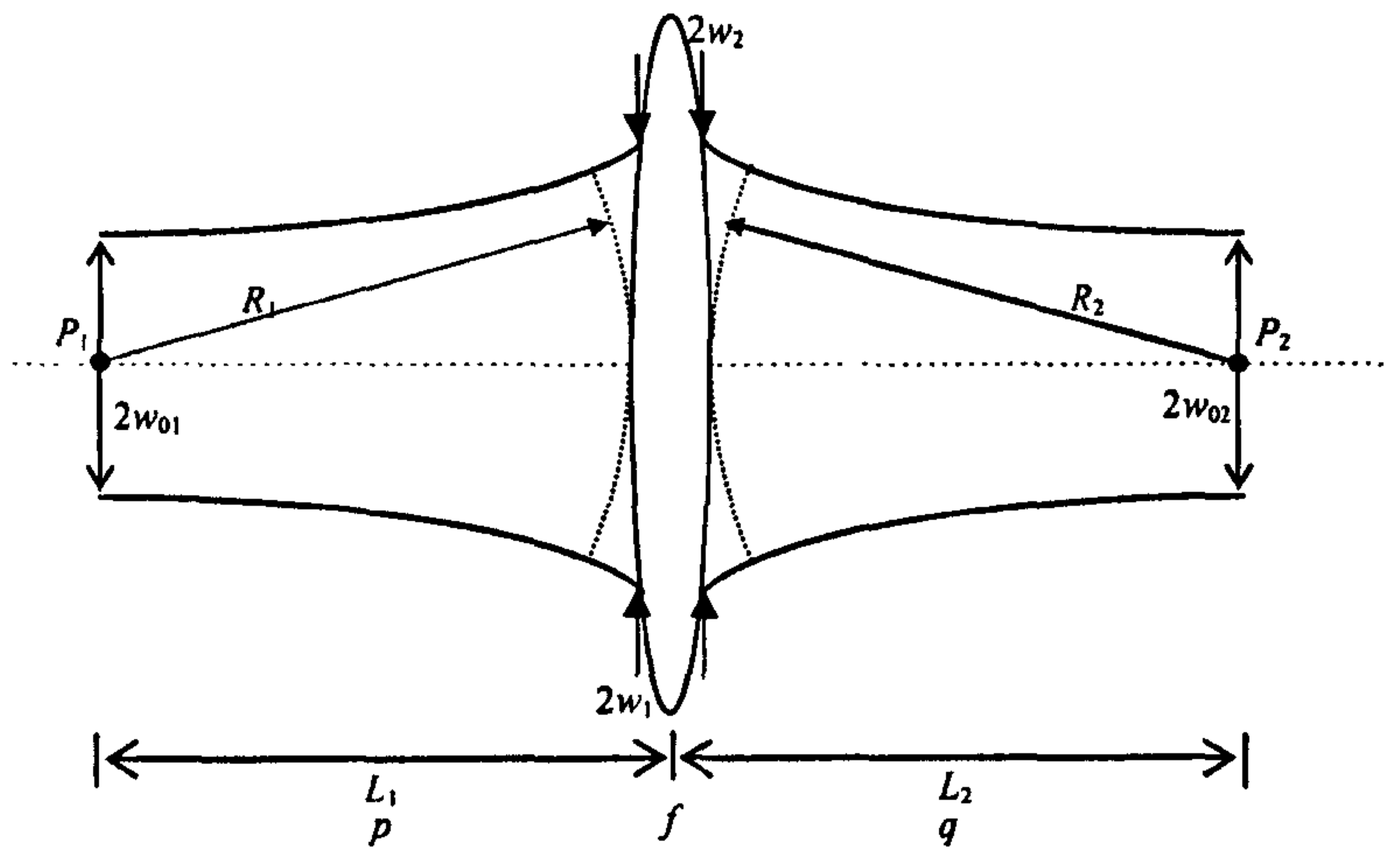

Fig. 1.11. Comparison of the focusing of a spherical wave and the focusing of a Gaussian beam by a lens of focal length f. (adapted from Svelto [3])

If the beam is focused by a thin lens, then the amplitude distribution must remain unchanged upon passing through the lens. There cannot be a discontinuous change of spot radius. Thus the beam spot size just after the lens, w_2, is equal to the beam spot size just before the lens, w_1,. I.e.

$$w_2 = w_1 \quad . \tag{1.69}$$

In order to calculate the corresponding wavefront curvature, the case of a spherical wave propagating through the same lens is considered. From geometrical optics there follows, the well-known result, that $\frac{1}{p}+\frac{1}{q}=\frac{1}{f}$. Since the radii of curvature R_1 and R_2 of the two spherical waves just before and just after the lens are equal to p and $-q$ respectively, it is implied that

$$\frac{1}{R_1}-\frac{1}{R_2}=\frac{1}{f} \quad . \tag{1.70}$$

Thus a Gaussian beam remains a Gaussian beam after passing through a thin lens system, hence the result also applies to a thick lens, as a thick lens can be regarded as a sequence of thin lenses. The spot radius w_{02} at the new beam waist and the distance L_2 of this waist from the lens can be obtained by using Eq. (1.56) and the first equation in Eqs. (1.57) in reverse:

$$L_1 = f \pm \left(\frac{w_{01}}{w_{02}}\right)\sqrt{f^2 - f_0^2}$$
$$L_2 = f \pm \left(\frac{w_{02}}{w_{01}}\right)\sqrt{f^2 - f_0^2} \quad . \tag{1.71}$$

From these both w_{02} and L_2 can be obtained. The quantity f_0 in Eq. (1.71) is given by Svelto [3] as

$$f_0 = \frac{\pi w_{01} w_{02}}{\lambda} \quad . \tag{1.72}$$

When the first waist is coincident with the first focal plane (L_1=f), the second waist also coincides with the second focal plane of the lens (L_2=f). In general, the planes of the two waists are not conjugated in accordance with the geometrical optics result, i.e. $\frac{1}{L_1} + \frac{1}{L_2} \neq \frac{1}{f}$. The explanation for this phenomenon is that a Gaussian beam undergoes a phase shift given by the second equation in Eqs. (1.57), referred to as the Gouy phase shift, when being focused by a lens. A phenomenon which does not occur when an ideal plane wave is focused by a lens.

Another important aspect to consider is the *aperture transmission*. Finite apertures will be present in any real optical system. The irradiance of a Gaussian beam falls off very rapidly with the radius beyond the spot radius w. The easiest way to calculate the total power of the Gaussian beam is to consider the power of the beam at the beam waist. Substituting Eq. (1.50.b) for the m=0, n=0 into Eq. (1.37) gives the following expression for the irradiance at a position **r**

$$I(\mathbf{r}) = \frac{1}{2} E_0^2 \sqrt{\frac{\varepsilon}{\mu_0}} \left(\frac{w_0}{w(z)}\right)^2 e^{-2\frac{\rho^2}{w(z)^2}} \quad . \tag{1.73}$$

Substituting $w(z)$=w_0 into Eq. (1.73) and evaluating the integral

$$P = \frac{1}{2} E_0^2 \sqrt{\frac{\varepsilon}{\mu_0}} \int_0^{2\pi} \int_0^{\infty} e^{-2\frac{\rho^2}{w_0^2}} \rho d\rho d\theta \quad , \tag{1.74.a}$$

where $\rho = \sqrt{x^2 + y^2}$ and $\theta = \arctan\left(\frac{y}{x}\right)$ are the usual plane polar coordinates, leads to the following expression for the beam power at the beam waist:

$$P = \frac{1}{4} E_0^2 \sqrt{\frac{\varepsilon}{\mu_0}} w_0^2 \pi \qquad (1.74.b)$$

Thus it can be seen from Eqs. (1.73) and (1.74.b) that the radial irradiance variation of a Gaussian beam is given by

$$I(\mathbf{r}) = \frac{2P}{\pi w(z)^2} e^{-\frac{2\rho^2}{w(z)^2}} \quad . \qquad (1.75)$$

Thus the power transmission, for a Gaussian beam of spot radius w passing through a centred circular aperture of diameter $2a$, is given by Siegman [14] as

$$\text{Power transmission} = \frac{2P}{\pi w^2} \int_0^{2\pi} \int_0^a e^{-\frac{2\rho^2}{w^2}} \rho d\rho d\theta = \left(1 - e^{-\frac{2a^2}{w^2}}\right) P \quad . \qquad (1.76)$$

An aperture with radius $a=w$ transmits ≈86% of the total power in the Gaussian beam. Thus one refers to this as the $\frac{1}{e}$ criterion for aperture size.

1.7. Definition of the Rayleigh range

The term Rayleigh range is sometimes used in antenna theory to describe the distance $z \approx \frac{d^2}{\lambda}$ that a collimated beam travels from an antenna of aperture diameter d (assuming $d>>\lambda$) before the beam begins to diverge significantly. As it is important to know how rapidly an ideal Gaussian beam will expand due to diffraction spreading as it propagates away from the waist region, it is necessary to find a parameter, which describes the distance a collimated Gaussian beam travels before it begins to spread significantly. If the input spot radius w_0 at the waist is made smaller, the beam expands more rapidly due to diffraction, i.e. the beam remains collimated over a shorter distance in the near-field and diverges at a larger angle in the far-field. The distance, which the beam travels from the

waist before the beam diameter increases by a factor $\sqrt{2}$, or in other words, before the beam area doubles, is given by the parameter

$$z = z_R \equiv \frac{\pi w_0^2}{\lambda} \quad = \text{Rayleigh range.} \tag{1.77}$$

Thus by taking the square root of Eq. (1.77) and substituting $z=z_R$ into Eq. (1.56) it is indeed found that $w(z)= \sqrt{2}\, w_0$. The Rayleigh range marks the approximate dividing line between the "near-field" (Fresnel) region and the "far-field" (Fraunhofer) region for a beam propagating outwards from a Gaussian waist. At the points $z = \pm z_R$ the radius of curvature is a minima, and its value is $R=b=2z_R$. The confocal parameter b is defined as the full distance between the $\sqrt{2}\, w_0$ spot radius points of a Gaussian beam, which is focused from an aperture down to a waist and then expands again

$$b = 2z_R = \frac{2\pi w_0^2}{\lambda} = \text{confocal parameter}. \tag{1.78}$$

Thus the confocal parameter is equal to twice the Rayleigh range.

1.8. The far-field

In the far-field ($z>>z_R$) the beam size expands linearly with distance [14]. By substituting Eq. (1.77) into Eq. (1.56), Eq. (1.56) can be written in terms of the beam waist radius and the Rayleigh range as

$$w(z) = w_0 \sqrt{1 + \left(\frac{z}{z_R}\right)^2} \quad . \tag{1.79}$$

Using the fact that in the far-field ($z>>z_R$), the $\frac{1}{e}$ spot radius $w(z)$, for the field amplitude in the far-field for a Gaussian beam coming from a waist with spot radius w_0, is given by

$$w(z) \approx \frac{w_0 z}{z_R} = \frac{\lambda z}{\pi w_0} \quad . \tag{1.80}$$

1.9. Focusing a Gaussian beam

The focusing of a collimated Gaussian beam can be viewed as the far-field beam problem in reverse as has been demonstrated in section 1.6.. Having derived Eq. (1.80) a very useful equation can be obtained by considering the fact that the waist region now becomes the focal spot of spot radius w_0 and the focusing lens can be viewed as being in the far-field at $z \approx \pm f$. If $w(f)$ is the Gaussian spot radius at the lens, Eq. (1.80) can be rewritten as follows

$$w_0 w(f) \approx \frac{\lambda f}{\pi} \quad . \tag{1.81}$$

This implies that the incident Gaussian beam should fill the aperture of the focusing lens to the largest extent possible without a severe loss of power due to the finite aperture of the lens and also without serious edge diffraction effects.

1.10. The need for a vector description of a focused laser beam

So far only a scalar solution to the Helmholtz equation has been considered. However in general there is a strong need for a vector description of a Gaussian beam. In the paraxial beam approximation the spherical wave is purely transverse, but as will be demonstrated in chapter 2, the spheroidal wave actually has a transverse and a longitudinal component. Thus in order to get a detailed description of the E.M. field of the beam, a vector description is required. It will be demonstrated in chapter 5 that in order to calculate the forces exerted by a focused beam on a dielectric sphere it is necessary to calculate the Maxwell stress tensor. These calculations require a vector description of the E.M. field. Additionally, when an E.M. field crosses the boundary between two media, a certain proportion of the incident field is reflected and a certain proportion of the field is transmitted. By calculating the Fresnel reflection and transmission coefficients it is possible to determine how much of the incident field is reflected and how much is transmitted. However it is demonstrated in chapter 5, that the Fresnel reflection and transmission coefficients are polarization dependent. It is thus necessary to take the polarization of the E.M. field, which is a vector quantity into account too. There is also another reason why a vector description is needed. At the beam waist and in the far-field the radius of curvature $R(z)$ of the spherical wavefront is infinite [14], i.e. $R(z=0)=\infty$ and $R(z=\infty)=\infty$. Thus the wave can be regarded as a plane wave. As the beam propagates

outwards from the beam waist, the wavefront becomes gradually curved, and the radius of curvature drops rapidly. For $z>>z_R$ the radius of curvature then increases and $R(z)\rightarrow z$, i.e. the Gaussian beam becomes essentially like a spherical wave centered at the beam waist. The strongest curvature of the wavefronts is observed at $z=z_R$, where $R(z_R)=2z_R$. As there is a rapid change of curvature of the wavefront in the near-field the direction of the field is important. Thus if the curvature of a field is of interest, then a vector description is required.

1.11. The different methods used to describe a focused Gaussian beam

Early mathematical descriptions of a focused Gaussian beam were based on solutions to the paraxial scalar wave equation. These solutions assume that the propagating wave is approximated as a purely transverse spherical wave; i.e. the wave has no longitudinal component. It was demonstrated that the solutions to the paraxial scalar wave equation in Cartesian coordinates are the Hermite-Gaussian beam modes and the solutions in cylindrical polar coordinates are the Laguerre-Gaussian beam modes. However, these solutions are not exact solutions to the scalar Helmholtz equation. Thus in order to obtain an exact mathematical description of a focused laser beam, it is necessary to find a separable solution to the scalar Helmholtz equation. Another method to describe a focused Gaussian beam is to use the Davis approximation [18], which is generally referred to as the fifth order Gaussian beam approximation. This procedure is an infinite series expansion in powers of the beam parameter s, where

$$s=\frac{1}{kw_0}. \tag{1.82}$$

This series expansion satisfies Maxwell's equations exactly. In the fifth order approximation the series expansion is truncated at s^4. Due to this truncation the fifth order approximation is not an exact solution of Maxwell's equations [19, 20]. Barton [19] used the Davis approximation in order to derive symmetric E.M. fields. Decamps [21] generalized the paraxial spherical wave by considering this wave in the complex plane. This method is referred to in the literature as the complex source point method. Other methods, described in the literature are methods based on Fourier series expansions [22, 23]. Landesman and Barrett [24] have assumed a spherical wave as the basic propagation function of the Gaussian beam. In order to obtain a solution to the scalar Helmholtz equation, they performed their calculations in the oblate spheroidal coordinate system.

Sheppard and Saghafi [25] as well as Ulanowski and Ludlow [26] independently pointed out, that a complex source point method cannot be a physical realizable description of a focused laser beam, since the presence of the source results in a singularity occurring in the focal plane at a radius equal to the Rayleigh range. In order to overcome this problem, Sheppard and Saghafi [25] as well as Ulanowski and Ludlow [26] introduced a complex sink. Hence it was demonstrated that the field produced by the sum of the source and the sink lead to a physically realizable solution to the scalar Helmholtz equation. Nieminen *et al.* [27] used a multipole expansion method to calculate the E.M. field and then point matched this field against the E.M. field determined by measurement or calculated using the paraxial approximation.

The aim of the following section is to present the most important models (excluding the work of Sheppard and Saghafi [25] and Ulanowski and Ludlow [26], as their work was published during the period of this research), which have been used to describe a focused Gaussian beam mathematically, in more detail and to discuss their shortcomings.

1.11.1. The fifth order Gaussian beam approximation

The paraxial Gaussian beam approximation has proven to be very successful in describing the characteristic radiation fields of stable spherical resonators. The difficulty with the theory is, that no exact solution to Maxwell's equations is obtained, instead a solution to the paraxial scalar wave equation is obtained, and further no procedure is given for deriving the higher order correction terms, which then would lead to an exact solution to Maxwell's equations. The second difficulty with this theory is that only the transverse component of the electric field, which satisfies the paraxial scalar wave equation, is worked out and the other two components are omitted. Lax, Louisell and McKnight [28] have overcome this problem by starting with the exact Maxwell equations and expanding the electric field vector in powers of s. They also pointed out, that it follows from the exact Maxwell equations, that for a plane polarised E.M. field, polarised in the x direction say, the electric field must be independent of the x coordinate. Thus in the derivation of the paraxial wave equation $\frac{\partial E_x}{\partial x}$ should have been set equal to zero. But as they describe later on in their paper, it is appropriate to set $\frac{\partial E_x}{\partial x} \neq 0$. Lax *et al.* [28] referred to this problem as an apparent paradox. The reason why there is no paradox is, that the lowest order expanded field is purely transverse. However for the next higher order a small longitudinal component of the field must be present and its size depends on s. Davis [18] simplified the

method presented by Lax *et al.* [28] by assuming that the E.M. vector potential $\mathbf{A}(\mathbf{r},t)$ is linearly polarised along one of the two transverse directions, in order for the non-vanishing transverse component of $\mathbf{A}(\mathbf{r},t)$ to obey the scalar wave equation. Davis states that this procedure is only beneficial in the free field case, since the assumption that the vector potential $\mathbf{A}(\mathbf{r},t)$ is linearly polarised fails when a current exists which is dependent on the electric field.

1.11.1.1. The derivation of the fifth order Gaussian beam approximation

Davis assumed a monochromatic beam within a homogeneous, isotropic, non-conducting (ρ=0), non-magnetic ($\mu=\mu_0$) dielectric medium ($\varepsilon=\varepsilon_0\varepsilon_r$). Maxwell's equations for such a medium are given by Eqs. (1.5 - 1.8). He introduced the vector and scalar potential $\mathbf{A}(\mathbf{r},t)$ and $\Phi(\mathbf{r},t)$ and related them to $\mathbf{E}(\mathbf{r},t)$ and $\mathbf{B}(\mathbf{r},t)$, with a harmonic time dependence of $e^{-i\omega t}$. Since the divergence of $\mathbf{B}(\mathbf{r},t)$ is zero (Eq. 1.6), $\mathbf{B}(\mathbf{r},t)$ can be written as

$$\mathbf{B}(\mathbf{r},t)=\nabla\times\mathbf{A}(\mathbf{r},t). \tag{1.83}$$

Thus substituting Eq. (1.83) into Eq. (1.8) yields

$$\nabla\times\mathbf{E}(\mathbf{r},t)=-\frac{\partial}{\partial t}\left(\nabla\times\mathbf{A}(\mathbf{r},t)\right),$$

or interchanging differentiation with respect to time and space gives

$$\nabla\times\left(\mathbf{E}(\mathbf{r},t)+\frac{\partial\mathbf{A}(\mathbf{r},t)}{\partial t}\right)=0 \quad . \tag{1.84}$$

It follows from Eq. (1.84), that the expression in brackets should be equal to the gradient of the scalar potential $\Phi(\mathbf{r},t)$:

$$\mathbf{E}(\mathbf{r},t)+\frac{\partial\mathbf{A}(\mathbf{r},t)}{\partial t}=-\nabla\Phi(\mathbf{r},t)$$

or

$$\mathbf{E}(\mathbf{r},t)=-\nabla\Phi(\mathbf{r},t)-\frac{\partial\mathbf{A}(\mathbf{r},t)}{\partial t} \quad . \tag{1.85}$$

Further in the considered case

$$\mathbf{H}(\mathbf{r},t)=\frac{\mathbf{B}(\mathbf{r},t)}{\mu_0} \tag{1.86}$$

and substituting Eq. (1.86) into Eq. (1.7) yields

$$\nabla\times\mathbf{H}(\mathbf{r},t)=\varepsilon\frac{\partial\mathbf{E}(\mathbf{r},t)}{\partial t}\quad , \tag{1.87}$$

substituting Eq. (1.86) into Eq. (1.83) gives

$$\mathbf{H}(\mathbf{r},t)=\frac{1}{\mu_0}(\nabla\times\mathbf{A}(\mathbf{r},t))\quad . \tag{1.88}$$

Taking the curl of Eq. (1.88) and substituting the result into Eq. (1.87) leads to

$$\frac{1}{\mu_0}\nabla\times(\nabla\times\mathbf{A}(\mathbf{r},t))=\varepsilon\frac{\partial\mathbf{E}(\mathbf{r},t)}{\partial t}\ . \tag{1.89}$$

Substituting Eq. (1.85) into Eq. (1.89) leads to

$$\frac{1}{\mu_0}\nabla\times(\nabla\times\mathbf{A}(\mathbf{r},t))=-\varepsilon\frac{\partial}{\partial t}\left(\nabla\Phi(\mathbf{r},t)+\frac{\partial\mathbf{A}(\mathbf{r},t)}{\partial t}\right). \tag{1.90}$$

Using the vector identity

$$\nabla\times(\nabla\times\mathbf{A})=\nabla(\nabla\bullet\mathbf{A})-\nabla^2\mathbf{A}$$

Eq. (1.90) can be rewritten as

$$\frac{1}{\mu_0}(\nabla(\nabla\bullet\mathbf{A}(\mathbf{r},t))-\nabla^2\mathbf{A}(\mathbf{r},t))=-\varepsilon\left(\nabla\frac{\partial\Phi(\mathbf{r},t)}{\partial t}+\frac{\partial^2\mathbf{A}(\mathbf{r},t)}{\partial t^2}\right). \tag{1.91}$$

Rearranging Eq. (1.91) gives:

$$\nabla^2\mathbf{A}(\mathbf{r},t)-\mu_0\varepsilon\frac{\partial^2\mathbf{A}(\mathbf{r},t)}{\partial t^2}-\nabla\left(\nabla\bullet\mathbf{A}(\mathbf{r},t)+\mu_0\varepsilon\frac{\partial\Phi(\mathbf{r},t)}{\partial t}\right)=0\,. \tag{1.92}$$

Taking the divergence of Eq. (1.85) and using Eq. (1.5)

$$\nabla\bullet\mathbf{E}(\mathbf{r},t)=-\nabla\bullet\left(\nabla\Phi(\mathbf{r},t)+\frac{\partial\mathbf{A}(\mathbf{r},t)}{\partial t}\right)=0$$

is obtained. Thus interchanging differentiation with respect to time and space gives

$$\nabla^2\Phi(\mathbf{r},t)+\frac{\partial}{\partial t}\nabla\bullet\mathbf{A}(\mathbf{r},t)=0\,. \tag{1.93}$$

From Eq. (1.92) and Eq. (1.93) it can be seen that the equations for $\mathbf{A}(\mathbf{r},t)$ and $\Phi(\mathbf{r},t)$ are not independent. Since $\mathbf{E}(\mathbf{r},t)$ and $\mathbf{B}(\mathbf{r},t)$ determine the force exerted on the charge, and thus are more directly linked to the physical world, then for a given $\mathbf{E}(\mathbf{r},t)$ and $\mathbf{B}(\mathbf{r},t)$ field, the vector potential $\mathbf{A}(\mathbf{r},t)$ cannot be uniquely defined by the relation given in Eq. (1.83). Hence there is some degree of arbitrariness. In order to uniquely define $\mathbf{A}(\mathbf{r},t)$, its divergence needs to be specified. By a gauge condition we understand the specification of the divergence of $\mathbf{A}(\mathbf{r},t)$. In the case considered we are working in the Lorentz gauge, where the divergence of $\mathbf{A}(\mathbf{r},t)$ is given by

$$\nabla\bullet\mathbf{A}(\mathbf{r},t)+\mu_0\varepsilon\frac{\partial\Phi(\mathbf{r},t)}{\partial t}=0\ \ . \tag{1.94}$$

Thus substituting Eq. (1.94) into Eq. (1.92) yields

$$\nabla^2\mathbf{A}(\mathbf{r},t)-\mu_0\varepsilon\frac{\partial^2\mathbf{A}(\mathbf{r},t)}{\partial t^2}=0 \tag{1.95}$$

and substituting Eq. (1.94) into Eq. (1.93) leads to

$$\nabla^2\Phi(\mathbf{r},t)-\mu_0\varepsilon\frac{\partial^2\Phi(\mathbf{r},t)}{\partial t^2}=0\,. \tag{1.96}$$

It can be seen form Eq. (1.95) and Eq. (1.96) that these are independent equations for $\mathbf{A}(\mathbf{r},t)$ and $\Phi(\mathbf{r},t)$. By substituting $v=\frac{1}{\sqrt{\mu_0\varepsilon}}, k=\frac{\omega}{v}=\frac{2\pi}{\lambda}$ and making use of the fact that $\frac{\partial^2\mathbf{A}(\mathbf{r},t)}{\partial t^2}=-\omega^2\mathbf{A}(\mathbf{r},t)$ and $\frac{\partial^2\Phi(\mathbf{r},t)}{\partial t^2}=-\omega^2\Phi(\mathbf{r},t)$, Eq. (1.95) and Eq. (1.96) can be rewritten as follows:

$$\nabla^2\mathbf{A}(\mathbf{r},t)+k^2\mathbf{A}(\mathbf{r},t)=0 \tag{1.97}$$

$$\nabla^2\Phi(\mathbf{r},t)+k^2\Phi(\mathbf{r},t)=0 \tag{1.98}$$

Rearranging Eq. (1.94) gives

$$\nabla\bullet\mathbf{A}(\mathbf{r},t)=-\mu_0\varepsilon\frac{\partial\Phi(\mathbf{r},t)}{\partial t} \quad . \tag{1.99}$$

Further, the chosen harmonic time dependence implies that $\frac{\partial\mathbf{A}(\mathbf{r},t)}{\partial t}=-i\omega\mathbf{A}(\mathbf{r},t)$ and $\frac{\partial\Phi(\mathbf{r},t)}{\partial t}=-i\omega\Phi(\mathbf{r},t)$. As next, from Eq. (1.99) the following expression for $\Phi(\mathbf{r},t)$ is found:

$$\Phi(\mathbf{r},t)=-\frac{i\omega}{k^2}\nabla\bullet\mathbf{A}(\mathbf{r},t) \quad . \tag{1.100}$$

Now Eq. (1.85) can be rewritten in terms of the vector potential $\mathbf{A}(\mathbf{r},t)$ as

$$\mathbf{E}(\mathbf{r},t)=\frac{i\omega}{k^2}\left(\nabla\left(\nabla\bullet\mathbf{A}(\mathbf{r},t)\right)+k^2\mathbf{A}(\mathbf{r},t)\right). \tag{1.101}$$

In order to describe a paraxial beam, $\mathbf{A}(\mathbf{r},t)$ is assumed to be polarised in the transverse direction, and it is also anticipated that the waves are nearly plane. A Cartesian coordinate system, with $\mathbf{A}(\mathbf{r},t)$ being polarised along the x axis and the beam propagating along the z axis is assumed. Thus in the scalar case $A_x(\mathbf{r},t)\,\hat{\mathbf{i}}=\mathbf{A}(\mathbf{r},t)$ and $(A_y(\mathbf{r},t)\,\hat{\mathbf{j}}=A_z(\mathbf{r},t)\,\hat{\mathbf{k}}=0)$. In

order for $A(\mathbf{r},t)$ to be a physical solution, $A(\mathbf{r},t)$ has to satisfy the scalar Helmholtz equation (Eq. 1.19). Thus by replacing $u(r)$ with $A(\mathbf{r})$ Eq. (1.19) can be rewritten as

$$\nabla^2 A(\mathbf{r}) + k^2 A(\mathbf{r}) = 0 \quad , \tag{1.102}$$

where $A(\mathbf{r})$ is given by

$$A(\mathbf{r}) = \psi(\mathbf{r}) e^{ikz} \quad . \tag{1.103}$$

For the next part of the derivation it is convenient to consider $\psi(x,y,z)e^{ikz}$ instead of $\psi(\mathbf{r})e^{ikz}$. It is also known from section 1.3., and replacing $u(r)$ with $\psi(x,y,z)$, that $\psi(x,y,z)$ is a slowly varying function in the z direction. Thus by substituting $\psi(x,y,z)e^{ikz}$ into Eq. (1.19) leads to

$$\nabla^2 \psi(x,y,z) + 2ik \frac{\partial \psi(x,y,z)}{\partial z} = 0 \ . \tag{1.104}$$

Davis introduced the dimensionless transverse variables $x = w_0 \xi$ and $y = w_0 \eta$. From section 1.7., it is known that there is a characteristic diffraction length, confocal parameter b, Davis [18] set $z = 2z_R \zeta$. Substituting these new variables into Eq. (1.104) leads to

$$\left(\frac{\partial^2}{\partial \xi^2} + \frac{\partial^2}{\partial \eta^2} \right) \psi(\xi,\eta,\zeta) + 2i \frac{\partial \psi(\xi,\eta,\zeta)}{\partial \zeta} + s^2 \frac{\partial^2 \psi(\xi,\eta,\zeta)}{\partial \zeta^2} = 0 \ , \tag{1.105}$$

where $s = \dfrac{1}{kw_0}$. If the beam waist radius w_0 is large compared to λ, then s is small compared to unity. In this case Davis [18] claims it to be natural to seek a series solution of Eq. (1.105) of the form

$$\psi(\xi,\eta,\zeta) = \psi_0(\xi,\eta,\zeta) + s^2 \psi_2(\xi,\eta,\zeta) + s^4 \psi_4(\xi,\eta,\zeta) + \ldots \tag{1.106}$$

where according to Barton [19]

$$\left(\frac{\partial^2}{\partial \xi^2} + \frac{\partial^2}{\partial \eta^2} + 2i \frac{\partial}{\partial \zeta} \right) \psi_0(\xi,\eta,\zeta) = 0 \tag{1.107}$$

$$\left(\frac{\partial^2}{\partial\xi^2}+\frac{\partial^2}{\partial\eta^2}+2i\frac{\partial}{\partial\zeta}\right)\psi_2(\xi,\eta,\zeta)=-\frac{\partial^2\psi_0(\xi,\eta,\zeta)}{\partial\zeta^2} \tag{1.108}$$

$$\left(\frac{\partial^2}{\partial\xi^2}+\frac{\partial^2}{\partial\eta^2}+2i\frac{\partial}{\partial\zeta}\right)\psi_4(\xi,\eta,\zeta)=-\frac{\partial^2\psi_2(\xi,\eta,\zeta)}{\partial\zeta^2} \tag{1.109}$$

Eq. (1.107) is the familiar paraxial beam equation, which has the solution

$$\psi_0(\xi,\eta,\zeta)=-iQe^{ip^2Q}\ , \tag{1.110}$$

where here $\rho^2=\xi^2+\eta^2$ and $Q=\dfrac{1}{i+2\zeta}$.

Davis [18] expressed Eq. (1.110) in the slightly different form, namely

$$\psi_0(\xi,\eta,\zeta)=e^{i\left(P+Q\rho^2\right)}\ , \tag{1.111}$$

where $iP=\ln(-iQ)$. Substituting the expression for ζ, and using Eq. (1.77), into Q leads to

$$Q=\frac{1}{\left(-i+\dfrac{\lambda z}{\pi w_0^2}\right)}\ .$$

Thus

$$-iQ=\frac{1}{\left(1+\dfrac{i\lambda z}{\pi w_0^2}\right)}\ . \tag{1.112}$$

Therefore

$$\ln(-iQ)=-\ln\left(1+\frac{i\lambda z}{\pi w_0^2}\right).$$

Hence

$$iP=-\ln\left(1+\frac{i\lambda z}{\pi w_0^2}\right).$$

P can be decomposed into its real and imaginary parts [21]. The real part of P represents the phase shift difference ϕ between the Gaussian beam and an ideal plane wave. The imaginary part of P produces an amplitude factor $\frac{w_0}{w(z)}$, which gives the expected intensity decrease on axis due to the expansion of the beam.

$$\mathrm{Re}(iP) = -\ln\left(\sqrt{1+\left(\frac{\lambda z}{\pi w_0^2}\right)}\right) \tag{1.113}$$

$$\mathrm{Im}(iP) = -\arctan\left(\frac{\lambda z}{\pi w_0^2}\right) \tag{1.114}$$

Further since $iP = \ln(-iQ)$, Eq. (1.111) can be written as

$$\psi_0(\xi,\eta,\zeta) = e^{iP}e^{iQ\rho^2} = -iQe^{iQ\rho^2}, \tag{1.115}$$

which is identical to Eq. (1.110).

Decomposing the product iQ into its real and imaginary part and using Eq. (1.77) when substituting ζ into Q, it is found that

$$Q = \frac{1}{-i+\frac{z}{z_R}},$$

and

$$\mathrm{Re}(iQ) = \frac{-1}{1+\left(\frac{z}{z_R}\right)^2}.$$

Which can be written, using Eq. (1.56) as

$$\mathrm{Re}(iQ) = -\frac{w_0^2}{w^2(z)} \quad . \tag{1.116}$$

The imaginary part of the product iQ is given by

$$\mathrm{Im}(iQ)=\frac{z_R}{z\left(1+\frac{z_R^2}{z^2}\right)}.$$

By using the first equation in Eqs. (1.57) together with Eq. (1.77) it is found that

$$\mathrm{Im}(iQ)=\frac{z_R}{R(z)}=\frac{kw_0^2}{2R(z)}. \tag{1.117}$$

Finally substituting Eqs. (1.116), (1.117) and (1.114), using the relationship of the second equation in Eqs. (1.57) into Eq. (1.115) leads to

$$\psi_{00}(x,y,z)=\frac{w_0}{w(z)}e^{-\left(\frac{x^2+y^2}{w^2(z)}\right)}e^{i\left(k\frac{\left(x^2+y^2\right)}{2R(z)}-\phi(z)\right)}$$

Hence $A(x,y,z)$ can be written for the lowest order mode as

$$A_{00}(x,y,z)=\frac{w_0}{w(z)}e^{-\left(\frac{x^2+y^2}{w^2(z)}\right)}e^{i\left(k\frac{\left(x^2+y^2\right)}{2R(z)}+kz-\phi(z)\right)},$$

which is identical to Eq. (1.50.a) for the lowest order.

By substituting Eq. (1.110) into Eq. (1.108) Davis [18] found

$$\psi_2(\xi,\eta,\zeta)=-\left(2iQ+i\rho^4Q^3\right)\psi_0(\xi,\eta,\zeta) \tag{1.118}$$

and by substituting Eq. (1.118) into Eq. (1.109) Barton [19] found

$$\psi_4(\xi,\eta,\zeta)=\left(-6Q^2-3\rho^4Q^4+2i\rho^6Q^5-0.5\rho^8Q^6\right)\psi_0(\xi,\eta,\zeta). \tag{1.119}$$

Substituting $\xi = \frac{x}{w_0}$, $\eta = \frac{y}{w_0}$ and $\zeta = \frac{z}{kw_0^2}$ into Eq. (1.103) and using the expansion given in Eq. (1.106), **A(r)** can be written in vector form to fifth order in *s* as

$$\mathbf{A}(\xi,\eta,\zeta) \approx \left(\psi_0(\xi,\eta,\zeta) + s^2\psi_2(\xi,\eta,\zeta) + s^4\psi_4(\xi,\eta,\zeta)\right)e^{\frac{i\zeta}{s^2}}\hat{\mathbf{i}} \tag{1.120}$$

Thus an expression for the E.M. field to fifth order in *s* can be obtained by substituting Eq. (1.120) into Eq. (1.101) and Eq. (1.88). However these expressions for the electric and magnetic field lack symmetry, beyond the first order case. Since $\mathbf{A}(\mathbf{r}) = A_x(\mathbf{r})\hat{\mathbf{i}}$ it can be seen that by calculating the curl of $\mathbf{A}(\mathbf{r})$

$$\mathbf{H}(\mathbf{r},t) = \frac{1}{\mu_0}(\nabla \times \mathbf{A}(\mathbf{r},t)) = \frac{1}{\mu_0}\left[\left(\frac{\partial A_z(\mathbf{r},t)}{\partial y} - \frac{\partial A_y(\mathbf{r},t)}{\partial z}\right)\hat{\mathbf{i}} + \left(\frac{\partial A_x(\mathbf{r},t)}{\partial z} - \frac{\partial A_z(\mathbf{r},t)}{\partial x}\right)\hat{\mathbf{j}} + \left(\frac{\partial A_y(\mathbf{r},t)}{\partial x} - \frac{\partial A_x(\mathbf{r},t)}{\partial y}\right)\hat{\mathbf{k}}\right]$$

that $H_x(\mathbf{r},t) = 0$ for all orders of *s*. Barton [19] has demonstrated that a Gaussian beam description, for which the electric and magnetic field component expressions are symmetric, can be obtained by repeating the derivation with

$$\mathbf{A}(\mathbf{r},t)' = A_y(\mathbf{r},t)'\hat{\mathbf{j}} = \psi(\mathbf{r},t)'e^{ikz}\hat{\mathbf{j}} \quad . \tag{1.121}$$

Barton [19] set

$$\mathbf{E}'(\mathbf{r},t) = \nabla \times \mathbf{A}'(\mathbf{r},t). \tag{1.122}$$

By substituting Eq. (1.122) into Eq. (1.7) it is found that

$$\nabla \times \mathbf{B}'(\mathbf{r},t) = \varepsilon\mu_0 \frac{\partial}{\partial t}(\nabla \times \mathbf{A}'(\mathbf{r},t)) \quad , \tag{1.123}$$

or, interchanging differentiation with respect to time and space and substituting Eq. (1.86) gives

$$\nabla \times \left(\frac{\mathbf{H}'(\mathbf{r},t)}{\varepsilon} - \frac{\partial \mathbf{A}'(\mathbf{r},t)}{\partial t}\right) = 0. \tag{1.124}$$

It follows from Eq. (1.124) that

$$\left(\frac{\mathbf{H}'(\mathbf{r},t)}{\varepsilon}-\frac{\partial\mathbf{A}'(\mathbf{r},t)}{\partial t}\right)=\nabla\Phi(\mathbf{r},t), \tag{1.125}$$

rearranging Eq. (1.125) leads to

$$\mathbf{H}'(\mathbf{r},t)=\varepsilon\left(\nabla\Phi(\mathbf{r},t)+\frac{\partial\mathbf{A}'(\mathbf{r},t)}{\partial t}\right) \tag{1.126}$$

and substituting Eq. (1.86) into Eq. (1.8) yields

$$\nabla\times\mathbf{E}'(\mathbf{r},t)=-\mu_0\frac{\partial\mathbf{H}'(\mathbf{r},t)}{\partial t}, \tag{1.127}$$

substituting Eq. (1.122) and Eq. (1.126) into Eq. (1.127) gives

$$\nabla\times(\nabla\times\mathbf{A}'(\mathbf{r},t))=-\mu_0\varepsilon\left(\nabla\frac{\partial\Phi(\mathbf{r},t)}{\partial t}+\frac{\partial^2\mathbf{A}'(\mathbf{r},t)}{\partial t^2}\right) \tag{1.128}$$

or

$$\nabla(\nabla\bullet\mathbf{A}'(\mathbf{r},t))-\nabla^2\mathbf{A}'(\mathbf{r},t)=-\mu_0\varepsilon\left(\nabla\frac{\partial\Phi(\mathbf{r},t)}{\partial t}+\frac{\partial^2\mathbf{A}'(\mathbf{r},t)}{\partial t^2}\right). \tag{1.129}$$

Rearranging Eq. (1.129) leads to

$$\nabla(\nabla\bullet\mathbf{A}'(\mathbf{r},t))-\nabla^2\mathbf{A}'(\mathbf{r},t)+\mu_0\varepsilon\left(\nabla\frac{\partial\Phi(\mathbf{r},t)}{\partial t}+\frac{\partial^2\mathbf{A}'(\mathbf{r},t)}{\partial t^2}\right)=0. \tag{1.130}$$

Since these derivations are done in the Lorentz gauge, Eq. (1.94) needs to be substituted into Eq. (1.130).

Thus

$$-\nabla^2\mathbf{A}'(\mathbf{r},t)+\mu_0\varepsilon\frac{\partial^2\mathbf{A}'(\mathbf{r},t)}{\partial t^2}=0$$

or

$$\nabla^2\mathbf{A}'(\mathbf{r},t)-\mu_0\varepsilon\frac{\partial^2\mathbf{A}'(\mathbf{r},t)}{\partial t^2}=0 \tag{1.131}$$

Taking the divergence of $\mathbf{H}'(\mathbf{r},t)$ and using Eq. (1.6), Eq. (1.86) and Eq. (1.126) leads to

$$\nabla\bullet\mathbf{H}'(\mathbf{r},t)=\varepsilon\nabla\bullet\left(\nabla\Phi(\mathbf{r},t)+\frac{\partial\mathbf{A}'(\mathbf{r},t)}{\partial t}\right)=0 \tag{1.132}$$

and interchanging differentiation with respect to time and space gives

$$\nabla^2\Phi(\mathbf{r},t)+\frac{\partial}{\partial t}\nabla\bullet\mathbf{A}'(\mathbf{r},t)=0. \tag{1.133}$$

By substituting Eq. (1.94) into Eq. (1.133) Eq. (1.96) is obtained.

It can be seen form Eq. (1.131) that an independent equation for $\mathbf{A}'(\mathbf{r},t)$ has been obtained. Since $\frac{\partial^2\mathbf{A}'(\mathbf{r},t)}{\partial t^2}=-\omega^2\mathbf{A}'(\mathbf{r},t)$, Eq. (1.131) can be rewritten as follows:

$$\nabla^2\mathbf{A}'(\mathbf{r},t)+k^2\mathbf{A}'(\mathbf{r},t)=0 \tag{1.134}$$

From Eq. (1.99) and Eq. (1.100), using $\frac{\partial\mathbf{A}'(\mathbf{r},t)}{\partial t}=-i\omega\mathbf{A}'(\mathbf{r},t)$, Eq. (1.125) can be rewritten in the following way:

$$\mathbf{H}'(\mathbf{r},t)=-\frac{i\omega\varepsilon}{k^2}\left(\nabla(\nabla\bullet\mathbf{A}'(\mathbf{r},t))+k^2\mathbf{A}'(\mathbf{r},t)\right). \tag{1.135}$$

Barton [19] added the solutions of Eq. (1.101) and Eq. (1.88) in an appropriate way to the solutions of Eq. (1.135) and Eq. (1.122) and divided the result by two. Thus he found the following expression for the E.M. field components, to fifth order in the parameter *s*.

$$E_r = E_0\{1+s^2(-\rho^2Q^2 - i\rho^4Q^3 - 2Q^2\xi^2)+s^4[2\rho^4Q^4 + 3i\rho^6Q^5 - 0.5\rho^8Q^6 + (8\rho^2Q^4 + 2i\rho^4Q^5)\xi^2]\}\psi_0(\xi,\eta,\zeta)e^{\frac{i\zeta}{s^2}}$$

$$E_t = E_0\{s^2(-2Q^2\xi\eta)+s^4[(8\rho^2Q^4 + 2i\rho^4Q^5)\xi\eta]\}\psi_0(\xi,\eta,\zeta)e^{\frac{i\zeta}{s^2}}$$

$$E_z = E_0\{s(-2Q\xi)+s^3[(6\rho^2Q^3 + 2i\rho^4Q^4)\xi]+s^5[(-20\rho^4Q^5 - 10i\rho^6Q^6 + \rho^8Q^7)\xi]\}\psi_0(\xi,\eta,\zeta)e^{\frac{i\zeta}{s^2}}$$

$$H_r = \sqrt{\varepsilon}E_0\{s^2(-2Q^2\xi\eta)+s^4[(8\rho^2Q^4 + 2i\rho^4Q^5)\xi\eta]\}\psi_0(\xi,\eta,\zeta)e^{\frac{i\zeta}{s^2}}$$

$$H_t = \sqrt{\varepsilon}E_0\{1+s^2(-\rho^2Q^2 - i\rho^4Q^3 - 2Q^2\eta^2)+s^4[2\rho^4Q^4 + 3i\rho^6Q^5 - 0.5\rho^8Q^6 + (8\rho^2Q^4 + 2i\rho^4Q^5)\eta^2]\}\psi_0(\xi,\eta,\zeta)e^{\frac{i\zeta}{s^2}}$$

$$H_z = \sqrt{\varepsilon}E_0\{s(-2Q\eta)+s^3[(6\rho^2Q^3 + 2i\rho^4Q^4)\eta]+s^5[(-20\rho^4Q^5 - 10i\rho^6Q^6 + \rho^8Q^7)\eta]\}\psi_0(\xi,\eta,\zeta)e^{\frac{i\zeta}{s^2}} \quad (1.136)$$

where $\psi_0(\xi,\eta,\zeta)$ is given by Eq. (1.110). E_0 in the Eqs. (1.136) is the electric field amplitude at the focal point of the beam ($\xi=\eta=\zeta=0$). Barton [19] then also stated that there exists the following relationship between the beam power P and $|E_0|^2$:

$$|E_0|^2 = \frac{4P}{\pi\sqrt{\varepsilon}cw_0^2(1+s^2+1.5s^4)} \quad (1.137)$$

The components of the E.M. field Eq. (1.136) and the relationship between the beam power and $|E_0|^2$, are the quantities required in order to compute the radiation forces (see Chapter 5).

1.11.1.2. <u>The limitations of the fifth order Gaussian beam approximation</u>

The fifth order Gaussian beam approximation is not an exact solution to Maxwell's equations. However, as was demonstrated in the derivations above, the fifth order Gaussian beam approximation is a solution to the paraxial wave equation as the beam parameter s tends to zero, i.e. in the paraxial limit. Barton [19] has tested the fifth order Gaussian beam approximation against Maxwell's equations and found that this approximation becomes less and less accurate as s becomes large. He found that if an error of 1% is acceptable, then the fifth order approximation can be used for s values less than 0.2, or in other words for ratios of wavelengths to beam waist radii of less than 1.26. Fig. 1.12.a) shows the irradiance profile, in the focal plane $z=y=0$, normalized to 1 at $x=0$, of a strongly ($s=\frac{1}{\sqrt{2}}$) focused Gaussian beam and Fig. 1.12.b) of a weaker ($s=0.2$) focused Gaussian beam in the focal plane $z=y=0$, normalized to 1 at $x=0$. It is apparent from Fig. 1.12.a) that the fifth

order Gaussian beam approximation produces an inappropriate profile for a tightly focused beam.

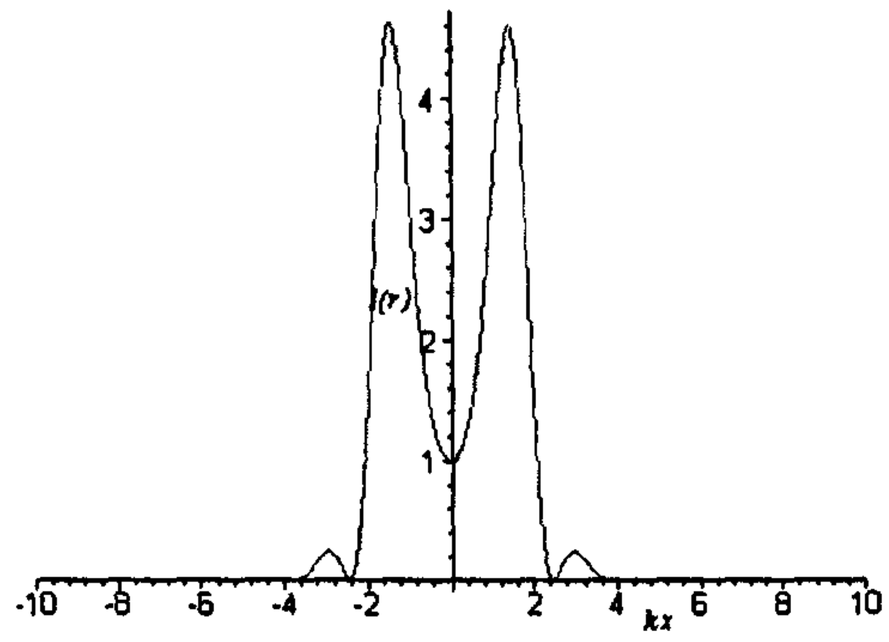

Fig. 1.12.a)
Irradiance profile of a strongly focused Gaussian beam in the focal plane z=y=0, normalized to 1 at x=0,

for a beam parameter $s = \frac{1}{\sqrt{2}}$.

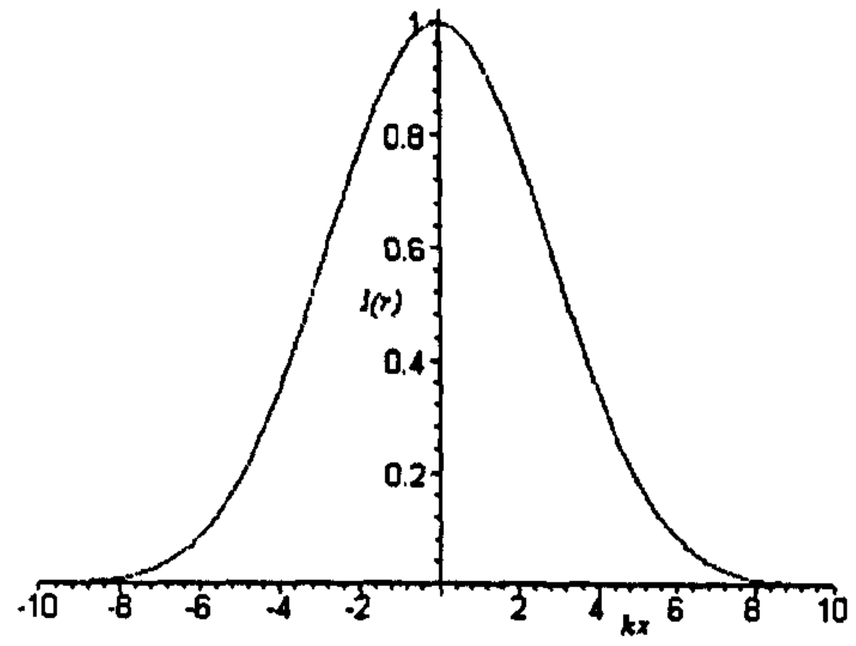

Fig. 1.12.b)
Irradiance profile of a weaker focused Gaussian beam in the focal plane z=y=0, normalized to 1 at x=0,

for a beam parameter s=0.2.

1.11.2. Gaussian spherical waves

In Eq. (1.39) the Green's function

$$G(\mathbf{r}_2|\mathbf{r}_1) = \frac{e^{ik|\mathbf{r}_2-\mathbf{r}_1|}}{|\mathbf{r}_2-\mathbf{r}_1|}, \tag{1.138}$$

which is an exact solution to the wave equation, was used in the Kirchhoff's diffraction integral. This Green's function represents a uniform spherical wave, diverging from a source point $P_1(\mathbf{r}_1)$. Hence the field $\tilde{u}(\mathbf{r}_2,\mathbf{r}_1)$, at a point $P_2(\mathbf{r}_2)$ due to a source at point $P_1(\mathbf{r}_1)$ can be written as:

$$\tilde{u}(\mathbf{r}_2,\mathbf{r}_1) = \frac{e^{ik|\mathbf{r}_2-\mathbf{r}_1|}}{|\mathbf{r}_2-\mathbf{r}_1|} \quad , \tag{1.139}$$

Again a small variation along the z axis is assumed. Thus using the binomial expansion, Eq. (1.139) can be written as

$$|\mathbf{r}_2-\mathbf{r}_1| = (z-z_0) + \frac{(x-x_0)^2+(y-y_0)^2}{2(z-z_0)} + \ldots \quad , \tag{1.140}$$

where for reasons of convenience the origin (x_0,y_0,z_0) of the Cartesian coordinate system is located at $P_1(\mathbf{r}_1)$. In the denominator of Eq. (1.138) even the quadratic term of Eq. (1.140) can be dropped [14].

If a uniform spherical wave diverging from a source point (x_0, y_0, z_0), and being observed at an observation point (x, y, z) is considered and if the axial distance z-z_0 between the source and observation points is sufficiently large compared to the transverse coordinates x_0, y_0 and x, y, then the field distribution produced by this wave at point x, y on the plane located at distance z can be written, using the paraxial approximation as

$$\tilde{u}(x,y,z)=\frac{1}{z-z_0}e^{ik\left(\frac{(x-x_0)^2+(y-y_0)^2}{2(z-z_0)}\right)}=\frac{1}{R(z)}e^{ik\left(\frac{(x-x_0)^2+(y-y_0)^2}{2R(z)}\right)} \quad , \tag{1.141}$$

where here $R(z)$=z-z_0 gives the radius of curvature of the spherical wave at plane z. The phase variation $e^{i\phi(x,y,z)}$ across the transverse plane at fixed z for such a paraxial spherical wave with radius of curvature $R(z)$ thus has the quadratic form

$$\phi(x,y,z)\equiv k\frac{(x-x_0)^2+(y-y_0)^2}{2(z-z_0)}=\frac{\pi}{\lambda}\frac{(x-x_0)^2+(y-y_0)^2}{R(z)} \quad . \tag{1.142}$$

The radius of curvature $R(z)$ of the wave at plane z can be written in a more general form as

$$R(z)=R_0+z-z_0 \quad , \tag{1.143}$$

with R_0 being the value at the earlier plane z_0. Thus the radius of curvature of such a spherical wave increases linearly with distance as the wave propagates forward to any other plane z.

1.11.3. The complex source point method

Decamps [21] derived the complex source point method. This method has been widely used in order to describe the radiation profile of a Gaussian beam. Using this method it was demonstrated by Sheppard and Saghafi [25], during the time period of this research, that it is possible to derive an exact solution to Maxwell's equations, but there is a problem with the physical interpretation of this method, i.e. what is a complex source? Or, since laser beams propagate in real space, how come a Gaussian beam needs to be described by a source located in the complex plane?

1.11.3.1. Introducing complex source point coordinates

A paraxial spherical wave in the form given in Eq. (1.141) *cannot by itself be a very useful analytical form for a real physical beam, however, because the amplitude of the spherical wave does not fall off with transverse distance from the axis. Such a wave instead extends out to infinity in the transverse direction and carries therefore an infinite amount of energy and power in the transverse plane (as well as having large deviation from a true sphere far off the axis)* [14]. Eqs. (1.141-1.143) satisfy the paraxial wave equation or the Huygens-Fresnel integral exactly for an arbitrary choice of source point co-ordinates x_0, y_0, z_0. It is thus implied that these co-ordinates are simply constant parameters, which cancel out identically when the spherical wave expression is put into the paraxial wave equation or the Huygens-Fresnel integral. Hence complex values for the source point co-ordinates can be used. For simplicity x_0, y_0 are set equal to zero and the axial location z_0 of the source point is converted into a *complex number*, by subtracting from it an arbitrary complex quantity q_o. Hence the pure real value z_0 in the spherical wave expression is replaced by the complex value z_0-q_0. This is equivalent to replacing the radius of curvature $R(z)=R_0+z-z_0$ with $q(z) = z-(z_o-q_o) = q_o+z-z_o$. Thus the value of the new "complex radius" at the source plane $z=z_0$ is just $q(z_o) = q_o$. The spherical wave divergence from this complex source point is obtained by replacing $R(z)$ with $q(z)$ in Eq. (1.141). Thus the divergence of the complex spherical wave can be written as

$$\tilde{u}(x,y,z) = \frac{1}{z-z_0+q_0} e^{ik\left(\frac{x^2+y^2}{2(z-z_0+q_0)}\right)} = \frac{1}{q(z)} e^{ik\left(\frac{x^2+y^2}{2q(z)}\right)} \quad , \qquad (1.144)$$

where the complex radius of curvature is given by

$$q(z) = q_0 + z - z_0 \quad . \qquad (1.145)$$

As $q(z)$is complex, the expression in Eq. (1.144) can be separated into a real and an imaginary part. If the quantity $\frac{1}{q(z)}$ is separated into its real and imaginary part in the form

$$\frac{1}{q(z)} \equiv \left[\frac{1}{q(z)}\right]_r + i\left[\frac{1}{q(z)}\right]_i \quad , \tag{1.146}$$

then the spherical wave expression can be rewritten as

$$\tilde{u}(x,y,z) = \frac{1}{q(z)} e^{\left(ik\frac{x^2+y^2}{2q_r(z)} - k\frac{x^2+y^2}{2q_i(z)}\right)} \quad , \tag{1.147}$$

remembering that $q_r(z)$ and $q_i(z)$ are always defined by Eq. (1.146).

The exponent for this complex source point beam has an imaginary quadratic transverse variation, corresponding to a spherical wave with a real radius of curvature, and a purely real quadratic transverse variation, which gives a Gaussian transverse amplitude profile, with a transverse fall-off determined by the imaginary part of $\frac{1}{q(z)}$ [14]. These variations are both contained in the complex radius of curvature $q(z)$ as given by Eq. (1.146).

1.11.3.2. Gaussian beam propagation in complex source point approach

The lowest order Gaussian beam, which is characterized by a spot size w_0 and a planar wavefront $R_0=\infty$ in the transverse dimension, at the beam waist ($z_0=0$) is considered. In this case Eqs. (1.57) can be rewritten, using Eqs. (1.77) as

$$R(z) = z + \frac{z_R^2}{z} \tag{1.148}$$

$$\phi = \tan^{-1}\left(\frac{z}{z_R}\right) \quad .$$

Since the free space parameter $q(z)$ obeys the following propagation law [14]

$$q(z) = q_0 + z = z - iz_R \quad , \tag{1.149}$$

with the initial value

$$q_0 = -i\frac{\pi w_0^2}{\lambda} = -iz_R \quad , \tag{1.150}$$

the normalized field pattern for such a Gaussian beam is given by [14]

$$\tilde{u}(x,y,z) = \sqrt{\frac{2}{\pi}}\frac{q_0}{w_0 q(z)} e^{ikz + ik\left(\frac{x^2+y^2}{2q(z)}\right)} = \sqrt{\frac{2}{\pi}}\frac{e^{ikz - i\phi(z)}}{w(z)} e^{\left(\frac{x^2+y^2}{w^2(z)} + ik\frac{x^2+y^2}{2R(z)}\right)}, \tag{1.151}$$

where the complex radius of curvature $q(z)$ is related to the spot size $w(z)$ and the radius of curvature $R(z)$ at any plane z by the definition

$$\frac{1}{q(z)} \equiv \frac{1}{R(z)} + i\frac{\lambda}{\pi w^2(z)} \quad . \tag{1.152}$$

At first sight it seems that the complex source point method is the ideal way in which to describe a propagating Gaussian beam. However as pointed out at the beginning of this section, laser beams propagate in real space, and the link between a source in the complex plane and such a beam is not physical, even though the expression given in Eq. (1.151) is identical to the expression in Eq. (1.50.a) for the 00 order.

1.11.4. The Fourier transform approach

The principle on which the Fourier transform approach is based is that a Gaussian beam can be decomposed into a set of infinite plane waves, all travelling at different angles to the axis of propagation. In the literature Mansuripur [22] and Kant [23] have based their models on the Fourier transform method. The idea to evaluate the diffraction integral in this way is good. However by decomposing the beam, automatically an approximation is introduced and it is thus impossible to find an exact solution to Maxwell's equations. Additionally the diffraction integral is evaluated numerically and thus no analytic solution is obtained.

1.11.5. The method based on spheroidal functions

Landesman and Barrett [24] showed that it is possible to consider a real source point spherical wave in the prolate spheroidal co-ordinate system, where the real source point is located at one of the foci of the prolate co-ordinate system. By then transforming this system into the oblate spheroidal co-ordinate system they transmuted a spherical wave with a real point source on axis into a Gaussian beam. However the wavefunction presented by [24] has a circular singularity of radius equal to the Rayleigh range, in the beam waist plane and a discontinuity occurring on the focal disk circumscribed by the singularity. As there is a singularity present, it implies that [24] found a solution, which violates the conservation of energy. It will be demonstrated in the next chapter that the discontinuity and the singularity can be removed. Hence the solution presented by [24] becomes physical in the sense that the energy of the beam is conserved and that the beam is propagating in the real space.

1.12. The need for an exact vector solution

Unfortunately, no exact, mathematical vector description of a Gaussian beam is available. Instead approximation models based on the fifth order Gaussian beam approximation [18, 19] and diffraction based approximations [22, 23] are in use. Recent studies have shown that the above approximation techniques are not accurate enough in some of the applications using strongly focused laser beams. Thus there is a need for a more accurate description of the Gaussian beam especially in areas such as optical trapping. Most notably, the existing theories are not adequate in cases where the laser beam is focused by a high numerical aperture lens. It has been discussed in this chapter that the previous attempts to obtain closed form analytical scalar as well as vector solutions for focused beams have failed – for example giving rise to singularities [24]. The only known accurate scalar description is the complex source point model with the introduction of a complex sink in order to cancel out the singularity present in the standard model [25]. The disadvantage of this model is the difficulty of its interpretation and visualisation. Thus in the following chapters, an accurate vector model, describing the Gaussian laser beam, will be developed, which uses [24] as a starting point, is singularity free and is an exact solution to Maxwell's equations, also satisfying the required boundary conditions at the beam waist, in the paraxial limit, and in the far-field. Since Landesman and Barrett [24] presented a

scalar solution to the Helmholtz equation, it is appropriate to find an exact scalar solution first. This solution is derived in chapter 2. As it is possible to construct a vector solution from a scalar solution, this solution will be derived in chapters 3 and 4. Once the vector solution is known, it is possible to calculate in chapter 5 the optical trapping forces exerted on a dielectric microsphere by a focused Gaussian laser beam.

References

[1] Schawlow, A. L. and Townes, C. H. (1958), *Phys. Rev.* **112**, 1940

[2] Fox, A. G. and Li, T. (1961), *Bell Syst. J.* **40**, 453

[3] Svelto, O and Hanna, D. C. (1982), Principles of lasers, 2nd edition, Plenum Press

[4] Fischetti, M. (2001), Gotcha!, *Scientific American*, March edition, 68-69

[5] Ashkin, A. (1970), Acceleration and trapping of particles by radiation pressure, *Phys. Rev. Lett.* **24**, 4, 156-159

[6] Berns, M. W. (1998), Laser Scissors and Tweezers, *Scientific American*, April edition, 52-57

[7] S. Chu(1992), Laser Trapping of Neutral Particles, *Scientific American*, February edition 71-76

[8] Ulanowski, Z., and Ludlow, I. K., (2000), Compact optical trapping microscope using a diode laser, *Meas. Sci. Technol.* **11**. 1778-1785

[9] Ashkin, A., Dziedzic, J. M., Schütze, K., Euteneuer, U.,Schliwa, M., (1990) Force generation measured in vivo by infrared laser trap. *Nature* **348**, 346-348

[10] Goodman, J. W. (1968), Introduction to Fourier Optics, McGraw-Hill

[11] Wangsness, R. K., (1986) Electromagnetic Fields 2nd edition, John Wiley & Sons

[12] Pedrotti, F. L. and Pedrotti, L. S. (1987), Introduction to optics, Prentice-Hall international edition

[13] Boyd, G. D. and Gordon, J. P. (1961), *Bell Syst. Tech. J.* **40**, 489

[14] Siegman, A. E., (1986) Lasers, University Science Books

[15] Boas, M. L., (1983), Mathematical methods in the physical sciences, John Wiley & Sons

[16] Vaughan, J. M., (1989), The Fabry-Perot Interferometer, Adam Hilger

[17] Tamm, C.,(1988), Frequency locking of two transverse optical modes of a laser *Phys. Rev. A.* **38**. 11., 5960-5963

[18] Davis, L. W. (1979), Theory of electromagnetic beams, Phys. Rev. A **19**, 1177-1179

[19] Barton, J. P. and Alexander, D. R. (1989) 5th - order corrected electromagnetic-field components for a fundamental Gaussian beam. *J. Appl. Phys.* **66**, 2800-2802.

[20] Lock, J. A. and Gousbet, G. (1994) Rigorous justification of the localised approximation to the beam shape coefficient in generalised Lorenz-Mie theory.I.On-axis beams. *J. Opt. Soc. Am. A* **11**, 2503-2515, and references therein.

[21] Decamps, G. A. (1971), Gaussian beam as a bundel of complex rays, *Electronics letters*, **7**, 23. 684-685

[22] Mansuripur, M. (1989) Certain computational aspects of vector diffraction

problems. *J. Opt. Soc. Am. A* 786-805. Erratum: *J. Opt. Soc. Am. A* **10,** 382-383.

[23] Kant, R. (1993) An analytical solution of vector diffraction for focusing optical-systems. *J. Mod. Optics* 40(2), 337-347.

[24] Landesman, B. T. and Barrett, H. H. (1988) Gaussian amplitude functions that are exact solutions to the scalar Helmholtz equation. *J. Opt. Soc. Am. A* **5,** 10, 1610-1619.

[25] Sheppard, C. J. R. , Saghafi, S. (1998) Beam modes beyond the paraxial approximation: a scalar treatment, *Phys. Rev. A* **57,** 4 p.2971-2979

[26] Ulanowski, Z., and Ludlow, I. K., (2000), Scalar field of nonparaxial Gaussian beams, *Opt. Lett.* **25,** 24. 1778-1785

[27] Nieminen, T. A., Rubinsztein-Dunlop, H. and Heckenberg, N. R. (2003), Multipole expansions of strongly focussed laser beams, *J. of Quantitative Spectroscopy and Radiative Transfer* **79-80,** 1005-1017

[28] Lax M, Louisell, W. H. and McKnight, W. B. (1975), From Maxwell to paraxial wave optics, *Phys. Rev. A* **11,** 4, 2971-2979

2. The solution to the scalar Helmholtz equation

2.1. Introduction

The aim of this chapter is to derive an exact set of solutions to the scalar Helmholtz equation. As was mentioned in chapter 1, such a set of solutions can be expressed in terms of spherical harmonics. In order to derive a solution to the Helmholtz equation which describes a laser beam used for optical tweezers, it is necessary to first determine the most suitable laser beam mode, used in interference, light scattering and entrapment applications, which was thought to be the TEM^{*}_{00} Laguerre-Gaussian beam mode. This beam mode satisfies the paraxial wave equation but is not an exact solution to the scalar Helmholtz equation. It will be demonstrated in section 2.4. that the lowest order beam mode, referred to as order 00, has an infinite beam power, and thus cannot be a physically realizable beam mode. However it will be demonstrated that order 01 has finite beam power and that the irradiance profile of this beam mode shows close resemblance with the one of TEM^{*}_{00}. Nevertheless it is useful, for didactic reasons, to use the order 00 beam mode as the starting point for all derivations.

Based on the cylindrical symmetry of the TEM^{*}_{00} beam mode about the axis of propagation, the Helmholtz equation will be separated in the most appropriate coordinate system which is, as it turns out, the oblate spheroidal coordinate system, in order to derive the exact solutions to the scalar Helmholtz equation. Since in the limit of infinitely short wavelength or large beam waist (paraxial limit), in the plane of the beam waist the spherical wavefronts of the TEM^{*}_{00} can be regarded as plane wavefronts, it is possible to test the derived solution with respect to satisfying the paraxial wave equation in this limit. In the far-field, the solution is expected to represent a spherical wave with its center at the origin. It is also worth mentioning that if the oblate spheroidal coordinate system is extended out to infinity, it turns into the spherical polar coordinate system. Therefore it is possible to test if the irradiance profile is Gaussian on the surface of the Gaussian reference sphere.

It will further be demonstrated, that the spheroidal wave model presented here and the complex source point model described by Sheppard and Saghafi [1] are identical and indeed satisfy the paraxial beam approximation, and in the limit of infinite radius of the principal surface (far-field limit), the irradiance profile is indeed Gaussian.

2.1.1. The most suitable laser beam mode

The most suitable laser beam mode for any of the following three areas of applications 1) interference, 2) light scattering and 3) entrapment is the TEM^{*}_{00} Laguerre-Gaussian mode. Such a beam mode can be produced by a HeNe laser. This beam mode is monochromatic, has a Gaussian irradiance profile at the beam waist given by

$$I(\mathbf{r}) = I_0 e^{\frac{-2\rho^2}{w_0^2}} \quad , \tag{2.1}$$

and has cylindrical symmetry about the z-axis. Hence the considered beam mode is a well-defined beam mode.

2.1.2. The scalar Helmholtz equation

The scalar Helmholtz equation (Eq. (1.19) with $\psi(r)$ replacing $u(r)$ is given by

$$(\nabla^2 + k^2)\psi(r) = 0 \quad . \tag{2.2}$$

This equation is only valid for steady monochromatic waves, and therefore transient waves are not included in the solution of this equation. Thus a valid description of a Gaussian beam must satisfy the Helmholtz equation and Maxwell's equations. Furthermore, according to the proof below, if $\psi(r)$ is a solution of the Helmholtz equation, then its complex conjugate is a solution as well.

Proof:

According to Eq. (2.2) $\quad [\nabla^2 + k^2]\psi(r) = 0.$

Hence, $\quad (\nabla^2 + k^2)^{*}\psi^{*}(r) = (\nabla^2 + k^2)\psi^{*}(r) = 0,$

where asterisk denotes complex conjugation and k is assumed to be real.

Since the laser cavity, which is being considered for interference, light scattering and the closely related entrapment applications has cylindrical geometry, it is convenient to represent the scalar Helmholtz equation in a different coordinate system than the Cartesian one.

2.2. Curvilinear coordinates

The family of curvilinear coordinates, which is used in this research, includes the following orthogonal coordinate systems: spherical polar coordinates, cylindrical polar coordinates, oblate spheroidal coordinates and prolate spheroidal coordinates. In order to change from one coordinate system to another, the rules of coordinate transformations given by Spiegel [2] have to be obeyed. The rectangular Cartesian coordinates x, y, z of any point can be expressed as functions of (u_1, u_2, u_3) and so

$$x=x(u_1, u_2, u_3), \qquad y=y(u_1, u_2, u_3) \quad \text{and} \quad z=z(u_1, u_2, u_3). \tag{2.3}$$

The assumption that Eqs. (2.3) can be solved in terms for u_1, u_2, u_3 in terms of x, y and z implies that

$$u_1=u_1(x, y, z), \qquad u_2=u_2(x, y, z) \quad \text{and} \quad u_3=u_3(x, y, z). \tag{2.4}$$

The functions given in Eqs. (2.3) and (2.4) are assumed to be single-valued and have continuous derivatives in order that the correspondence between (x, y, z) and (u_1, u_2, u_3) is unique. If the position vector of a point P is defined as $\mathbf{r} = x\hat{\mathbf{i}} + y\hat{\mathbf{j}} + z\hat{\mathbf{k}}$, then the three scalar Eqs. (2.3) can be written as a single vector equation $\mathbf{r}=\mathbf{r}(u_1, u_2, u_3)$. A tangent vector to the curve u_1 at the point P, for which u_2 and u_3 are constants, is given by $\frac{\partial \mathbf{r}}{\partial u_1}$. Therefore the unit tangent vector $\mathbf{e}_1$ in this direction is $\mathbf{e}_1 = \frac{\frac{\partial \mathbf{r}}{\partial u_1}}{\left|\frac{\partial \mathbf{r}}{\partial u_1}\right|}$, so that $\frac{\partial \mathbf{r}}{\partial u_1} = h_1\mathbf{e}_1$, where $h_1 = \left|\frac{\partial \mathbf{r}}{\partial u_1}\right|$. Similarly if $\mathbf{e}_2$ and $\mathbf{e}_3$ are unit tangent vectors to u_2 and u_3 curves at P respectively, then $\frac{\partial \mathbf{r}}{\partial u_2} = h_2\mathbf{e}_2$ and $\frac{\partial \mathbf{r}}{\partial u_3} = h_3\mathbf{e}_3$, where $h_2 = \left|\frac{\partial \mathbf{r}}{\partial u_2}\right|$ and $h_3 = \left|\frac{\partial \mathbf{r}}{\partial u_3}\right|$. The functions h_1, h_2 and h_3 are called "scale factors" and the unit vectors $\mathbf{e}_1$, $\mathbf{e}_2$ and $\mathbf{e}_3$ are in the direction of increasing u_1, u_2 and u_3 respectively. In order to express the scalar Helmholtz equation and Maxwell's equations in the various coordinate systems, it is necessary to express the Laplacian in these coordinate systems. For this purpose the Laplacian in curvilinear coordinates can be written in its most general form as .

$$\nabla^2 = \frac{1}{h_1 h_2 h_3}\left[\frac{\partial}{\partial u_1}\left(\frac{h_2 h_3}{h_1}\frac{\partial}{\partial u_1}\right)+\frac{\partial}{\partial u_2}\left(\frac{h_1 h_3}{h_2}\frac{\partial}{\partial u_2}\right)+\frac{\partial}{\partial u_3}\left(\frac{h_1 h_2}{h_3}\frac{\partial}{\partial u_3}\right)\right]. \tag{2.5}$$

2.2.1. Example 1: The scalar Helmholtz equation in spherical coordinates

The spherical polar coordinates are related to the Cartesian coordinates as follows:

$$\begin{aligned} x &= r\sin\theta\cos\phi \\ y &= r\sin\theta\sin\phi \\ z &= r\cos\theta \end{aligned} \tag{2.6}$$

or

$$\begin{aligned} r &= \sqrt{x^2+y^2+z^2} \\ \theta &= \tan^{-1}\left(\frac{\sqrt{x^2+y^2}}{z}\right) \\ \phi &= \tan^{-1}\left(\frac{y}{x}\right). \end{aligned} \tag{2.7}$$

The scale factors in this coordinate system can be evaluated from Eq. (2.6), using the method given in the previous section and setting $u_1=r$, $u_2=\theta$ and $u_3=\phi$ in the following manner:

$$h_1 = \left|\frac{\partial \mathbf{r}}{\partial u_1}\right| = \sqrt{\left(\frac{\partial x}{\partial r}\right)^2+\left(\frac{\partial y}{\partial r}\right)^2+\left(\frac{\partial z}{\partial r}\right)^2} = \sqrt{\sin^2\theta\cos^2\phi+\sin^2\theta\sin^2\phi+\cos^2\theta}$$

and using the fact that $\sin^2\alpha+\cos^2\alpha=1$

$$h_1 = \sqrt{\sin^2\theta\left(\cos^2\phi+\sin^2\phi\right)+\cos^2\theta} = 1$$

$$h_2 = \left|\frac{\partial \mathbf{r}}{\partial u_2}\right| = \sqrt{\left(\frac{\partial x}{\partial \theta}\right)^2+\left(\frac{\partial y}{\partial \theta}\right)^2+\left(\frac{\partial z}{\partial \theta}\right)^2} = r\sqrt{\cos^2\theta\cos^2\phi+\cos^2\theta\sin^2\phi+\sin^2\theta} = r$$

and

$$h_3 = \left|\frac{\partial \mathbf{r}}{\partial u_3}\right| = \sqrt{\left(\frac{\partial x}{\partial \phi}\right)^2 + \left(\frac{\partial y}{\partial \phi}\right)^2 + \left(\frac{\partial z}{\partial \phi}\right)^2} = r\sqrt{\sin^2\theta \sin^2\phi + \sin^2\theta \cos^2\phi} = r\sin\theta \,. \tag{2.8}$$

The square of the unit length element is given by:

$$ds^2 = (h_1 du_1)^2 + (h_2 du_2)^2 + (h_3 du_3)^2$$

and therefore

$$h_1 = h_r = 1, \quad h_2 = h_\theta = r, \quad h_3 = h_\phi = r\sin\theta \quad .$$

On substitution of these scale factors into Eq. (2.5), the Laplacian of the scalar function $\psi(r,\theta,\phi)$ in spherical polar coordinates is given by

$$\nabla^2\psi(r,\theta,\phi) = \frac{1}{r^2}\frac{\partial}{\partial r}\left(r^2\frac{\partial\psi(r,\theta,\phi)}{\partial r}\right) + \frac{1}{r^2\sin\theta}\frac{\partial}{\partial\theta}\left(\sin\theta\frac{\partial\psi(r,\theta,\phi)}{\partial\theta}\right) + \frac{1}{r^2\sin^2\theta}\frac{\partial^2\psi(r,\theta,\phi)}{\partial\phi^2} \,. \tag{2.9}$$

If the solutions to the Helmholtz equation Eq. (2.2) is written in product form, $\psi(r,\theta,\phi) = R(r)\Theta(\theta)\Phi(\phi)$, it is possible to separate the Helmholtz equation into equations for each different variable.

The radial equation associated with Eq. (2.2) can then be written as

$$r^2\frac{d^2R(r)}{dr^2} + 2r\frac{dR(r)}{dr} + [k^2r^2 - n(n+1)]R(r) = 0 \,. \tag{2.10}$$

Solutions to Eq. (2.10) are the spherical Bessel functions, $j_n(r)$ or spherical Neumann functions $y_n(r)$ or the spherical Hankel functions of the first and second kind, $h_n^{(1)}(r)$ and $h_n^{(2)}(r)$.

The Bessel functions

$$J_p(x)=\sum_{n=0}^{\infty}\frac{(-1)^n}{\Gamma(n+1)\Gamma(n+p+1)}\left(\frac{x}{2}\right)^{2n+p},$$

where $J_p(x)$ is called the Bessel function of the first kind [3] of order p, where p is a constant, but not necessarily an integer, and $\Gamma(q)$ is the gamma function, defined as

$$\Gamma(q)=\int_0^{\infty}x^{q-1}e^{-x}dx, \qquad q>0.$$

The second solution to Bessel's equation is $J_{-p}(x)=(-1)^p J_p(x)$. In this case p is an integer. Here the first and second solutions are two dependent solutions of Bessel's equation

$$x^2y''+xy'+\left(x^2-p^2\right)y=0.$$

Where a dash denotes first derivative with respect to x and two dashes denote second derivative with respect to x. The combination of the first and second solution of Bessel's equation is called the Neumann function

$$N_p(x)=Y_p(x)=\frac{\cos(\pi p)J_p(x)-J_{-p}(x)}{\sin(\pi p)}.$$

The Hankel functions of the first and second kind

$$H_p^{(1)}(x)=J_p(x)+iN_p(x)$$
$$H_p^{(2)}(x)=J_p(x)-iN_p(x)$$

If $p=\frac{2n+1}{2}=n+\frac{1}{2}$, n a positive integer, then $J_p(x)$ and $N_p(x)$ are called Bessel functions of half odd integral order; they can be expressed in terms of $\sin(x)$, $\cos(x)$ and powers of x. The spherical Bessel functions are closely related to them as can be seen from the formulae in Eqs. (2.11.a) and (2.11.b).

The spherical Bessel functions

$$j_n(x)=\sqrt{\frac{\pi}{2x}}J_{(2n+1)/2}(x)=x^n\left(-\frac{1}{x}\frac{d}{dx}\right)^n\left(\frac{\sin x}{x}\right)$$
$$y_n(x)=\sqrt{\frac{\pi}{2x}}Y_{(2n+1)/2}(x)=-x^n\left(-\frac{1}{x}\frac{d}{dx}\right)^n\left(\frac{\cos x}{x}\right) \quad , \qquad (2.11.a)$$

are solutions to the spherical Bessel equation,

$$x^2y''+2xy'+[k^2x^2-n(n+1)]y=0,$$

with the corresponding spherical Hankel functions of the first and second kind

$$h_n^{(1)}(x)=j_n(x)+iy_n(x)$$
$$h_n^{(2)}(x)=j_n(x)-iy_n(x) \quad . \qquad (2.11.b)$$

Solving Eqs.(2.11.a) leads to the following expressions for n=0, 1, 2.

n	$j_n(x)$	$y_n(x)$
0	$j_0(x)=\frac{\sin x}{x}$	$y_0(x)=-\frac{\cos x}{x}$
1	$j_1(x)=\frac{\sin x}{x^2}-\frac{\cos x}{x}$	$y_1(x)=-\frac{\cos x}{x^2}-\frac{\sin x}{x}$
2	$j_2(x)=\frac{3\sin x}{x^3}-\frac{3\cos x}{x^2}-\frac{\sin x}{x}$	$y_2(x)=-\frac{3\cos x}{x^3}-\frac{3\sin x}{x^2}+\frac{\cos x}{x}$

Table 2.1. Expressions for spherical Bessel and spherical Neumann functions of order n=0,1,2.

The separated polar angular equation associated with Eq. (2.2) is the associated Legendre equation

$$\frac{1}{\sin\theta}\frac{d}{d\theta}\left[\sin\theta\frac{d\Theta(\theta)}{d\theta}\right]+\left[n(n+1)-\frac{m^2}{\sin^2\theta}\right]\Theta(\theta)=0 \quad . \qquad (2.12)$$

In the case where θ ranges from zero to π, the constant n must be an integer.

Thus the solutions to Eq. (2.12) are

$$\Theta(\theta) = P_n^m(\cos\theta) \quad , \tag{2.13}$$

where $P_n^m(\cos\theta)$ are the associated Legendre functions, with $m = 0, 1, 2,\ldots$and $n \geq m$.

The associated Legendre functions

Using Rodrigues formula [3], the associated Legendre functions are defined as

$$P_n^m(s) = \frac{1}{2^n n!}\left(1-s^2\right)^{m/2}\frac{d^{n+m}}{ds^{n+m}}\left(s^2-1\right)^n \quad . \tag{2.14}$$

In the case where $\cos\theta > 1$, the angle is complex.

Solving Eq.(2.14) leads to the following expressions for n=0, 1, 2 and m=0, 1.

n \ m	0	1
0	$P_0^0(s) = 1$	-
1	$P_1^0(s) = s$	$P_1^1(s) = \sqrt{1-s^2}$
2	$P_2^0(s) = \frac{1}{2}(3s^2-1)$	$P_2^1(s) = 3s\sqrt{1-s^2}$

Table 2.2. Expressions for the associated Legendre functions for values of n=0,1,2 and m=0,1

The separated azimuthal equation associated with Eq. (2.2) is

$$\frac{1}{\Phi(\phi)}\frac{d^2\Phi(\phi)}{d\phi^2} + m^2 = 0 \quad . \tag{2.15}$$

It immediately follows from Eq. (2.15) that Φ is periodic in ϕ with period 2π. The general solutions of Eq. (2.15) is

$$\Phi = A\cos(m\phi) + B\sin(m\phi) \, .$$

or

$$\Phi = e^{\pm im\phi}. \tag{2.16}$$

The solutions to the separated Helmholtz equations can be multiplied together in order to give a combined eigensolution to the scalar Helmholtz equation, which is the product of these separable solutions. Landesman and Barrett [4] presented the solution

$$\psi_{nm}(r,\theta,\phi) = h_n^{(1)}(r) P_n^m(\cos\theta) e^{\pm im\phi}\ , \tag{2.17}$$

where only one of the spherical Bessel functions, namely the Hankel function of the first kind, representing an outward traveling wave is used. The $e^{\pm\, im\phi}$ solution to Eq. (2.16) was chosen, because of it being of the most general form.

2.2.2. Example 2: The oblate spheroidal coordinate system

The oblate spheroidal coordinate system is an orthogonal coordinate system. With d a constant, the parametric equations relating the oblate spheroidal coordinates to the Cartesian coordinates are given by Landesman and Barrett [4] as

$$\begin{aligned} x &= d\cosh\mu\sin\theta\cos\phi \\ y &= d\cosh\mu\sin\theta\sin\phi \\ z &= d\sinh\mu\cos\theta \end{aligned} \tag{2.18}$$

with either

$$0 \le \theta \le \pi,\quad 0 \le \mu < \infty,\quad 0 \le \phi \le 2\pi$$

or

$$0 \le \theta \le 2\pi,\quad -\infty < \mu < \infty,\quad 0 \le \phi \le 2\pi\ .$$

Substituting ξ=sinhμ and η=cosθ into Eq. (2.18) leads to the alternative parametric equations

$$\begin{aligned} x &= d\sqrt{1+\xi^2}\sqrt{1-\eta^2}\cos\phi \\ y &= d\sqrt{1+\xi^2}\sqrt{1-\eta^2}\sin\phi \\ z &= d\xi\eta \end{aligned}\ , \tag{2.19}$$

with

$$-1 \le \eta \le 1, \quad 0 \le \xi < \infty, \quad 0 \le \phi \le 2\pi$$

or

$$0 \le \eta \le 1, \quad -\infty < \xi < \infty, \quad 0 \le \phi \le 2\pi .$$

The scale factors for this coordinate system can be calculated, using the method described in section 2.2.. From Eqs. (2.19), (here, $u_1=\xi$, $u_2=\eta$ and $u_3=\phi$) it is found that

$$h_1 = h_\xi = \left|\frac{\partial \mathbf{r}}{\partial u_1}\right| = \sqrt{\left(\frac{\partial x}{\partial \xi}\right)^2 + \left(\frac{\partial y}{\partial \xi}\right)^2 + \left(\frac{\partial z}{\partial \xi}\right)^2} = d\sqrt{\frac{\xi^2+\eta^2}{1+\xi^2}},$$

$$h_2 = h_\eta = \left|\frac{\partial \mathbf{r}}{\partial u_2}\right| = \sqrt{\left(\frac{\partial x}{\partial \eta}\right)^2 + \left(\frac{\partial y}{\partial \eta}\right)^2 + \left(\frac{\partial z}{\partial \eta}\right)^2} = d\sqrt{\frac{\xi^2+\eta^2}{1-\eta^2}}$$

and

$$h_3 = h_\phi = \left|\frac{\partial \mathbf{r}}{\partial u_3}\right| = \sqrt{\left(\frac{\partial x}{\partial \phi}\right)^2 + \left(\frac{\partial y}{\partial \phi}\right)^2 + \left(\frac{\partial z}{\partial \phi}\right)^2} = d\sqrt{1+\xi^2}\sqrt{1-\eta^2} \qquad (2.20)$$

The square of the unit length element is given by

$$ds^2 = (h_1 du_1)^2 + (h_2 du_2)^2 + (h_3 du_3)^2 .$$

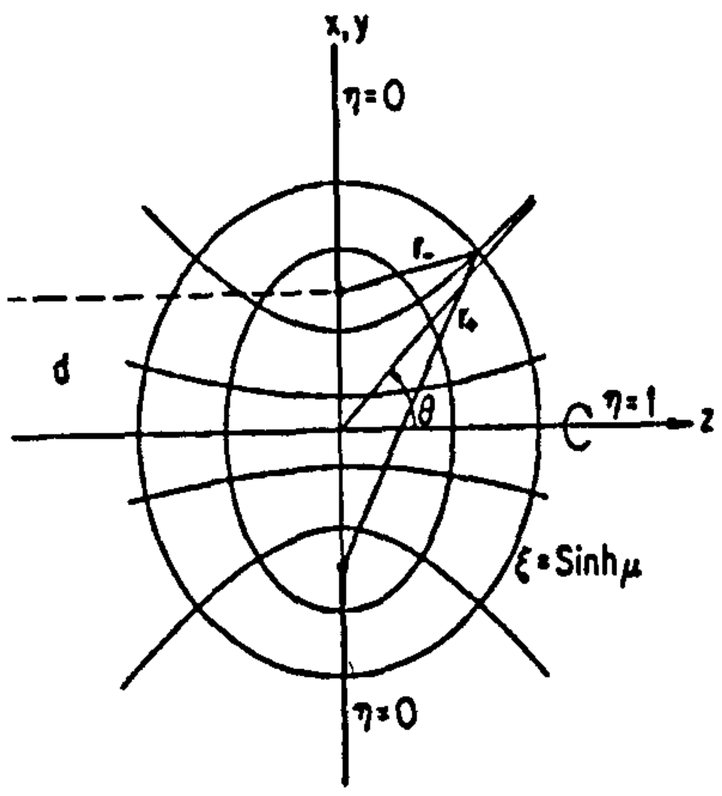

Fig. 2.1. Oblate spheroidal coordinate system (taken from [4])

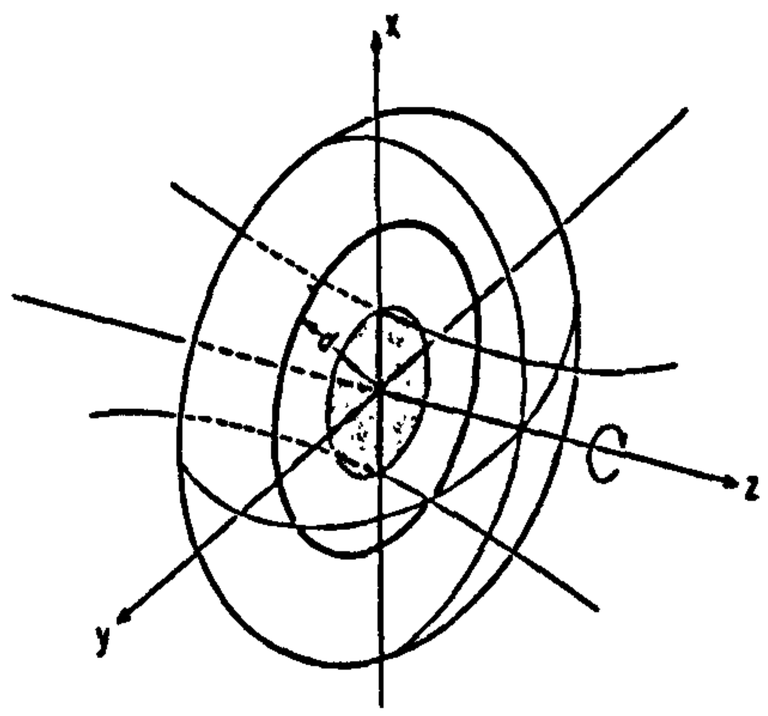

Fig. 2.2. Focal circle for the oblate spheroidal coordinate system (taken from [4])

The oblate spheroidal coordinate system is formed by rotating a system of confocal ellipses and hyperbolas about the minor axis (z axis) of the ellipse. It is seen from Fig. 2.2. [4] that the focus of the oblate spheroidal coordinate system is a circle in the x-y plane. The spacing of the foci of the ellipses/hyperbolas, is $2d$. Later on it will be demonstrated, that d is the same as the Rayleigh range [5]. The hyperboloids of revolution consist of one single continuous sheets. The physical motivation for the introduction of this coordinate system is, that the ellipses are related to the wavefronts. The contour of constant amplitude in the beam is represented as a hyperboloid of one sheet. In Fig. 2.1. the distances between ellipses / hyperbolae and the foci are shown as r_+ and r_- respectively:

$$r_+ = d\left[\sqrt{1+\xi^2} + \sqrt{1-\eta^2}\right]$$
$$r_- = d\left[\sqrt{1+\xi^2} - \sqrt{1-\eta^2}\right] \quad . \tag{2.21}$$

In the oblate spheroidal coordinate system, the surface $|\xi|$=constant > 0 is an oblate ellipsoid with major axis of length $2d\cosh\mu$ and minor axis of length $2d|\sinh\mu|$. The surface $\xi = 0$ is a circular disk of radius d centered at the origin in the x-y plane. The surface $|\eta|$= constant < 1 is a hyperboloid of revolution of one sheet whose asymptotes pass through the origin inclined at an angle $\theta = \cos^{-1}\eta$ with the z axis. The surface $\eta = 0$ is the x-y plane, except for the circular disk $\xi = 0$. The surface ϕ = constant is the azimuthal plane containing the z axis. The angle ϕ is measured from the x-z plane.

2.2.3. Example 3: The prolate spheroidal coordinate system

The prolate spheroidal coordinate system is an orthogonal coordinate system. With d a constant, the parametric equations relating the prolate spheroidal coordinates to the Cartesian coordinates, are given by Landesman and Barrett [4] as

$$\begin{aligned} x &= d\sinh\mu\sin\theta\cos\phi \\ y &= d\sinh\mu\sin\theta\sin\phi \\ z &= d\cosh\mu\cos\theta \end{aligned} \qquad (2.22)$$

where

$$0 \le \theta \le \pi, \quad 0 \le \mu < \infty, \quad 0 \le \phi \le 2\pi$$

Substituting ξ=coshμ and η=cosθ into Eq. (2.22) leads to the alternative parametric equations

$$\begin{aligned} x &= d\sqrt{\xi^2-1}\sqrt{1-\eta^2}\cos\phi \\ y &= d\sqrt{\xi^2-1}\sqrt{1-\eta^2}\sin\phi \\ z &= d\xi\eta \end{aligned} \quad , \qquad (2.23)$$

with

$$-1 \le \eta \le 1, \quad 1 \le \xi < \infty, \quad 0 \le \phi \le 2\pi$$

The scale factors for this coordinate system can be calculated, using the method described in section 2.2. From Eq. (2.23) (here, u_1=ξ, u_2=η and u_3=ϕ) it is found that

$$h_1 = h_\xi = \left|\frac{\partial \mathbf{r}}{\partial u_1}\right| = \sqrt{\left(\frac{\partial x}{\partial \xi}\right)^2 + \left(\frac{\partial y}{\partial \xi}\right)^2 + \left(\frac{\partial z}{\partial \xi}\right)^2} = d\sqrt{\frac{\xi^2-\eta^2}{\xi^2-1}},$$

$$h_2 = h_\eta = \left|\frac{\partial \mathbf{r}}{\partial u_2}\right| = \sqrt{\left(\frac{\partial x}{\partial \eta}\right)^2 + \left(\frac{\partial y}{\partial \eta}\right)^2 + \left(\frac{\partial z}{\partial \eta}\right)^2} = d\sqrt{\frac{\xi^2-\eta^2}{1-\eta^2}}$$

and

$$h_3 = h_\phi = \left|\frac{\partial \mathbf{r}}{\partial u_3}\right| = \sqrt{\left(\frac{\partial x}{\partial \phi}\right)^2 + \left(\frac{\partial y}{\partial \phi}\right)^2 + \left(\frac{\partial z}{\partial \phi}\right)^2} = d\sqrt{\xi^2-1}\sqrt{1-\eta^2}\,. \qquad (2.24)$$

The square of the unit length element is given by

$$ds^2 = (h_1 du_1)^2 + (h_2 du_2)^2 + (h_3 du_3)^2 .$$

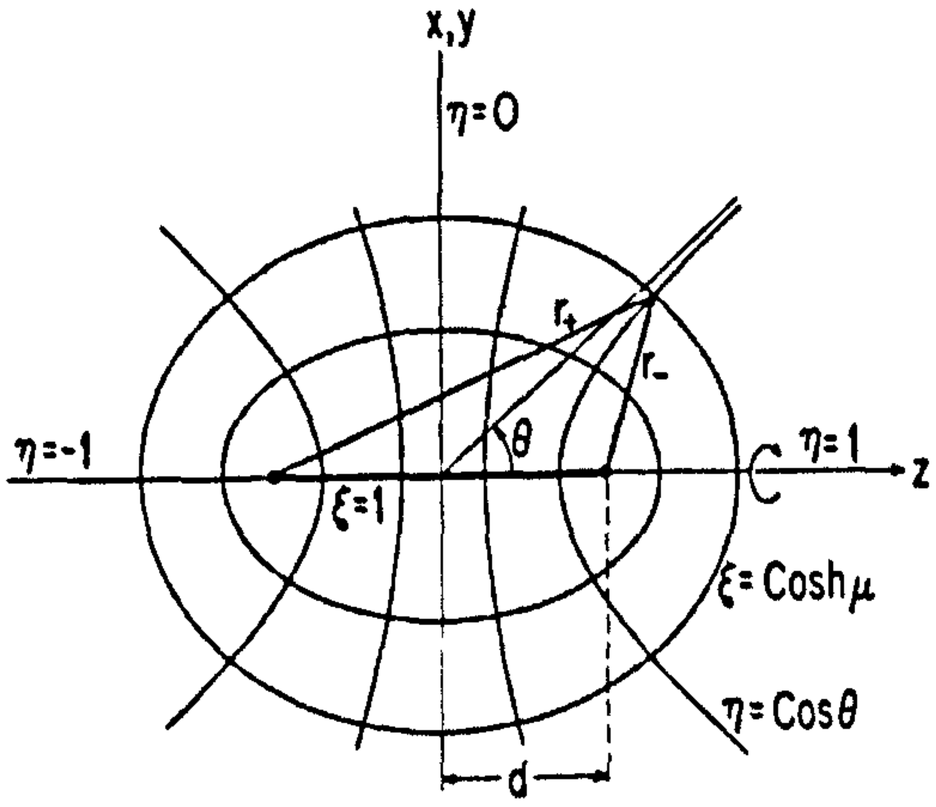

Fig. 2.3. Prolate spheroidal coordinate system (taken from [4])

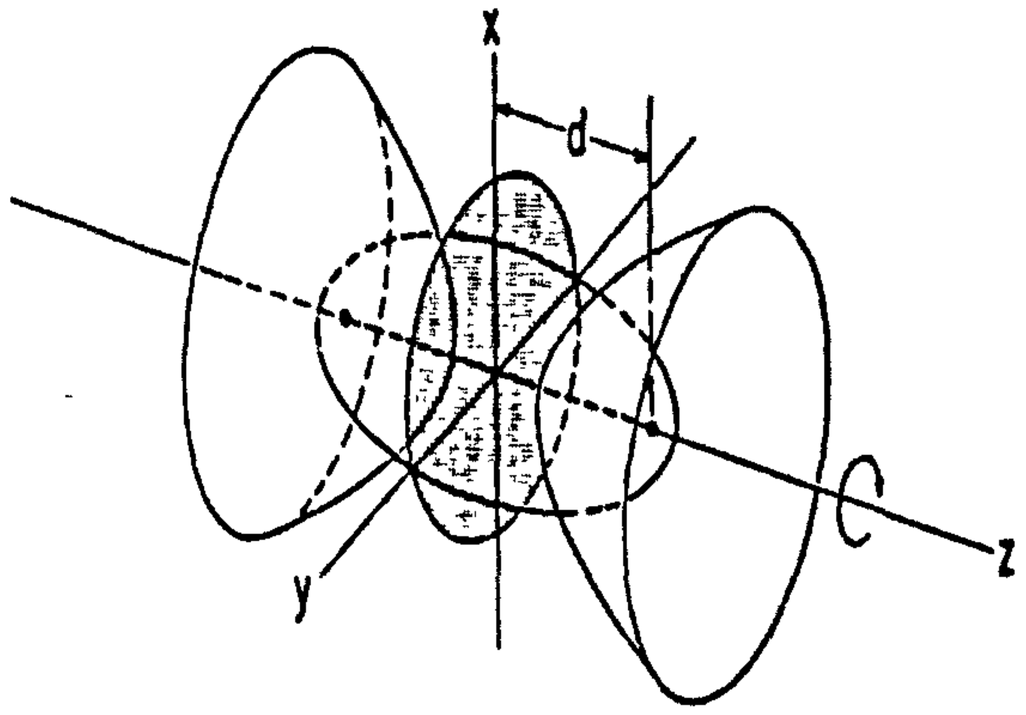

Fig. 2.4. Focal points for the prolate spheroidal coordinate system (taken from [4])

The prolate spheroidal coordinate system is formed by rotating a system of confocal ellipses and hyperbolas about the major axis (z axis) of the ellipse. The foci of the prolate spheroidal coordinate system occur on this axis and are located symmetrically about the origin of the Cartesian coordinates at a distance equal to d from the origin [4]. (see Fig. 2.3. and Fig. 2.4). The hyperboloids of revolution consist of two separate sheets. In Fig. 2.3. the distances between ellipses / hyperbolae and the foci are shown as r_+ and r_- respectively:

$$\begin{aligned} r_+ &= d(\xi + \eta) \\ r_- &= d(\xi - \eta) \end{aligned} \quad . \tag{2.25}$$

In the prolate spheroidal coordinate system, the surface $|\xi|$=constant > 1 is a prolate ellipsoid with major axis of length $2d\xi$ and minor axis of length $2d \sinh\mu$. The surface $\xi = 1$ is a straight line along the z axis from z=-d to z=+d. The surface $|\eta|$ = constant < 1 is a hyperboloid of revolution of two sheets whose asymptotes pass through the origin inclined at an angle $\theta = \cos^{-1}\eta$ with the z axis. The surface $|\eta| = 1$ is the part of the z-axis for which $|z| > d$. The surface ϕ = constant is the azimuthal plane containing the z axis. The angle ϕ is measured from the x-z plane.

2.2.4. The scalar Helmholtz equation in oblate spheroidal coordinates

By substituting the scale factors from Eq. (2.20) into Eq. (2.5) the scalar Helmholtz equation in oblate spheroidal coordinates is obtained. This equation can be written as

$$(\nabla^2 + k^2)\psi(\xi,\eta,\phi) = \frac{\partial}{\partial\xi}\left[(1+\xi^2)\frac{\partial\psi(\xi,\eta,\phi)}{\partial\xi}\right] + \frac{\partial}{\partial\eta}\left[(1-\eta^2)\frac{\partial\psi(\xi,\eta,\phi)}{\partial\eta}\right] + \frac{\xi^2+\eta^2}{(1+\xi^2)(1-\eta^2)}\frac{\partial^2\psi(\xi,\eta,\phi)}{\partial\phi^2} + k^2d^2(\xi^2+\eta^2)\psi(\xi,\eta,\phi) = 0 \quad . \tag{2.26}$$

Landesman and Barrett [4] have demonstrated that Eq. (2.26) is not directly separable. They argued, that since the oblate spheroidal coordinate system, when extended out to infinity, turns into the spherical polar coordinate system, the wavefunction given by Eq. (2.17) is necessarily a solution to Eq. (2.26) when the oblate spheroidal coordinate system is extended out to infinity. Using rather complicated coordinate transformations from prolate spheroidal coordinates into oblate spheroidal coordinates, they found that the argument (s) of the associated Legendre functions can be expressed as

$$s = \frac{1+i\xi\eta}{\eta+i\xi} \tag{2.27}$$

in oblate spheroidal coordinates, denoted by (O/S), and the argument of the spherical Bessel function, i.e. r, can be expressed as

$$t = kd(\xi\text{-}i\eta) \tag{2.28}$$

in oblate spheroidal coordinates. Making these substitutions Landesman and Barrett showed that

$$\psi_{mn}^{(1)}(\xi,\eta,\phi)_{O/S} = e^{-kd}h_n^{(1)}(t)P_n^m(s)e^{im\phi}, \tag{2.29}$$

indeed represents a complete set of solutions to the scalar Helmholtz equation in oblate spheroidal coordinates, where $h_n^{(1)}(t)$ is the Hankel function of the first kind. At first sight there could be reason for concern that the argument of the associated Legendre functions is complex. However from Rodrigues formula (Eq. (2.14)) it can be seen that there is no restriction attached to the argument (s) of the associated Legendre functions. It can similarly be seen from section 2.2.1. that there is no restriction attached to the argument (x)

of the spherical Bessel functions. Furthermore from Fig. 2.5., showing the spherical polar coordinate system superimposed on the prolate spheroidal coordinate system, it can be seen that if the point source is located at the focus *f'* of the prolate spheroidal coordinate system instead of at the centre of the spherical polar coordinate system *f*, as is the case when the coordinate system of choice is the spherical polar coordinate system, then $\cos(\theta') = \frac{z+d}{r'}$, instead of $\cos(\theta) = \frac{z}{r}$. Using the coordinate transformation from prolate spheroidal coordinates, denoted by (P/S), to oblate spheroidal coordinates given by Landesman and Barrett [4] as $\xi_{(P/S)} = \pm i\xi_{(O/S)}$ and using Eq. (2.19) it can be seen that $\cos(\theta') = \frac{z+d}{r'}$ is indeed equal to *s*. Therefore $-1 \leq s \leq 1$.

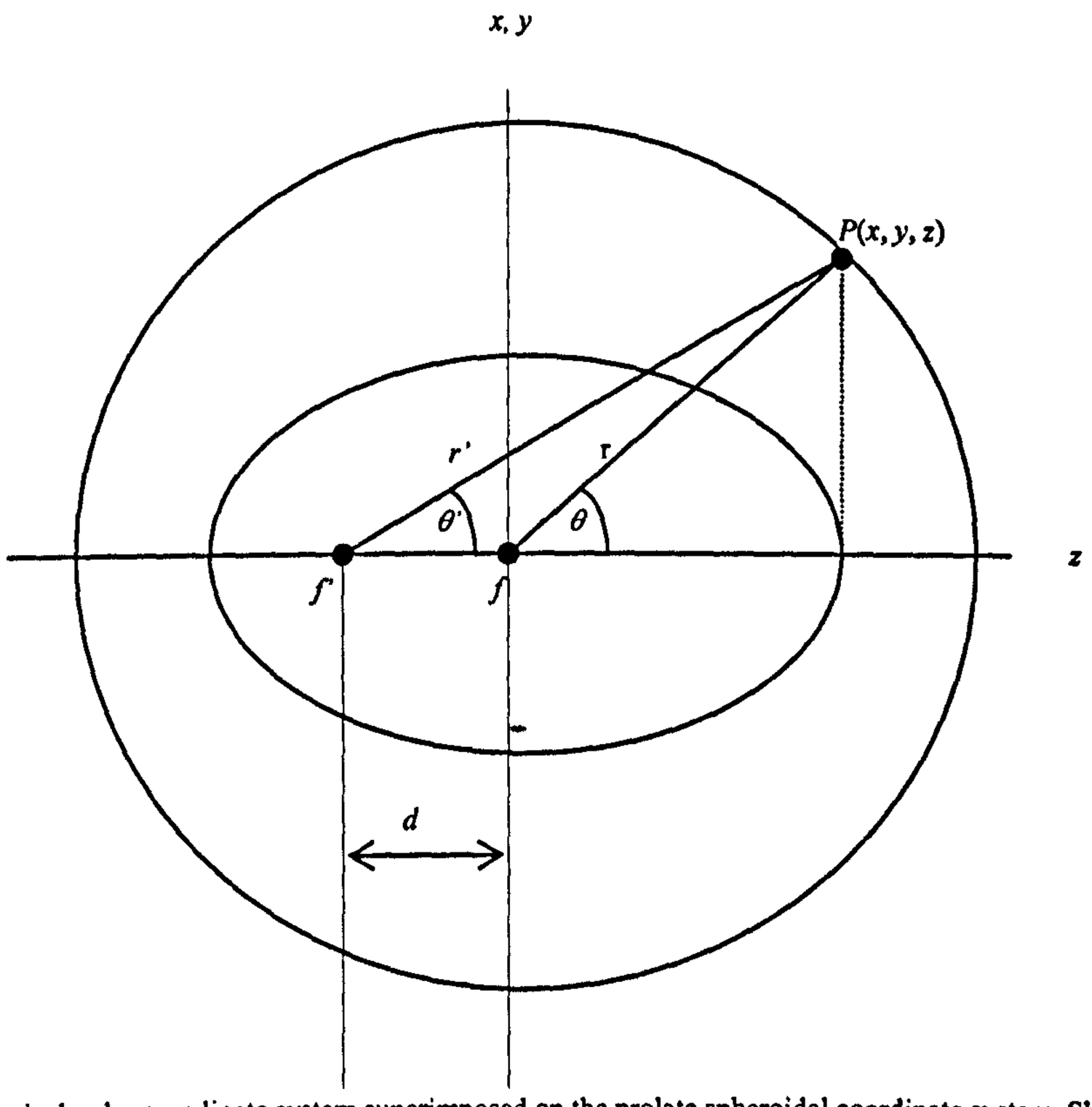

Fig. 2.5. The spherical polar coordinate system superimposed on the prolate spheroidal coordinate system. Showing the geometry of the spherical polar coordinate system whose origin is shifted to one of the foci of the prolate spheroidal coordinate system.

It was mentioned in section 1.11.5. that the approach from Landesman and Barrett [4] violates the principle of conservation of energy. This will be demonstrated in the next section and a new scalar solution will be presented which satisfies the conservation of energy criterion.

2.3. The exact solutions to the scalar Helmholtz equation

In their work Landesman and Barrett [4] assumed a spherical wave expanding outwards from a real point source located at $z=-d$, in prolate spheroidal coordinates (see Fig. 2.5.) as the basic propagation function of the Gaussian beam instead of the complex point source on the axis. In order to determine a solution to the scalar Helmholtz equation, a general solution that is separable in the coordinate system of choice has to be assumed. The oblate spheroidal coordinate system is well-suited to express the propagation of a Gaussian beam due to the simplicity of describing a contour of constant amplitude in the beam as a hyperboloid of one sheet, which is one of the oblate spheroidal coordinate surfaces. The ellipses can be related to the wavefronts. The focus in the oblate spheroidal coordinate system is a circle perpendicular to the z axis.

Eq. (2.29) can be interpreted as a spherical wave expanding outward from the focal point. Substituting $m=n=0$ into Eq. (2.29) leads to

$$\psi_{00}^{(1)}(\xi,\eta)=\frac{e^{-kd}e^{it}}{it} \quad . \tag{2.30}$$

and substituting $m=0$, $n=1$ into Eq. (2.29) leads to

$$\psi_{01}^{(1)}(\xi,\eta)=-\frac{e^{-kd}e^{it}}{t}\left(1+\frac{i}{t}\right)s \quad . \tag{2.31}$$

By investigating the properties of these functions, it is found that there exists a circular singularity of radius d in the beam waist plane and a discontinuity occurring on the focal disk circumscribed by the singularity for $\psi_{00}^{(1)}(\xi,\eta)$ and $\psi_{01}^{(1)}(\xi,\eta)$. Thus the function $\psi_{mn}^{(1)}(\xi,\eta,\phi)$, which is a solution to the Helmholtz equation, is not a valid solution, due to the singularity being an apparent violation to the conservation of energy [5]. A graphical representation of the circular singularity of radius d in the beam waist plane can be seen from Figs. 2.6. and 2.7.. Fig. 2.6. shows also clearly the discontinuity at the beam waist.

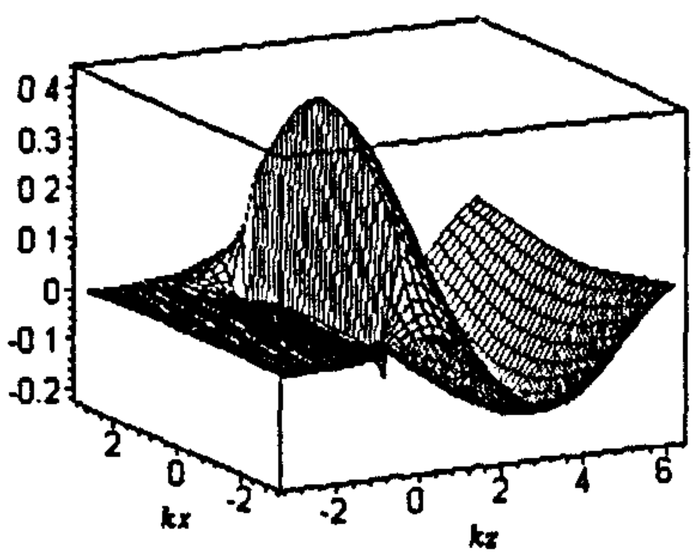

Fig. 2.6. Plot of the real part of the wave given by Eq. (2.30) for m=n=0 k=1, d=2.3, and y=0 in the vicinity of the geometric focus, showing the singularity and the discontinuity. (Adapted from [5])

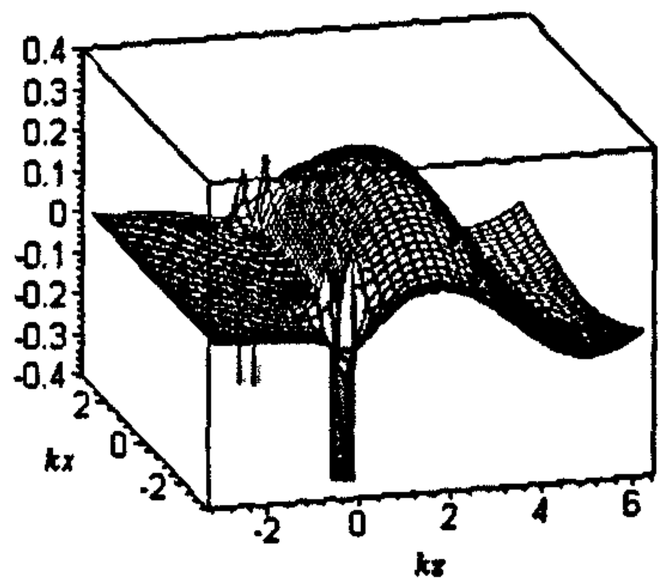

Fig. 2.7. Plot of the real part of the wave given by Eq. (2.31) for m=0, n=1, k=1, d=2.3 and y=0 in the vicinity of the geometric focus, showing the singularity.

In order for the functions to represent physical solutions, they must satisfy the wave equation and Maxwell's equations and must be singularity free. By plotting the real part of the amplitude A of $\psi_{00}^{(1)}(\xi,\eta)$ and $\psi_{01}^{(1)}(\xi,\eta)$ respectively along the z axis, it can be seen from Figs. 2.8. and 2.9. that the discontinuity arises at the beam waist.

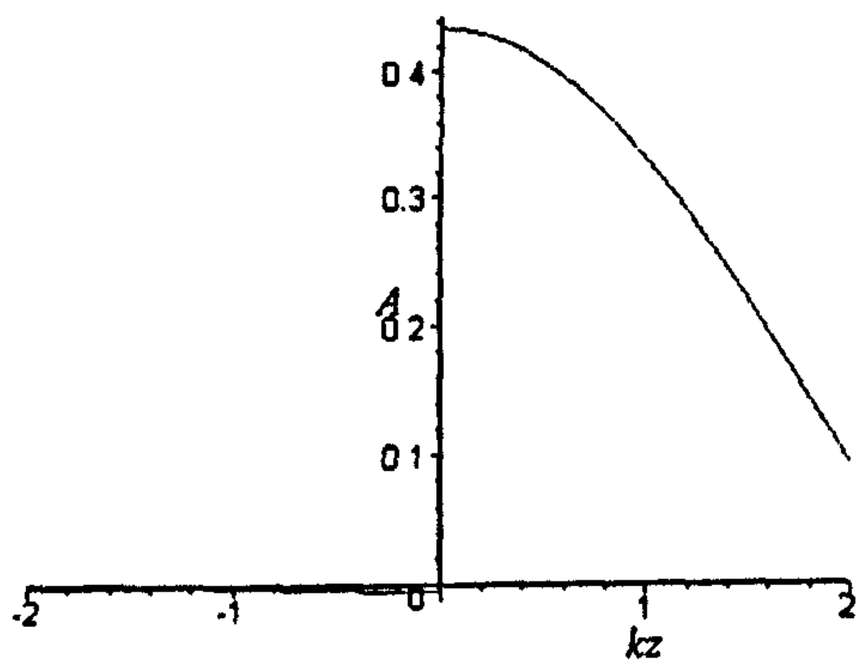

Fig. 2.8. Plot of the real part of the wave given by Eq. (2.30) for m=n=0, k=1, d=2.3 and x=y=0 in the vicinity of the geometric focus, showing the discontinuity.

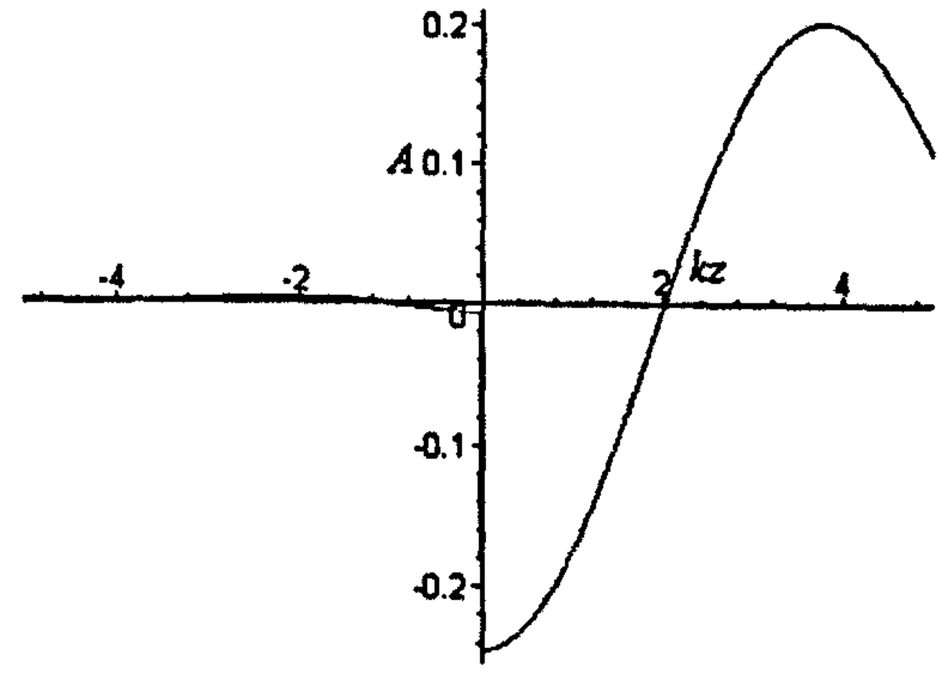

Fig. 2.9. Plot of the real part of the wave given by Eq. (2.31) for m=0, n=1, k=1, d=2.3 and x=y=0 in the vicinity of the geometric focus, showing the discontinuity.

By plotting the real part of the amplitude A of $\psi_{00}^{(1)}(\xi,\eta)$ and $\psi_{01}^{(1)}(\xi,\eta)$ respectively along the x axis, it can be seen from Figs. 2.10. and 2.11. that the circular singularity of radius d arises at the beam waist.

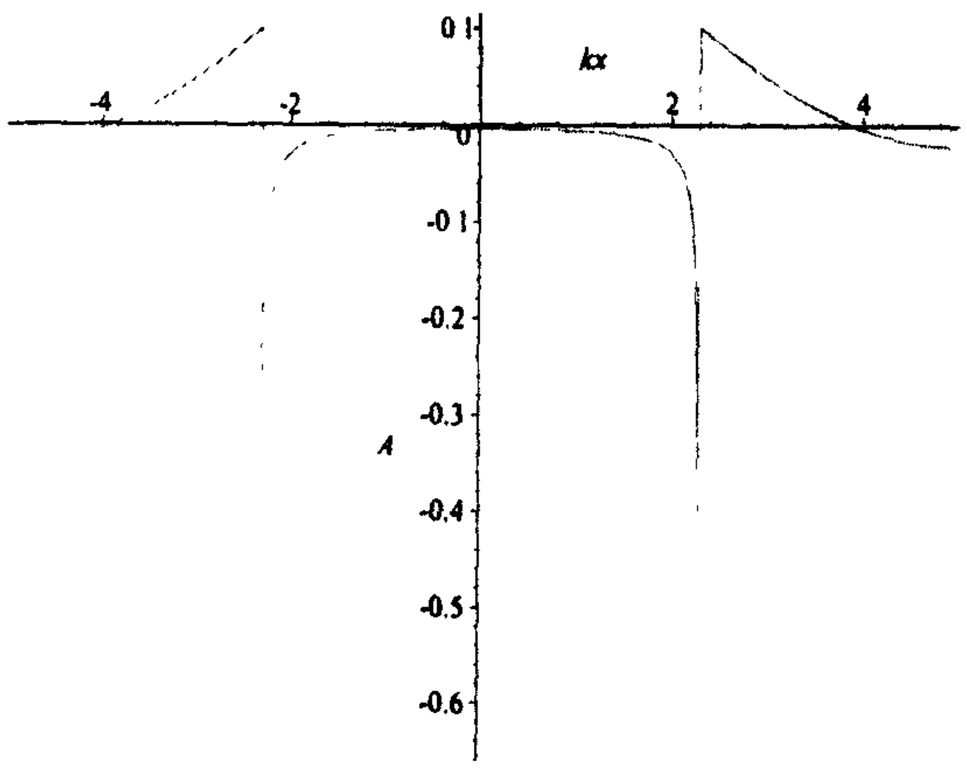

Fig. 2.10. Plot of the real part of the wave given by Eq. (2 30) for m=n=0, k=1, d=2.3 and y=z=0 at the geometric focus, showing the singularity.

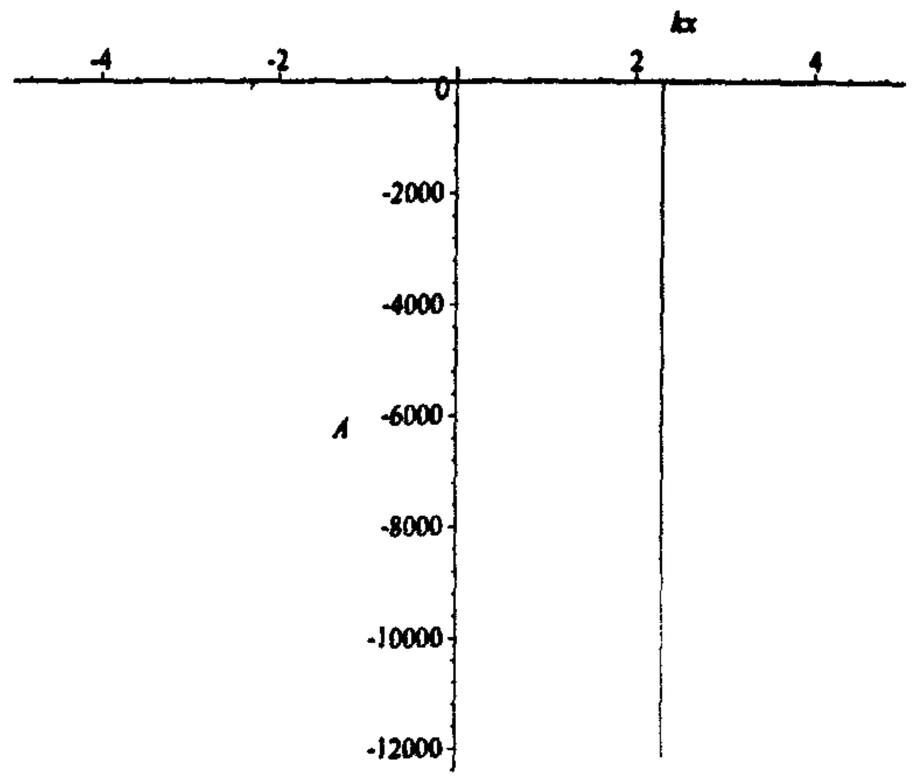

Fig. 2.11. Plot of the real part of the wave given by Eq. (2.31) for m=0, n=1, k=1, d=2.3 and y=z=0 at the geometric focus, showing the singularity.

Since $\psi^{(1)}{}_{mn}(\xi,\eta,\phi)_{O/S}$ represents an outward travelling wave, it can be said that

$$\psi^{(2)}_{mn}(\xi,\eta,\phi)_{O/S} = e^{-ikd}h^{(2)}_n(t)P^m_n(s)e^{im\phi}, \tag{2.32}$$

represents a complete set of solutions to the Helmholtz equation in oblate spheroidal coordinates, representing an inward travelling wave. Where $h_n{}^{(2)}(t)$ is the Hankel function of the second kind, of order n.

Substituting m=n=0 into Eq. (2.32) leads to `

$$\psi^{(2)}_{00}(\xi,\eta) = -\frac{e^{-ikd}e^{-ik}}{it} \quad . \tag{2.33}$$

and substituting m=0, n=1 into Eq. (2.32) leads to

$$\psi^{(2)}_{01}(\xi,\eta) = \frac{e^{-ikd}e^{-ik}}{t}\left(\frac{i}{t}-1\right)s \quad . \tag{2.34}$$

It can be clearly seen from Figs. 2.12. and 2.13. that the waves based on Eqs. (2.33) and (2.34) respectively, also have a circular singularity of radius d in the beam waist plane and a discontinuity occurring on the focal disk circumscribed by the singularity.

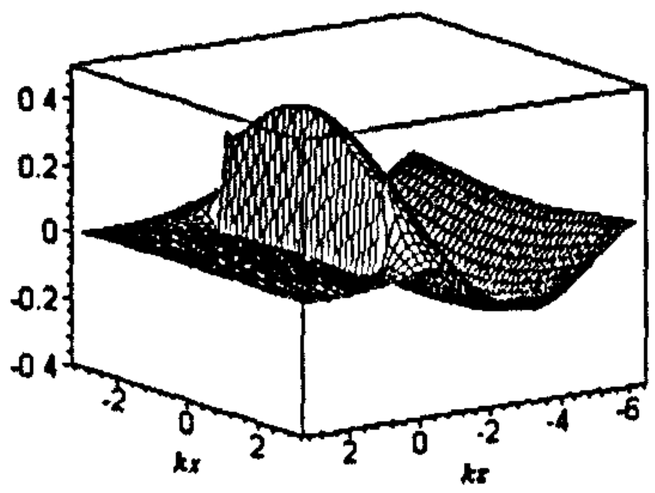

Fig. 2.12. Plot of the real part of the wave given by Eq. (2.33) for m=n=0, k=1, d=2.3 and y=0 in the vicinity of the geometric focus, showing the singularity and the discontinuity.

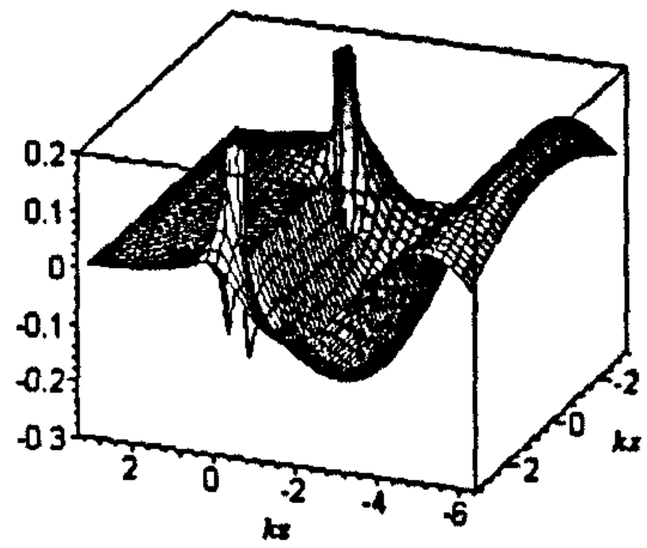

Fig. 2.13. Plot of the real part of the wave given by Eq. (2.34) for m=0, n=1, k=1, d=2.3 and y=0 in the vicinity of the geometrical focus, showing the singularity.

By plotting the real part of the amplitude A of $\psi_{00}^{(2)}(\xi,\eta)$ and $\psi_{01}^{(2)}(\xi,\eta)$ respectively along the z axis, it can be seen from Figs. 2.14. and 2.15. that the discontinuity arises at the beam waist.

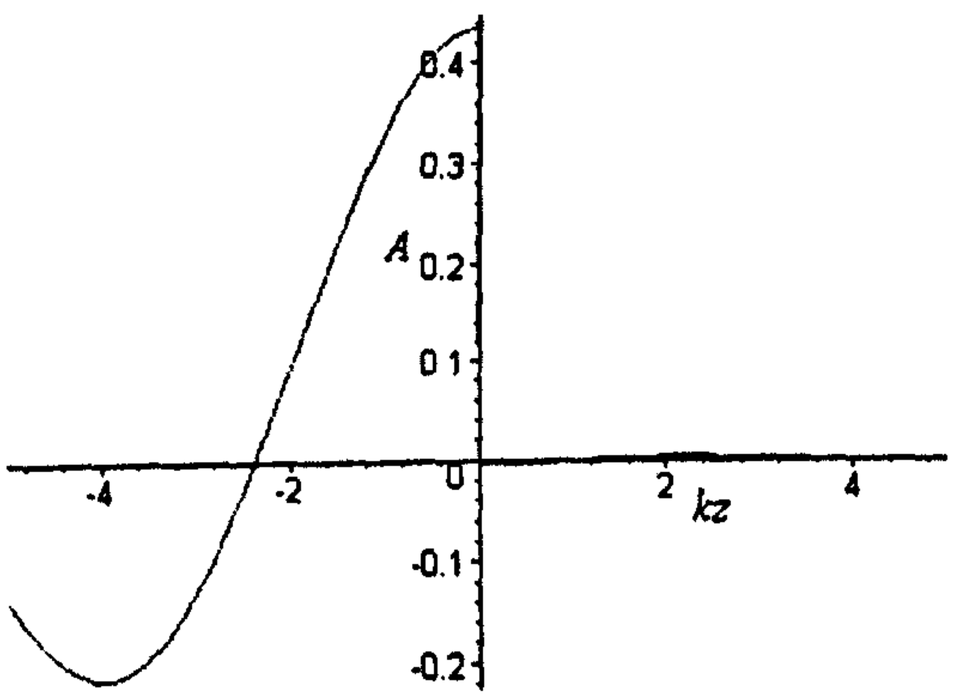

Fig. 2.14. Plot of the real part of the wave given by Eq. (2.33) for m=n=0, k=1, d=2.3 and x=y=0 in the vicinity of the geometric focus, showing the discontinuity.

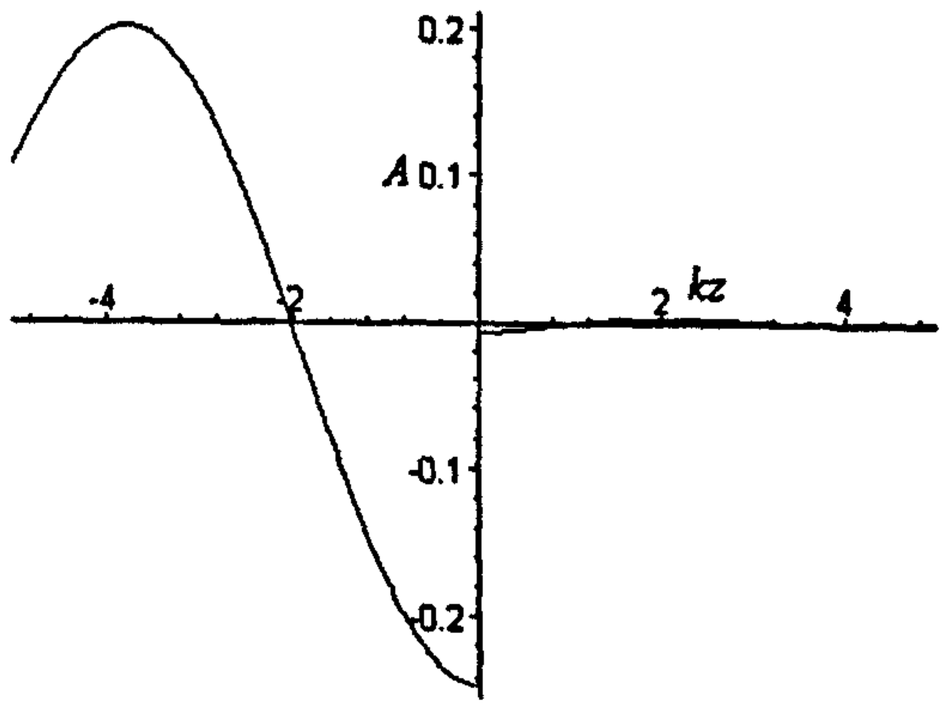

Fig. 2.15. Plot of the real part of the wave given by Eq. (2.34) for m=0, n=1, k=1, d=2.3 and x=y=0 in the vicinity of the geometric focus, showing the discontinuity.

By plotting the real part of the amplitude A of $\psi_{00}^{(2)}(\xi,\eta)$ and $\psi_{01}^{(2)}(\xi,\eta)$ respectively along the x axis, it can be seen from Figs. 2.16. and 2.17. that the circular singularity of radius d arises at the beam waist.

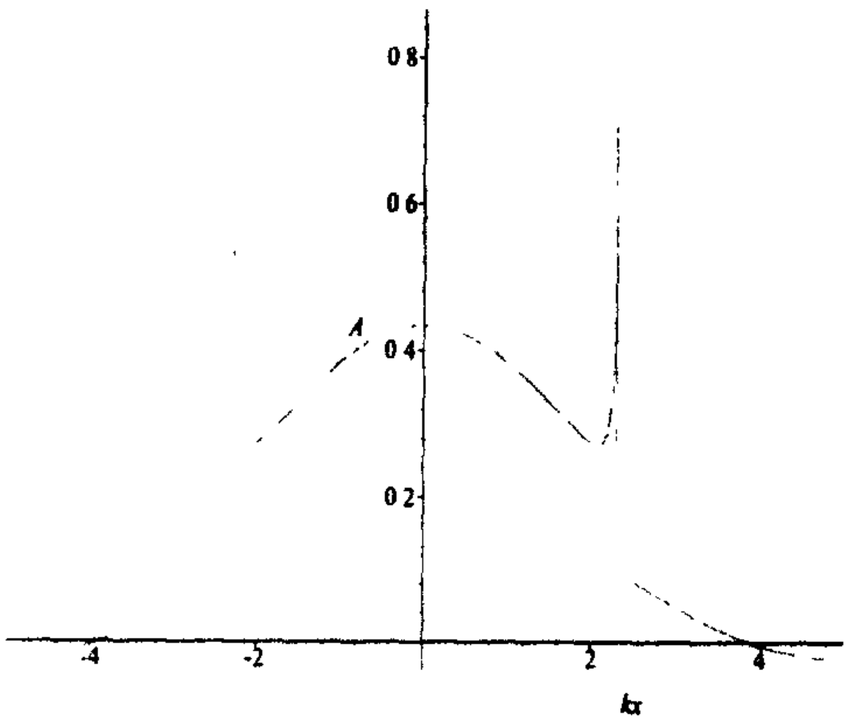

Fig. 2.16. Plot of the real part of the wave given by Eq. (2.33) for $m=n=0$, $k=1$, $d=2.3$ and $y=z=0$ at the geometric focus, showing the singularity.

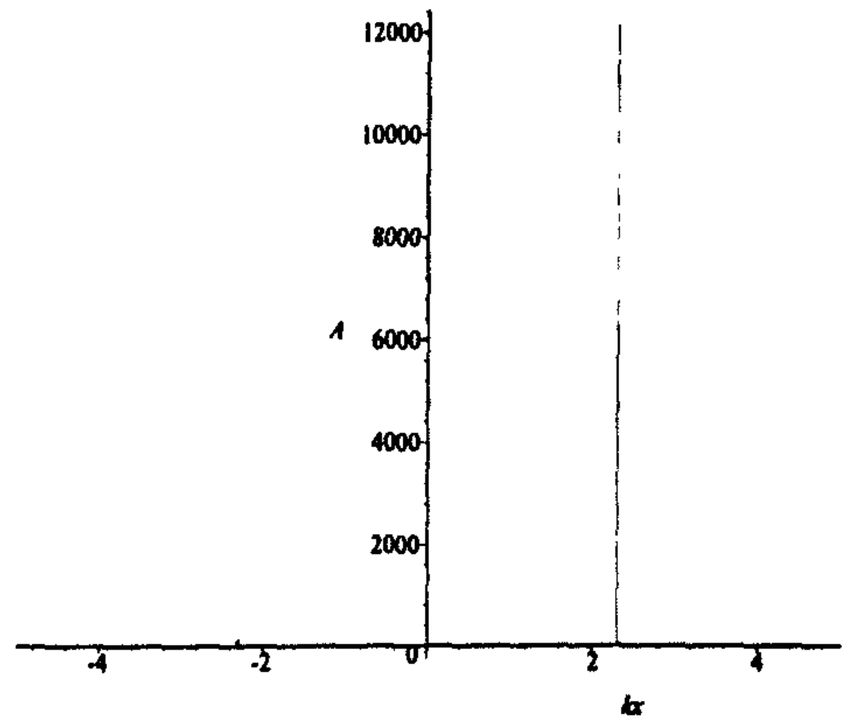

Fig. 2.17. Plot of the real part of the wave given by given by Eq. (2.34) for $m=0$, $n=1$, $k=1$, $d=2.3$ and $y=z=0$ at the geometric focus, showing the singularity.

On close inspection of table 2.1. it can be seen that the spherical Bessel functions $j_n(x)$ are regular since the limit of $\frac{\sin x}{x}$, and $\frac{\sin x}{x^2}-\frac{\cos x}{x}$ as x tends to infinity is 0 and the limit as x tends to 0 is 1 and 0 respectively.

Proof:

In order to calculate the limit of $j_0(x)$, L' Hopital's rule can be applied directly, since for $x=0$, $j_0(x)=\frac{0}{0}$. Thus using L' Hopital's rule it is found that $\lim_{x\to 0}\left(\frac{\sin x}{x}\right)=\lim_{x\to 0}\left(\frac{\cos x}{1}\right)=1$.

In the case of $j_1(x)$ the function has to be transformed into

$j_1(x)=\frac{1}{x^2}(\sin x - x\cos x)$ in order to apply L' Hopital's rule. Then

$$\lim_{x\to 0}\left(\frac{\sin x - x\cos x}{x^2}\right)=\lim_{x\to 0}\left(\frac{\cos x-\cos x+x\sin x}{2x}\right)=\lim_{x\to 0}\left(\frac{\sin x}{2}\right)=0.$$

The Neumann functions $y_n(x)$ on the other hand are not regular, since

$$\lim_{x\to 0}\left(-\frac{\cos x}{x}\right)=-\infty$$

$$\lim_{x\to \infty}\left(-\frac{\cos x}{x}\right)=0$$

$$\lim_{x\to 0}\left(-\frac{\cos x}{x^2}-\frac{\sin x}{x}\right)=-\infty$$

$$\lim_{x\to \infty}\left(-\frac{\cos x}{x^2}-\frac{\sin x}{x}\right)=0 \quad .$$

Thus the Hankel functions $h_n^{(1)}(x)$ and $h_n^{(2)}(x)$ are not regular either [7].

It can be seen from Eqs. (2.11.b) that

$$\frac{1}{2}\left(h_n^{(1)}(x)+h_n^{(2)}(x)\right)=j_n(x) \quad . \tag{2.35}$$

Since Eq. (2.35) does not contain the Neumann function, the chosen superposition is regular. Adding Eq. (2.30) and (2.33) leads to

$$\psi_{00}(\xi,\eta)=e^{-kd}\frac{\sin t}{t} \quad . \tag{2.36}$$

Similarly adding Eq. (2.31) and (2.34) leads to

$$\psi_{01}(\xi,\eta)=e^{-kd}\left(\frac{\sin t}{t^2}-\frac{\cos t}{t}\right)s \quad . \tag{2.37}$$

Thus by forming a superposition of $\psi^{(1)}{}_{mn}(\xi,\eta,\phi)_{O/S}$ and $\psi^{(2)}{}_{mn}(\xi,\eta,\phi)_{O/S}$ in accordance with Eq. (2.35) it is found that the singularities and discontinuities cancel out, and a physical solution is thus obtained. Graphically this can be clearly seen from Figs. 2.18. and 2.19. for $\psi_{00}(\xi,\eta)$ and $\psi_{01}(\xi,\eta)$ respectively.

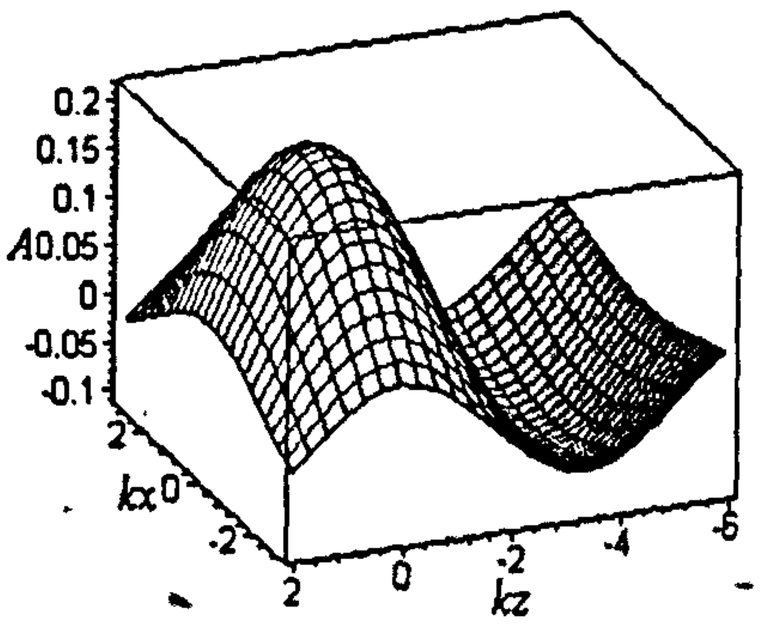

Fig. 2.18. Plot of the real part of the combined wave, given by Eq. (2.36) for m=0, n=0, k=1, d=2.3 and y=0 in the vicinity of the geometric focus, showing no singularity and no discontinuity.

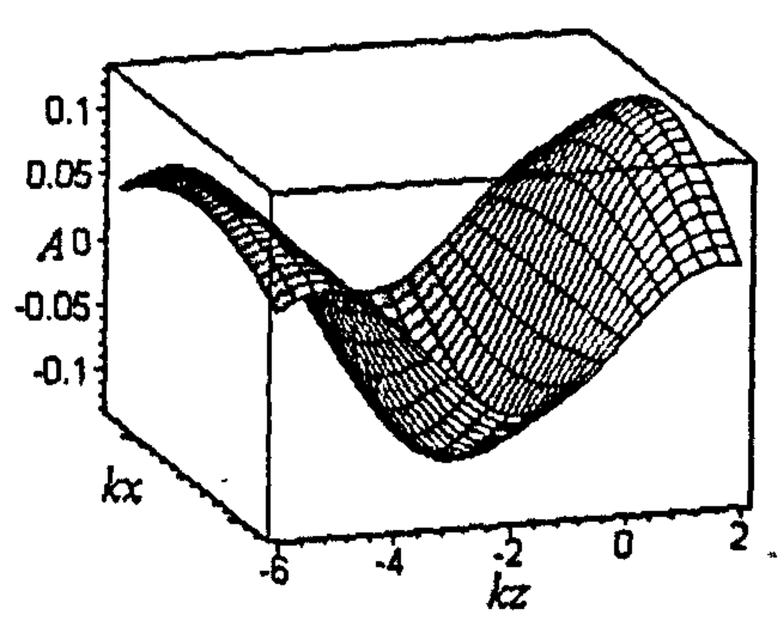

Fig. 2.19. Plot of the real part of the combined wave, given by Eq. (2.37), for m=0, n=1, k=1, d=2.3 and y=0 in the vicinity of the geometric focus, showing no singularity.

Therefore the general solution to the wave equation can be written as

$$\psi_{mn}(\xi,\eta,\phi) = e^{-kd} j_n(t) P_n^m(s) e^{\pm im\phi} \quad . \tag{2.38}$$

Based on the derivations of Landesman and Barrett [4], it can be seen that the focal radius d in oblate spheroidal coordinates is identical to the Rayleigh range (see section 1.7), thus from here on d is referred to as the Rayleigh range.

In order to avoid complicated coordinate transformations in the future, it is appropriate at this stage to identify that t is related to the complex radius R, used in the complex source point method. In the literature R is usually defined as

$$R = \sqrt{x^2 + y^2 + (z - id)^2} \quad , \tag{2.39}$$

where x, y and z are the Cartesian coordinates. By squaring the equations in Eq. (2.19), using the fact that $\sin^2\phi + \cos^2\phi = 1$ and substituting the expressions for x^2, y^2 and z^2 into Eq. (2.39); this equation can be rewritten in terms of ξ and η as

$$R = d\sqrt{(1+\xi^2)(1-\eta^2) + (\xi^2\eta^2 - 2i\xi\eta - 1)} = d\sqrt{\xi^2 - 2i\xi\eta - \eta^2} = d(\xi - i\eta),$$

or

$$t = kR \quad . \tag{2.40}$$

Similarly s can be expressed in terms of the complex radius as

$$s = \frac{(z - id)}{R} \quad . \tag{2.41}$$

Therefore the singularity-free spheroidal wave model for the lowest order is identical to the complex source-sink point model presented in [1].

Furthermore, it is now possible to prove, using Eq. (2.39), that the oblate spheroidal coordinate system is indeed identical to the spherical coordinate system, if extended out to infinity.

Proof:

Eq. (2.39) can be written in spherical polar coordinates, using Eqs. (2.6), as

$R = \sqrt{r^2 - 2ird\cos\theta - d^2}$, using the binomial expansion theorem,

$$R = \sqrt{r^2 - 2ird\cos\theta - d^2} \approx r - \frac{1}{2}\left(2id\cos\theta - \frac{d^2}{r}\right)$$

and

$$\lim_{r\to\infty}\left(\frac{R}{r}\right) = \lim_{r\to\infty}\left(1 - \frac{1}{2}\left(\frac{2id\cos\theta}{r} - \frac{d^2}{r^2}\right)\right) = 1 .$$

Thus by substituting Eqs. (2.40) and (2.41) into Eq. (2.38), the general solution can be written as [5]

$$\psi_{mn}(x,y,z) = e^{-kd} j_n(kR) P_n^m\left(\frac{z-id}{R}\right) e^{\pm im\phi} \quad . \tag{2.42}$$

The problem with the physical interpretation of the complex source point method is resolved since the complex spherical wave with a complex point source on the axis is mathematically identical to the real spherical wave with a real point source on axis in the prolate spheroidal coordinate system. The superposition $\psi_{00}(x,y,z)$ can be interpreted as having a source and a sink on axis, i.e. a source on axis for the outward travelling wave and a sink on axis for the inward travelling wave. This superposition is a solution to the scalar Helmholtz equation, since the spherical Bessel functions are a solution to the radial equation (Eq. 2.10).

Substituting Eqs. (2.40) and (2.41) into Eq. (2.36) leads to

$$\psi_{00}(x,y,z) = e^{-kd}\frac{\sin kR}{kR} \quad . \tag{2.43}$$

and similarly substituting Eqs. (2.40) and (2.41) into Eq. (2.37) leads to

$$\psi_{01}(x,y,z) = e^{-kd}\left(\frac{\sin kR}{k^2R^2} - \frac{\cos kR}{kR}\right)\left(\frac{z-id}{R}\right) \quad . \tag{2.44}$$

In order to establish the kind of properties the $\psi_{00}(x,y,z)$ and $\psi_{01}(x,y,z)$ functions have as these waves propagate in time, equation (2.43) and equation (2.44) are normalised to 1 at the origin ($x=y=z=0$). The normalisation constants are given by

$$Nc_{00} = \sqrt{\psi_{00}(0,0,0)\psi_{00}^{*}(0,0,0)} = e^{-kd}\frac{\sinh kd}{kd}$$

$$Nc_{01} = \sqrt{\psi_{10}(0,0,0)\psi_{01}^{*}(0,0,0)} = e^{-kd}\left(-\frac{\sinh kd}{k^2d^2}+\frac{\cosh kd}{kd}\right) \tag{2.45}$$

Thus the normalised functions are

$$\psi_{00,norm}(x,y,z) = \frac{\psi_{00}(x,y,z)}{Nc_{00}} = \frac{kd\sin kR}{kR\sinh kd} \tag{2.46}$$

and

$$\psi_{01,norm}(x,y,z) = \frac{\psi_{01}(x,y,z)}{Nc_{01}} = \frac{\left(\frac{\sin kR}{k^2R^2}-\frac{\cos kR}{kR}\right)\left(\frac{z-id}{R}\right)}{\left(-\frac{\sinh kd}{k^2d^2}+\frac{\cosh kd}{kd}\right)}. \tag{2.47}$$

In order to take the time dependence $e^{-i\omega t}$ into account, these functions are multiplied by $e^{-i\pi\frac{t}{4}}$. Figs. 2.20. show the real part of the normalised amplitude $\psi_{00,norm}(x,y,z)$ at time $t=0,1,2,3,4$ for $k=1$ and $d=2.3$ and $(x,y,z)=(0,y,0)$ (a), $(x,y,z)=(x,0,0)$ (b) and

$(x,y,z)=(0,0,z)$ (c).

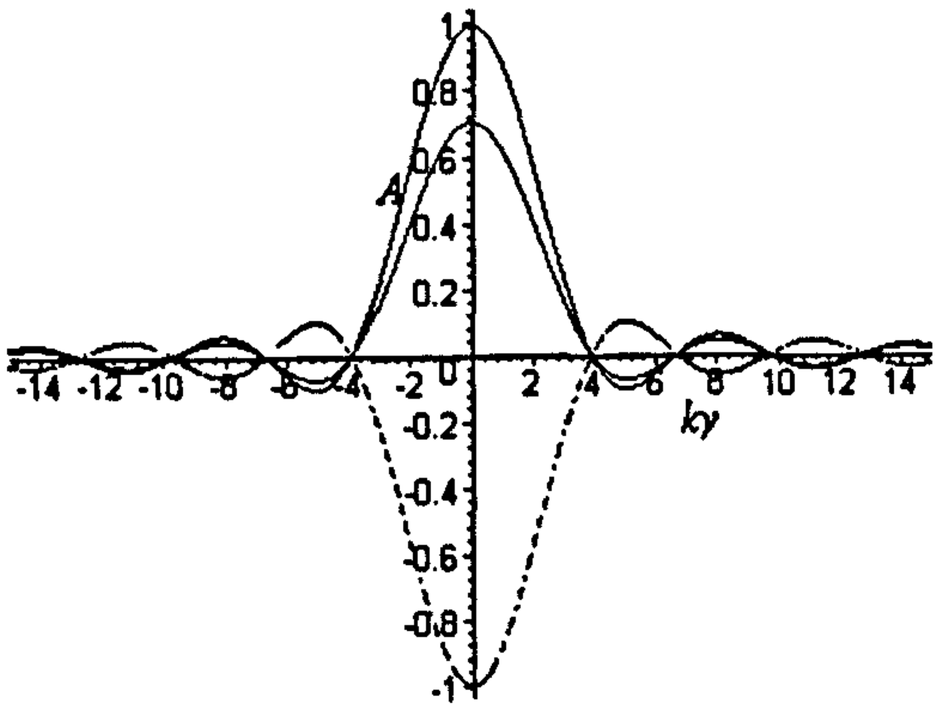

Fig. 2.20.a) Real part of the amplitude of $\psi_{00,norm}(0,y,0)$ normalised to 1 at $x=y=z=0$ along the y axis for $k=1$, $d=2.3$. Time $t=0$ (red), $t=1$ (blue), $t=2$ (not visible, flat line on top of y axis) $t=3$ (yellow), $t=4$ (black).

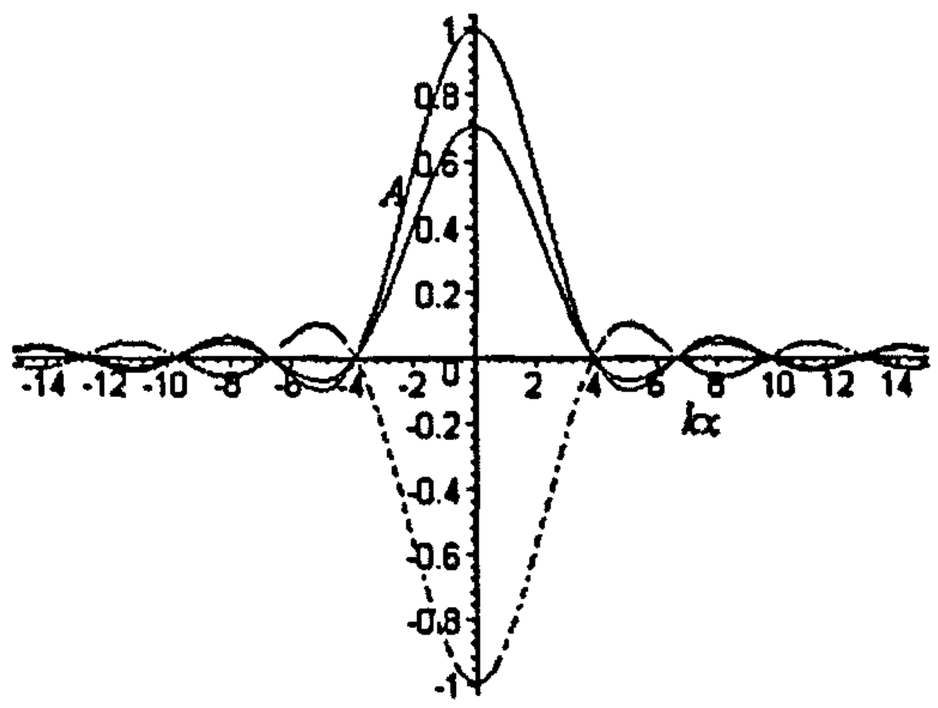

Fig. 2.20.b) Real part of the amplitude of $\psi_{00,norm}(x,0,0)$ normalised to 1 at $x=y=z=0$ along the x axis for $k=1$, $d=2.3$. Time $t=0$ (red), $t=1$ (blue), $t=2$ (not visible, flat line on top of x axis) $t=3$ (yellow), $t=4$ (black).

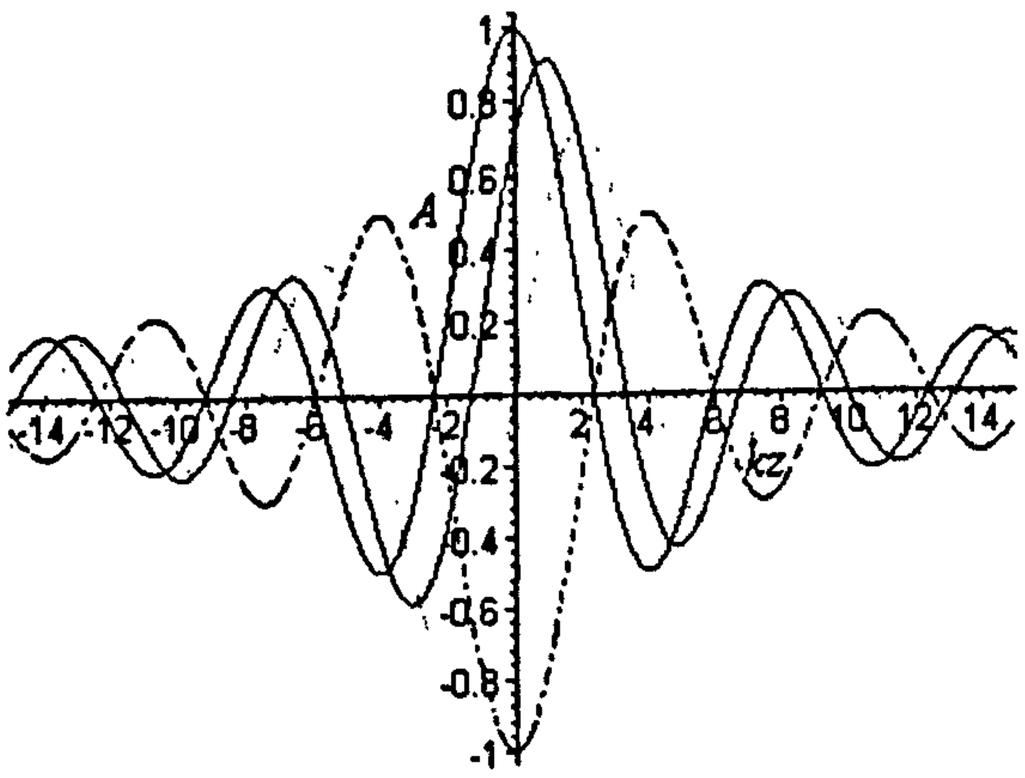

Fig. 2.20.c) Real part of the amplitude of $\psi_{00,norm}(0,0,z)$ normalised to 1 at $x=y=z=0$ along the z axis for $k=1$, $d=2.3$. Time $t=0$ (red), $t=1$ (blue), $t=2$ (green), $t=3$ (yellow), $t=4$ (black).

It can be clearly seen from Fig. 2.20.a) and Fig. 2.20.b) that the superposition of the outgoing and incoming wave gives rise to a pure standing wave at the beam waist. This is due to interference of the outgoing and incoming wave. From Fig. 2.20.c) it can be seen that the superposition of the outgoing and incoming wave gives rise to a wave which propagates along the z axis which has no component propagating along the x or y direction at the beam waist.

Fig. 2.21. show the real part of the normalised amplitude $\psi_{01,norm}(x,y,z)$ at time $t=0,1,2,3,4$ for $k=1$ and $d=2.3$. and $(x,y,z)= (0,y,0)$ (a), $(x,y,z)= (x,0,0)$ (b) and $(x,y,z)=(0,0,z)$ (c).

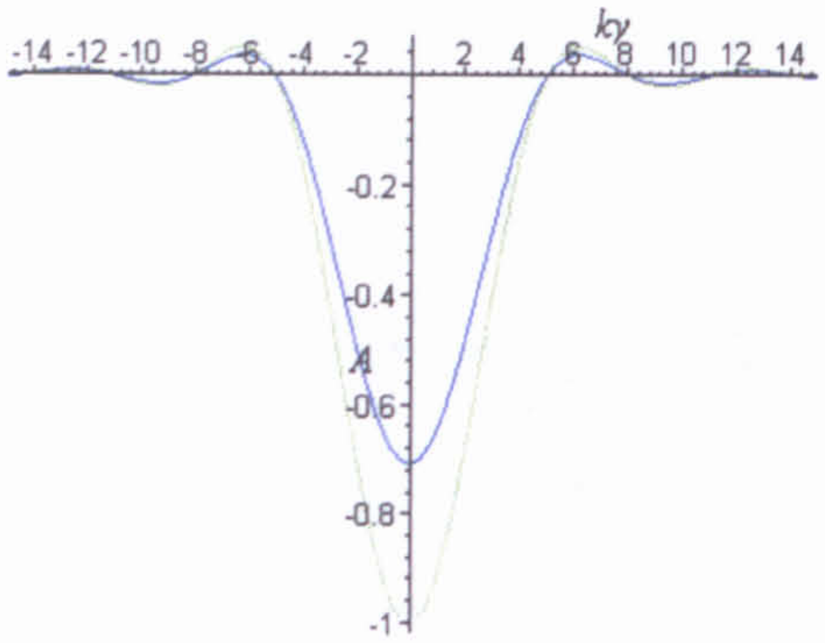

Fig. 2.21.a) Real part of the amplitude of $\psi_{01,norm}(0,y,0)$ normalised to 1 at $x=y=z=0$ along the y axis for $k=1$ and $d=2.3$. Time $t=0$ and $t=4$ (not visible, flat lines on top of y axis), $t=1$ (blue), $t=2$ (green), $t=3$ (not visible since overlapped by $t=1$).

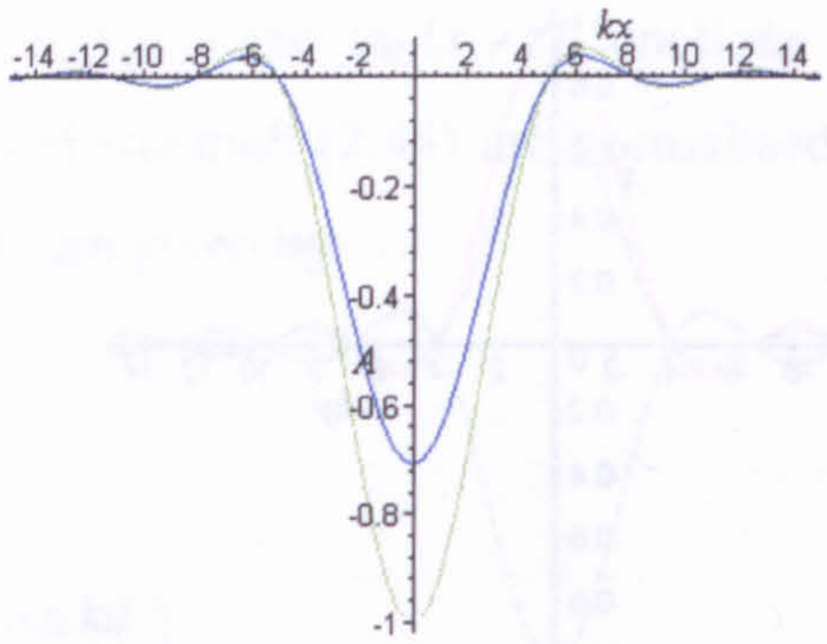

Fig. 2.21.b) Real part of the amplitude of $\psi_{01,norm}(x,0,0)$ normalised to 1 at $x=y=z=0$ along the x axis for $k=1$ and $d=2.3$. Time $t=0$ and $t=4$ (not visible, flat lines on top of x axis), $t=1$ (blue), $t=2$ (green), $t=3$ (not visible since overlapped by $t=1$).

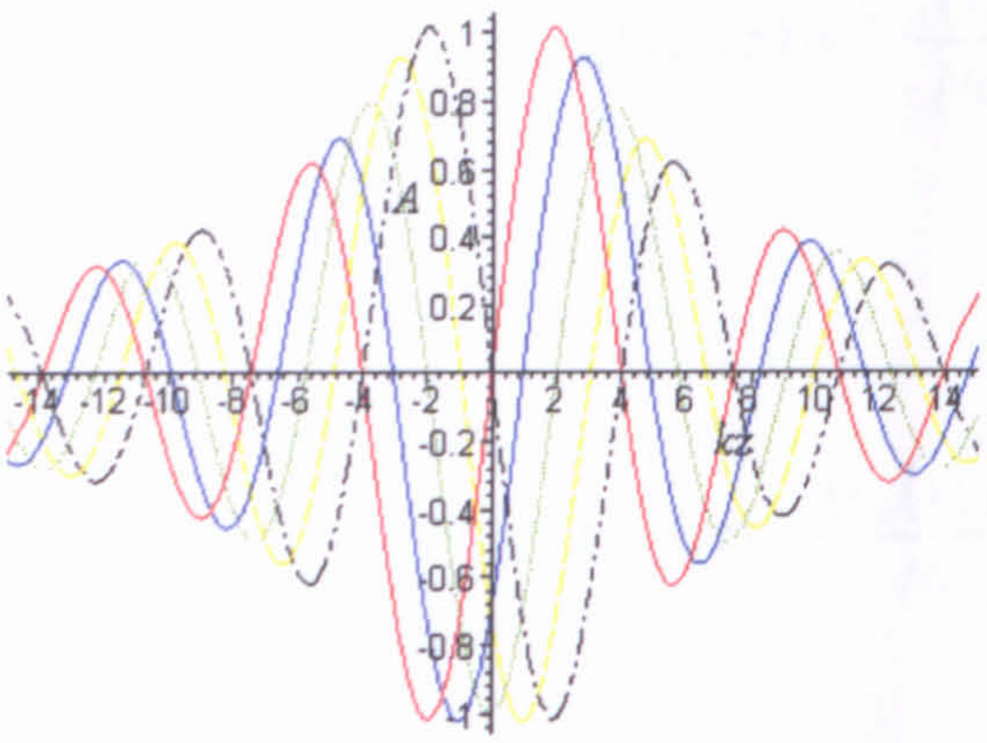

Fig. 2.21.c) Real part of the amplitude of $\psi_{01,norm}(0,0,z)$ normalised to 1 at $x=y=z=0$ along the z axis for $k=1$, and $d=2.3$. Time $t=0$ (red), $t=1$ (blue), $t=2$ (green), $t=3$ (yellow), $t=4$ (black).

It can be clearly seen from Fig. 2.21.a) and Fig. 2.21.b) that also in the case $\psi_{01,norm}(x,y,z)$ the superposition of the outgoing and incoming wave gives rise to a pure standing wave at the beam waist. From Fig. 2.21.c) it can be seen, like in the case of $\psi_{00,norm}(x,y,z)$ that the superposition of the outgoing and incoming wave gives rise to a wave which propagates along the z axis which has no component propagating along the x or y direction at the beam waist. The main difference between the standing wave produced by $\psi_{00,norm}(x,y,z)$ and $\psi_{01,norm}(x,y,z)$ is in their phases.

Fig. 2.22.a), Fig. 2.23.a), Fig. 2.24.a) Fig. 2.25.a) and Fig. 2.26.a) show a three dimensional view of the real part of $\psi_{00,norm}(x,0,z)$ for $k=1$, $d=2.3$ and values of time $t=0,1,2,3$ and 4 in the $y=0$ plane. Fig. 2.22.b), Fig. 2.23.b), Fig. 2.24.b) Fig. 2.25.b) and Fig. 2.26.b) show the corresponding amplitude contours.

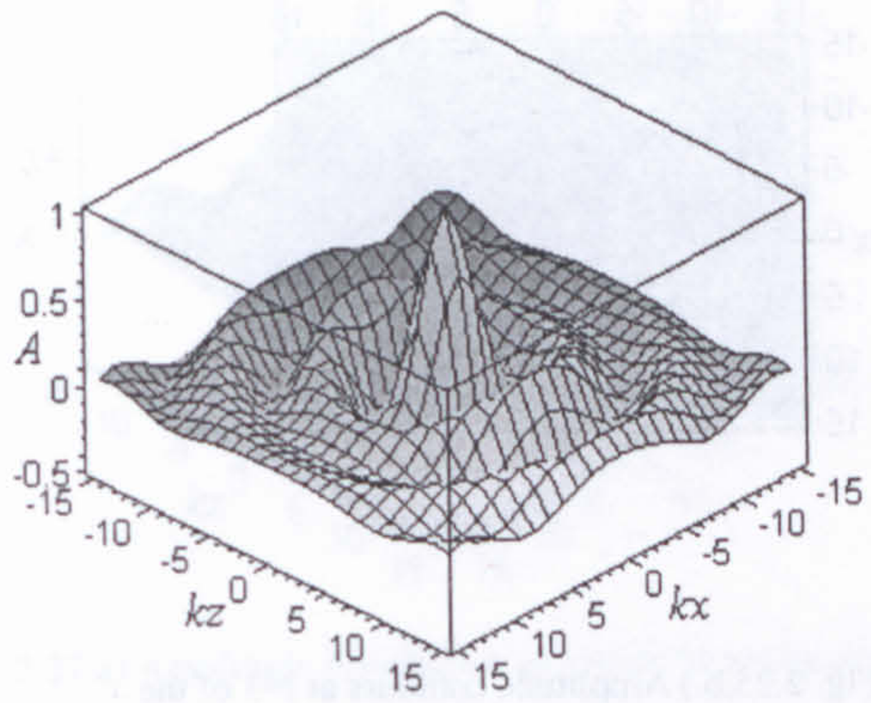

Fig. 2.22.a) Amplitude distribution at t=0 of the real part of $\psi_{00,norm}(x,0,z)$, for k=1 and d=2.3.

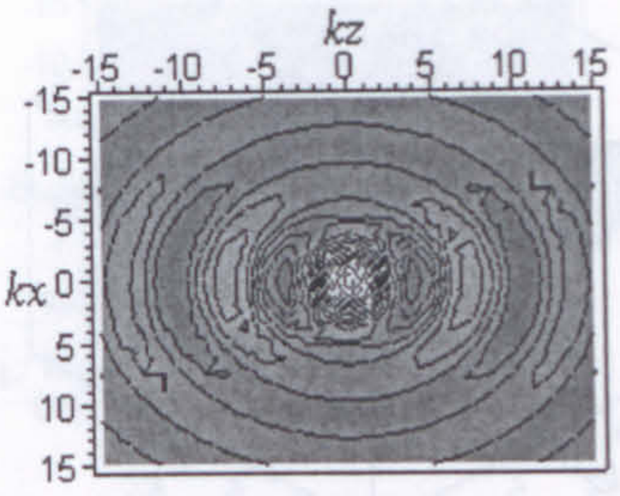

Fig. 2.22.b.) Amplitude contours at t=0 of the real part of $\psi_{00,norm}(x,0,z)$, for k=1 and d=2.3 in the plane of the beam axis.

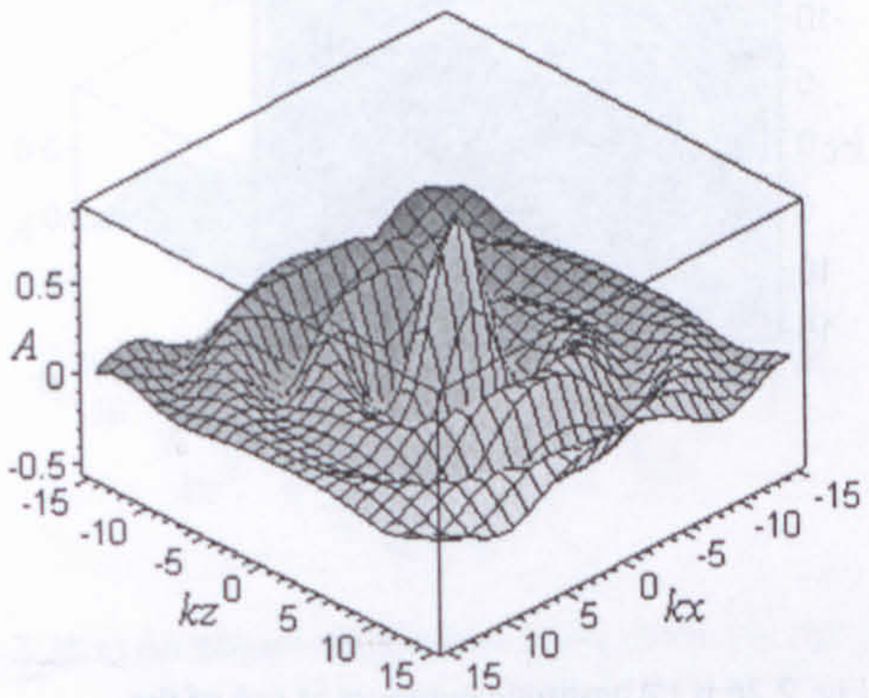

Fig. 2.23.a) Amplitude distribution at t=1 of the real part of $\psi_{00,norm}(x,0,z)$, for k=1 and d=2.3.

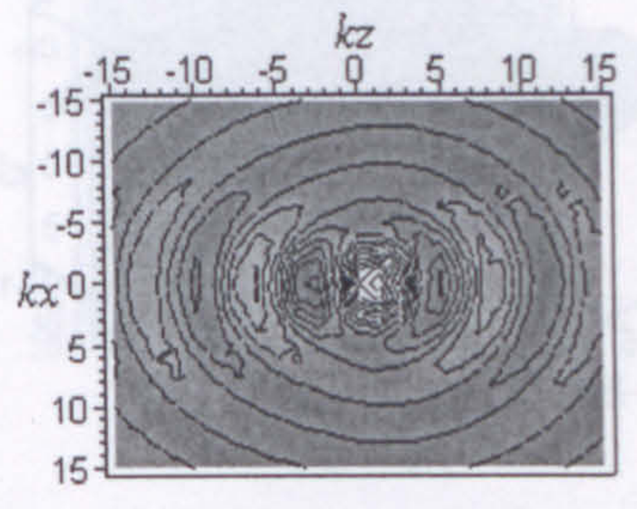

Fig. 2.23.b.) Amplitude contours at t=1 of the real part of $\psi_{00,norm}(x,0,z)$, for k=1 and d=2.3 in the plane of the beam axis.

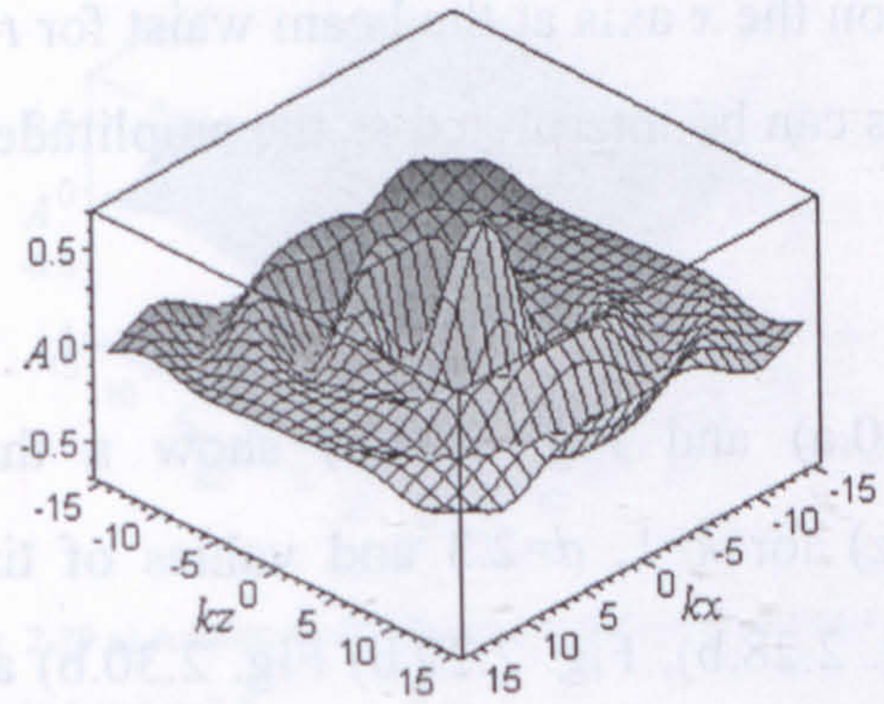

Fig. 2.24.a) Amplitude distribution at t=2 of the real part of $\psi_{00,norm}(x,0,z)$, for k=1 and d=2.3.

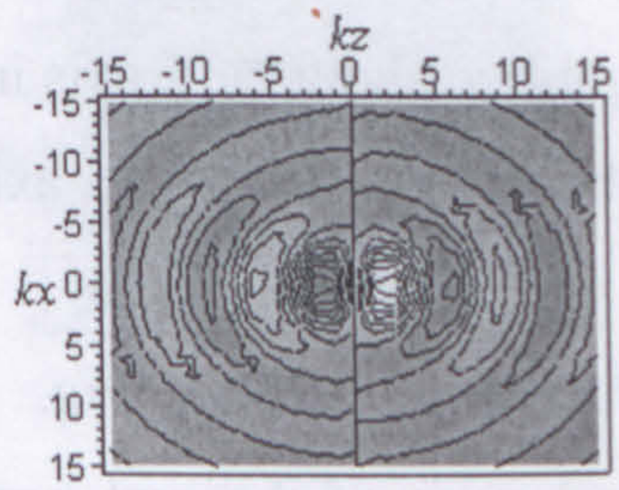

Fig. 2.24.b.) Amplitude contours at t=2 of the real part of $\psi_{00,norm}(x,0,z)$, for k=1 and d=2.3 in the plane of the beam axis.

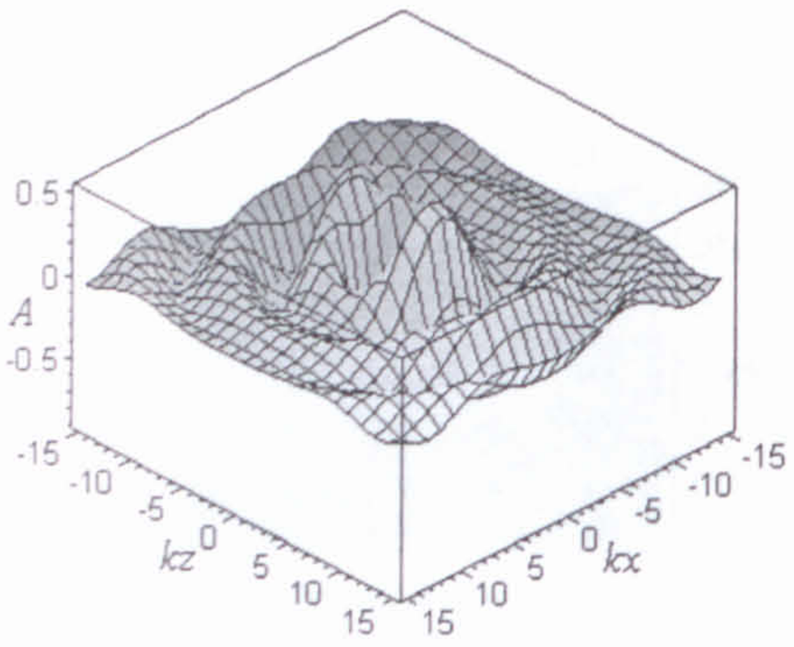

Fig. 2.25.a) Amplitude distribution at t=3 of the real part of $\psi_{00,norm}(x,0,z)$, for k=1 and d=2.3.

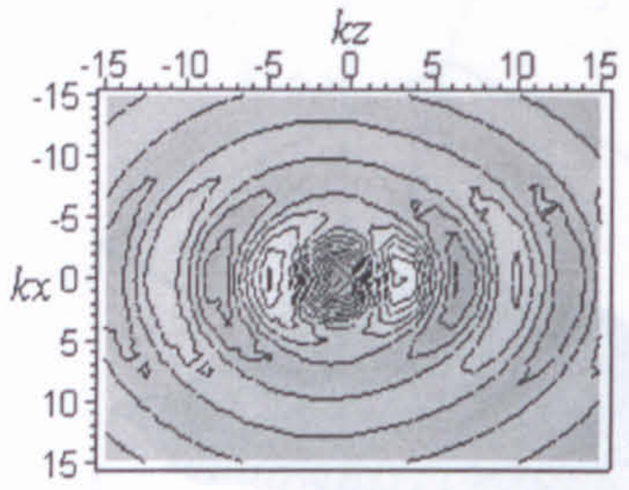

Fig. 2.25.b.) Amplitude contours at t=3 of the real part of $\psi_{00,norm}(x,0,z)$, for k=1 and d=2.3 in the plane of the beam axis.

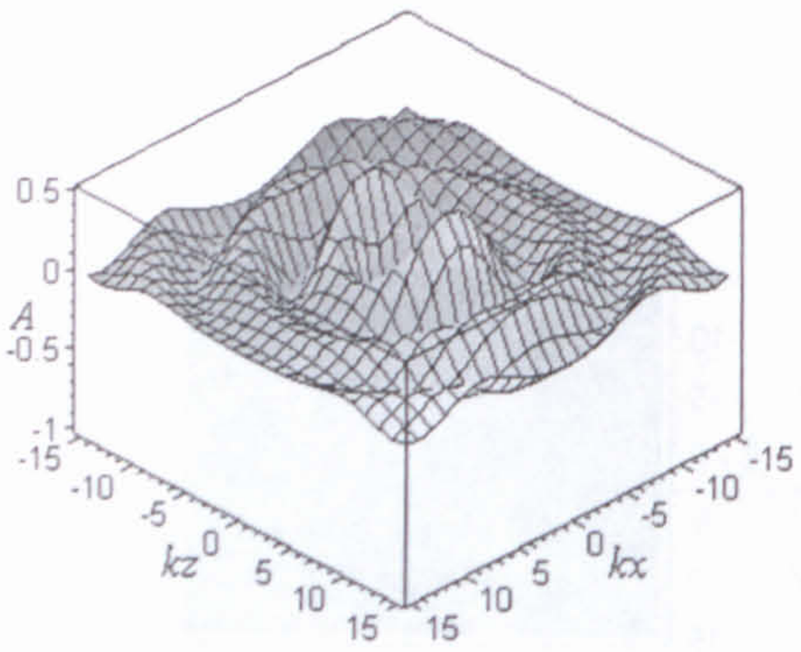

Fig. 2.26.a) Amplitude distribution at t=4 of the real part of $\psi_{00,norm}(x,0,z)$, for k=1 and d=2.3.

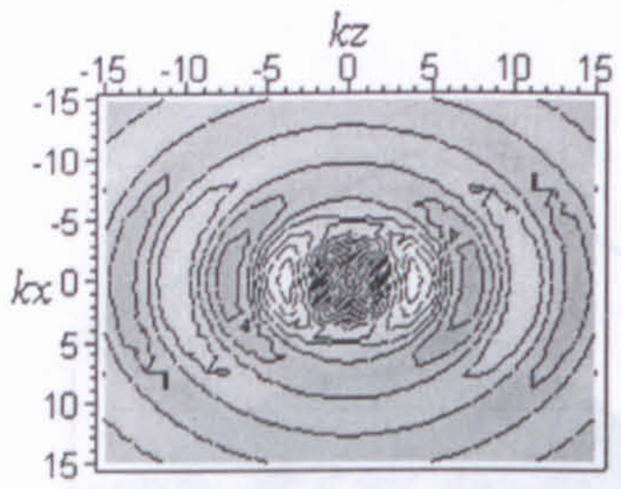

Fig. 2.26.b.) Amplitude contours at t=4 of the real part of $\psi_{00,norm}(x,0,z)$, for k=1 and d=2.3 in the plane of the beam axis.

From Fig. 2.20.b) it is seen that the wave vanishes on the x axis at the beam waist for t=2. The straight line along the x axis in Fig. 2.24.b) thus can be interpreted as the amplitude of the wave being zero along the x axis.

Fig. 2.27.a), Fig. 2.28.a), Fig. 2.29.a) Fig. 2.30.a) and Fig. 2.31.a) show a three dimensional view of the real part of $\psi_{01,norm}(x,0,z)$ for k=1, d=2.3 and values of time t=0,1,2,3 and 4 in the y=0 plane. Fig. 2.27.b), Fig. 2.28.b), Fig. 2.29.b) Fig. 2.30.b) and Fig. 2.31.b) show the corresponding amplitude contours.

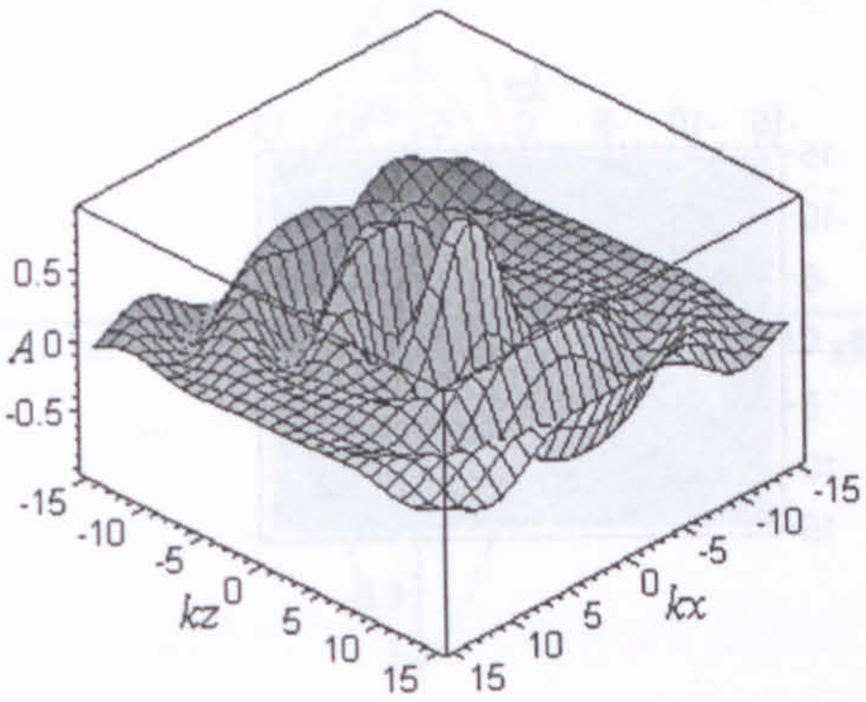

Fig. 2.27.a) Amplitude distribution at t=0 of the real part of $\psi_{01,norm}(x,0,z)$, for k=1 and d=2.3.

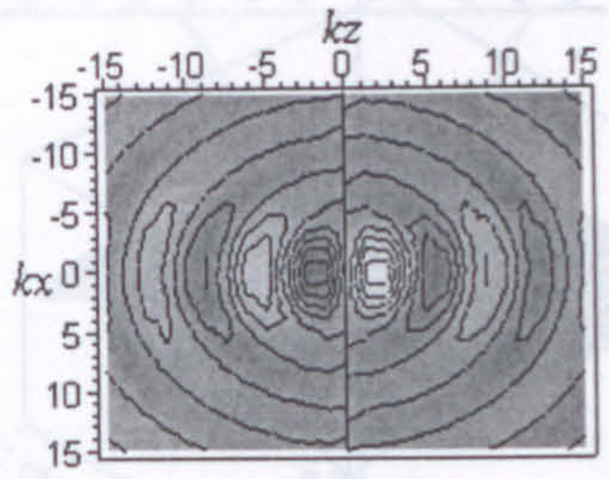

Fig. 2.27.b.) Amplitude contours at t=0 of the real part of $\psi_{01,norm}(x,0,z)$, for k=1 and d=2.3 in the plane of the beam axis.

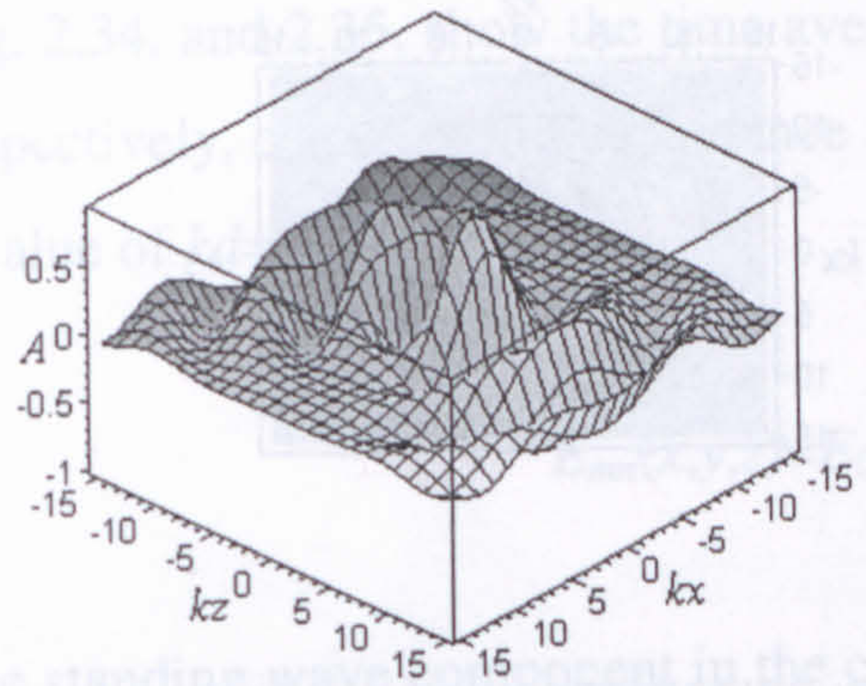

Fig. 2.28.a) Amplitude distribution at t=1 of the real part of $\psi_{01,norm}(x,0,z)$, for k=1 and d=2.3.

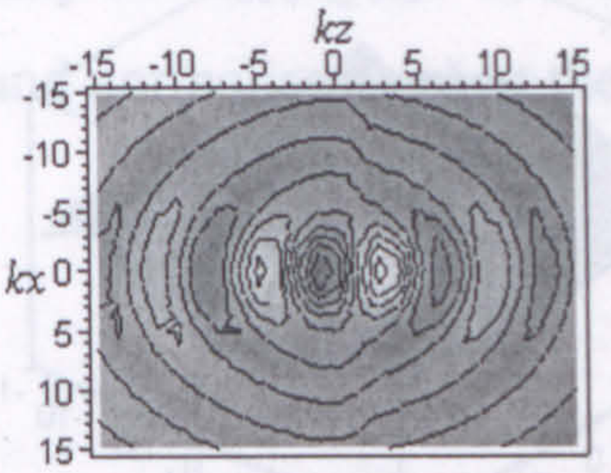

Fig. 2.28.b.) Amplitude contours at t=1 of the real part of $\psi_{01,norm}(x,0,z)$, for k=1 and d=2.3 in the plane of the beam axis.

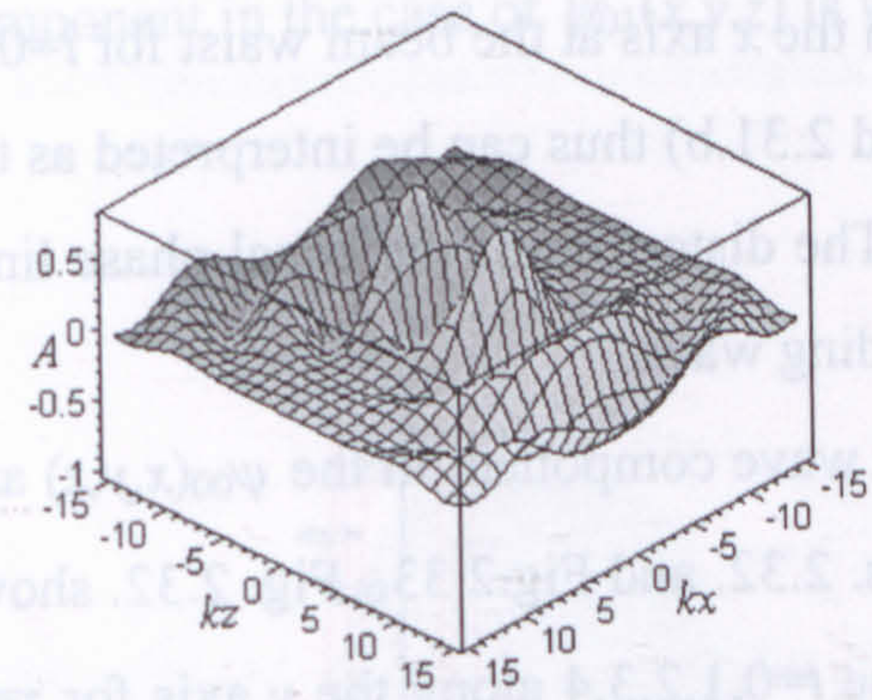

Fig. 2.29.a) Amplitude distribution at t=2 of the real part of $\psi_{01,norm}(x,0,z)$, for k=1 and d=2.3.

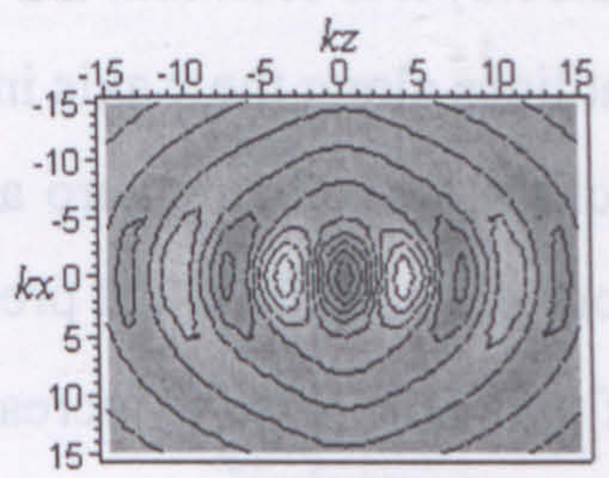

Fig. 2.29.b.) Amplitude contours at t=2 of the real part of $\psi_{01,norm}(x,0,z)$, for k=1 and d=2.3 in the plane of the beam axis.

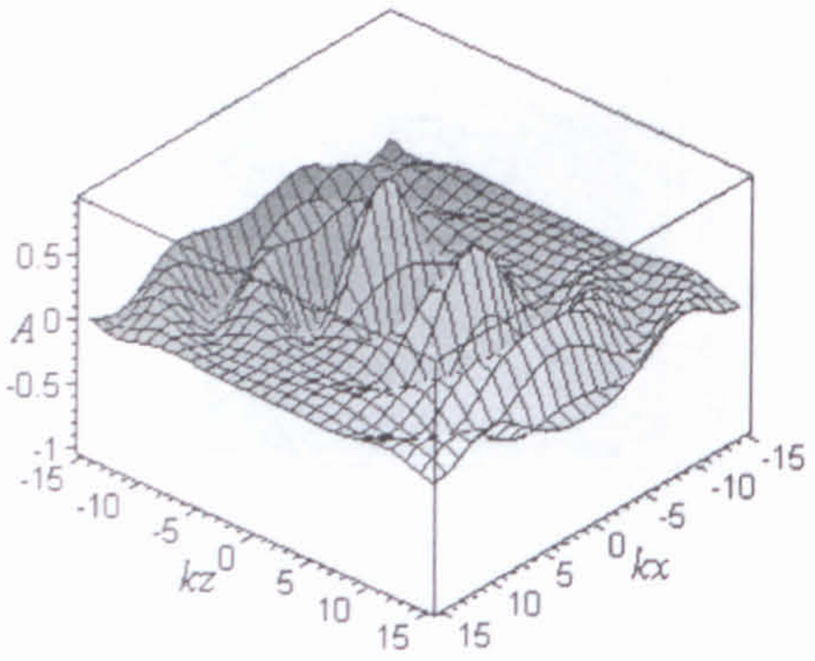

Fig. 2.30.a) Amplitude distribution at t=3 of the real part of $\psi_{01,norm}(x,0,z)$, for k=1 and d=2.3.

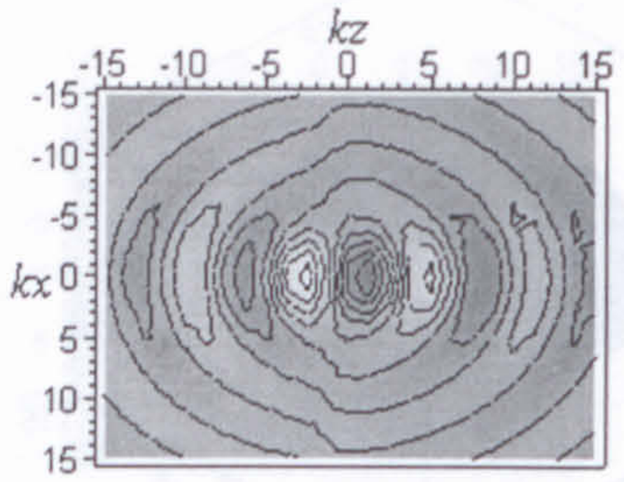

Fig. 2.30.b.) Amplitude contours at t=3 of the real part of $\psi_{01,norm}(x,0,z)$, for k=1 and d=2.3 in the plane of the beam axis.

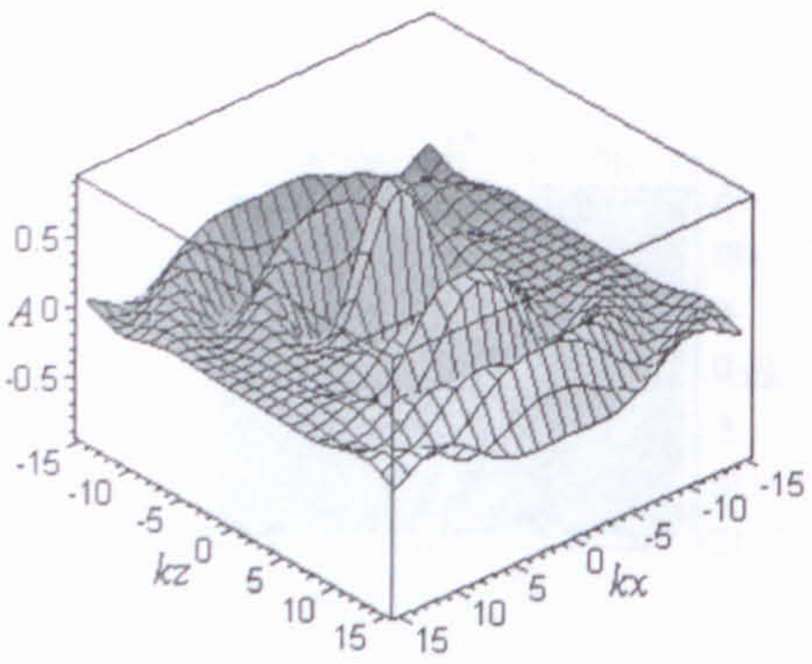

Fig. 2.31.a) Amplitude distribution at t=4 of the real part of $\psi_{01,norm}(x,0,z)$, for k=1 and d=2.3.

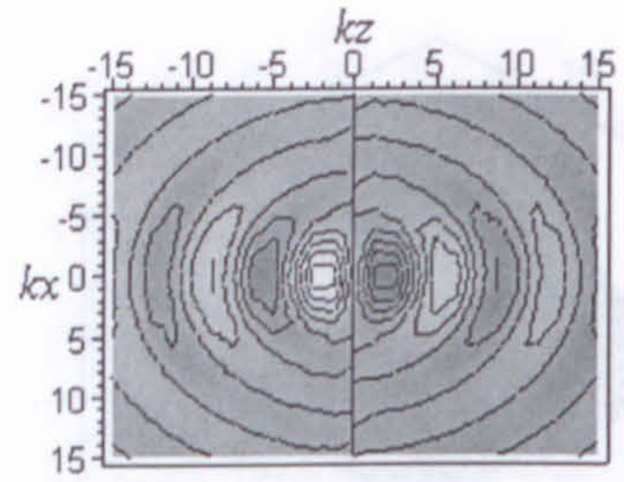

Fig. 2.31.b.) Amplitude contours at t=4 of the real part of $\psi_{01,norm}(x,0,z)$, for k=1 and d=2.3 in the plane of the beam axis.

From Fig. 2.21.b) it is seen that the wave vanishes on the x axis at the beam waist for t=0,4. The straight lines along the x axis in Figs. 2.27.b) and 2.31.b) thus can be interpreted as the amplitude of the wave being zero along the x axis. The distortion of the equal phase lines in the contour plots is due to the presence of the standing wave.

However if the value of kd is increased, the standing wave component in the $\psi_{00}(x,y,z)$ and $\psi_{01}(x,y,z)$ is reduced greatly as can be seen from Figs. 2.32. and Fig.2.33.. Fig. 2.32. shows the real part of the amplitude of $\psi_{00,norm}(x,y,z)$ at time t=0,1,2,3,4 along the y axis for z=0, k=1 and d=5. Fig. 2.33. shows the corresponding real part of $\psi_{01,norm}(x,y,z)$.

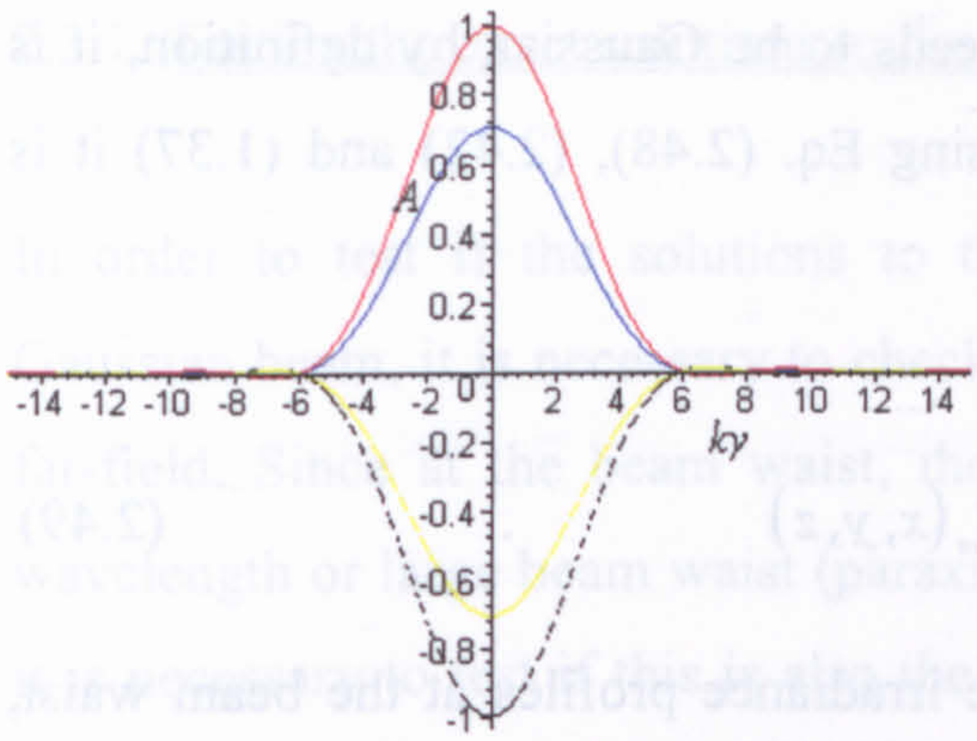

Fig. 2.32. Real part of the amplitude of $\psi_{00,norm}(0,y,0)$ along the y axis for k=1, d=5. Time t=0 (red), t=1 (blue), t=2 (not visible, flat line on top of y axis) t=3 (yellow), t=4 (black).

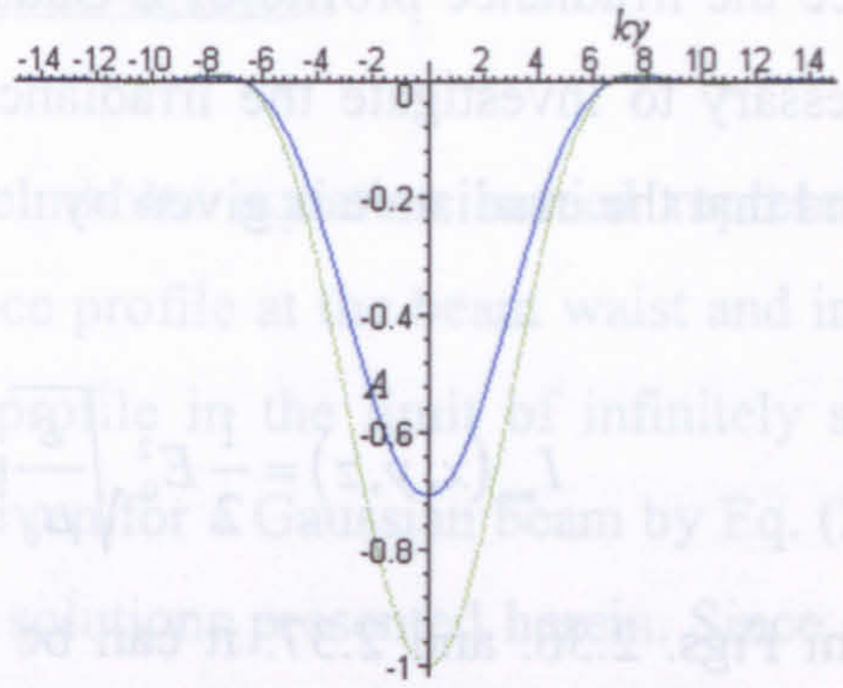

Fig. 2.33. Real part of the amplitude of $\psi_{01,norm}(0,y,0)$ along the y axis for k=1, d=5. Time t=0 and t=4 (not visible, flat line on top of y axis), t=1 (blue), t=2 (green), t=3 (not visible since overlapped by t=1).

Fig. 2.34. and 2.35. show the time averaged energy density of $\langle u_{00}(x,y,z)\rangle$ and $\langle u_{01}(x,y,z)\rangle$ respectively, calculated in accordance with Eq. (1. 35) and normalised to 1 at the origin for a value of kd=1, where

$$E_{mn}(x,y,z)=E_0\,\psi_{mn}(x,y,z) \quad . \tag{2.48}$$

The standing wave component in the case of $\psi_{00}(x,y,z)$ and $\psi_{01}(x,y,z)$ grows significantly as the product kd is reduced. However in the case of $\psi_{01}(x,y,z)$ this component dies off more rapidly than in the case of $\psi_{00}(x,y,z)$. It can therefore be concluded that the standing wave component in the case of $\psi_{01}(x,y,z)$ is weaker than in the case of $\psi_{00}(x,y,z)$.

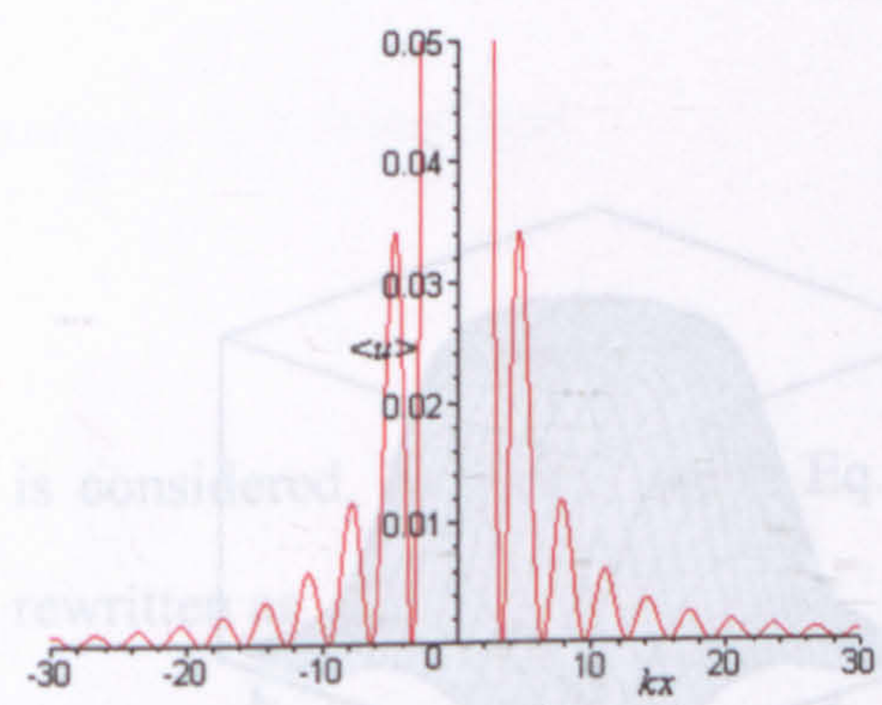

Fig. 2.34. Time averaged energy density plot for $\langle u_{00}(x,y,z)\rangle$ with kd=1in the focal plane z=y=0 and normalised to 1 at x=0.

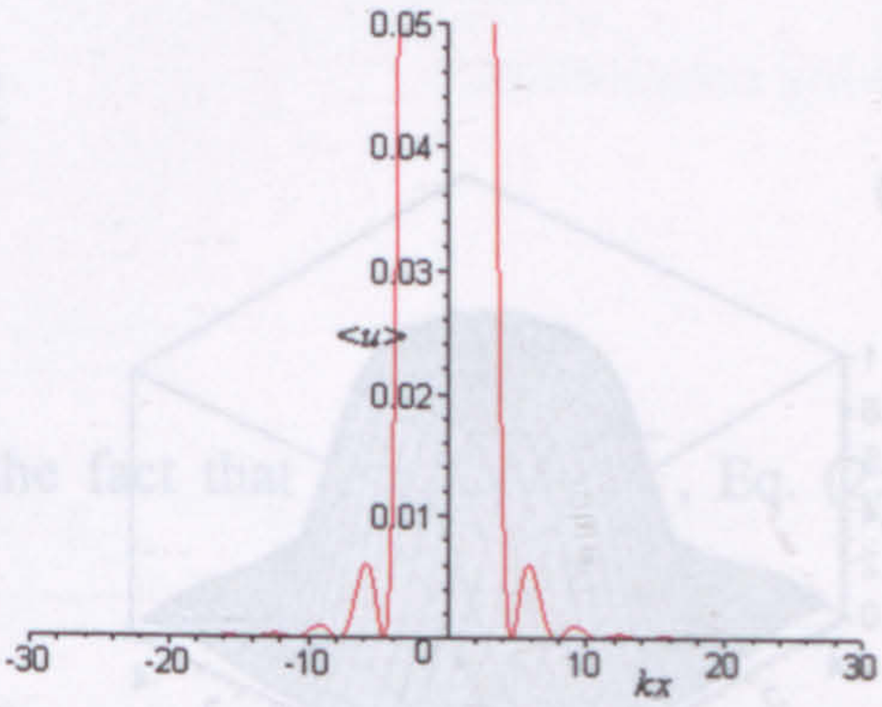

Fig. 2.35. Time averaged energy density plot for $\langle u_{01}(x,y,z)\rangle$ with kd=1in the focal plane z=y=0 and normalised to 1 at x=0.

It was pointed out by Ulanowski and Ludlow [5] that in order to produce such interference, a focusing element that subtends a solid angle greater than 2π is required.

Since the irradiance profile of a Gaussian beam needs to be Gaussian by definition, it is necessary to investigate the irradiance profile. Using Eq. (2.48), (2.42) and (1.37) it is found that the irradiance is given by

$$I_{mn}(x,y,z)=\frac{1}{2}E_0^2\sqrt{\frac{\varepsilon}{\mu_0}}\psi_{mn}(x,y,z)\psi_{mn}^*(x,y,z) \quad . \tag{2.49}$$

From Figs. 2.36. and 2.37. it can be seen that the irradiance profiles at the beam waist, normalised to 1 at $x=y=z=0$, of $\psi_{00}(x,y,z)$ and $\psi_{01}(x,y,z)$ are indeed Gaussian. The irradiance profiles, normalised to 1, of $\psi_{11}(x,y,z)$ and $\psi_{12}(x,y,z)$ though resemble the irradiance profile of the donut mode (Figs. 2.38. and 2.39.). Thus the beam modes, that can be considered to represent a focused Gaussian beam are the orders based on $\psi_{00}(x,y,z)$ and $\psi_{01}(x,y,z)$.

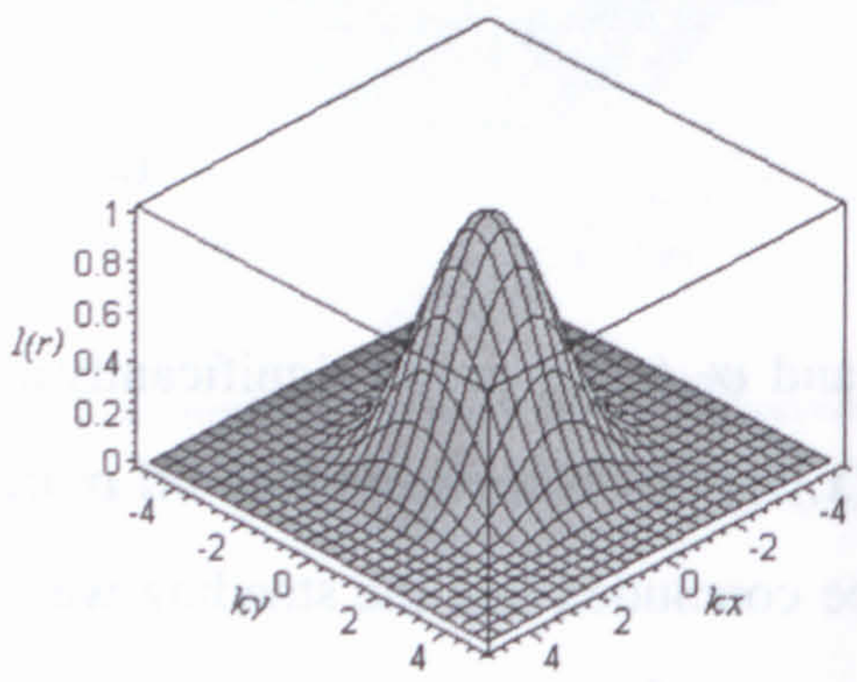

Fig. 2.36. Irradiance profile of the $\psi_{00}(x,y,z)$ beam mode at the beam waist for k=1 and d=2.3, normalised to 1.

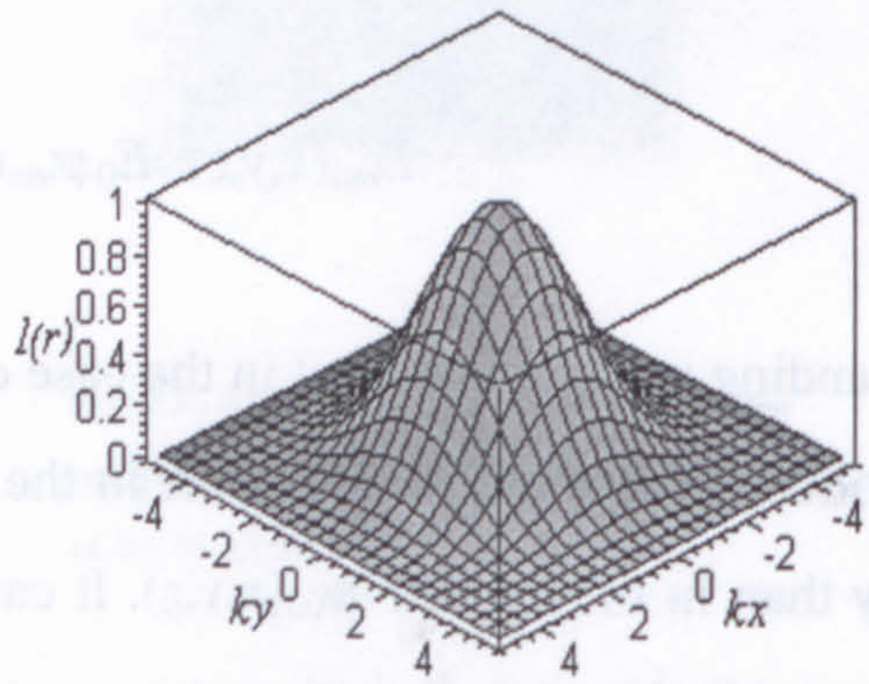

Fig. 2.37. Irradiance profile of the $\psi_{01}(x,y,z)$ beam mode at the beam waist for k=1 and d=2.3, normalised to 1.

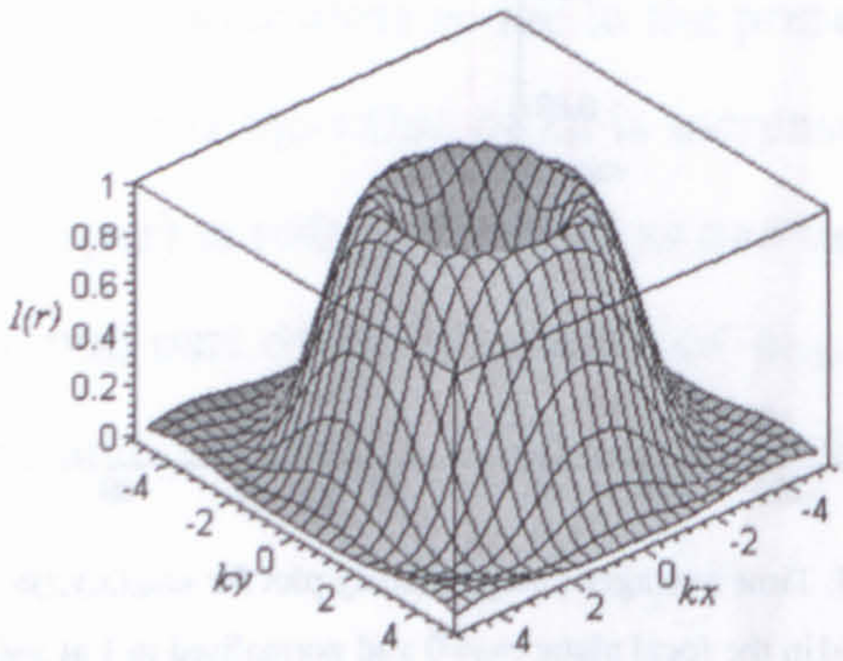

Fig. 2.38. Irradiance profile of the $\psi_{11}(x,y,z)$ beam mode at the beam waist for k=1 and d=2.3, normalised to 1.

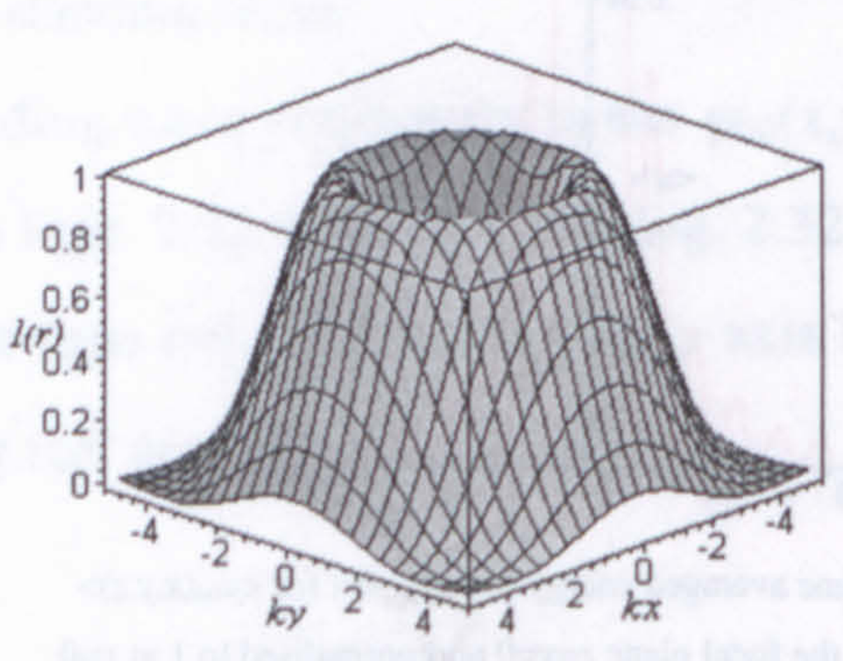

Fig. 2.39. Irradiance profile of the $\psi_{12}(x,y,z)$ beam mode at the beam waist for k=1 and d=2.3, normalised to 1.

2.3.1. Testing the exact solutions to the scalar Helmholtz equation

In order to test if the solutions to the scalar Helmholtz equation indeed represent a Gaussian beam, it is necessary to check the irradiance profile at the beam waist and in the far-field. Since at the beam waist, the irradiance profile in the limit of infinitely short wavelength or large beam waist (paraxial limit) is given for a Gaussian beam by Eq. (2.1), it is necessary to test if this is also the case for the solutions presented herein. Since only the irradiance profile due to $\psi_{00}(x,y,z)$ and $\psi_{01}(x,y,z)$ have what looks like a Gaussian irradiance profile, it is necessary to check, if their irradiance profile indeed is given by Eq. (2.1) in the paraxial limit. In the far-field, the solution is expected to represent a spherical wave with its centre at the origin. The irradiance profile due to $\psi_{00}(x,y,z)$ and $\psi_{01}(x,y,z)$, in the far-field should according to Ulanowski and Ludlow [5] be similar to the irradiance profile of an aberration free lens which obeys the sine condition, illuminated by a paraxial Gaussian beam.

2.3.1.1. Testing the results against the paraxial Gaussian beam approximation

In order to test the wavefunctions $\psi_{00}(x,y,z)$ and $\psi_{01}(x,y,z)$ against the paraxial Gaussian beam approximation, these functions are investigated at the beam waist (z=0). In order to make a direct comparison with Eq.(2.1), the ratio

$$\frac{I(\mathbf{r})}{I_0} = e^{-\frac{2\rho^2}{w_0^2}} \tag{2.50}$$

is considered. However, using Eq. (1.77) and the fact that $\rho = \sqrt{x^2 + y^2}$, Eq. (2.50) is rewritten as

$$\frac{I(x,y,0)}{I_0} = e^{\frac{k\left(x^2+y^2\right)}{d}} \tag{2.51}$$

In the case of $\psi_{00}(x,y,z)$ the irradiance is given, in accordance with Eq. (2.49) by

$$I(x,y,0)_{00} = \frac{E_0^2}{2}\sqrt{\frac{\varepsilon}{\mu_0}}\frac{e^{-2kd}\left(e^{k\sqrt{-x^2-y^2+d^2}} - e^{-k\sqrt{-x^2-y^2+d^2}}\right)^2}{k^2\left(-x^2-y^2+d^2\right)} \quad . \tag{2.52}$$

The normalisation constant I_0 is referred to in this case as $I_{0,00}$, and is obtained by setting x and y equal to zero in Eq. (2.52). Thus

$$I_{0,00} = \frac{1}{2}E_0^2\sqrt{\frac{\varepsilon}{\mu_0}}\frac{e^{-2kd}\left(e^{kd} - e^{-kd}\right)^2}{k^2d^2} \quad . \tag{2.53}$$

Similarly in the case of $\psi_{01}(x,y,z)$ the irradiance is given, in accordance with Eq. (2.49) by

$$I(x,y,0)_{01} = \frac{1}{2}E_0^2\sqrt{\frac{\varepsilon}{\mu_0}}\frac{e^{-2kd}d^2\left(\frac{e^{k\sqrt{-x^2-y^2+d^2}} - e^{-k\sqrt{-x^2-y^2+d^2}}}{k^2\left(x^2+y^2-d^2\right)} + \frac{e^{k\sqrt{-x^2-y^2+d^2}} + e^{-k\sqrt{-x^2-y^2+d^2}}}{k\sqrt{-x^2-y^2+d^2}}\right)^2}{\left(-x^2-y^2+d^2\right)} . \tag{2.54}$$

The normalisation constant I_0 is referred to in this case as $I_{0,01}$, and is obtained by setting x and y equal to zero in Eq. (2.54). Thus

$$I_{0,01} = \frac{1}{2}E_0^2\sqrt{\frac{\varepsilon}{\mu_0}}e^{-2kd}\left(-\frac{e^{kd} - e^{-kd}}{k^2d^2} + \frac{e^{kd} + e^{-kd}}{kd}\right)^2 \quad . \tag{2.55}$$

However since the limit when the product kd goes to infinity, which means that the beam is paraxial with infinitely short wavelength, is of interest, it is convenient to perform the following substitution:

$$p = kd$$

$$k^2 = \frac{kkd}{d} = \frac{kp}{d} .$$

Hence $I(x,y,0)_{00}$ and $I(x,y,0)_{01}$ can be rewritten in terms of p as

$$I(x,y,0)_{00} = \frac{1}{2}E_0^2\sqrt{\frac{\varepsilon}{\mu_0}}\frac{e^{-2p}\left(e^{\sqrt{-\frac{kpx^2}{d}-\frac{kpy^2}{d}+p^2}}-e^{-\sqrt{-\frac{kpx^2}{d}-\frac{kpy^2}{d}+p^2}}\right)^2}{-\frac{kpx^2}{d}-\frac{kpy^2}{d}+p^2} \tag{2.56}$$

and

$$I(x,y,0)_{01} = \frac{1}{2}E_0^2\sqrt{\frac{\varepsilon}{\mu_0}}\frac{e^{-2p}p^2\left(\frac{e^{\sqrt{\frac{kpx^2}{d}+\frac{kpy^2}{d}+p^2}}-e^{-\sqrt{\frac{kpx^2}{d}+\frac{kpy^2}{d}+p^2}}}{\frac{kpx^2}{d}+\frac{kpy^2}{d}-p^2}+\frac{e^{\sqrt{\frac{kpx^2}{d}+\frac{kpy^2}{d}+p^2}}+e^{-\sqrt{\frac{kpx^2}{d}+\frac{kpy^2}{d}+p^2}}}{\sqrt{-\frac{kpx^2}{d}-\frac{kpy^2}{d}+p^2}}\right)^2}{-\frac{kpx^2}{d}-\frac{kpy^2}{d}+p^2}. \tag{2.57}$$

Similarly $I_{0,00}$ and $I_{0,01}$ can be rewritten in terms of p as

$$I_{0,00} = \frac{1}{2}E_0^2\sqrt{\frac{\varepsilon}{\mu_0}}\frac{e^{-2p}\left(e^{p}-e^{-p}\right)^2}{p^2} \tag{2.58}$$

and

$$I_{0,01} = \frac{1}{2}E_0^2\sqrt{\frac{\varepsilon}{\mu_0}}e^{-2p}\left(-\frac{e^{p}-e^{-p}}{p^2}+\frac{e^{p}+e^{-p}}{p}\right)^2. \tag{2.59}$$

The last step is to calculate the ratios $\frac{I(x,y,0)_{00}}{I_{0,00}}$ and $\frac{I(x,y,0)_{01}}{I_{0,01}}$ in the limit as p tends to infinity. It is found that

$$\lim_{p\to\infty}\left(\frac{I(x,y,0)_{00}}{I_{0,00}}\right) = e^{-\frac{k\left(x^2+y^2\right)}{d}}$$
$$\lim_{p\to\infty}\left(\frac{I(x,y,0)_{01}}{I_{0,01}}\right) = e^{-\frac{k\left(x^2+y^2\right)}{d}} \tag{2.60}$$

Comparing the results from Eqs. (2.60) with the result for a lowest order Laguerre-Gaussian beam mode TEM^{*}_{00}, Eq. (2.51), it can be seen that these results are identical. Thus the scalar solutions have the correct form in the paraxial limit.

2.3.1.2. Testing the results at infinite radius of the Gaussian reference surface

It has been suggested by Ulanowski and Ludlow [5] that in order to represent the wave of a paraxial Gaussian beam focused by an aberration-free lens which obeys the Abbe sine condition, in the limit where the radius of the Gaussian reference sphere goes to infinity, the ratio $Q(\alpha)$, of the irradiance $I(r,\alpha)$ and $I(r,0)$ should be of the form

$$Q(\alpha)=\lim_{r\to\infty}\left(\frac{I(r,\alpha)}{I(r,0)}\right)=\cos(\alpha)e^{\left(-2\frac{\sin(\alpha)^2}{\gamma^2}\right)} \quad , \tag{2.61}$$

where α is the angle between $-\pi/2$ and $\pi/2$ on the Gaussian reference sphere and $I(r,0)$ is the on axis normalisation constant . As can be seen from Fig. 2.40., the width of the Gaussian distribution is dependent on the γ value of Eq. (2.61), where γ is a dimensionless parameter representing the width of the paraxial beam with respect to the focal length of the lens and measured at the point at which the irradiance function drops to $\frac{1}{e^2}$.

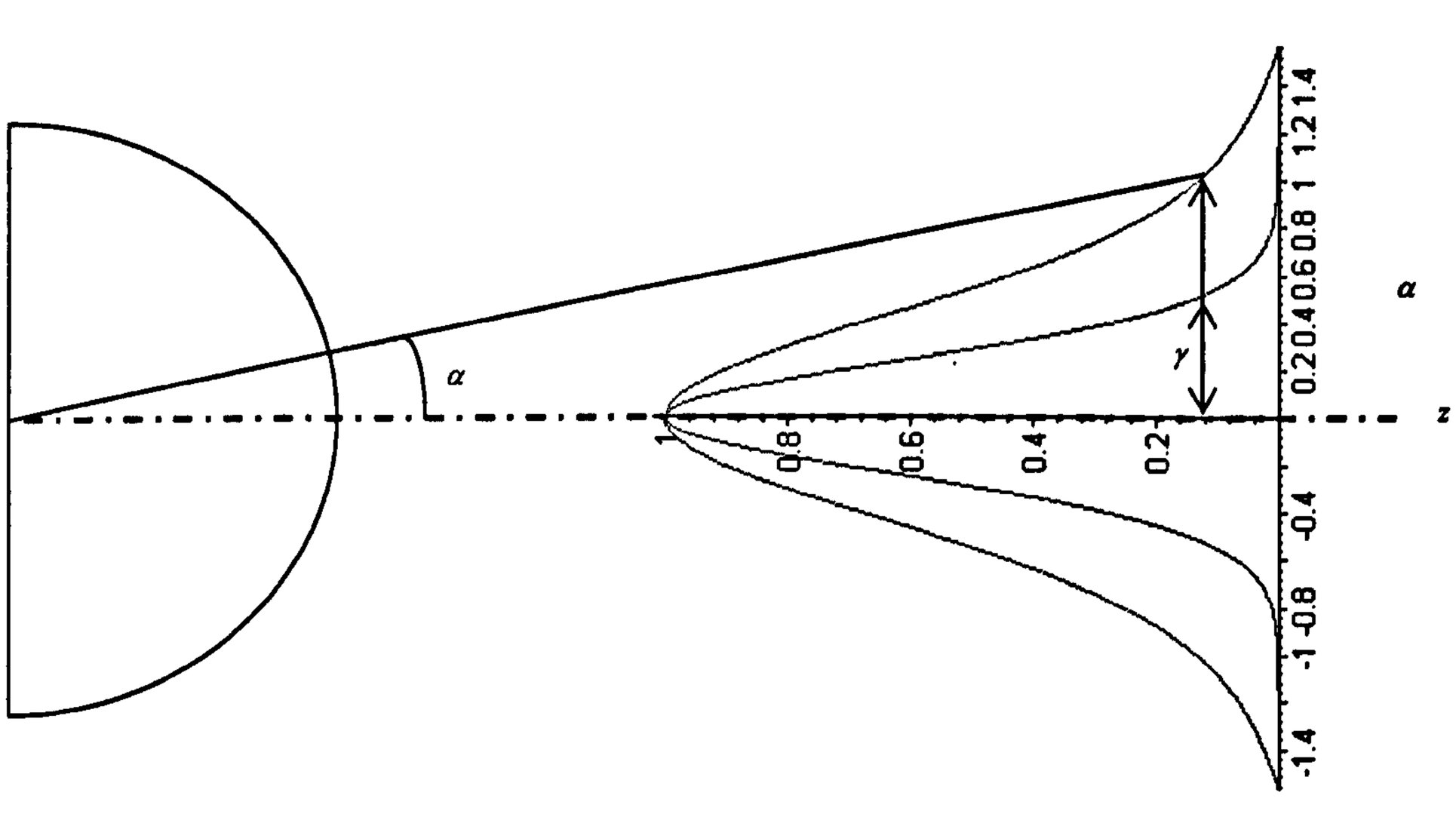

Gaussian reference surface (principal surface)

$Q(\alpha)$ for two different γ values.

Fig. 2.40. The irradiance distribution on the Gaussian reference sphere

Ulanowski and Ludlow [5] state that since the wave in Eq.(2.36) is the sum of the incoming part (Eq. (2.30)) and the outgoing part (Eq. (2.33)) of the same wave, it is legitimate to examine these parts separately for the purpose of investigating boundary

conditions. Since this statement is true for any order *mn*, only the outward travelling wave i.e. $\psi^{(1)}{}_{mn}(x,y,z)$ is considered in the far-field.

In order to calculate the irradiance profile due to $\psi^{(1)}{}_{00}(x,y,z)$ and $\psi^{(1)}{}_{01}(x,y,z)$ on the Gaussian reference sphere it is convenient to express these functions in spherical polar coordinates. In the following calculations the only variables are the Rayleigh range d and the radius of the Gaussian reference sphere r. The complex radius in spherical polar coordinates is obtained by substituting Eqs. (2.6) into Eq. (2.39). Since the normalised irradiance on the reference sphere is of interest, θ in Eqs. (2.6) is replaced by α. However, as the irradiance is proportional to the product of the wavefunction and its complex conjugate, it is useful to use separate expressions for the complex radius and its complex conjugate in spherical polar coordinates, namely

$$\begin{aligned} R_{sp} &= \sqrt{r^2 - 2ird\cos\alpha - d^2} \\ R_{sp}^{*} &= \sqrt{r^2 + 2ird\cos\alpha - d^2} \end{aligned} \tag{2.62}$$

The wavefunctions $\psi^{(1)}{}_{00}(r,\alpha)$ and $\psi^{(1)}{}_{01}(r,\alpha)$ in spherical polar coordinates can be written as

$$\begin{aligned} \psi_{00}^{(1)}(r,\alpha) &= -\frac{ie^{-kd}e^{ik\sqrt{r^2-2ird\cos\alpha-d^2}}}{k\sqrt{r^2-2ird\cos\alpha-d^2}} = -\frac{ie^{-kd}e^{ikR_{sp}}}{kR_{sp}} \\ \psi_{01}^{(1)}(r,\alpha) &= \frac{e^{-kd}e^{ik\sqrt{r^2-2ird\cos\alpha-d^2}}\left(-\dfrac{i}{k\sqrt{r^2-2ird\cos\alpha-d^2}}-1\right)(r\cos\alpha-id)}{k\left(r^2-2ird\cos\alpha-d^2\right)} \\ &= \frac{e^{-kd}e^{ikR_{sp}}}{kR_{sp}^2}\left(\frac{1}{ikR_{sp}}-1\right)(r\cos\alpha-id) \end{aligned} . \tag{2.63}$$

In order to calculate the corresponding normalisation constants $I^{(1)}{}_{0,00}(r,0)$ and $I^{(1)}{}_{0,01}(r,0)$ respectively on the axis, it can be seen from Eqs.(2.6) (replacing θ with α), that sin (α) needs to be zero. Hence α=0, z=r and R_{sp}=r-id. By substituting these values into Eqs. (2.63) and multiplying these equations with their complex conjugates and $\frac{1}{2}E_0^2\sqrt{\frac{\varepsilon}{\mu_0}}$, the following values for $I^{(1)}{}_{0,00}(r,0)$ and $I^{(1)}{}_{0,01}(r,0)$ are obtained:

$$I_{0,00}^{(1)}(r,0)=\frac{1}{2}E_0^2\sqrt{\frac{\varepsilon}{\mu_0}}\frac{1}{k^2\left(r^2+d^2\right)}$$
$$I_{0,01}^{(1)}(r,0)=\frac{1}{2}E_0^2\sqrt{\frac{\varepsilon}{\mu_0}}\frac{k^2\left(r^2+d^2\right)+1-2kd}{k^4\left(r^2+d^2\right)^2} \quad . \tag{2.64}$$

In order to calculate the irradiance normalised to 1 in the far-field limit, i.e. as $r\to\infty$, an analytic expression for the normalised irradiance due to $\psi^{(1)}{}_{00}(r,\alpha)$ and due to $\psi^{(1)}{}_{01}(r,\alpha)$ needs to be obtained. Since R_{sp} and its complex conjugate are different for r^2-d^2<0 and r^2-d^2>0 it is necessary to calculate the roots of R_{sp} and its complex conjugate explicitly. This is achieved by using the general formulae given by Abramowitz and Stegun [7] as

$$z=\rho e^{i\theta}=\rho(\cos\theta+i\sin\theta)=x+iy$$
$$|z|=\sqrt{x^2+y^2}=\rho$$
$$\arg z=\arctan\left(\frac{y}{x}\right)=\theta=\arctan\left(\frac{\mathrm{Im}}{\mathrm{Re}}\right) \quad , \tag{2.65}$$
$$\sqrt{z}=\sqrt{\rho}e^{\frac{1}{2}i\theta}$$

where z represents a complex variable, "Re" stands for the real part and "Im" represents the imaginary part. In order to use Eqs. (2.65) effectively, it is necessary to write the irradiance due to $\psi^{(1)}{}_{00}(r,\alpha)$ and the irradiance due to $\psi^{(1)}{}_{01}(r,\alpha)$ in the following form

$$I_{00}^{(1)}(r,\alpha)=\frac{1}{2}E_0^2\sqrt{\frac{\varepsilon}{\mu_0}}\frac{e^{-2kd}e^{ik\left(R_{sp}-R_{sp}^*\right)}}{k^2\sqrt{\left(r^2-d^2\right)^2+4r^2d^2\cos^2\alpha}}$$
$$I_{01}^{(1)}(r,\alpha)=\frac{1}{2}E_0^2\sqrt{\frac{\varepsilon}{\mu_0}}\frac{e^{-2kd}\left(\frac{1}{ikR_{sp}}-1\right)(r\cos\alpha-id)\left(-\frac{1}{ikR_{sp}^*}-1\right)(r\cos\alpha+id)}{k^2\left[\left(r^2-d^2\right)^2+4r^2d^2\cos^2\alpha\right]}e^{ik\left(R_{sp}-R_{sp}^*\right)} \quad . \tag{2.66}$$

Further it is necessary to evaluate $e^{ik\left(R_{sp}-R_{sp}^*\right)}$ explicitly. This is achieved by defining a new variable

$$a=R_{sp}-R_{sp}^*=\sqrt{r^2-2ird\cos\alpha-d^2}-\sqrt{r^2+2ird\cos\alpha-d^2} \quad . \tag{2.67}$$

Thus the exponent can be written as *ika*. Now, the two terms in Eq. (2.67) can be identified as the roots of two complex variables. In order to evaluate these roots it is useful to define two further variables

$$a_1 = r^2 - 2ird\cos\alpha - d^2$$
$$a_2 = r^2 + 2ird\cos\alpha - d^2 \quad . \tag{2.68}$$

In order to find the roots of a_1 and a_2, the arguments θ_1 and θ_2 are found from Eq. (2.65) using the real and imaginary parts of a_1 and a_2 respectively. The modulus ρ_1 and ρ_2 of a_1 and a_2 is also obtained from Eq. (2.65). By performing these calculations the following expressions

$$\begin{aligned}
&\mathrm{Re}[a_1] = \mathrm{Re}[a_2] = r^2 - d^2 \\
&\mathrm{Im}[a_1] = -2rd\cos\alpha \\
&\mathrm{Im}[a_2] = 2rd\cos\alpha \\
&\theta_1 = -\arctan\left(2\frac{rd\cos\alpha}{r^2 - d^2}\right) \\
&\theta_2 = \arctan\left(2\frac{rd\cos\alpha}{r^2 - d^2}\right) \\
&\rho_1 = \rho_2 = \sqrt{\left(r^2 - d^2\right)^2 + 4r^2d^2\cos^2\alpha}
\end{aligned} \tag{2.69}$$

are obtained.

Substituting the expressions form Eqs. (2.69) into Eq. (2.65), $e^{ik\left(R_{sp} - R_{sp}^*\right)}$ can be written as

$$e^{\left(2k\left[\left(r^2-d^2\right)^2+4r^2d^2\cos^2\alpha\right]^{1/4}\sin\left(\frac{1}{2}\arctan\left(2\frac{rd\cos\alpha}{r^2-d^2}\right)\right)\right)} . \tag{2.70}$$

By substituting Eq. (2.70) into Eqs. (2.66) and dividing these equations with the corresponding normalisation constants $I^{(1)}_{0,00}(r,0)$ and $I^{(1)}_{0,01}(r,0)$ respectively, given in Eqs. (2.64), the following ratios due to $\psi^{(1)}_{00}(r,\alpha)$ and $\psi^{(1)}_{01}(r,\alpha)$ are obtained:

$$\frac{I^{(1)}_{00}(r,\alpha)}{I^{(1)}_{0,00}(r,0)} = \frac{e^{-2kd}e^{\left(2k\left[\left(r^2-d^2\right)^2+4r^2d^2\cos^2\alpha\right]^{1/4}\sin\left(\frac{1}{2}\arctan\left(2\frac{rd\cos\alpha}{r^2-d^2}\right)\right)\right)}\left(r^2+d^2\right)}{\sqrt{\left(r^2+d^2\right)^2+4r^2d^2\cos^2\alpha}}$$

$$\frac{I^{(1)}_{01}(r,\alpha)}{I^{(1)}_{0,01}(r,0)} = \frac{k^2e^{-2kd}\left(\frac{1}{ikR_{sp}}-1\right)\left(r\cos\alpha - id\right)\left(-\frac{1}{ikR^*_{sp}}-1\right)\left(r\cos\alpha + id\right)\left(r^2+d^2\right)^2}{\left[\left(r^2-d^2\right)^2+4r^2d^2\cos^2\alpha\right]\left[k^2\left(r^2+d^2\right)+1-2kd\right]} \times$$
$$e^{\left(2k\left[\left(r^2-d^2\right)^2+4r^2d^2\cos^2\alpha\right]^{1/4}\sin\left(\frac{1}{2}\arctan\left(2\frac{rd\cos\alpha}{r^2-d^2}\right)\right)\right)} . \tag{2.71}$$

In the far-field limit these ratios become

$$Q_{00}(\alpha) = \lim_{r\to\infty}\left(\frac{I_{00}^{(1)}(r,\alpha)}{I_{0,00}^{(1)}(r,0)}\right) = e^{-2kd(1-\cos\alpha)}$$
$$Q_{01}(\alpha) = \lim_{r\to\infty}\left(\frac{I_{01}^{(1)}(r,\alpha)}{I_{0,01}^{(1)}(r,0)}\right) = \cos^2(\alpha)e^{-2kd(1-\cos\alpha)} \qquad (2.72)$$

Ulanowski and Ludlow [5] identified γ in Eq. (2.61) to be

$$\gamma = \frac{w}{f},$$

where w is the beam radius and f is the focal length. It can be clearly seen that Eqs. (2.72) are not equal to Eq. (2.61). Further Ulanowski and Ludlow [5] state that although the forms of the first of Eqs. (2.72) and Eq. (2.61) are different, there is a close resemblance, since $2(1 - \cos\alpha) = 4\sin^2\frac{\alpha}{2}$, and the two irradiances become approximately equal if $\frac{2f^2}{kw^2}$ is set equal to $d = \frac{kw_0^2}{2}$, therefore establishing a direct correspondence between the beam parameters before and after focusing. Using these relations, $\gamma = \sqrt{\frac{2}{kd}}$. Figs. 2.41.-2.46. show a comparison of the irradiance profiles, normalised to 1 on axis, for different values of kd, of the function $Q(\alpha)$ given in Eq. (2.61) and $Q_{00}(\alpha)$ in the far-field limit, given by the first of Eqs. (2.72).

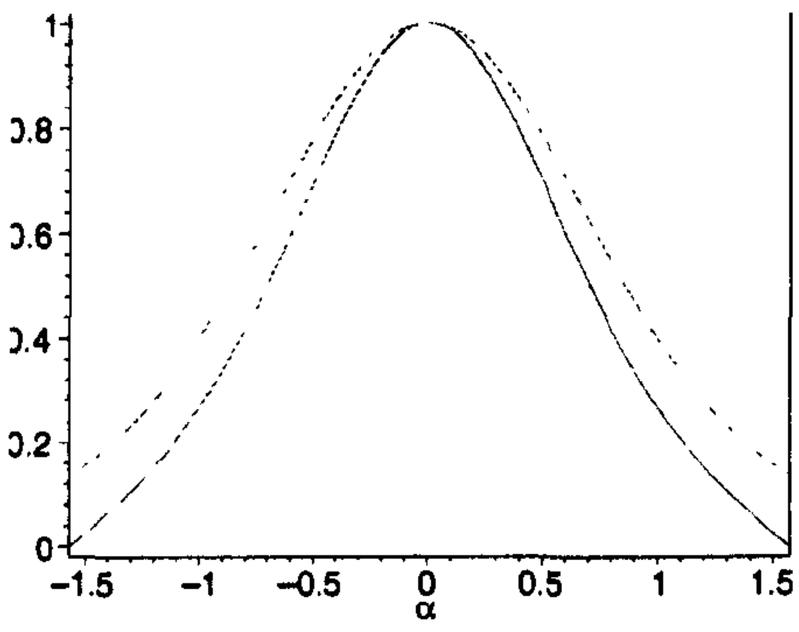

Fig. 2.41. Comparison between $Q_{00}(\alpha)$ (dotted curve) and $Q(\alpha)$ (solid curve) for kd=1.

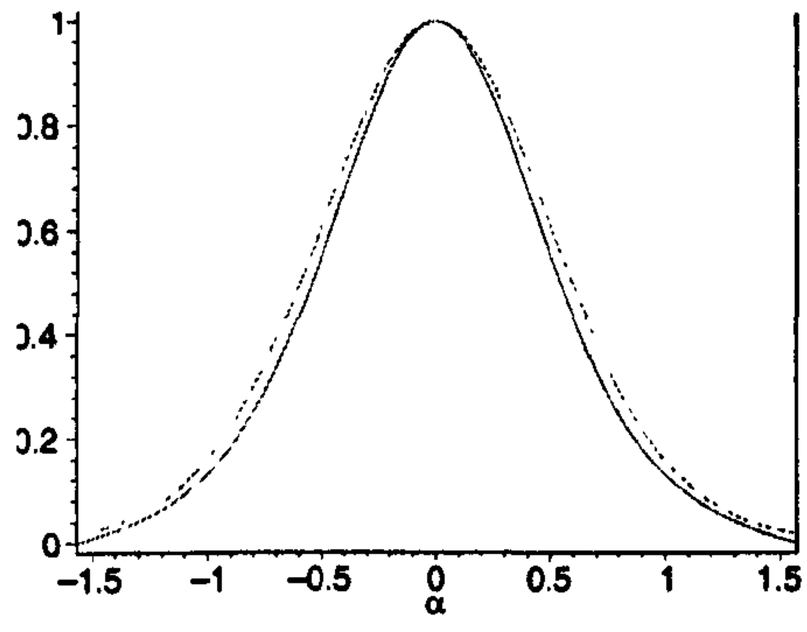

Fig. 2.42. Comparison between $Q_{00}(\alpha)$ (dotted curve) and $Q(\alpha)$ (solid curve) for kd=2.

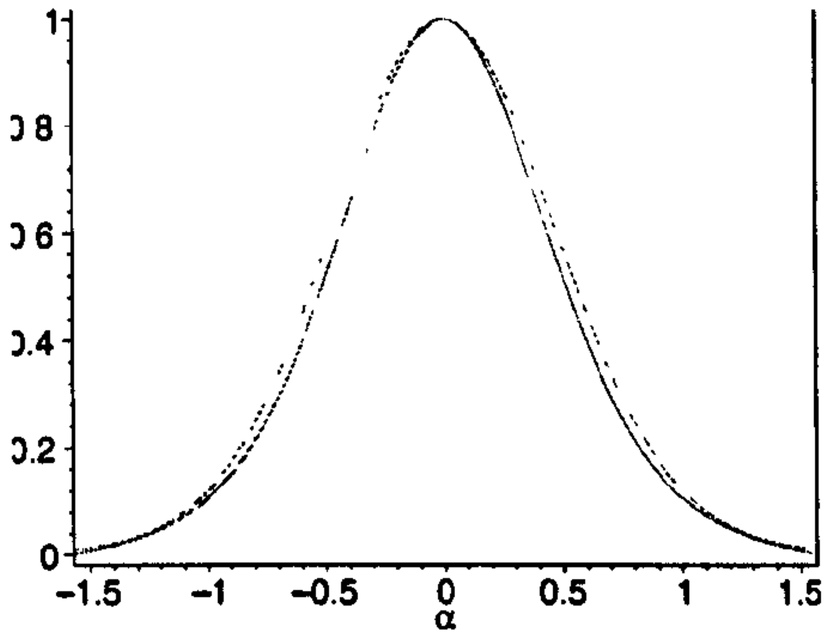

Fig. 2.43. Comparison between $Q_{00}(\alpha)$ (dotted curve) and $Q(\alpha)$ (solid curve) for kd=2.3.

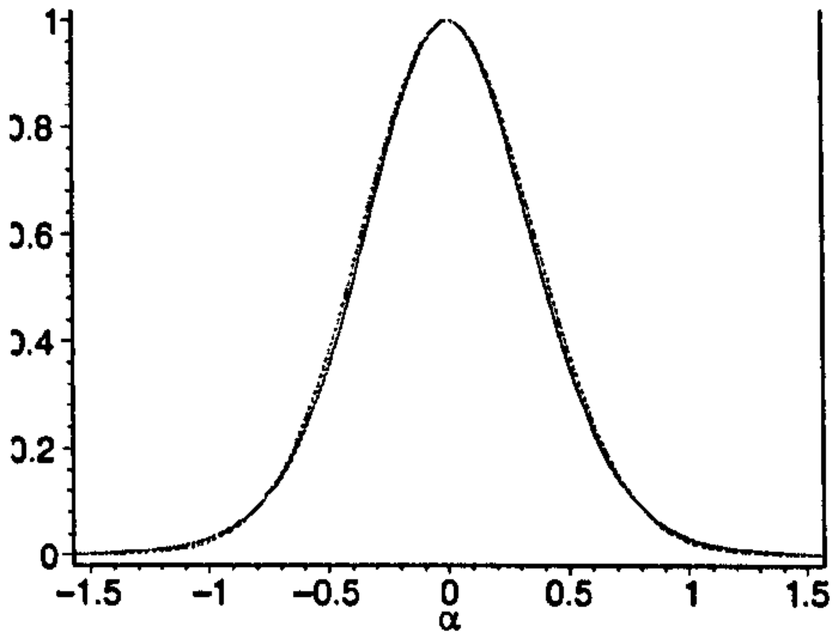

Fig. 2.44. Comparison between $Q_{00}(\alpha)$ (dotted curve) and $Q(\alpha)$ (solid curve) for kd=4.

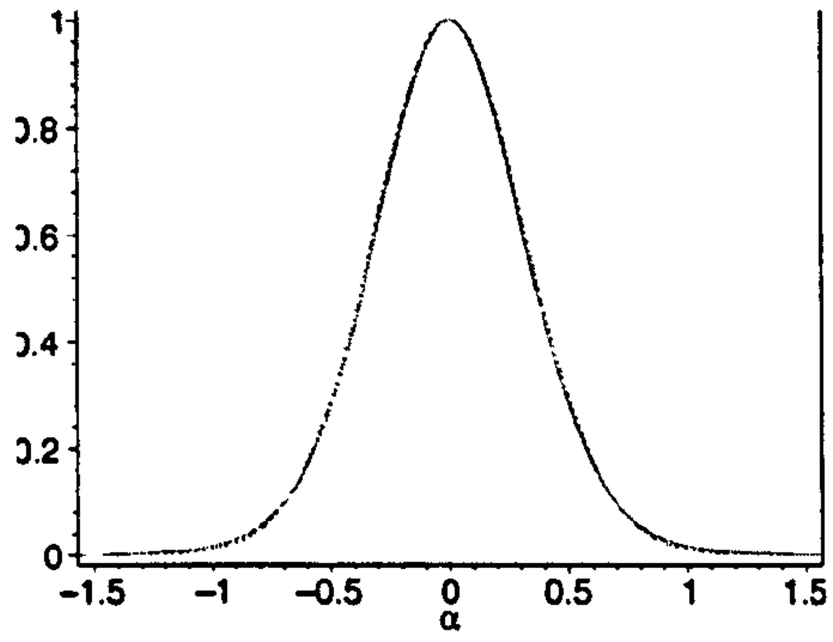

Fig. 2.45. Comparison between $Q_{00}(\alpha)$ (dotted curve) and $Q(\alpha)$ (solid curve) for kd=5.

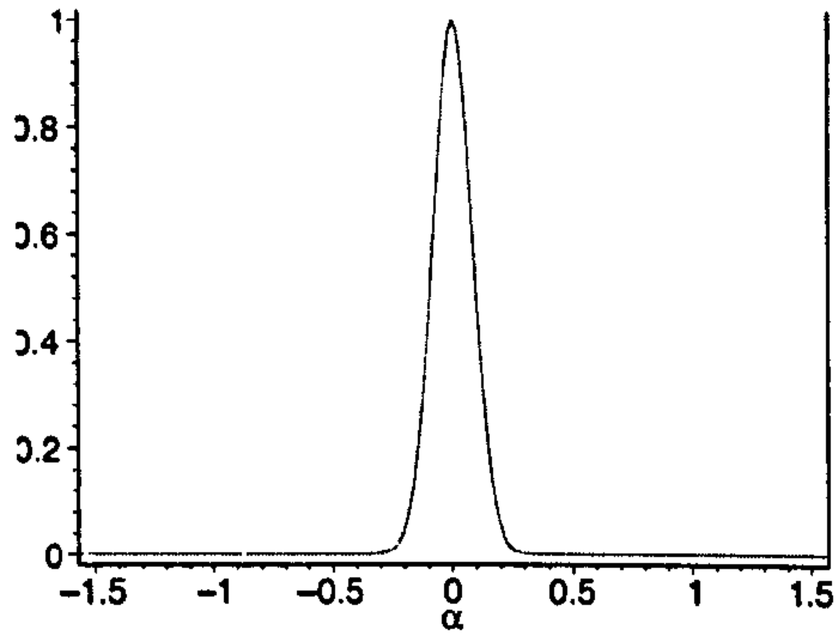

Fig. 2.46. Comparison between $Q_{00}(\alpha)$ (dotted curve) and $Q(\alpha)$ (solid curve) for kd=75.

It can be clearly seen from these figures, that the difference between the two functions increases with decreasing kd. Figs. 2.47.-2.52. show a comparison of the irradiance profiles, normalised to 1 on axis, for different values of kd, of the function $Q(\alpha)$ given in Eq. (2.61) and $Q_{01}(\alpha)$ in the far-field limit, given by the second of Eqs. (2.72).

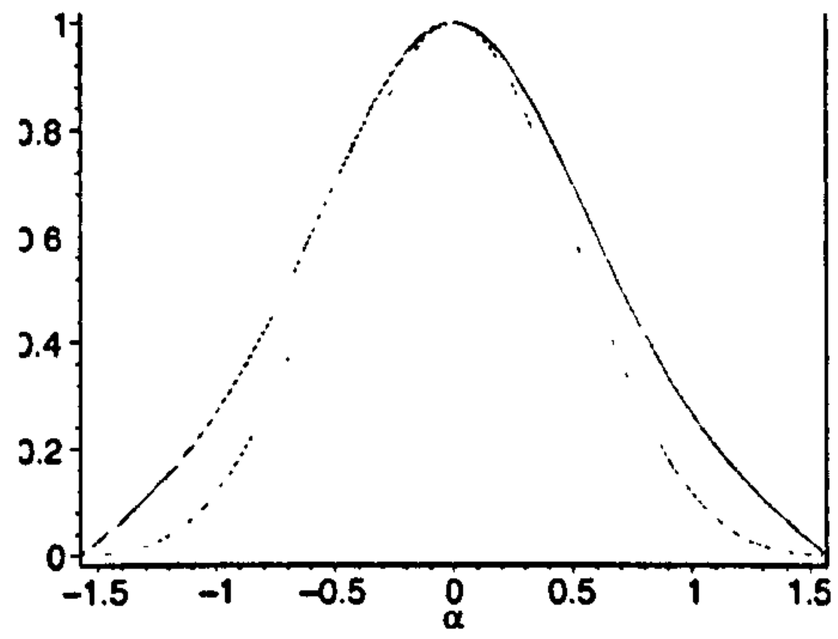

Fig. 2.47. Comparison between $Q_{01}(\alpha)$ (dotted curve) and $Q(\alpha)$ (solid curve) for kd=1.

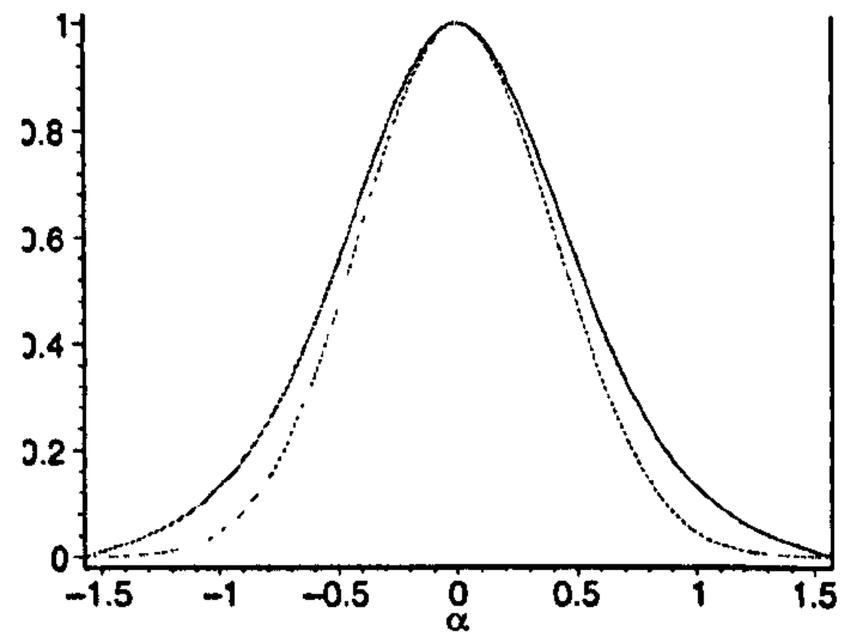

Fig. 2.48. Comparison between $Q_{01}(\alpha)$ (dotted curve) and $Q(\alpha)$ (solid curve) for kd=2.

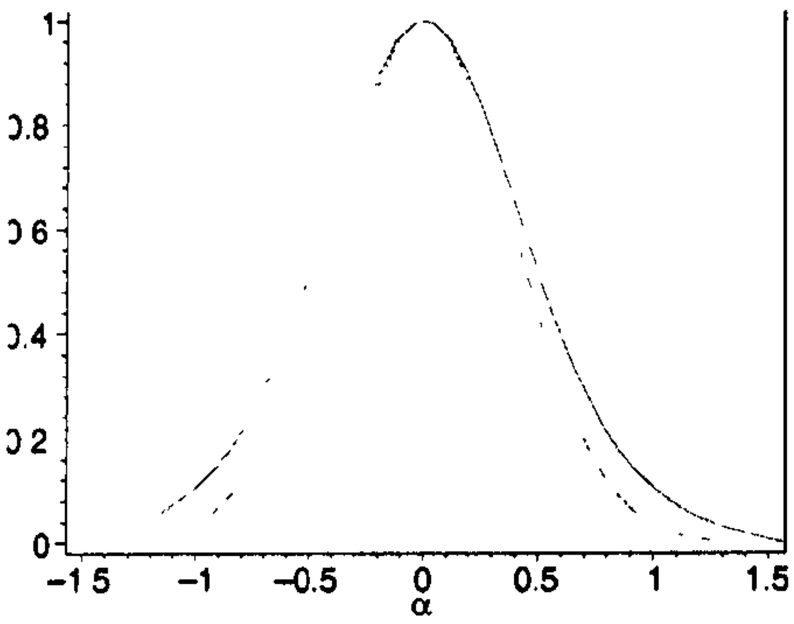

Fig. 2.49. Comparison between $Q_{01}(\alpha)$ (dotted curve) and $Q(\alpha)$ (solid curve) for kd=2.3.

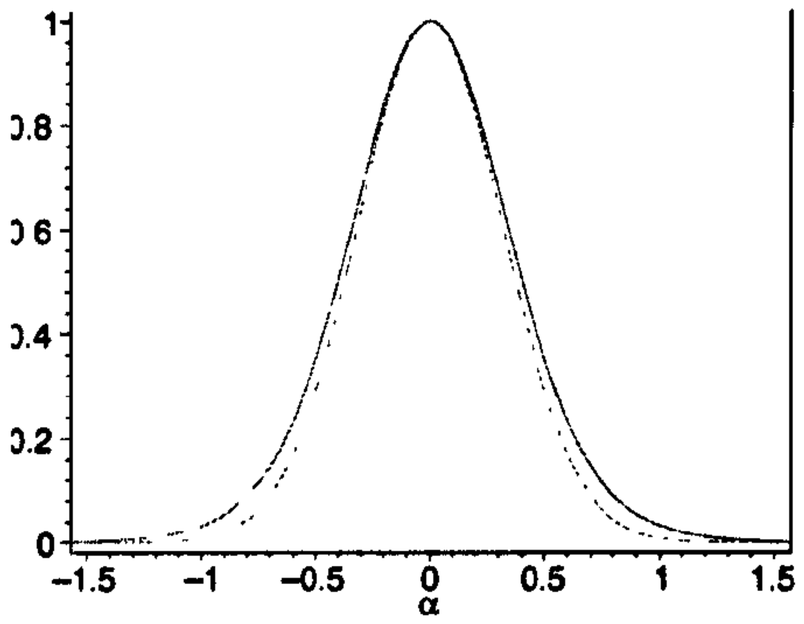

Fig. 2.50. Comparison between $Q_{01}(\alpha)$ (dotted curve) and $Q(\alpha)$ (solid curve) for kd=4.

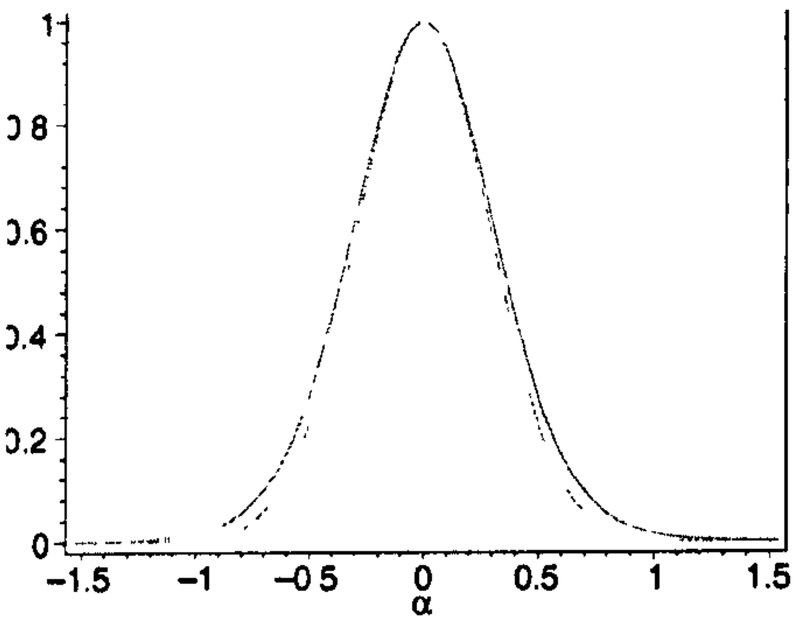

Fig. 2.51. Comparison between $Q_{01}(\alpha)$ (dotted curve) and $Q(\alpha)$ (solid curve) for kd=5.

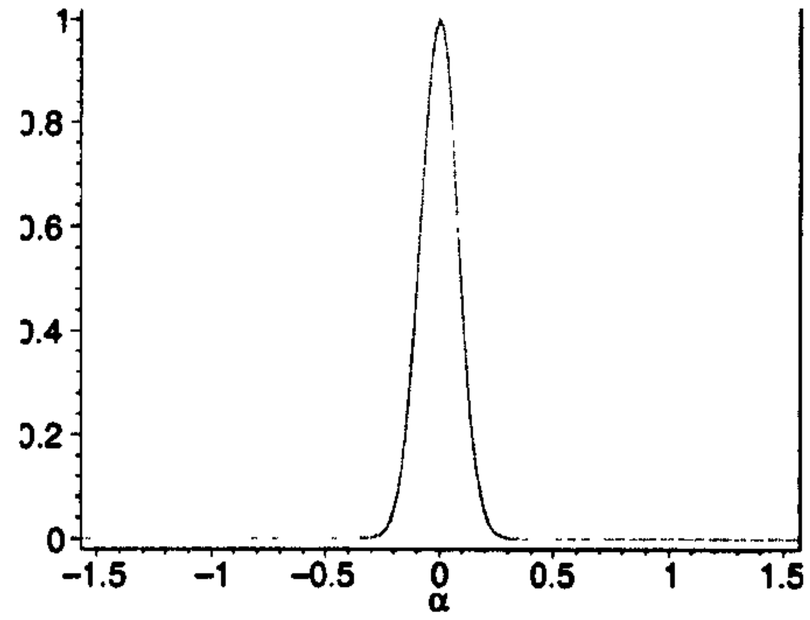

Fig. 2.52. Comparison between $Q_{01}(\alpha)$ (dotted curve) and $Q(\alpha)$ (solid curve) for kd=75.

Again it can be clearly seen that the difference between the two functions becomes large for low kd. However by comparing Figs. 2.41. and 2.47., both for a value of kd=1, it can be seen that in the case of $Q_{00}(\alpha)$ the function does not go to zero at $\alpha = \pm\frac{\pi}{2}$, where in the case of $Q_{01}(\alpha)$ the function does. It is mentioned by Ulanowski and Ludlow [5] in the discussion of $Q_{00}(\alpha)$, that "*although the agreement between* [$Q(\alpha)$ and $Q_{00}(\alpha)$] *is very close even for small values of kd, it has to be concluded that the scalar field based on* $\psi^{(1)}_{00}(x,y,z)$, *does not exactly represent the field of a Gaussian beam focused by an aberration-free lens that obeys the sine condition, and that it rather could be thought of as the complete field of a Gaussian wave that is spherical in the far-field and which is further characterised by a boundless angular extent on the surface of a sphere, in the same way as a paraxial Gaussian beam has an infinite extent in any transverse plane.*" From the analysis so far, it is apparent that both $\psi_{00}(x,y,z)$ and $\psi_{01}(x,y,z)$ are reasonably good candidates for descriptions of a Gaussian beam focused by an aberration-free lens that obeys the sine condition. Though it can be further concluded that $\psi_{01}(x,y,z)$ fulfils the requirement of producing the correct normalised irradiance profile in the far-field limit

slightly better than $\psi_{00}(x,y,z)$ since the irradiance profile goes to zero at $\alpha = \pm\frac{\pi}{2}$, even though for values of $kd = [2,..,5]$, $Q_{00}(\alpha)$ seems to fit the irradiance profile $Q(\alpha)$ better.

2.4. The calculations of the beam power based on $\psi_{00}(x,y,z)$ and $\psi_{01}(x,y,z)$

The last criterion is, that the beam power needs to be finite. In this section the beam power of the two lowest order functions $\psi_{00}(x,y,z)$ and $\psi_{01}(x,y,z)$ will be discussed. In accordance with Eq. (1.74.a) the time averaged beam power P at the beam waist (i.e. z=0) can be written as

$$P = \frac{1}{2}E_0^2\sqrt{\frac{\varepsilon}{\mu_0}}\int_0^{\infty}\int_0^{2\pi}\rho\psi_{mn}(x,y,0)\psi_{mn}(x,y,0)^{*}\,d\rho d\phi \quad , \tag{2.73}$$

where $\rho = \sqrt{x^2+y^2}$ is the radial and ϕ is the azimuthal co-ordinate. In the z=0 plane the complex radius given by Eq. (2.39) can be written as

$$R_{z=0} = \sqrt{\rho^2 - d^2} \quad . \tag{2.74}$$

Thus it can be seen from Eq. (2.74) that, inside the focal circle ($\rho^2<d^2$) the radius is complex and outside the focal circle ($\rho^2>d^2$) it is real. This implies that the integration needs to be performed in two separate regions, a region inside the focal circle and a region outside the focal circle. As the argument of the spherical Bessel functions $j_0(kR)$ and $j_1(kR)$ is kR it is useful to use the substitution of variables

$$\begin{aligned} u &= kR_{z=0} = i\sqrt{p^2 - \frac{kp\rho^2}{z_0}} \quad ;\text{for } \rho^2 < z_0^{\,2} \\ v &= kR_{z=0} = -i\sqrt{p^2 - \frac{kp\rho^2}{z_0}} \quad ;\text{for } \rho^2 > z_0^{\,2} \\ \frac{\partial u}{\partial \rho} &= \frac{kp\rho}{uz_0} \\ \frac{\partial v}{\partial \rho} &= \frac{kp\rho}{vz_0} \end{aligned} \quad , \tag{2.75}$$

where $p=kz_0$. It is therefore also possible to calculate the time averaged beam power, for validation purposes, in the paraxial limit in an easy manner. Since in the integral Eq. (2.74) the product $\rho d\rho$ is used, it is useful to write

$$\rho d\rho = \frac{uz_0 \partial u}{kp} \quad ; \text{ for } \rho^2 < z_0^2$$

and

$$\rho d\rho = \frac{vz_0 \partial v}{kp} \quad ; \text{ for } \rho^2 > z_0^2 \quad , \tag{2.76}$$

where in Eqs. (2.75) and (2.76) the Rayleigh range is denoted by z_0, instead of d, in order to avoid confusion between d denoting the Rayleigh range and d denoting the derivative. In order to validate the beam power due to $\psi_{00}(x,y,z)$ and $\psi_{01}(x,y,z)$ in the paraxial limit, it is useful to normalise the irradiance of these beams to unity at $x=y=z=0$. These normalisation constants are given by Eq. (2.58) for $I_{0,00}$ and Eq. (2.59) for $I_{0,01}$. The integral in Eq. (2.73) can then be written, integrating the two regions separately as

$$P = \frac{1}{2} E_0^2 \sqrt{\frac{\varepsilon}{\mu_0}} \left[\int_{ip}^{0} \int_{0}^{2\pi} \psi_{mn}(x,y,0) \psi_{mn}^{*}(x,y) u du d\phi + \int_{0}^{\infty} \int_{0}^{2\pi} \psi_{mn}(x,y,0) \psi_{mn}^{*}(x,y) v dv d\phi \right] \quad . \tag{2.77}$$

The lower limit of the integration with respect to the radial integral was calculated by substituting $\rho=0$ into the expression for u. On the focal circle, $\rho^2=d^2$, the upper limit of integration $u=0$. Since the irradiances due to $\psi_{00}(x,y,z)$ and $\psi_{01}(x,y,z)$ are singularity-free, it is implied that these functions are continuous across the boundary at $\rho^2=d^2$. Therefore the upper limit of the first integral is equal to the lower limit of the second integral. Evaluating the integrals given by Eq. (2.77) for the lowest order, $\psi_{00}(x,y,z)$ leads to an infinite beam power, since the second integral in Eq. (2.77) is equal to infinity. It was Lekner [6] who pointed this out. He also stated that the second integral given by Eq. (2.77) is infinite for any wavefunction given by $\psi_{mn}(x,y,z)$, with even m-n, and that the integral is finite for odd m-n. The ratio of the beam power due to $\psi_{01}(x,y,z)$ and $I_{0,01}$ is

$$\frac{P}{I_{0,01}} = \frac{\pi p d}{2k} \left[\frac{e^{-2p}(2-4p^2) - e^{-4p}(1+2p) - 1 + 2p}{e^{-2p}\left[e^{-p}(1+p) + e^{p}(1-p)\right]^2} \right] \quad . \tag{2.78}$$

In order to calculate the normalised beam power in the paraxial limit, again $\frac{P}{I_{0,01}}$ has to be calculated in the limit as p tends to infinity. It is found that

$$\lim_{p\to\infty}\left(\frac{P}{I_{0,01}}\right)=\frac{\pi d}{k} \quad . \tag{2.79}$$

In the case of a Hermite-Gaussian beam, I_0 at the beam waist, i.e at the origin (x=y=z=0), is obtained by substituting ρ=0 and w_0=$w(z)$ into Eq. (1.73). Thus for a Hemite-Gaussian beam I_0 at the beam waist is given by

$$I_0=\frac{1}{2}E_0^2\sqrt{\frac{\varepsilon}{\mu_0}} \quad . \tag{2.80}$$

Dividing the power P for a Hermite-Gaussian beam, given by Eq. (1.74.b) by I_0 given by Eq. (2.80) leads to the following ratio

$$\frac{P}{I_0}=\frac{1}{2}\pi w_0^2 \, . \tag{2.81}$$

By substituting Eq. (1.77) into Eq. (2.79), it can be seen that these equations are identical. Therefore the result presented in Eq. (2.78) is correct, even though Sheppard [9] states that $\psi_{00}(x,y,z)$ could be used, if the integral is performed over a finite range for ρ. However, in this research preference is given to $\psi_{01}(x,y,z)$, since it can be shown without making any approximations that $\psi_{01}(x,y,z)$ has all the required properties for describing a Gaussian beam.

2.5. Conclusion

In this chapter a set of solutions to the scalar Helmholtz equation has been derived. This set of solutions resembles, as can be seen graphically by comparing Figs.(2.36.-2.39) with Figs. 1.8.a) and 1.9.a), the Laguerre-Gaussian functions [5]. The reason for this resemblance was described by Landesman [10], even though he only considered the incoming wave, due to the fact that the spheroidal-Gaussian mode solutions are circularly symmetric. Furthermore it is shown therein that there is an obvious correspondence between the Laguerre (0, n) orders and the spheroidal (n, n) orders, and the Laguerre (0, 1) and (0, 2) orders are identical to the Hermite (0, 1) and (1, 1) orders respectively. The lowest order solutions $\psi_{00}(x,y,z)$ and $\psi_{01}(x,y,z)$ tend to a paraxial Gaussian beam in the paraxial limit. In the far-field limit there is a problem with the irradiance profile of the $\psi_{00}(x,y,z)$, since the irradiance profile for very small kd does not drop to zero at $\alpha = \pm\frac{\pi}{2}$ on the Gaussian reference sphere. For large values of kd, the irradiance profile drops of asymptotically to zero, due to the exponential decay. The far-field irradiance profile of $\psi_{01}(x,y,z)$ is slightly different than expected, but as will be demonstrated in chapter 4, where the vector solutions are considered, it turns out to be acceptable. At the beam waist, for small values of kd a standing wave is produced due to the interference of the incoming and outgoing wave. Since the scalar wavefunction $\psi_{01}(x,y,z)$ satisfies all the requirements for representing a Gaussian beam mathematically, the vector solution based on this function will be used in chapter 5 to calculate the forces exerted on a micro particle.

References

[1] Sheppard, C. J. R., Saghafi, S., (1998), Electromagnetic Gaussian beams beyond the paraxial approximation. *J. Opt. Soc. Am.* **16,** *No.* **6,** 1381-1386

[2] Spiegel M. R.,(1959), Vector analysis and an introduction to tensor analysis, Schaum's outlines, McGraw-Hill

[3] Boas, M. L.,(1983), Mathematical methods in the physical sciences, 2nd edition, John Wiley & Sons

[4] Landesman, B. T. & Barrett, H. H., (1988), Gaussian amplitude functions that are exact solutions to the scalar Helmholtz equation. *J. Opt. Soc. Am. A* **5,** 1610-1619.

[5] Ulanowski, Z., Ludlow, I. K., (2000), Scalar fields of nonparaxial Gaussian beams, *Optics letters.* 25, No. **24**. 1792-1794

[6] Lekner, J., (2001), TM, TE and 'TEM' beam modes: exact solutions and their problems, *J. Opt. A*: *Pure Appl. Opt.* **3**. 407-412

[7] Abramowitz, M., Stegun, I. A., (1970), Handbook of mathematical functions, Dover Publications.

[8] Berkey D. D., (1988), Calculus, second edition, Saunders College Publishing

[9] Sheppard, C. J. R., (2002), Comments on TM, TE and 'TEM' beam modes: exact solutions and their problems, *J. Opt. A*: *Pure Appl. Opt.* **4**. 217

[10] Landesman, B. T.,(1996), Comparison of paraxial and non paraxial Spheroidal-Gaussian modes with Hermite-Gaussian and Laguerre-Gaussian. *SPIE* **2870,** 163-172.

3. The solutions to the vector Helmholtz equation

3.1. Introduction

In the last chapter, an exact scalar solution to the scalar Helmholtz equation was derived. However, it is known from chapter 1, that the electric field intensity $\mathbf{E}(\mathbf{r},t)$, the magnetic field intensity $\mathbf{H}(\mathbf{r},t)$ and the Poynting vector $\mathbf{S}(\mathbf{r},t)$ are vector quantities and thus a solution to the scalar Helmholtz equation is not sufficient in order to describe the E.M. field of a Gaussian beam. Additionally any E.M. field has a state of polarisation. In order to incorporate the polarisation property and to accurately calculate the forces exerted on a micro particle by a focused laser beam, it is necessary to derive a vector description of the E.M. field. For this E.M. field to be physical, the four Maxwell's equations and the wave equation need to be satisfied. For reasons of simplicity, as in the scalar case, a time harmonic dependence $e^{-i\omega t}$ is assumed. It is therefore possible to consider the time independent part of the wave equation, i.e. the Helmholtz equation first. The aim of this and the next chapter is to seek vector solutions, based on the scalar solutions presented in chapter 2, which

a) describe a Gaussian beam.
b) are exact solutions to the vector wave equation.
c) satisfy the four Maxwell's equations.
d) propagate along the positive z axis.
e) have the correct behaviour in the paraxial limit.
f) have the correct far-field behaviour.
g) have finite beam power.

3.1.1. The vector Helmholtz equation

The vector Helmholtz equation has the same form as the scalar Helmholtz equation. The only difference is, that in the vector case the operator $(\nabla^2 + k^2)$ operates on a vector, where in the scalar case it operated on a scalar. Therefore the vector Helmholtz equation is given by [1]

$$\nabla^2\mathbf{F}(\mathbf{r},t)+k^2\mathbf{F}(\mathbf{r},t)=\nabla(\nabla\bullet\mathbf{F}(\mathbf{r},t))-\nabla\times(\nabla\times\mathbf{F}(\mathbf{r},t))+k^2\mathbf{F}(\mathbf{r},t)=0. \qquad (3.1)$$

The vector solution $\mathbf{F}(\mathbf{r},t)$ of this equation can always be separated into a longitudinal and a transverse part. Furthermore, in the non-relativistic case, the following five equations,

$$\begin{aligned}
&\mathbf{F}(\mathbf{r},t)=\mathbf{F}_l(\mathbf{r},t)+\mathbf{F}_t(\mathbf{r},t)\\
&\mathbf{F}_l(\mathbf{r},t)=\nabla\Phi(\mathbf{r},t)\\
&\mathbf{F}_t(\mathbf{r},t)=\nabla\times\mathbf{A}(\mathbf{r},t)\\
&\nabla\times\mathbf{F}_l(\mathbf{r},t)=0\\
&\nabla\bullet\mathbf{F}_t(\mathbf{r},t)=0
\end{aligned} \tag{3.2}$$

hold, where $\Phi(\mathbf{r},t)$ is the *scalar potential* and $\mathbf{A}(\mathbf{r},t)$ is the *vector potential*. These potentials were already briefly discussed in section 1.11.1.. Even though the vector potential $\mathbf{A}(\mathbf{r},t)$ has a longitudinal part $\mathbf{A}_l(\mathbf{r},t)$ and transverse part, $\mathbf{A}_t(\mathbf{r},t)$, only the transverse part of $\mathbf{A}(\mathbf{r},t)$ has a physical meaning, since by taking the curl of $\mathbf{A}(\mathbf{r},t)$ in order to obtain $\mathbf{F}(\mathbf{r},t)$ the longitudinal part $\mathbf{A}_l(\mathbf{r},t)$ is eliminated. It is therefore legitimate to state that $\mathbf{F}(\mathbf{r},t)$ has zero divergence, since $\nabla\bullet(\nabla\times\mathbf{A})=0$.

3.2. The vector solution

The solution of the vector Helmholtz equation, which will be derived in this chapter, is based on the superposition of the incoming and outgoing beam, i.e. $\psi_{mn}(x,y,z)$, which, as has been demonstrated in chapter 2, is a solution to the scalar Helmholtz equation.

3.2.1. How to construct a vector function from a scalar function

There are various ways in which a vector solution can be constructed from a scalar solution. One of these ways was demonstrated in section 1.11.1.1.. Another approach, which is based on Whittaker potentials, was recently used in a similar context by Volyar [2]. However, in this research a slightly different approach has been chosen. Again, like in the other two derivations, a constant guiding vector (polarisation vector) is selected, but this time, the constant guiding vector is multiplied with the scalar function $\psi_{mn}(x,y,z)$, in order to polarise this function. Then the curl of this product is computed and the result multiplied by $\frac{1}{k}$, where $k=\omega\sqrt{\varepsilon\mu_0}$, to give a dimensionless vector function $\mathbf{M}_{mn}(\mathbf{r},t)$. The curl of $\mathbf{M}_{mn}(\mathbf{r},t)$ is calculated and the result multiplied by $\frac{1}{k}$ in order to obtain a second

dimensionless vector function $\mathbf{N}_{mn}(\mathbf{r},t)$. However, by using this approach, the obtained vector functions cannot be directly identified as the electric and magnetic field vectors. Nevertheless this derivation leads to two vector functions, which are related to the electric and magnetic field vectors. The E.M. field vectors are then written as a linear superposition of the $\mathbf{M}_{mn}(\mathbf{r},t)$ and $\mathbf{N}_{mn}(\mathbf{r},t)$ functions. The motivation to use this approach is that the E.M. field can be constructed in such a way as to meet all the criteria, such as for example the E.M. field being correctly polarised in the far-field, imposed in this particular problem. The mathematical background of this method is described for example in Bohren and Huffman [3].

The physical realisable time-harmonic E.M. field in a linear, isotropic, homogeneous medium, must satisfy the wave equation (Eq. (1.12) and Eq. (1.13))
and be divergence free in accordance with Eqs. (1.5) and (1.6). It can also be seen from Eqs. (1.7) and (1.8) that there exists the following interdependence between $\mathbf{E}(\mathbf{r},t)$ and $\mathbf{H}(\mathbf{r},t)$:

$$\begin{aligned} \nabla \times \mathbf{E}(\mathbf{r},t) &= i\omega\mu_0 \mathbf{H}(\mathbf{r},t), \\ \nabla \times \mathbf{H}(\mathbf{r},t) &= -i\omega\varepsilon \mathbf{E}(\mathbf{r},t). \end{aligned} \tag{3.3}$$

According to Bohren and Huffman [3] the $\mathbf{M}_{mn}(\mathbf{r},t)$ function can be constructed from any *scalar* function $\psi_{mn}(x,y,z)$, which satisfies the scalar Helmholtz equation, and an arbitrary *constant* vector **c**. It has been demonstrated in section 1.11.1.1. that it is convenient to polarise the scalar function $\psi_{mn}(x,y,z)$ along the x or the y axis. However in order to increase the amount of choice, three different $\mathbf{M}_{mn}(\mathbf{r},t)$ functions are constructed, by using three constant guiding vectors. According to Ludlow [4] (see Appendix) the constant guiding vector is given by

$$\mathbf{c} = c_x\hat{\mathbf{i}} + c_y\hat{\mathbf{j}} + c_z\hat{\mathbf{k}} \quad . \tag{3.4}$$

A natural choice is to polarise the scalar function along the x, y and z axis. Thus the first constant guiding vector is obtained by substituting c_x=1 and c_y=c_z=0 into Eq. (3.4). Thus

$$\mathbf{c}^1 = \begin{pmatrix} 1 \\ 0 \\ 0 \end{pmatrix}. \tag{3.5}$$

The second constant guiding vector is obtained by substituting c_y=1 and c_x=c_z=0 into Eq. (3.4). Thus

$$\mathbf{c}^2 = \begin{pmatrix} 0 \\ 1 \\ 0 \end{pmatrix}. \tag{3.6}$$

The third constant guiding vector is obtained by substituting c_z=1 and c_x=c_y=0 into Eq. (3.4). Thus

$$\mathbf{c}^3 = \begin{pmatrix} 0 \\ 0 \\ 1 \end{pmatrix}. \tag{3.7}$$

Theoretically it would have been possible to use other values for c_x, c_y and c_z, but it is unnecessary because any other constant guiding vector can be represented as a linear superposition of the vectors given in Eqs.(3.5)-(3.7). In accordance with Bohren and Huffman [3] $\mathbf{M}_{mn}^{\gamma}(\mathbf{r},t)$, where γ=1,2,3, can be written at time t=0 as

$$\mathbf{M}_{mn}^{1}(x,y,z) = \frac{\nabla \times \left(\mathbf{c}^1 \psi_{mn}(x,y,z)\right)}{k}, \tag{3.8.a}$$

$$\mathbf{M}_{mn}^{2}(x,y,z) = \frac{\nabla \times \left(\mathbf{c}^2 \psi_{mn}(x,y,z)\right)}{k} \tag{3.8.b}$$

and

$$\mathbf{M}_{mn}^{3}(x,y,z) = \frac{\nabla \times \left(\mathbf{c}^3 \psi_{mn}(x,y,z)\right)}{k}, \tag{3.8.c}$$

It is useful at this point to remember that

$$\nabla \times \mathbf{V}(x,y,z) = \left(\frac{\partial V_z(x,y,z)}{\partial y} \frac{\partial V_y(x,y,z)}{\partial z}\right)\hat{\mathbf{i}} + \left(\frac{\partial V_x(x,y,z)}{\partial z} \frac{\partial V_z(x,y,z)}{\partial x}\right)\hat{\mathbf{j}} + \left(\frac{\partial V_y(x,y,z)}{\partial x} \frac{\partial V_x(x,y,z)}{\partial y}\right)\hat{\mathbf{k}}, \tag{3.9}$$

where $\mathbf{V}(x,y,z)$ is an arbitrary vector in Cartesian coordinates. Since the scalar function $\psi_{mn}(x,y,z)$ given by Eq.(2.42) contains the spherical Bessel functions and the associated Legendre functions, it is useful to be aware of their recurrence relations and derivatives.

The differentiation formulae for the spherical Bessel functions are [5]

$$\left(\frac{1}{x}\frac{d}{dx}\right)^l\left[x^{n+1}j_n(x)\right]=x^{n-l+1}j_{n-l}(x)$$

$$\left(\frac{1}{x}\frac{d}{dx}\right)^l\left[\frac{j_n(x)}{x^n}\right]=(-1)^l x^{-n-l}j_{n+l}(x), \tag{3.10}$$

$$(n=0,\pm1,\pm2,\ldots)$$

$$(l=1,2,3,\ldots)$$

with the recurrence relations

$$j_{n-1}(x)+j_{n+1}(x)=\frac{(2n+1)}{x}j_n(x)$$

$$nj_{n-1}(x)-(n+1)j_{n+1}(x)=(2n+1)\frac{dj_n(x)}{dx}$$

$$\frac{n+1}{x}j_n(x)+\frac{dj_n(x)}{dx}=j_{n-1}(x) \tag{3.11}$$

$$\frac{n}{x}j_n(x)-\frac{dj_n(x)}{dx}=j_{n+1}(x)$$

$$(n=0,\pm1,\pm2,\ldots)$$

Thus in order to calculate the derivatives of the spherical Bessel function, which are needed in order to calculate the curl of the product of the constant vector and the scalar function, it is sensible to rearrange the 3rd and 4th recurrence relation to read

$$\frac{dj_n(x)}{dx}=j_{n-1}(x)-\frac{n+1}{x}j_n(x)$$

$$\frac{dj_n(x)}{dx}=\frac{n}{x}j_n(x)-j_{n+1}(x) \tag{3.12}$$

Similarly the differentiation formula for the associated Legendre functions is [5]:

$$\frac{dP_n^m(s)}{ds} = \frac{nsP_n^m(s) - (m+n)P_{n-1}^m(s)}{(s^2-1)}$$

or using the recurrence relation $(n-m+1)P_{n+1}^m(s) = (2n+1)sP_n^m(s) - (n+m)P_{n-1}^m(s)$

$$\frac{dP_n^m(s)}{ds} = \frac{(n+1)sP_n^m(s) - (n-m+1)P_{n+1}^m(s)}{1-s^2} \quad . \tag{3.13}$$

$(n = 0,\pm1,\pm2,...)$
$(m = 1,2,3,...)$

In order to get a deeper insight into the relationships between the various orders of the spherical Bessel functions and their derivatives it is convenient to consider the formulae for the spherical Bessel functions (Table (2.1)) and the following derivatives of the spherical Bessel functions for orders n=0,1,2.

n	$\frac{dj_n(x)}{dx}$
0	$\frac{dj_0(x)}{dx} = -j_1(x)$
1	$\frac{dj_1(x)}{dx} = -j_2(x) + \frac{j_1(x)}{x} = j_0(x) - \frac{2}{x}j_1(x)$
2	$\frac{dj_2(x)}{dx} = \frac{1}{x}(-3j_2(x) + j_0(x) - \cos x) = j_1(x) - \frac{3}{x}j_2(x) = \frac{2}{x}j_2(x) - j_3(x)$

Table 3.1. The derivatives for orders n=0,1,2 of the spherical Bessel functions

Similarly, it is convenient to consider the formulae for the associated Legendre functions (Table (2.2)) and the following derivatives of the associated Legendre functions for orders n=0,1,2. and m=0,1.

n \ m	0	1
0	$\frac{dP_0^0(s)}{ds}=0$	-
1	$\frac{dP_1^0(s)}{ds}=1$	$\frac{dP_1^1(s)}{ds}=\frac{-s}{\sqrt{1-s^2}}$
2	$\frac{dP_2^0(s)}{ds}=3s$	$\frac{dP_2^1(s)}{ds}=3\sqrt{1-s^2}\left(1-\frac{s^2}{(1-s^2)}\right)$

Table 3.2. The derivatives for orders n=0,1,2 and m=0,1 of the associated Legendre functions.

From the three $\mathbf{M}_{mn}^{r}(\mathbf{r},t)$ functions (Eqs.(3.8.a),(3.8.b) and (3.8.c)) it is now possible in accordance with Bohren and Huffman [3] to write another three vector function $\mathbf{N}_{mn}^{r}(\mathbf{r},t)$. These functions can be written at time t=0 as

$$\mathbf{N}_{mn}^{1}(x,y,z)=\frac{\nabla\times\mathbf{M}_{mn}^{1}(x,y,z)}{k} \quad , \tag{3.14.a}$$

$$\mathbf{N}_{mn}^{2}(x,y,z)=\frac{\nabla\times\mathbf{M}_{mn}^{2}(x,y,z)}{k} \tag{3.14.b}$$

and

$$\mathbf{N}_{mn}^{3}(x,y,z)=\frac{\nabla\times\mathbf{M}_{mn}^{3}(x,y,z)}{k} \quad . \tag{3.14.c}$$

In order to calculate the $\mathbf{N}_{mn}^{r}(x,y,z)$ functions explicitly, it is necessary to be aware of the formulae for the second derivatives of the spherical Bessel functions

$$\frac{d^2j_n(x)}{dx^2}=\frac{n(n-1)}{x^2}j_n(x)-\frac{2n+1}{x}j_{n+1}(x)+j_{n+2}(x) \tag{3.15}$$

and the associated Legendre functions

$$\frac{d^2P_n^m(s)}{ds^2}=\frac{n\left[s^2(n-1)-1\right]P_n^m(s)-(m+n)\left[s(2n-3)P_{n-1}^m(s)-(m+n-1)P_{n-2}^m(s)\right]}{\left(s^2-1\right)^2}$$

or

$$\frac{d^2P_n^m(s)}{ds^2} = \frac{(n+1)\left[1+(n+2)s^2\right]P_n^m(s)-(n-m+1)(2n+5)sP_{n+1}^m(s)+(n-m+1)(n-m+2)P_{n+2}^m(s)}{\left(1-s^2\right)^2} \quad . \tag{3.16}$$

The solutions of Eq. (3.15) for orders n=0,1,2 are given in table 3.3..

n	$\frac{d^2 j_n(x)}{dx^2}$
0	$\frac{d^2 j_0(x)}{dx^2} = -\frac{j_1(x)}{x} + j_2(x) = \frac{2}{x} j_1(x) - j_0(x)$
1	$\frac{d^2 j_1(x)}{dx^2} = -\frac{3}{x} j_2(x) + j_3(x)$
2	$\frac{d^2 j_2(x)}{dx^2} = \frac{2}{x^2} j_2(x) - \frac{5}{x} j_3(x) + j_4(x)$

Table 3.3. The second derivatives for orders n=0,1,2 of the spherical Bessel functions

The solutions of Eq. (3.16) for orders n=0,1,2. and m=0,1 are given in table 3.4..

n \ m	0	1
0	$\frac{d^2 P_0^0(s)}{ds^2} = 0$	-
1	$\frac{d^2 P_1^0(s)}{ds^2} = 0$	$\frac{d^2 P_1^1(s)}{ds^2} = -\frac{\sqrt{1-s^2}}{\left(s^2-1\right)^2}$
2	$\frac{d^2 P_2^0(s)}{ds^2} = 3$	$\frac{d^2 P_2^1(s)}{ds^2} = \frac{3s\sqrt{1-s^2}\left(2s^2-3\right)}{\left(s^2-1\right)^2}$

Table 3.4. The second derivatives for orders n=0,1,2 and m=0,1 of the associated Legendre functions.

Since the divergence of the curl of a vector is zero, it follows that the divergences of $\mathbf{M}_{mn}^r(\mathbf{r},t)$ and $\mathbf{N}_{mn}^r(\mathbf{r},t)$ are zero. It is further mentioned by Bohren and Huffman [3] that

$$\nabla \times \mathbf{N}_{nm}^r(\mathbf{r},t) = k\mathbf{M}_{nm}^r(\mathbf{r},t)$$

or

$$\nabla \times \mathbf{N}^{r}_{nm}(\mathbf{r},t) - k\mathbf{M}^{r}_{nm}(\mathbf{r},t) = 0\,. \tag{3.17}$$

The derived $\mathbf{M}^{r}_{mn}(\mathbf{r},t)$ and $\mathbf{N}^{r}_{mn}(\mathbf{r},t)$ vector functions have all the required properties of an E.M. field. However, it has to be noted that $\mathbf{M}^{r}_{mn}(\mathbf{r},t)$ and $\mathbf{N}^{r}_{mn}(\mathbf{r},t)$ are not equivalent to $\mathbf{E}(\mathbf{r},t)$ and $\mathbf{H}(\mathbf{r},t)$, but are related to them. The $\mathbf{E}(\mathbf{r},t)$ and $\mathbf{H}(\mathbf{r},t)$ vectors can be constructed, as mentioned earlier, by a linear superposition of the $\mathbf{M}^{r}_{mn}(\mathbf{r},t)$ and $\mathbf{N}^{r}_{mn}(\mathbf{r},t)$ vectors, since

$$\nabla \bullet (\mathbf{A}+\mathbf{B}) = \nabla \bullet \mathbf{A} + \nabla \bullet \mathbf{B}$$

and

$$\nabla \times (\mathbf{A}+\mathbf{B}) = \nabla \times \mathbf{A} + \nabla \times \mathbf{B}\,,$$

where here **A** and **B** are both arbitrary differentiable vector functions.

3.2.2. Constructing the $\mathbf{M}^{r}_{mn}(x,y,z)$ and $\mathbf{N}^{r}_{mn}(x,y,z)$ functions due to $\psi_{mn}(x,y,z)$

In this section, the vector $\mathbf{M}^{r}_{mn}(x,y,z)$ and $\mathbf{N}^{r}_{mn}(x,y,z)$ functions, in Cartesian coordinates, based on the scalar function $\psi_{00}(x,y,z)$, $\psi_{01}(x,y,z)$ and $\psi_{11}(x,y,z)$ are derived.

3.2.2.1. Example 1: Constructing the $\mathbf{M}^{r}_{00}(x,y,z)$ and $\mathbf{N}^{r}_{00}(x,y,z)$ functions due to $\psi_{00}(x,y,z)$

With the help from tables (2.1.) and (2.2.) Eq. (2.43) can be written as

$$\psi_{00}(x,y,z) = e^{-kd}\, j_0(kR)\,. \tag{3.18}$$

From the derivations given in section 3.2.1. it follows that by multiplying Eq. (3.18) with Eqs.(3.5), (3.6) and (3.7) respectively that

$$\psi_{00}(x,y,z)\mathbf{c}^1 = \begin{pmatrix} e^{-kd} j_0(kR) \\ 0 \\ 0 \end{pmatrix} \quad , \tag{3.19.a}$$

$$\psi_{00}(x,y,z)\mathbf{c}^2 = \begin{pmatrix} 0 \\ e^{-kd} j_0(kR) \\ 0 \end{pmatrix} \tag{3.19.b}$$

and

$$\psi_{00}(x,y,z)\mathbf{c}^3 = \begin{pmatrix} 0 \\ 0 \\ e^{-kd} j_0(kR) \end{pmatrix} \quad . \tag{3.19.c}$$

By taking the curl of the vector function given by Eqs. (3.19.a), it can be seen in accordance with Eq.(3.9), that the only non-zero terms obtained from Eq.(3.9) are:

$$\frac{\partial V_x(x,y,z)}{\partial z}\hat{\mathbf{j}} \text{ and} - \frac{\partial V_x(x,y,z)}{\partial y}\hat{\mathbf{k}} \quad , \tag{3.20}$$

where here $V_x(x,y,z)=e^{-kd}j_0(kR)$. So from Eq. (3.12) it can be seen that

$$\begin{aligned} \frac{\partial V_x(x,y,z)}{\partial z} &= e^{-kd}\frac{d}{dR}j_0(kR)k\frac{dR}{dz} = \frac{-ke^{-kd}(z-id)}{R}j_1(kR) \\ -\frac{\partial V_x(x,y,z)}{\partial y} &= e^{-kd}\frac{d}{dy}j_0(kR)k\frac{dR}{dy} = \frac{ke^{-kd}y}{R}j_1(kR) \end{aligned} \quad , \tag{3.21}$$

since from table (3.1.) $\frac{dj_0(kR)}{d(kR)} = -j_1(kR)$.

Additionally, as k is a constant $\frac{d(kR)}{dz} = k\frac{dR}{dz}$, $\frac{d(kR)}{dy} = k\frac{dR}{dy}$ and $\frac{d(kR)}{dx} = k\frac{dR}{dx}$.

Thus taking the curl of Eq. (3.19.a) and multiplying the result by $\frac{1}{k}$ leads to

$$\mathbf{M}^1_{00}(x,y,z) = \frac{e^{-kd}j_1(kR)}{R}\begin{pmatrix} 0 \\ -(z-id) \\ y \end{pmatrix} \quad . \tag{3.22.a}$$

Similarly by taking the curl of Eqs. (3.19.b) and (3.19.c) and multiplying the results by $\frac{1}{k}$ leads to

$$\mathbf{M}_{00}^{2}(x,y,z)=\frac{e^{-kd}j_1(kR)}{R}\begin{pmatrix}(z-id)\\0\\-x\end{pmatrix} \tag{3.22.b}$$

and

$$\mathbf{M}_{00}^{3}(x,y,z)=\frac{e^{-kd}j_1(kR)}{R}\begin{pmatrix}-y\\x\\0\end{pmatrix} \quad . \tag{3.22.c}$$

By taking the curl of Eq. (3.22.a), it can be seen from Eq. (3.9), that since the first component of the vector function in Eq. (3.22.a) is zero, only four partial derivatives of the curl of $\mathbf{M}_{00}^{1}(x,y,z)$ are non zero. With the help of Eq. (3.20) these non zero partial derivatives can be written as

$$\frac{\partial \mathbf{M}_{00}^{1}(x,y,z)_z}{\partial y}\hat{\mathbf{i}}=-\frac{\partial^2 V_x(x,y,z)}{\partial y^2}\hat{\mathbf{i}},\quad -\frac{\partial \mathbf{M}_{00}^{1}(x,y,z)_y}{\partial z}\hat{\mathbf{i}}=-\frac{\partial^2 V_x(x,y,z)}{\partial z^2}\hat{\mathbf{i}},$$
$$-\frac{\mathbf{M}_{00}^{1}(x,y,z)_z}{\partial x}\hat{\mathbf{j}}=\frac{\partial^2 V_x(x,y,z)}{\partial x\partial y}\hat{\mathbf{j}},$$
$$\frac{\partial \mathbf{M}_{00}^{1}(x,y,z)_y}{\partial x}\hat{\mathbf{k}}=\frac{\partial^2 V_x(x,y,z)}{\partial x\partial z}\hat{\mathbf{k}}$$

Thus taking the curl of Eq. (3.22.a) and multiplying the result by $\frac{1}{k}$ leads to

$$\mathbf{N}_{00}^{1}(x,y,z)=\frac{e^{-kd}j_2(kR)}{R^2}\begin{pmatrix}2R\frac{j_1(kR)}{kj_2(kR)}-(R^2-x^2)\\xy\\x(z-id)\end{pmatrix} \quad . \tag{3.23.a}$$

Similarly by taking the curl of Eqs. (3.22.b) and (3.22.c) and multiplying the results by $\frac{1}{k}$ the following functions

$$\mathbf{N}_{00}^{2}(x,y,z)=\frac{e^{-kd}j_2(kR)}{R^2}\begin{pmatrix} xy \\ 2R\dfrac{j_1(kR)}{kj_2(kR)}-(R^2-y^2) \\ y(z-id)\end{pmatrix} \tag{3.23.b}$$

and

$$\mathbf{N}_{00}^{3}(x,y,z)=\frac{e^{-kd}j_2(kR)}{R^2}\begin{pmatrix} x(z-id) \\ y(z-id) \\ 2R\dfrac{j_1(kR)}{kj_2(kR)}-(x^2+y^2)\end{pmatrix} \tag{3.23.c}$$

are obtained. As the E.M. wave is propagating along the *z*-axis in Cartesian coordinates, it can be assumed, that a sensible superposition for the $\mathbf{E}(\mathbf{r},t)$ and $\mathbf{H}(\mathbf{r},t)$ fields will only involve the transverse $\mathbf{M}_{mn}^{1}(\mathbf{r},t)$, $\mathbf{M}_{mn}^{2}(\mathbf{r},t)$, $\mathbf{N}_{mn}^{1}(\mathbf{r},t)$and $\mathbf{N}_{mn}^{2}(\mathbf{r},t)$ functions, i.e. the $\mathbf{M}_{mn}^{\gamma}(\mathbf{r},t)$ and $\mathbf{N}_{mn}^{\gamma}(\mathbf{r},t)$ functions based on the $\mathbf{c}^1$ and $\mathbf{c}^2$ guiding vectors, nevertheless for completeness the $\mathbf{M}_{mn}^{3}(\mathbf{r},t)$ and $\mathbf{N}_{mn}^{3}(\mathbf{r},t)$ functions based on the $\mathbf{c}^3$ guiding vector are given as well. An additional indication that the $\mathbf{M}_{00}^{3}(\mathbf{r},t)$ and $\mathbf{N}_{00}^{3}(\mathbf{r},t)$ functions are not likely candidates for making up the E.M. field is that all the three components of the $\mathbf{M}_{00}^{3}(\mathbf{r},t)$ function are zero at the origin (see Eq. (3.22.c)).

3.2.2.2. Example 2: Constructing the $\mathbf{M}^{\gamma}_{01}(x,y,z)$ and $\mathbf{N}^{\gamma}_{01}(x,y,z)$ functions due to $\psi_{01}(x,y,z)$

The same derivation can now be applied to $\psi_{01}(x,y,z)$. With the help from tables (2.1.) and (2.2.) Eq. (2.44) can be written as

$$\psi_{01}(x,y,z)=e^{-kd}j_1(kR)\left(\frac{z-id}{R}\right), \tag{3.24}$$

leading to the following $\mathbf{M}_{01}^{\gamma}(x,y,z)$ functions:

$$\mathbf{M}_{01}^{1}(x,y,z)=\frac{e^{-kd}j_2(kR)}{R^2}\begin{pmatrix} 0 \\ \dfrac{Rj_1(kR)}{kj_2(kR)}-(z-id)^2 \\ y(z-id)\end{pmatrix}, \tag{3.25.a}$$

$$\mathbf{M}_{01}^{2}(x,y,z)=\frac{e^{-kd}\,j_2(kR)}{R^2}\begin{pmatrix}-\dfrac{Rj_1(kR)}{kj_2(kR)}+(z-id)^2\\0\\-x(z-id)\end{pmatrix} \tag{3.25.b}$$

and

$$\mathbf{M}_{01}^{3}(x,y,z)=\frac{e^{-kd}\,j_2(kR)(z-id)}{R^2}\begin{pmatrix}-y\\x\\0\end{pmatrix}\quad . \tag{3.25.c}$$

By taking the curl of the $\mathbf{M}_{01}^{1}(x,y,z)$, $\mathbf{M}_{01}^{2}(x,y,z)$ and $\mathbf{M}_{01}^{3}(x,y,z)$ functions given by Eqs.(3.25.a), (3.25.b) and (3.25.c) and multiplying the results by $\frac{1}{k}$, the following $\mathbf{N}_{01}^{r}(x,y,z)$ functions

$$\mathbf{N}_{01}^{1}(x,y,z)=\frac{e^{-kd}\,j_2(kR)}{kR^4}\begin{pmatrix}(z-id)\left[4R^2-(R^2-x^2)\left(5-\dfrac{kRj_1(kR)}{j_2(kR)}\right)\right]\\xy(z-id)\left(5-\dfrac{kRj_1(kR)}{j_2(kR)}\right)\\-x\left(R^2-(z-id)^2\left(5-\dfrac{kRj_1(kR)}{j_2(kR)}\right)\right)\end{pmatrix}\quad , \tag{3.26.a}$$

$$\mathbf{N}_{01}^{2}(x,y,z)=\frac{e^{-kd}\,j_2(kR)}{kR^4}\begin{pmatrix}xy(z-id)\left(5-\dfrac{kRj_1(kR)}{j_2(kR)}\right)\\(z-id)\left[4R^2-(R^2-y^2)\left(5-\dfrac{kRj_1(kR)}{j_2(kR)}\right)\right]\\-y\left(R^2-(z-id)^2\left(5-\dfrac{kRj_1(kR)}{j_2(kR)}\right)\right)\end{pmatrix} \tag{3.26.b}$$

and

$$\mathbf{N}_{01}^{3}(x,y,z)=\frac{e^{-kd}\,j_2(kR)}{kR^4}\begin{pmatrix}-x\left(R^2-(z-id)^2\left(5-\dfrac{kRj_1(kR)}{j_2(kR)}\right)\right)\\-y\left(R^2-(z-id)^2\left(5-\dfrac{kRj_1(kR)}{j_2(kR)}\right)\right)\\(z-id)\left(2R^2-(x^2+y^2)\left(5-\dfrac{kRj_1(kR)}{j_2(kR)}\right)\right)\end{pmatrix} \tag{3.26.c}$$

are obtained. Again it can be seen that the $\mathbf{M}_{01}^{3}(\mathbf{r},t)$ and $\mathbf{N}_{01}^{3}(\mathbf{r},t)$ functions are not likely candidates for making up the E.M. field, since all the three components of the $\mathbf{M}_{01}^{3}(\mathbf{r},t)$ function are zero at the origin (see Eq. (3.25.c)).

3.2.2.3. Example 3: Constructing the $\mathbf{M}^{r}_{11}(x,y,z)$ and $\mathbf{N}_{11}{}^{r}(x,y,z)$ functions due to $\psi_{11}(x,y,z)$

The same derivation can now be applied to $\psi_{11}(x,y,z)$. With the help from tables (2.1.) and (2.2.) and substituting n=m=1 into Eq. (2.42), $\psi_{11}(x,y,z)$ can be written as

$$\psi_{11}(x,y,z)=\frac{e^{-kd}e^{i\phi}}{R}\sqrt{x^2+y^2}\,j_1(kR) \quad , \tag{3.27}$$

where $\phi=\arctan\left(\frac{y}{x}\right)$, leading to the following $\mathbf{M}_{11}^{r}(x,y,z)$ functions:

$$\mathbf{M}_{11}^{1}(x,y,z)=\frac{j_2(kR)e^{-kd}e^{i\phi}}{R^2\sqrt{x^2+y^2}}\begin{pmatrix}0\\-(z-id)(x^2+y^2)\\y(x^2+y^2)-\dfrac{Rj_1(kR)(y+ix)}{kj_2(kR)}\end{pmatrix} \quad , \tag{3.28.a}$$

$$\mathbf{M}_{11}^{2}(x,y,z)=\frac{j_2(kR)e^{-kd}e^{i\phi}}{R^2\sqrt{x^2+y^2}}\begin{pmatrix}(z-id)(x^2+y^2)\\0\\-x(x^2+y^2)+\dfrac{Rj_1(kR)(x-iy)}{kj_2(kR)}\end{pmatrix} \tag{3.28.b}$$

and

$$\mathbf{M}_{11}^{3}(x,y,z)=\frac{j_2(kR)e^{-kd}e^{i\phi}}{R^2\sqrt{x^2+y^2}}\begin{pmatrix}-y(x^2+y^2)+\dfrac{Rj_1(kR)(y+ix)}{kj_2(kR)}\\x(x^2+y^2)-\dfrac{Rj_1(kR)(x-iy)}{kj_2(kR)}\\0\end{pmatrix}. \tag{3.28.c}$$

By taking the curl of the $\mathbf{M}_{11}^{1}(x,y,z)$, $\mathbf{M}_{11}^{2}(x,y,z)$ and $\mathbf{M}_{11}^{3}(x,y,z)$ functions given by Eqs.(3.28.a), (3.28.b) and (3.28.c), and multiplying the results by $\frac{1}{k}$, the following $\mathbf{N}_{11}^{r}(x,y,z)$ functions

$$\mathbf{N}_{11}^{1}(x,y,z)=\frac{j_2(kR)e^{-kd}e^{i\phi}}{kR^4\sqrt{x^2+y^2}}\begin{pmatrix} 2R^2\left(x^2+ixy+2y^2\right)-\left(R^2-x^2\right)\left(x^2+y^2\right)\left(5-\dfrac{kRj_1(kR)}{j_2(kR)}\right) \\ -R^2\left(ix^2+2xy-iy^2\right)+xy\left(x^2+y^2\right)\left(5-\dfrac{kRj_1(kR)}{j_2(kR)}\right) \\ R^2(z-id)(-x+iy)+x(z-id)\left(x^2+y^2\right)\left(5-\dfrac{kRj_1(kR)}{j_2(kR)}\right) \end{pmatrix} \quad , (3.29.a)$$

$$\mathbf{N}_{11}^{2}(x,y,z)=\frac{j_2(kR)e^{-kd}e^{i\phi}}{kR^4\sqrt{x^2+y^2}}\begin{pmatrix} -R^2\left(ix^2+2xy-iy^2\right)+xy\left(x^2+y^2\right)\left(5-\dfrac{kRj_1(kR)}{j_2(kR)}\right) \\ 2R^2\left(2x^2-ixy+y^2\right)-\left(R^2-y^2\right)\left(x^2+y^2\right)\left(5-\dfrac{kRj_1(kR)}{j_2(kR)}\right) \\ R^2(z-id)(-ix-y)+y(z-id)\left(x^2+y^2\right)\left(5-\dfrac{kRj_1(kR)}{j_2(kR)}\right) \end{pmatrix} \quad (3.29.b)$$

and

$$\mathbf{N}_{11}^{3}(x,y,z)=\frac{j_2(kR)e^{-kd}e^{i\phi}}{kR^4\sqrt{x^2+y^2}}\begin{pmatrix} (z-id)\left(-R^2(x-iy)+x\left(x^2+y^2\right)\left(5-\dfrac{kRj_1(kR)}{j_2(kR)}\right)\right) \\ (z-id)\left(-R^2(y+ix)+y\left(x^2+y^2\right)\left(5-\dfrac{kRj_1(kR)}{j_2(kR)}\right)\right) \\ 4R^2\left(x^2+y^2\right)-\left(x^2+y^2\right)^2\left(5-\dfrac{kRj_1(kR)}{j_2(kR)}\right) \end{pmatrix} \quad (3.29.c)$$

are obtained. In the next section it is demonstrated, that these $\mathbf{M}_{mn}^{r}(x,y,z)$ and $\mathbf{N}_{mn}^{r}(x,y,z)$ functions can be easily obtained for any scalar function $\psi_{mn}(x,y,z)$.

3.2.3. Constructing the vector function of arbitrary order *mn*

In the previous section, the $\mathbf{M}_{mn}^{r}(x,y,z)$ and $\mathbf{N}_{mn}^{r}(x,y,z)$ functions were calculated for specific values of m and n. By performing these calculations it was pointed out that

the $\mathbf{M}^{\gamma}_{mn}(x,y,z)$ and $\mathbf{N}^{\gamma}_{mn}(x,y,z)$ consist of a product of spherical Bessel functions and associated Legendre functions and two exponential functions. As the procedure of taking the curl of a vector involves differentiation, it is important to consider Eqs. (3.12), (3.13), (3.15) and (3.16) as well as tables (3.1.), (3.2.), (3.3.) and (3.4.) carefully. From inspection of the $\mathbf{M}^{\gamma}_{mn}(x,y,z)$ and $\mathbf{N}^{\gamma}_{mn}(x,y,z)$ functions in the previous sections it becomes clear that it is possible to find a closed form description for the vector $\mathbf{M}^{\gamma}_{mn}(x,y,z)$ and $\mathbf{N}^{\gamma}_{mn}(x,y,z)$ functions of general order. In order to calculate the $\mathbf{M}^{1}_{mn}(x,y,z)$ function the scalar function given by Eq. (2.42) is multiplied with the guiding vector $\mathbf{c}^1$. This vector function can then be written as

$$\psi_{mn}(x,y,z)\mathbf{c}^1 = \begin{pmatrix} e^{-kd} j_n(kR) P_n^m(s) e^{im\phi} \\ 0 \\ 0 \end{pmatrix} \quad . \tag{3.30}$$

Next the curl of Eq. (3.30) is taken and the result multiplied by $\frac{1}{k}$, remembering that from equation (3.20) the only non-zero terms of Eq. (3.9) are $\frac{\partial V_x(x,y,z)}{\partial z}\hat{\mathbf{j}}$ and $-\frac{\partial V(x,y,z)_x}{\partial y}\hat{\mathbf{k}}$, where here $V_x(x,y,z) = e^{-kd} j_n(kR) P_n^m(s) e^{im\phi}$. Hence

$$\mathbf{M}^{1}_{mn}(x,y,z) = \frac{e^{-kd}e^{im\phi} j_n(kR) P_n^m(s)}{k} \begin{pmatrix} 0 \\ \left(-\frac{n(z-id)R}{x^2+y^2} + \frac{(m+n)R^2 P^m_{n-1}(s)}{P_n^m(s)(x^2+y^2)}\right)\frac{\partial s}{\partial z} + k\left(\frac{n}{kR} - \frac{j_{n+1}(kR)}{j_n(kR)}\right)\frac{\partial R}{\partial z} \\ \left(\frac{n(z-id)R}{x^2+y^2} - \frac{(m+n)R^2 P^m_{n-1}(s)}{P_n^m(s)(x^2+y^2)}\right)\frac{\partial s}{\partial y} - k\left(\frac{n}{kR} - \frac{j_{n+1}(kR)}{j_n(kR)}\right)\frac{\partial R}{\partial y} - \frac{imx}{x^2+y^2} \end{pmatrix}, \tag{3.31}$$

where $P_n^m(s) = P_n^m\left(\frac{z-id}{R}\right)$ as stated earlier. All the derivatives of R, s and $e^{i\phi}$ are given in tables 3.5.-3.8. at the end of this section.

Since the first component of the $\mathbf{M}^{1}_{mn}(x,y,z)$ vector in Eq. (3.31) is zero, only the following four partial derivatives of the curl of $\mathbf{M}^{1}_{mn}(x,y,z)$ are non zero:

$$\frac{\partial \mathbf{M}^1_{mn}(x,y,z)_z}{\partial y}\hat{\mathbf{i}} = -\frac{\partial^2 V_x(x,y,z)}{\partial y^2}\hat{\mathbf{i}},\ -\frac{\partial \mathbf{M}^1_{mn}(x,y,z)_y}{\partial z}\hat{\mathbf{i}} = -\frac{\partial^2 V_x(x,y,z)}{\partial z^2}\hat{\mathbf{i}},$$
$$-\frac{\mathbf{M}^1_{mn}(x,y,z)_z}{\partial x}\hat{\mathbf{j}} = \frac{\partial^2 V_x(x,y,z)}{\partial x \partial y}\hat{\mathbf{j}},$$
$$\frac{\partial \mathbf{M}^1_{mn}(x,y,z)_y}{\partial x}\hat{\mathbf{k}} = \frac{\partial^2 V_x(x,y,z)}{\partial x \partial z}\hat{\mathbf{k}}$$

Thus the $\mathbf{N}^1_{mn}(x,y,z)$ function can be written as

$$\mathbf{N}^1_{mn}(x,y,z) = \frac{e^{-kd}P_n^m(s)j_n(kR)e^{im\phi}}{k^2}\begin{pmatrix} N^1_x \\ N^1_y \\ N^1_z \end{pmatrix} \tag{3.32}$$

where:

$$N^1_x = -\left(\begin{array}{l} \frac{1}{P_n^m(s)}\left(\frac{\partial^2 P_n^m(s)}{\partial y^2}+\frac{\partial^2 P_n^m(s)}{\partial z^2}\right)+\frac{1}{j_n(kR)}\left(\frac{\partial^2 j_n(kR)}{\partial y^2}+\frac{\partial^2 j_n(kR)}{\partial z^2}\right)+\frac{1}{e^{im\phi}}\left(\frac{\partial^2 e^{im\phi}}{\partial y^2}\right)+ \\ \frac{2}{P_n^m(s)j_n(kR)}\left(\frac{\partial P_n^m(s)}{\partial y}\frac{\partial j_n(kR)}{\partial y}+\frac{\partial P_n^m(s)}{\partial z}\frac{\partial j_n(kR)}{\partial z}\right)+\frac{2}{P_n^m(s)e^{im\phi}}\left(\frac{\partial P_n^m(s)}{\partial y}\frac{\partial e^{im\phi}}{\partial y}\right)+ \\ \frac{2}{j_n(kR)e^{im\phi}}\left(\frac{\partial j_n(kR)}{\partial y}\frac{\partial e^{im\phi}}{\partial y}\right) \end{array}\right)$$

$$N^1_y = \left(\begin{array}{l} \frac{1}{P_n^m(s)}\left(\frac{\partial^2 P_n^m(s)}{\partial x \partial y}\right)+\frac{1}{e^{im\phi}}\left(\frac{\partial^2 e^{im\phi}}{\partial x \partial y}\right)+\frac{1}{j_n(kR)}\left(\frac{\partial^2 j_n(kR)}{\partial x \partial y}\right)+ \\ \frac{1}{P_n^m(s)j_n(kR)}\left(\frac{\partial P_n^m(s)}{\partial y}\frac{\partial j_n(kR)}{\partial x}+\frac{\partial P_n^m(s)}{\partial x}\frac{\partial j_n(kR)}{\partial y}\right) \\ +\frac{1}{P_n^m(s)e^{im\phi}}\left(\frac{\partial P_n^m(s)}{\partial y}\frac{\partial e^{im\phi}}{\partial x}+\frac{\partial P_n^m(s)}{\partial x}\frac{\partial e^{im\phi}}{\partial y}\right)+\frac{1}{j_n(kR)e^{im\phi}}\left(\frac{\partial j_n(kR)}{\partial y}\frac{\partial e^{im\phi}}{\partial x}+\frac{\partial j_n(kR)}{\partial x}\frac{\partial e^{im\phi}}{\partial y}\right) \end{array}\right)$$

$$N^1_z = \left(\begin{array}{l} \frac{1}{P_n^m(s)}\left(\frac{\partial^2 P_n^m(s)}{\partial x \partial z}\right)+\frac{1}{j_n(kR)}\left(\frac{\partial^2 j_n(kR)}{\partial x \partial z}\right)+\frac{1}{P_n^m(s)j_n(kR)}\left(\frac{\partial P_n^m(s)}{\partial z}\frac{\partial j_n(kR)}{\partial x}+\frac{\partial P_n^m(s)}{\partial x}\frac{\partial j_n(kR)}{\partial z}\right)+ \\ \frac{1}{j_n(kR)e^{im\phi}}\left(\frac{\partial j_n(kR)}{\partial z}\frac{\partial e^{im\phi}}{\partial x}\right)+\frac{1}{P_n^m(s)e^{im\phi}}\left(\frac{\partial P_n^m(s)}{\partial z}\frac{\partial e^{im\phi}}{\partial x}\right) \end{array}\right).$$

Using the same technique as above, the $\mathbf{M}^2_{mn}(x,y,z)$, $\mathbf{N}^2_{mn}(x,y,z)$, $\mathbf{M}^3_{mn}(x,y,z)$ and $\mathbf{N}^3_{mn}(x,y,z)$ functions can be computed. They are

$$\mathbf{M}^2_{mn}(x,y,z)=\frac{-e^{-kd}e^{im\phi}j_n(kR)P_n^m(s)}{k}\begin{pmatrix}\left(\frac{-n(z-id)R}{x^2+y^2}+\frac{(m+n)R^2P^m_{n-1}(s)}{(x^2+y^2)P^m_n(s)}\right)\frac{\partial s}{\partial z}+k\left(\frac{n}{kR}-\frac{j_{n+1}(kR)}{j_n(kR)}\right)\frac{\partial R}{\partial z}\\ 0\\ \left(\frac{n(z-id)R}{x^2+y^2}-\frac{(m+n)R^2P^m_{n-1}(s)}{(x^2+y^2)P^m_n(s)}\right)\frac{\partial s}{\partial x}-k\left(\frac{n}{kR}-\frac{j_{n+1}(kR)}{j_n(kR)}\right)\frac{\partial R}{\partial x}+\frac{imy}{(x^2+y^2)}\end{pmatrix},$$

$$\mathbf{M}^3_{mn}(x,y,z)=\frac{e^{-kd}e^{im\phi}j_n(kR)P_n^m(s)}{k}\begin{pmatrix}-\left(\frac{n(z-id)R}{x^2+y^2}-\frac{(m+n)R^2P^m_{n-1}(s)}{(x^2+y^2)P^m_n(s)}\right)\frac{\partial s}{\partial y}+k\left(\frac{n}{kR}-\frac{j_{n+1}(kR)}{j_n(kR)}\right)\frac{\partial R}{\partial y}+\frac{imx}{(x^2+y^2)}\\ \left(\frac{n(z-id)R}{x^2+y^2}-\frac{(m+n)R^2P^m_{n-1}(s)}{(x^2+y^2)P^m_n(s)}\right)\frac{\partial s}{\partial x}-k\left(\frac{n}{kR}-\frac{j_{n+1}(kR)}{j_n(kR)}\right)\frac{\partial R}{\partial x}+\frac{imy}{(x^2+y^2)}\\ 0\end{pmatrix},$$

$$\mathbf{N}^2_{mn}(x,y,z)=\frac{e^{-kd}P_n^m(s)j_n(kR)e^{im\phi}}{k^2}\begin{pmatrix}N_x^2\\ N_y^2\\ N_z^2\end{pmatrix}$$

where:

$$N_x^2=\begin{pmatrix}\frac{1}{P_n^m(s)}\left(\frac{\partial^2 P_n^m(s)}{\partial x\partial y}\right)+\frac{1}{j_n(kR)}\left(\frac{\partial^2 j_n(kR)}{\partial x\partial y}\right)+\frac{1}{e^{im\phi}}\frac{\partial^2 e^{im\phi}}{\partial x\partial y}+\frac{1}{P_n^m(s)j_n(kR)}\left(\frac{\partial P_n^m(s)}{\partial y}\frac{\partial j_n(kR)}{\partial x}+\frac{\partial P_n^m(s)}{\partial x}\frac{\partial j_n(kR)}{\partial y}\right)+\\ \frac{1}{P_n^m(s)e^{im\phi}}\left(\frac{\partial P_n^m(s)}{\partial y}\frac{\partial e^{im\phi}}{\partial x}+\frac{\partial P_n^m(s)}{\partial x}\frac{\partial e^{im\phi}}{\partial y}\right)+\frac{1}{j_n(kR)e^{im\phi}}\left(\frac{\partial j_n(kR)}{\partial y}\frac{\partial e^{im\phi}}{\partial x}+\frac{\partial j_n(kR)}{\partial x}\frac{\partial e^{im\phi}}{\partial y}\right)\end{pmatrix}$$

$$N_y^2 = \left(\begin{array}{l} \frac{1}{P_n^m(s)} \left(\frac{\partial^2 P_n^m(s)}{\partial z^2} + \frac{\partial^2 P_n^m(s)}{\partial x^2} \right) + \frac{1}{e^{im\phi}} \left(\frac{\partial^2 e^{im\phi}}{\partial x^2} \right) + \frac{1}{j_n(kR)} \left(\frac{\partial^2 j_n(kR)}{\partial z^2} + \frac{\partial^2 j_n(kR)}{\partial x^2} \right) + \\ \frac{2}{P_n^m(s) j_n(kR)} \left(\frac{\partial P_n^m(s)}{\partial z} \frac{\partial j_n(kR)}{\partial z} + \frac{\partial P_n^m(s)}{\partial x} \frac{\partial j_n(kR)}{\partial x} \right) + \frac{2}{P_n^m(s) e^{im\phi}} \left(\frac{\partial P_n^m(s)}{\partial x} \frac{\partial e^{im\phi}}{\partial x} \right) + \\ \frac{2}{j_n(kR) e^{im\phi}} \left(\frac{\partial j_n(kR)}{\partial x} \frac{\partial e^{im\phi}}{\partial x} \right) \end{array} \right)$$

$$N_z^2 = \left(\begin{array}{l} \frac{1}{P_n^m(s)} \left(\frac{\partial^2 P_n^m(s)}{\partial y \partial z} \right) + \frac{1}{j_n(kR)} \left(\frac{\partial^2 j_n(kR)}{\partial y \partial z} \right) + \frac{1}{P_n^m(s) j_n(kR)} \left(\frac{\partial P_n^m(s)}{\partial z} \frac{\partial j_n(kR)}{\partial y} + \frac{\partial P_n^m(s)}{\partial y} \frac{\partial j_n(kR)}{\partial z} \right) + \\ \frac{1}{j_n(kR) e^{im\phi}} \left(\frac{\partial j_n(kR)}{\partial z} \frac{\partial e^{im\phi}}{\partial y} \right) + \frac{1}{P_n^m(s) e^{im\phi}} \left(\frac{\partial P_n^m(s)}{\partial z} \frac{\partial e^{im\phi}}{\partial y} \right) \end{array} \right)$$

and

$$\mathbf{N}_{mn}^3(x,y,z) = \frac{e^{-kd} P_n^m(s) j_n(kR) e^{im\phi}}{k^2} \begin{pmatrix} N_x^3 \\ N_y^3 \\ N_z^3 \end{pmatrix}$$

where

$$N_x^3 = \left(\begin{array}{l} \frac{1}{P_n^m(s)} \left(\frac{\partial^2 P_n^m(s)}{\partial x \partial z} \right) + \frac{1}{j_n(kR)} \frac{\partial^2 j_n(kR)}{\partial x \partial z} + \frac{1}{P_n^m(s) j_n(kR)} \left(\frac{\partial P_n^m(s)}{\partial z} \frac{\partial j_n(kR)}{\partial x} + \frac{\partial P_n^m(s)}{\partial x} \frac{\partial j_n(kR)}{\partial z} \right) + \\ \frac{1}{j_n(kR) e^{im\phi}} \left(\frac{\partial j_n(kR)}{\partial z} \frac{\partial e^{im\phi}}{\partial x} \right) + \frac{1}{P_n^m(s) e^{im\phi}} \left(\frac{\partial P_n^m(s)}{\partial z} \frac{\partial e^{im\phi}}{\partial x} \right) \end{array} \right)$$

$$N_y^3 = \left(\begin{array}{l} \frac{1}{P_n^m(s)} \left(\frac{\partial^2 P_n^m(s)}{\partial y \partial z} \right) + \frac{1}{j_n(kR)} \left(\frac{\partial^2 j_n(kR)}{\partial y \partial z} \right) + \frac{1}{P_n^m(s) j_n(kR)} \left(\frac{\partial P_n^m(s)}{\partial z} \frac{\partial j_n(kR)}{\partial y} + \frac{\partial P_n^m(s)}{\partial y} \frac{\partial j_n(kR)}{\partial z} \right) + \\ \frac{1}{P_n^m(s) e^{im\phi}} \left(\frac{\partial P_n^m(s)}{\partial z} \frac{\partial e^{im\phi}}{\partial y} \right) + \frac{1}{j_n(kR) e^{im\phi}} \left(\frac{\partial j_n(kR)}{\partial z} \frac{\partial e^{im\phi}}{\partial y} \right) \end{array} \right)$$

$$N_z^3 = -\left(\begin{array}{l} \dfrac{1}{P_n^m(s)}\left(\dfrac{\partial^2 P_n^m(s)}{\partial x^2}+\dfrac{\partial^2 P_n^m(s)}{\partial y^2}\right)+\dfrac{1}{e^{jm\phi}}\left(\dfrac{\partial^2 e^{jm\phi}}{\partial x^2}+\dfrac{\partial^2 e^{jm\phi}}{\partial y^2}\right)+\dfrac{1}{j_n(kR)}\left(\dfrac{\partial^2 j_n(kR)}{\partial x^2}+\dfrac{\partial^2 j_n(kR)}{\partial y^2}\right)+ \\ \dfrac{2}{P_n^m(s)j_n(kR)}\left(\dfrac{\partial P_n^m(s)}{\partial x}\dfrac{\partial j_n(kR)}{\partial x}+\dfrac{\partial P_n^m(s)}{\partial y}\dfrac{\partial j_n(kR)}{\partial y}\right)+\dfrac{2}{P_n^m(s)e^{jm\phi}}\left(\dfrac{\partial P_n^m(s)}{\partial x}\dfrac{\partial e^{jm\phi}}{\partial x}+\dfrac{\partial P_n^m(s)}{\partial y}\dfrac{\partial e^{jm\phi}}{\partial y}\right)+ \\ \dfrac{2}{j_n(kR)e^{jm\phi}}\left(\dfrac{\partial j_n(kR)}{\partial x}\dfrac{\partial e^{jm\phi}}{\partial x}+\dfrac{\partial j_n(kR)}{\partial y}\dfrac{\partial e^{jm\phi}}{\partial y}\right) \end{array} \right).$$

The various derivatives which are used in the $\mathbf{M}_{mn}^1(x,y,z)$, $\mathbf{M}_{mn}^2(x,y,z)$, $\mathbf{M}_{mn}^3(x,y,z)$, $\mathbf{N}_{mn}^1(x,y,z)$, $\mathbf{N}_{mn}^2(x,y,z)$ and $\mathbf{N}_{mn}^3(x,y,z)$ functions can be seen from tables 3.5.-3.8. below.

$$\frac{\partial R}{\partial x}=\frac{x}{R}, \qquad \frac{\partial^2 R}{\partial x^2}=\frac{-x^2}{R^3}+\frac{1}{R}$$

$$\frac{\partial R}{\partial y}=\frac{y}{R}, \qquad \frac{\partial^2 R}{\partial y^2}=\frac{-y^2}{R^3}+\frac{1}{R}$$

$$\frac{\partial R}{\partial z}=\frac{(z-id)}{R}, \qquad \frac{\partial^2 R}{\partial z^2}=\frac{-(z-id)^2}{R^3}+\frac{1}{R}$$

$$\frac{\partial s}{\partial x}=\frac{-x(z-id)}{R^3}, \qquad \frac{\partial^2 s}{\partial x^2}=\frac{3x^2(z-id)}{R^5}-\frac{(z-id)}{R^3}$$

$$\frac{\partial s}{\partial y}=\frac{y(z-id)}{R^3}, \qquad \frac{\partial^2 s}{\partial y^2}=\frac{3y^2(z-id)}{R^5}-\frac{(z-id)}{R^3}$$

$$\frac{\partial s}{\partial z}=\frac{1}{R}-\frac{(z-id)^2}{R^3}, \qquad \frac{\partial^2 s}{\partial z^2}=\frac{3(z-id)^3}{R^5}-\frac{3(z-id)}{R^3}$$

$$\frac{\partial^2 R}{\partial x\partial y}=-\frac{xy}{R^3}, \qquad \frac{\partial^2 R}{\partial x\partial z}=-\frac{x(z-id)}{R^3}, \qquad \frac{\partial^2 R}{\partial y\partial z}=-\frac{y(z-id)}{R^3}$$

$$\frac{\partial^2 s}{\partial x\partial y}=\frac{3xy(z-id)}{R^5}, \qquad \frac{\partial^2 s}{\partial x\partial z}=-\frac{x}{R^3}+\frac{3x(z-id)^2}{R^5}, \qquad \frac{\partial^2 s}{\partial y\partial z}=-\frac{y}{R^3}+\frac{3y(z-id)^2}{R^5}$$

Table 3.5. The derivatives of s and R

$$\frac{\partial P_n^m(s)}{\partial x} = \frac{R^2 P_n^m(s)}{x^2+y^2}\left(-\frac{n(z-id)}{R}+\frac{(m+n)P_{n-1}^m(s)}{P_n^m(s)}\right)\frac{\partial s}{\partial x}$$

$$\frac{\partial^2 P_n^m(s)}{\partial x^2} = \frac{\partial^2 P_n^m(s)}{\partial s^2}\left(\frac{\partial s}{\partial x}\right)^2+\frac{\partial P_n^m(s)}{\partial s}\frac{\partial^2 s}{\partial x^2}$$

$$\frac{\partial P_n^m(s)}{\partial y} = \frac{R^2 P_n^m(s)}{x^2+y^2}\left(-\frac{n(z-id)}{R}+\frac{(m+n)P_{n-1}^m(s)}{P_n^m(s)}\right)\frac{\partial s}{\partial y}$$

$$\frac{\partial^2 P_n^m(s)}{\partial y^2} = \frac{\partial^2 P_n^m(s)}{\partial s^2}\left(\frac{\partial s}{\partial y}\right)^2+\frac{\partial P_n^m(s)}{\partial s}\frac{\partial^2 s}{\partial y^2}$$

$$\frac{\partial P_n^m(s)}{\partial z} = \frac{R^2 P_n^m(s)}{x^2+y^2}\left(-\frac{n(z-id)}{R}+\frac{(m+n)P_{n-1}^m(s)}{P_n^m(s)}\right)\frac{\partial s}{\partial z}$$

$$\frac{\partial^2 P_n^m(s)}{\partial z^2} = \frac{\partial^2 P_n^m(s)}{\partial s^2}\left(\frac{\partial s}{\partial z}\right)^2+\frac{\partial P_n^m(s)}{\partial s}\frac{\partial^2 s}{\partial z^2}$$

$$\frac{\partial^2 P_n^m(s)}{\partial x\partial y} = \frac{\partial^2 P_n^m(s)}{\partial s^2}\left(\frac{\partial s}{\partial y}\frac{\partial s}{\partial x}\right)+\frac{\partial P_n^m(s)}{\partial s}\frac{\partial^2 s}{\partial x\partial y}$$

$$\frac{\partial^2 P_n^m(s)}{\partial x\partial z} = \frac{\partial^2 P_n^m(s)}{\partial s^2}\left(\frac{\partial s}{\partial z}\frac{\partial s}{\partial x}\right)+\frac{\partial P_n^m(s)}{\partial s}\frac{\partial^2 s}{\partial x\partial z}$$

$$\frac{\partial^2 P_n^m(s)}{\partial y\partial z} = \frac{\partial^2 P_n^m(s)}{\partial s^2}\left(\frac{\partial s}{\partial z}\frac{\partial s}{\partial y}\right)+\frac{\partial P_n^m(s)}{\partial s}\frac{\partial^2 s}{\partial y\partial z}$$

Table 3.6. Some derivatives of the associate Legendre functions

$$\frac{\partial j_n(kR)}{\partial x} = \frac{\partial j_n(kR)}{\partial(kR)}k\frac{\partial R}{\partial x}, \qquad \frac{\partial^2 j_n(kR)}{\partial x^2} = \frac{\partial^2 j_n(kR)}{\partial(kR)^2}k^2\left(\frac{\partial R}{\partial x}\right)^2+\frac{\partial j_n(kR)}{\partial(kR)}k\frac{\partial^2 R}{\partial x^2}$$

$$\frac{\partial j_n(kR)}{\partial y} = \frac{\partial j_n(kR)}{\partial(kR)}k\frac{\partial R}{\partial y}, \qquad \frac{\partial^2 j_n(kR)}{\partial y^2} = \frac{\partial^2 j_n(kR)}{\partial(kR)^2}k^2\left(\frac{\partial R}{\partial y}\right)^2+\frac{\partial j_n(kR)}{\partial(kR)}k\frac{\partial^2 R}{\partial y^2}$$

$$\frac{\partial j_n(kR)}{\partial z} = \frac{\partial j_n(kR)}{\partial(kR)}k\frac{\partial R}{\partial z}, \qquad \frac{\partial^2 j_n(kR)}{\partial z^2} = \frac{\partial^2 j_n(kR)}{\partial(kR)^2}k^2\left(\frac{\partial R}{\partial z}\right)^2+\frac{\partial j_n(kR)}{\partial(kR)}k\frac{\partial^2 R}{\partial z^2}$$

$$\frac{\partial^2 j_n(kR)}{\partial x\partial y} = \frac{\partial^2 j_n(kR)}{\partial(kR)^2}k^2\left(\frac{\partial R}{\partial y}\frac{\partial R}{\partial x}\right)+\frac{\partial j_n(kR)}{\partial(kR)}k\frac{\partial^2 R}{\partial x\partial y}$$

$$\frac{\partial^2 j_n(kR)}{\partial x\partial z} = \frac{\partial^2 j_n(kR)}{\partial(kR)^2}k^2\left(\frac{\partial R}{\partial z}\frac{\partial R}{\partial x}\right)+\frac{\partial j_n(kR)}{\partial(kR)}k\frac{\partial^2 R}{\partial x\partial z}$$

$$\frac{\partial^2 j_n(kR)}{\partial y\partial z} = \frac{\partial^2 j_n(kR)}{\partial(kR)^2}k^2\left(\frac{\partial R}{\partial z}\frac{\partial R}{\partial y}\right)+\frac{\partial j_n(kR)}{\partial(kR)}k\frac{\partial^2 R}{\partial y\partial z}$$

Table 3.7. Some derivatives of the spherical Bessel functions

$$\frac{\partial^2 e^{im\phi}}{\partial x^2} = \frac{mye^{im\phi}}{\left(x^2+y^2\right)}\left(\frac{2i}{x}-\frac{2iy^2}{x\left(x^2+y^2\right)}-\frac{my}{\left(x^2+y^2\right)}\right)$$

$$\frac{\partial^2 e^{im\phi}}{\partial y^2} = -\frac{mxe^{im\phi}}{\left(x^2+y^2\right)^2}(2iy+mx)$$

$$\frac{\partial^2 e^{im\phi}}{\partial z^2} = 0$$

$$\frac{\partial^2 e^{im\phi}}{\partial x\partial y} = \frac{me^{im\phi}}{\left(x^2+y^2\right)}\left(-i+\frac{2iy^2}{\left(x^2+y^2\right)}+\frac{mxy}{\left(x^2+y^2\right)}\right)$$

$$\frac{\partial^2 e^{im\phi}}{\partial x\partial z} = \frac{\partial^2 e^{im\phi}}{\partial y\partial z} = 0$$

Table 3.8. Some derivatives of the azimuthal function

The $\mathbf{M}^{r}_{mn}(x,y,z)$ and $\mathbf{N}^{r}_{mn}(x,y,z)$ functions given in this section satisfy the vector wave equation.

3.3. Conclusion

In this chapter, a method has been presented by which it is possible to construct solutions to the vector Helmholtz equation based on solutions to the scalar Helmholtz equation. The presented vector solutions do not directly represent the electric and magnetic fields, but are related to them. It is the aim of the next chapter to investigate these vector solutions and then to form a linear superposition of these vector solutions in order to derive the E.M. field. Since a solution is required which represents a Gaussian beam, it can also be concluded that the $\mathbf{M}^{3}_{00}(\mathbf{r},t)$, $\mathbf{M}^{3}_{01}(\mathbf{r},t)$, $\mathbf{N}^{3}_{00}(\mathbf{r},t)$ and $\mathbf{N}^{3}_{01}(\mathbf{r},t)$ are not likely to be present in the superposition of the E.M. field, since all the components of $\mathbf{M}^{3}_{00}(\mathbf{r},t)$ and $\mathbf{M}^{3}_{01}(\mathbf{r},t)$ are zero at the origin.

References

[1] Morse, P.M., Feshbach, H., (19530, Methods of Theoretical Physics, Part II, Mc Graw-Hill Book Company, Inc. p.1762.

[2] Volyar, A. V. (2000), Nonparaxial Gaussian Beams: 1. Vector Fields, *Tech. Phys. Lett.* **26**, *No. 7, p. 573-575.*

[3] Bohren, C. F., Huffman, D. R., (1983), Absorption and Scattering of Light by Small Particles, John Wiley & Sons.

[4] Ludlow, I. K., unpublished.

[5] Abramowitz , M. , Stegun, I. A., (1970), Handbook of mathematical functions, Dover Publications.

4. The Electromagnetic Field

4. 1. Introduction

In the previous chapter exact solutions to the vector Helmholtz equation have been presented. The aim of this chapter is to derive an E.M. field, which satisfies the criteria outlined at the beginning of chapter 3. As indicated in the previous chapter, the E.M. field will be constructed as a linear superposition of the $\mathbf{M}^{r}_{00}(x,y,z)$ and $\mathbf{N}^{r}_{00}(x,y,z)$ functions for the lowest order 00 and as a linear superposition of $\mathbf{M}^{r}_{01}(x,y,z)$ and $\mathbf{N}^{r}_{01}(x,y,z)$ for order 01. The first task is to investigate the properties of these functions based on the scalar functions of orders 00 and 01, since only these two orders have a Gaussian irradiance profile. It is known, assuming an $e^{-i\omega t}$ time dependence, from Eqs. (3.3), (3.8.a-3.8.c) and (3.14.a-3.14.c) that the E.M. field will have the following form:

$$\mathbf{E}(\mathbf{r},t) = E_0 \sum_{\gamma=1}^{3} \left(\alpha_\gamma \mathbf{M}^{\gamma}_{mn}(\mathbf{r},t) + \beta_\gamma \mathbf{N}^{\gamma}_{mn}(\mathbf{r},t)\right) \tag{4.1.a}$$

$$\mathbf{H}(\mathbf{r},t) = -iE_0 \sqrt{\frac{\varepsilon}{\mu_0}} \sum_{\gamma=1}^{3} \left(\alpha_\gamma \mathbf{N}^{\gamma}_{mn}(\mathbf{r},t) + \beta_\gamma \mathbf{M}^{\gamma}_{mn}(\mathbf{r},t)\right), \tag{4.1.b}$$

where α_γ and β_γ are complex constants. Thus in order to derive the correct E.M. field, the constants α_γ and β_γ need to be determined with the help of the criteria a)-g) mentioned in section 3.1. From criterion a) it is known that m=0 and n=0 or 1. However the only criterion which gives a clear indication of the values for α_γ and β_γ, is criterion f). Since in the far-field limit the wavefronts of the Gaussian beam are plane wavefronts, it is implied that the polarisation pattern in the far-field limit of a Gaussian beam is identical to the polarisation pattern in the far-field limit, produced by focusing a plane wave with an aberration-free sine condition lens, as derived by Richards and Wolf [1]. Thus the next task is, to find values for α_γ and β_γ which lead to the same polarisation pattern as the one given in Richards and Wolf [1]. However the irradiance distribution of the Gaussian beam will be different from the irradiance distribution of the plane wave, as has been demonstrated in chapter 2.

4.2. The far-field

Applying the formulae derived by Richards and Wolf [1] for the electric and magnetic field components in the far field, it is possible to write these components on the reference sphere that represents the principal surface of an aberration-free lens that obeys the sine condition and is illuminated by a plane wave in Cartesian coordinates as [1]:

$$\begin{aligned} E_x &\propto \cos\theta + \sin^2\phi(1-\cos\theta) \\ E_y &\propto (\cos\theta - 1)\cos\phi\sin\phi \\ E_z &\propto -\sin\theta\cos\phi \\ H_x &\propto (\cos\theta - 1)\cos\phi\sin\phi \\ H_y &\propto 1 - \sin^2\phi(1-\cos\theta) \\ H_z &\propto -\sin\theta\sin\phi \quad . \end{aligned} \tag{4.2}$$

In order to test if the superposition of the $\mathbf{M}_{00}^{\gamma}(\mathbf{r},t)$ and $\mathbf{N}_{00}^{\gamma}(\mathbf{r},t)$ functions and the $\mathbf{M}_{01}^{\gamma}(\mathbf{r},t)$ and $\mathbf{N}_{01}^{\gamma}(\mathbf{r},t)$ functions respectively, which form the E.M. fields satisfies the Richards and Wolf far-field boundary conditions, it is legitimate to consider, as in the scalar case, only the $\mathbf{M}_{mn}^{\gamma}(\mathbf{r},t)$ and $\mathbf{N}_{mn}^{\gamma}(\mathbf{r},t)$ functions based on the outward travelling wave, defined as $\mathbf{M}_{mn}^{\gamma(1)}(\mathbf{r},t)$ and $\mathbf{N}_{mn}^{\gamma(1)}(\mathbf{r},t)$. These functions are transformed into spherical polar coordinates in order to find expressions for them in the limit of infinite radius of the reference sphere. These expressions are then transformed back into Cartesian coordinates and compared with Eq. (4.2).

4.2.1. The transformation matrix

The transformation matrix required in order to transform the $\mathbf{M}_{mn}^{\gamma(1)}(\mathbf{r},t)$ and $\mathbf{N}_{mn}^{\gamma(1)}(\mathbf{r},t)$ functions from Cartesian coordinates into spherical polar coordinates can be derived in the following manner: According to Morse and Feshbach [2] the direction cosines for the u_n axis with respect to the x, y, z axis can be written in terms of the derivatives relating x, y, z and the u's in either of two ways:

$$a_p = \frac{1}{h_p}\frac{\partial x}{\partial u_p} = h_p \frac{\partial u_p}{\partial x}$$
$$b_p = \frac{1}{h_p}\frac{\partial y}{\partial u_p} = h_p \frac{\partial u_p}{\partial y} \qquad (4.3)$$
$$c_p = \frac{1}{h_p}\frac{\partial z}{\partial u_p} = h_p \frac{\partial u_p}{\partial z}$$

where p=1, 2, 3, depending on whether x, y, z are given in terms of the u's or the u's in terms of x, y, z. Hence the transformation matrix, which transforms a vector $\mathbf{V}(r, \theta, \phi)$ in spherical polar coordinates into a vector $\mathbf{V}(x, y, z)$ in Cartesian coordinates can be written as

$$\begin{pmatrix} V_x \\ V_y \\ V_z \end{pmatrix} = \begin{vmatrix} \frac{1}{h_1}\frac{\partial x}{\partial r} & \frac{1}{h_2}\frac{\partial x}{\partial \theta} & \frac{1}{h_3}\frac{\partial x}{\partial \phi} \\ \frac{1}{h_1}\frac{\partial y}{\partial r} & \frac{1}{h_2}\frac{\partial y}{\partial \theta} & \frac{1}{h_3}\frac{\partial y}{\partial \phi} \\ \frac{1}{h_1}\frac{\partial z}{\partial r} & \frac{1}{h_2}\frac{\partial z}{\partial \theta} & \frac{1}{h_3}\frac{\partial z}{\partial \phi} \end{vmatrix} \begin{pmatrix} V_r \\ V_\theta \\ V_\phi \end{pmatrix} . \qquad (4.4)$$

Eq. (4.4) can be written with the help of Eqs. (2.6) and substituting the scale factors given in section (2.2.1.) as

$$\begin{pmatrix} V_x \\ V_y \\ V_z \end{pmatrix} = \begin{vmatrix} \sin\theta\cos\phi & \cos\theta\cos\phi & -\sin\phi \\ \sin\theta\sin\phi & \cos\theta\sin\phi & \cos\phi \\ \cos\theta & -\sin\theta & 0 \end{vmatrix} \begin{pmatrix} V_r \\ V_\theta \\ V_\phi \end{pmatrix} . \qquad (4.5)$$

The matrix which transforms a vector $\mathbf{V}(x, y, z)$ in Cartesian coordinates into a vector $\mathbf{V}(r, \theta, \phi)$ in spherical polar coordinates is the transpose [3] of the matrix in Eq. (4.5)

$$\begin{pmatrix} V_r \\ V_\theta \\ V_\phi \end{pmatrix} = \begin{vmatrix} \sin\theta\cos\phi & \sin\theta\sin\phi & \cos\theta \\ \cos\theta\cos\phi & \cos\theta\sin\phi & -\sin\theta \\ -\sin\phi & \cos\phi & 0 \end{vmatrix} \begin{pmatrix} V_x \\ V_y \\ V_z \end{pmatrix} . \qquad (4.6)$$

By substituting Eqs. (4.2) into Eq. (4.6), it is found that the Richards and Wolf far-field conditions [1] can be written in spherical polar coordinates as

$$
\begin{aligned}
&E_r(r,\theta,\phi)=0\\
&E_\theta(r,\theta,\phi)\propto\cos\phi\\
&E_\phi(r,\theta,\phi)\propto-\sin\phi\\
&H_r(r,\theta,\phi)=0\\
&H_\theta(r,\theta,\phi)\propto\sin\phi\\
&H_\phi(r,\theta,\phi)\propto\cos\phi \quad .
\end{aligned}
\tag{4.7}
$$

4.2.2. The derivation of the E.M. field as a superposition of the **M** and **N** functions

All the derivations in this section will be made at time t=0. It has been mentioned in chapter 3, that the $\mathbf{M}^{1}_{mn}(x,y,z)$, $\mathbf{M}^{2}_{mn}(x,y,z)$, $\mathbf{N}^{1}_{mn}(x,y,z)$ and $\mathbf{N}^{2}_{mn}(x,y,z)$ are the most likely vector functions to be used for the construction of the E.M. field. Thus in this section these four functions are considered. The vector functions, based on the outward travelling wave, $\mathbf{M}^{1(1)}_{mn}(x,y,z)$, $\mathbf{M}^{2(1)}_{mn}(x,y,z)$, $\mathbf{N}^{1(1)}_{mn}(x,y,z)$ and $\mathbf{N}^{2(1)}_{mn}(x,y,z)$ are transformed into spherical polar coordinates, by expressing x, y, z in terms of r, θ, ϕ, using the relations given by Eqs. (2.6) and then substituting them into the right hand side of Eq. (4.6). Performing these calculations, the $\mathbf{M}^{1(1)}_{00}(r,\theta,\phi)$, $\mathbf{M}^{2(1)}_{00}(r,\theta,\phi)$, $\mathbf{N}^{1(1)}_{00}(r,\theta,\phi)$ and $\mathbf{N}^{2(1)}_{00}(r,\theta,\phi)$ functions can be written in spherical polar coordinates as

$$
\mathbf{M}^{1(1)}_{00}(r,\theta,\phi)=\frac{e^{-kd}h_1^{(1)}(kR_{sp})}{R_{sp}}\begin{pmatrix} id\sin\theta\sin\phi\\ \sin\phi(id\cos\theta-r)\\ \cos\phi(id-r\cos\theta)\end{pmatrix} \quad , \tag{4.8}
$$

$$
\mathbf{M}^{2(1)}_{00}(r,\theta,\phi)=\frac{e^{-kd}h_1^{(1)}(kR_{sp})}{R_{sp}}\begin{pmatrix} -id\sin\theta\cos\phi\\ \cos\phi(r-id\cos\theta)\\ \sin\phi(id-r\cos\theta)\end{pmatrix} \quad , \tag{4.9}
$$

$$\mathbf{N}_{\infty}^{1(1)}(r,\theta,\phi)=\frac{e^{-kd}h_2^{(1)}(kR_{sp})}{kR_{sp}^2}\begin{pmatrix}\dfrac{\sin\theta\cos\phi\begin{pmatrix}2R_{sp}h_1^{(1)}(kR_{sp})+\\ ikdh_2^{(1)}(kR_{sp})r\cos\theta+kd^2h_2^{(1)}(kR_{sp})\end{pmatrix}}{h_2^{(1)}(kR_{sp})}\\ \dfrac{\cos\theta\cos\phi\begin{pmatrix}2R_{sp}h_1^{(1)}(kR_{sp})+ikdh_2^{(1)}(kR_{sp})r\cos\theta+\\ kd^2h_2^{(1)}(kR_{sp})-kr^2h_2^{(1)}(kR_{sp})+\dfrac{ikdrh_2^{(1)}(kR_{sp})}{\cos\theta}\end{pmatrix}}{h_2^{(1)}(kR_{sp})}\\ \dfrac{-\sin\phi\begin{pmatrix}2R_{sp}h_1^{(1)}(kR_{sp})-kr^2h_2^{(1)}(kR_{sp})+\\ 2ikdh_2^{(1)}(kR_{sp})r\cos\theta+kd^2h_2^{(1)}(kR_{sp})\end{pmatrix}}{h_2^{(1)}(kR_{sp})}\end{pmatrix} \tag{4.10}$$

and

$$\mathbf{N}_{00}^{2(1)}(r,\theta,\phi)=\frac{e^{-kd}h_2^{(1)}(kR_{sp})}{kR_{sp}^2}\begin{pmatrix}\dfrac{\sin\theta\sin\phi\begin{pmatrix}2R_{sp}h_1^{(1)}(kR_{sp})+\\ ikdh_2^{(1)}(kR_{sp})r\cos\theta+kd^2h_2^{(1)}(kR_{sp})\end{pmatrix}}{h_2^{(1)}(kR_{sp})}\\ \dfrac{\cos\theta\sin\phi\begin{pmatrix}2R_{sp}h_1^{(1)}(kR_{sp})+ikdh_2^{(1)}(kR_{sp})r\cos\theta+\\ kd^2h_2^{(1)}(kR_{sp})-kr^2h_2^{(1)}(kR_{sp})+\dfrac{ikdrh_2^{(1)}(kR_{sp})}{\cos\theta}\end{pmatrix}}{h_2^{(1)}(kR_{sp})}\\ \dfrac{\cos\phi\begin{pmatrix}2R_{sp}h_1^{(1)}(kR_{sp})-kr^2h_2^{(1)}(kR_{sp})+\\ 2ikdh_2^{(1)}(kR_{sp})r\cos\theta+kd^2h_2^{(1)}(kR_{sp})\end{pmatrix}}{h_2^{(1)}(kR_{sp})}\end{pmatrix}, \tag{4.11}$$

where the Hankel functions of the first kind are given explicitly as

$$\begin{aligned}h_0^{(1)}(kR_{sp})&=\frac{e^{ikR_{sp}}}{ikR_{sp}}\\ h_1^{(1)}(kR_{sp})&=\frac{e^{ikR_{sp}}}{kR_{sp}}\left(\frac{1}{ikR_{sp}}-1\right)\\ h_2^{(1)}(kR_{sp})&=\frac{e^{ikR_{sp}}}{kR_{sp}}\left(\frac{3}{ik^2R_{sp}^2}-\frac{3}{kR_{sp}}+i\right)\end{aligned}\quad , \tag{4.12}$$

with R_{sp} being the complex radius in spherical polar coordinates, given by

$$R_{sp} = \sqrt{r^2 - 2ird\cos\theta - d^2} \quad . \tag{4.13}$$

Following this same procedure, the $\mathbf{M}_{o1}^{1(1)}(r,\theta,\phi)$, $\mathbf{M}_{o1}^{2(1)}(r,\theta,\phi)$, $\mathbf{N}_{o1}^{1(1)}(r,\theta,\phi)$ and $\mathbf{N}_{o1}^{1(1)}(r,\theta,\phi)$ functions can be written as

$$\mathbf{M}_{o1}^{1(1)}(r,\theta,\phi) = \frac{e^{-kd}\left(r\cos\theta - id\right)h_2^{(1)}\left(kR_{sp}\right)}{R_{sp}^2}\begin{pmatrix} \sin\theta\sin\phi\left(\dfrac{R_{sp}h_1^{(1)}\left(kR_{sp}\right)}{k\left(r\cos\theta - id\right)h_2^{(1)}\left(kR_{sp}\right)} + id\right) \\ \sin\phi\left(\cos\theta\left(\dfrac{R_{sp}h_1^{(1)}\left(kR_{sp}\right)}{k\left(r\cos\theta - id\right)h_2^{(1)}\left(kR_{sp}\right)} - r\cos\theta + id\right) - r\sin^2\theta\right) \\ \cos\phi\left(\dfrac{R_{sp}h_1^{(1)}\left(kR_{sp}\right)}{k\left(r\cos\theta - id\right)h_2^{(1)}\left(kR_{sp}\right)} - r\cos\theta + id\right) \end{pmatrix}, \tag{4.14}$$

$$\mathbf{M}_{o1}^{2(1)}(r,\theta,\phi) = -\frac{e^{-kd}\left(r\cos\theta - id\right)h_2^{(1)}\left(kR_{sp}\right)}{R_{sp}^2}\begin{pmatrix} \sin\theta\cos\phi\left(\dfrac{R_{sp}h_1^{(1)}\left(kR_{sp}\right)}{k\left(r\cos\theta - id\right)h_2^{(1)}\left(kR_{sp}\right)} + id\right) \\ \cos\phi\left(\cos\theta\left(\dfrac{R_{sp}h_1^{(1)}\left(kR_{sp}\right)}{k\left(r\cos\theta - id\right)h_2^{(1)}\left(kR_{sp}\right)} - r\cos\theta + id\right) - r\sin^2\theta\right) \\ \sin\phi\left(-\dfrac{R_{sp}h_1^{(1)}\left(kR_{sp}\right)}{k\left(r\cos\theta - id\right)h_2^{(1)}\left(kR_{sp}\right)} + r\cos\theta - id\right) \end{pmatrix}, \tag{4.15}$$

$$\mathbf{N}_{o1}^{1(1)}(r,\theta,\phi) = \frac{e^{-kd}\left(r\cos\theta - id\right)h_2^{(1)}\left(kR_{sp}\right)}{kR_{sp}^4}\begin{pmatrix} \sin\theta\cos\phi\left(4R_{sp}^2 - \left(r\cos\theta - id\right)^2\left(5 - \dfrac{kR_{sp}h_1^{(1)}\left(kR_{sp}\right)}{h_2^{(1)}\left(kR_{sp}\right)}\right) - \right. \\ \left. r\cos\theta\left(\dfrac{R_{sp}^2}{r\cos\theta - id} - \left(r\cos\theta - id\right)\left(5 - \dfrac{kR_{sp}h_1^{(1)}\left(kR_{sp}\right)}{h_2^{(1)}\left(kR_{sp}\right)}\right)\right)\right) \\ \cos\phi\left(\cos\theta\left(4R_{sp}^2 - \left(r\cos\theta - id\right)^2\left(5 - \dfrac{kR_{sp}h_1^{(1)}\left(kR_{sp}\right)}{h_2^{(1)}\left(kR_{sp}\right)}\right)\right) + \right. \\ \left. r\sin^2\theta\left(\dfrac{R_{sp}^2}{r\cos\theta - id} - \left(r\cos\theta - id\right)\left(5 - \dfrac{kR_{sp}h_1^{(1)}\left(kR_{sp}\right)}{h_2^{(1)}\left(kR_{sp}\right)}\right)\right)\right) \\ -\sin\phi\left(4R_{sp}^2 - \left(\begin{matrix} r^2\sin^2\theta + \\ \left(r\cos\theta - id\right)^2 \end{matrix}\right)\left(5 - \dfrac{kR_{sp}h_1^{(1)}\left(kR_{sp}\right)}{h_2^{(1)}\left(kR_{sp}\right)}\right)\right) \end{pmatrix}, \tag{4.16}$$

and

$$\mathbf{N}_{01}^{2(1)}(r,\theta,\phi)=\frac{e^{-kd}(r\cos\theta-id)h_2^{(1)}(kR_{sp})}{kR_{sp}^4}\begin{pmatrix}\sin\theta\sin\phi\begin{pmatrix}4R_{sp}^2-(r\cos\theta-id)^2\left(5-\dfrac{kR_{sp}h_1^{(1)}(kR_{sp})}{h_2^{(1)}(kR_{sp})}\right)-\\ r\cos\theta\left(\dfrac{R_{sp}^2}{r\cos\theta-id}-(r\cos\theta-id)\left(5-\dfrac{kR_{sp}h_1^{(1)}(kR_{sp})}{h_2^{(1)}(kR_{sp})}\right)\right)\end{pmatrix}\\ \sin\phi\begin{pmatrix}\cos\theta\left(4R_{sp}^2-(r\cos\theta-id)^2\left(5-\dfrac{kR_{sp}h_1^{(1)}(kR_{sp})}{h_2^{(1)}(kR_{sp})}\right)\right)+\\ r\sin^2\theta\left(\dfrac{R_{sp}^2}{r\cos\theta-id}-(r\cos\theta-id)\left(5-\dfrac{kR_{sp}h_1^{(1)}(kR_{sp})}{h_2^{(1)}(kR_{sp})}\right)\right)\end{pmatrix}\\ \cos\phi\left(4R_{sp}^2-\begin{pmatrix}r^2\sin^2\theta+\\ (r\cos\theta-id)^2\end{pmatrix}\left(5-\dfrac{kR_{sp}h_1^{(1)}(kR_{sp})}{h_2^{(1)}(kR_{sp})}\right)\right)\end{pmatrix} \tag{4.17}$$

The next step is to investigate these functions for order 00 in the far-field limit. Like in the scalar case, these functions are normalised on axis, i.e. θ=0 is substituted into the normalisation constant. In order to proceed with the analysis, it is convenient to rewrite Eqs. (4.8) - (4.11) as

$$\mathbf{M}_{00}^{1(1)}(r,\theta,\phi)=A_{00}(r,\theta)\begin{pmatrix}id\sin\theta\sin\phi\\ \sin\phi(id\cos\theta-r)\\ \cos\phi(id-r\cos\theta)\end{pmatrix}, \tag{4.18}$$

$$\mathbf{M}_{00}^{2(1)}(r,\theta,\phi)=A_{00}(r,\theta)\begin{pmatrix}-id\sin\theta\cos\phi\\ \cos\phi(r-id\cos\theta)\\ \sin\phi(id-r\cos\theta)\end{pmatrix}, \tag{4.19}$$

$$\mathbf{N}_{00}^{1(1)}(r,\theta,\phi)=B_{00}(r,\theta)\begin{pmatrix}\dfrac{\sin\theta\cos\phi\left(2R_{sp}h_1^{(1)}(kR_{sp})+ikdh_2^{(1)}(kR_{sp})r\cos\theta+kd^2h_2^{(1)}(kR_{sp})\right)}{h_2^{(1)}(kR_{sp})}\\ \dfrac{\cos\theta\cos\phi\left(2R_{sp}h_1^{(1)}(kR_{sp})+ikdh_2^{(1)}(kR_{sp})r\cos\theta+kd^2h_2^{(1)}(kR_{sp})-kr^2h_2^{(1)}(kR_{sp})+\dfrac{ikdrh_2^{(1)}(kR_{sp})}{\cos\theta}\right)}{h_2^{(1)}(kR_{sp})}\\ \dfrac{-\sin\phi\left(2R_{sp}h_1^{(1)}(kR_{sp})-kr^2h_2^{(1)}(kR_{sp})+2ikdh_2^{(1)}(kR_{sp})r\cos\theta+kd^2h_2^{(1)}(kR_{sp})\right)}{h_2^{(1)}(kR_{sp})}\end{pmatrix} \tag{4.20}$$

and

$$\mathbf{N}_{00}^{2(1)}(r,\theta,\phi)=B_{00}(r,\theta)\begin{pmatrix}\dfrac{\sin\theta\sin\phi\left(2R_{sp}h_1^{(1)}(kR_{sp})+ikdh_2^{(1)}(kR_{sp})\right)r\cos\theta+kd^2h_2^{(1)}(kR_{sp})\right)}{h_2^{(1)}(kR_{sp})}\\ \dfrac{\cos\theta\sin\phi\left(2R_{sp}h_1^{(1)}(kR_{sp})+ikdh_2^{(1)}(kR_{sp})\right)r\cos\theta+kd^2h_2^{(1)}(kR_{sp})-kr^2h_2^{(1)}(kR_{sp})+\dfrac{ikdrh_2^{(1)}(kR_{sp})}{\cos\theta}\right)}{h_2^{(1)}(kR_{sp})}\\ \dfrac{\cos\phi\left(2R_{sp}h_1^{(1)}(kR_{sp})-kr^2h_2^{(1)}(kR_{sp})+2ikdh_2^{(1)}(kR_{sp})\right)r\cos\theta+kd^2h_2^{(1)}(kR_{sp})\right)}{h_2^{(1)}(kR_{sp})}\end{pmatrix}, \tag{4.21}$$

where

$$A_{00}(r,\theta)=\frac{e^{-kd}h_1^{(1)}(kR_{sp})}{R_{sp}} \tag{4.22}$$

and

$$B_{00}(r,\theta)=\frac{e^{-kd}h_2^{(1)}(kR_{sp})}{kR_{sp}^2}\ . \tag{4.23}$$

Since the limit of the product of two functions is equal to the product of the limit of these functions, it is possible to first evaluate the time averaged amplitude factors $A_{00}(r,\theta)$ and $B_{00}(r,\theta)$. Furthermore since the Poynting vector is based on the cross product of $\mathbf{E}(\mathbf{r},t)$ and $\mathbf{H}^*(\mathbf{r},t)$ it is necessary to additionally check the products $A_{00}(r,\theta)\ B^*_{00}(r,\theta)$ and $A^*_{00}(r,\theta)B_{00}(r,\theta)$. Using the same method as in chapter 2, it is found that

$$\lim_{r\to\infty}\left(\sqrt{\frac{A_{00}(r,\theta)A_{00}^*(r,\theta)}{A_{00}(r,0)A_{00}^*(r,0)}}\right)=\lim_{r\to\infty}\left(\sqrt{\frac{B_{00}(r,\theta)B_{00}^*(r,\theta)}{B_{00}(r,0)B_{00}^*(r,0)}}\right)=\lim_{r\to\infty}\left(\sqrt{\frac{A_{00}(r,\theta)B_{00}^*(r,\theta)}{A_{00}(r,0)B_{00}^*(r,0)}}\right)=$$
$$\lim_{r\to\infty}\left(\sqrt{\frac{A_{00}^*(r,\theta)B_{00}(r,\theta)}{A_{00}^*(r,0)B_{00}(r,0)}}\right)=\lim_{r\to\infty}\left(\frac{A_{00}(r,\theta)}{A_{00}(r,0)}\right)=\lim_{r\to\infty}\left(\frac{B_{00}(r,\theta)}{B_{00}(r,0)}\right)=\sqrt{e^{-2kd(1-\cos\theta)}}=e^{-kd(1-\cos\theta)} \tag{4.24}$$

It can be seen by comparing Eqs. (4.24) with the first equation of Eqs. (2.72) that Eqs. (4.24) are equal to the square root of the first equation of Eqs. (2.72). Thus a clear relationship between the far-field limit of the scalar and vector functions is established. It is important to mention, that since $A_{00}(r,\theta)$ and $B_{00}(r,\theta)$, which are multiplied with their

complex conjugates, these products are real and any information regarding the signs of $A_{00}(r,\theta)$ and $B_{00}(r,\theta)$ is lost. The same is true for all the other calculations of Eq. (4.24). It is now possible, since the amplitude factors $A_{00}(r,\theta)$ and $B_{00}(r,\theta)$ are known in the far-field limit, to multiply the vectors $\mathbf{M}_{00}^{1(1)}(r,\theta,\phi)$ and $\mathbf{M}_{00}^{2(1)}(r,\theta,\phi)$ by $\frac{1}{A_{00}(r,\theta)}$ and $\mathbf{N}_{00}^{1(1)}(r,\theta,\phi)$ and $\mathbf{N}_{00}^{2(1)}(r,\theta,\phi)$ by $\frac{1}{B_{00}(r,\theta)}$. Thus a new set of vector functions $\mathbf{m}_{00}^{1(1)}(r,\theta,\phi)$, $\mathbf{m}_{00}^{2(1)}(r,\theta,\phi)$, $\mathbf{n}_{00}^{1(1)}(r,\theta,\phi)$ and $\mathbf{n}_{00}^{2(1)}(r,\theta,\phi)$ can be defined as

$$\mathbf{m}_{00}^{1(1)}(r,\theta,\phi)=\begin{pmatrix} id\sin\theta\sin\phi \\ \sin\phi(id\cos\theta-r) \\ \cos\phi(id-r\cos\theta) \end{pmatrix}, \tag{4.25}$$

$$\mathbf{m}_{00}^{2(1)}(r,\theta,\phi)=\begin{pmatrix} -id\sin\theta\cos\phi \\ \cos\phi(r-id\cos\theta) \\ \sin\phi(id-r\cos\theta) \end{pmatrix}, \tag{4.26}$$

$$\mathbf{n}_{00}^{1(1)}(r,\theta,\phi)=\begin{pmatrix} \dfrac{\sin\theta\cos\phi\left(2R_{sp}h_1^{(1)}(kR_{sp})+ikdh_2^{(1)}(kR_{sp})r\cos\theta+kd^2h_2^{(1)}(kR_{sp})\right)}{h_2^{(1)}(kR_{sp})} \\ \dfrac{\cos\theta\cos\phi\left(2R_{sp}h_1^{(1)}(kR_{sp})+ikdh_2^{(1)}(kR_{sp})r\cos\theta+kd^2h_2^{(1)}(kR_{sp})-kr^2h_2^{(1)}(kR_{sp})+\dfrac{ikdrh_2^{(1)}(kR_{sp})}{\cos\theta}\right)}{h_2^{(1)}(kR_{sp})} \\ \dfrac{-\sin\phi\left(2R_{sp}h_1^{(1)}(kR_{sp})-kr^2h_2^{(1)}(kR_{sp})+2ikdh_2^{(1)}(kR_{sp})r\cos\theta+kd^2h_2^{(1)}(kR_{sp})\right)}{h_2^{(1)}(kR_{sp})} \end{pmatrix} \tag{4.27}$$

and

$$\mathbf{n}_{00}^{2(1)}(r,\theta,\phi)=\begin{pmatrix} \dfrac{\sin\theta\sin\phi\left(2R_{sp}h_1^{(1)}(kR_{sp})+ikdh_2^{(1)}(kR_{sp})r\cos\theta+kd^2h_2^{(1)}(kR_{sp})\right)}{h_2^{(1)}(kR_{sp})} \\ \dfrac{\cos\theta\sin\phi\left(2R_{sp}h_1^{(1)}(kR_{sp})+ikdh_2^{(1)}(kR_{sp})r\cos\theta+kd^2h_2^{(1)}(kR_{sp})-kr^2h_2^{(1)}(kR_{sp})+\dfrac{ikdrh_2^{(1)}(kR_{sp})}{\cos\theta}\right)}{h_2^{(1)}(kR_{sp})} \\ \dfrac{\cos\phi\left(2R_{sp}h_1^{(1)}(kR_{sp})-kr^2h_2^{(1)}(kR_{sp})+2ikdh_2^{(1)}(kR_{sp})r\cos\theta+kd^2h_2^{(1)}(kR_{sp})\right)}{h_2^{(1)}(kR_{sp})} \end{pmatrix}. \tag{4.28}$$

In order to evaluate these vector components in the far-field limit, it is necessary to normalise these vectors. The normalisation constants are chosen to be

$$NK_{\mathbf{m}_{00}^{1(1)}}(r,0,\phi)=\sqrt{\mathbf{m}_{00,r}^{1(1)}(r,0,\phi)\mathbf{m}_{00,r}^{1(1)*}(r,0,\phi)+\mathbf{m}_{00,\theta}^{1(1)}(r,0,\phi)\mathbf{m}_{00,\theta}^{1(1)*}(r,0,\phi)+\mathbf{m}_{00,\phi}^{1(1)}(r,0,\phi)\mathbf{m}_{00,\phi}^{1(1)*}(r,0,\phi)}$$

$$NK_{\mathbf{m}_{00}^{2(1)}}(r,0,\phi)=\sqrt{\mathbf{m}_{00,r}^{2(1)}(r,0,\phi)\mathbf{m}_{00,r}^{2(1)*}(r,0,\phi)+\mathbf{m}_{00,\theta}^{2(1)}(r,0,\phi)\mathbf{m}_{00,\theta}^{2(1)*}(r,0,\phi)+\mathbf{m}_{00,\phi}^{2(1)}(r,0,\phi)\mathbf{m}_{00,\phi}^{2(1)*}(r,0,\phi)}$$

$$NK_{\mathbf{n}_{00}^{1(1)}}(r,0,\phi)=\sqrt{\mathbf{n}_{00,r}^{1(1)}(r,0,\phi)\mathbf{n}_{00,r}^{1(1)*}(r,0,\phi)+\mathbf{n}_{00,\theta}^{1(1)}(r,0,\phi)\mathbf{n}_{00,\theta}^{1(1)*}(r,0,\phi)+\mathbf{n}_{00,\phi}^{1(1)}(r,0,\phi)\mathbf{n}_{00,\phi}^{1(1)*}(r,0,\phi)}$$

and

$$NK_{\mathbf{n}_{00}^{2(1)}}(r,0,\phi)=\sqrt{\mathbf{n}_{00,r}^{2(1)}(r,0,\phi)\mathbf{n}_{00,r}^{2(1)*}(r,0,\phi)+\mathbf{n}_{00,\theta}^{2(1)}(r,0,\phi)\mathbf{n}_{00,\theta}^{2(1)*}(r,0,\phi)+\mathbf{n}_{00,\phi}^{2(1)}(r,0,\phi)\mathbf{n}_{00,\phi}^{2(1)*}(r,0,\phi)}\,. \quad (4.29)$$

Additionally, $\theta=0$ is substituted into the normalisation constants, since the functions are normalised on the $\theta=0$ axis as mentioned earlier. Performing now the calculation of the limit of the normalised functions leads to

$$\lim_{r\to\infty}\left(\frac{\mathbf{m}_{00}^{1(1)}(r,\theta,\phi)}{NK_{\mathbf{m}_{00}^{1(1)}}(r,0,\phi)}\right)=-\begin{pmatrix}0\\ \sin\phi\\ \cos\theta\cos\phi\end{pmatrix}\quad , \quad (4.30)$$

$$\lim_{r\to\infty}\left(\frac{\mathbf{m}_{00}^{2(1)}(r,\theta,\phi)}{NK_{\mathbf{m}_{00}^{2(1)}}(r,0,\phi)}\right)=\begin{pmatrix}0\\ \cos\phi\\ -\cos\theta\sin\phi\end{pmatrix}\quad , \quad (4.31)$$

$$\lim_{r\to\infty}\left(\frac{\mathbf{n}_{00}^{1(1)}(r,\theta,\phi)}{NK_{\mathbf{n}_{00}^{1(1)}}(r,0,\phi)}\right)=i\begin{pmatrix}0\\ \cos\theta\cos\phi\\ -\sin\phi\end{pmatrix} \quad (4.32)$$

and

$$\lim_{r\to\infty}\left(\frac{\mathbf{n}_{00}^{2(1)}(r,\theta,\phi)}{NK_{\mathbf{n}_{00}^{2(1)}}(r,0,\phi)}\right)=i\begin{pmatrix}0\\ \cos\theta\sin\phi\\ \cos\phi\end{pmatrix}\quad . \quad (4.33)$$

Repeating this procedure for order 01 leads to

$$\lim_{r\to\infty}\left(\sqrt{\frac{A_{01}(r,\theta)A_{01}^{*}(r,\theta)}{A_{01}(r,0)A_{01}^{*}(r,0)}}\right)=\lim_{r\to\infty}\left(\sqrt{\frac{B_{01}(r,\theta)B_{01}^{*}(r,\theta)}{B_{01}(r,0)B_{01}^{*}(r,0)}}\right)=\lim_{r\to\infty}\left(\sqrt{\frac{A_{01}(r,\theta)B_{01}^{*}(r,\theta)}{A_{01}(r,0)B_{01}^{*}(r,0)}}\right)=$$

$$\lim_{r\to\infty}\left(\sqrt{\frac{A_{01}^{*}(r,\theta)B_{01}(r,\theta)}{A_{01}^{*}(r,0)B_{01}(r,0)}}\right)=\lim_{r\to\infty}\left(\frac{A_{01}(r,\theta)}{A_{01}(r,0)}\right)=\lim_{r\to\infty}\left(\frac{B_{01}(r,\theta)}{B_{01}(r,0)}\right)=\sqrt{\cos^{2}\theta e^{-2kd(1-\cos\theta)}}=\cos\theta e^{-kd(1-\cos\theta)}\text{,}$$

(4.34)

where

$$A_{01}(r,\theta)=\frac{e^{-kd}h_{2}^{(1)}(kR_{sp})(r\cos\theta-id)}{R_{sp}^{2}}$$

and

$$B_{01}(r,\theta)=\frac{e^{-kd}h_{2}^{(1)}(kR_{sp})(r\cos\theta-id)}{kR_{sp}^{4}};$$

$$\lim_{r\to\infty}\left(\frac{\mathbf{m}_{01}^{1(1)}(r,\theta,\phi)}{NK_{\mathbf{m}_{01}^{1(1)}}(r,0,\phi)}\right)=-\begin{pmatrix}0\\\sin\phi\\\cos\theta\cos\phi\end{pmatrix},\tag{4.35}$$

$$\lim_{r\to\infty}\left(\frac{\mathbf{m}_{01}^{2(1)}(r,\theta,\phi)}{NK_{\mathbf{m}_{01}^{2(1)}}(r,0,\phi)}\right)=\begin{pmatrix}0\\\cos\phi\\-\cos\theta\sin\phi\end{pmatrix},\tag{4.36}$$

$$\lim_{r\to\infty}\left(\frac{\mathbf{n}_{01}^{1(1)}(r,\theta,\phi)}{NK_{\mathbf{n}_{01}^{1(1)}}(r,0,\phi)}\right)=i\begin{pmatrix}0\\\cos\theta\cos\phi\\-\sin\phi\end{pmatrix}\tag{4.37}$$

and

$$\lim_{r\to\infty}\left(\frac{\mathbf{n}_{01}^{2(1)}(r,\theta,\phi)}{NK_{\mathbf{n}_{01}^{2(1)}}(r,0,\phi)}\right)=i\begin{pmatrix}0\\\cos\theta\sin\phi\\\cos\phi\end{pmatrix},\tag{4.38}$$

where the normalisation constants $NK_{\mathbf{m}_{01}^{1(1)}}(r,0,\phi)$, $NK_{\mathbf{m}_{01}^{2(1)}}(r,0,\phi)$, $NK_{\mathbf{n}_{01}^{1(1)}}(r,0,\phi)$ and $NK_{\mathbf{n}_{01}^{2(1)}}(r,0,\phi)$ were calculated in accordance with Eqs. (4.29). Again like in the case of order 00, it can be seen by comparing Eq. (4.34) with the second equation of Eqs. (2.72) that Eq. (4.34) is equal to the square root of the second equation of Eqs. (2.72). Thus a

clear relationship between the far-field limit of the scalar and vector functions is established. It can be seen by comparing Eqs.(4.30) - (4.33) with Eqs. (4.35) - (4.38) that the vector components of order 00 and order 01 are identical in the far-field limit. Furthermore, as expected, the radial components in Eqs.(4.30)-(4.33) and Eqs. (4.35)-(4.38) are all zero. Figs 4.1. show field plots of the $\mathbf{M}_{01}^{1(1)}(\theta,\phi)$ and $i\mathbf{N}_{01}^{2(1)}(\theta,\phi)$ functions respectively on the surface of a Gaussian reference hemisphere mapped onto a circle of radius $\frac{\pi}{2}$ in the far-field limit.

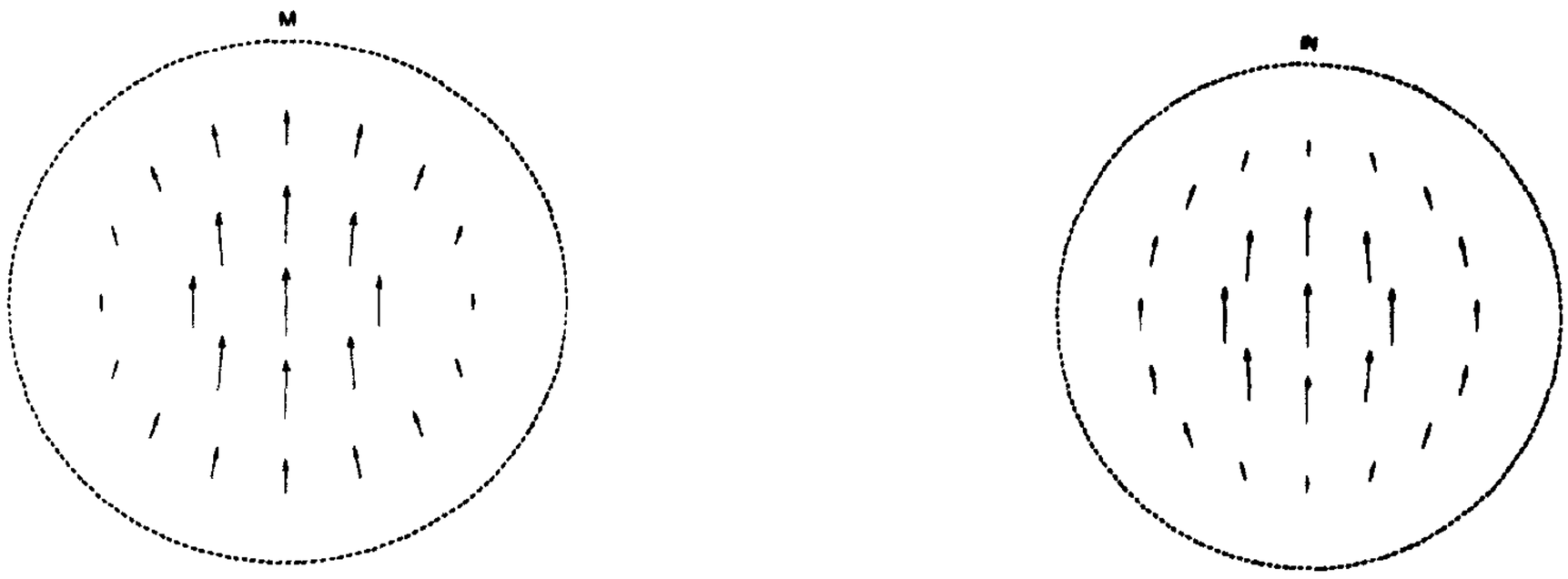

Fig 4. 1. Field plots of the $\mathbf{M}_{01}^{(1)1}(\theta,\phi)$ and $i\mathbf{N}_{01}^{(2)1}(\theta,\phi)$ functions on the surface of a Gaussian reference hemisphere mapped onto a circle of radius $\frac{\pi}{2}$ in the far-field limit.

It can be seen from Figs. 4.1. or by inspecting Eqs. (4.7), Eqs.(4.30) - (4. 33) and Eqs. (4.35) - (4.38) that a suitable trial superposition for the electric field is

$$\mathbf{E}_{mn}(r,\theta,\phi) = E_0(\mathbf{M}_{mn}^{(1)}(r,\theta,\phi) + i\mathbf{N}_{mn}^{(2)}(r,\theta,\phi)), \tag{4.39}$$

since this electric field for m=0 and n=0 or 1 has the same polarisation pattern as the one given by Eq. (4.7). The magnetic field can be written in accordance with Eq. (4.1.b) as

$$\mathbf{H}_{mn}(r,\theta,\phi) = -iE_0\sqrt{\frac{\varepsilon}{\mu_0}}(i\mathbf{M}_{mn}^{(2)}(r,\theta,\phi) + \mathbf{N}_{mn}^{(1)}(r,\theta,\phi)). \tag{4.40}$$

It can also be seen from Eqs. (4.39) and (4.40) that, as expected, the vector functions derived form the polarisation with the constant guiding vector $\mathbf{c}^3$ are not needed to form the E.M. field. The next step is to compare the superposition of the $\mathbf{m}_{mn}^{1(1)}(x,y,z)$, $\mathbf{m}_{mn}^{2(1)}(x,y,z)$, $\mathbf{n}_{mn}^{1(1)}(x,y,z)$ and $\mathbf{n}_{mn}^{2(1)}(x,y,z)$ functions of both orders with Eqs. (4.2). It is to note at this point that any signs in front of these vectors, as mentioned earlier, are meaningless, since the signs of the amplitude functions $A_{00}(r,\theta)$, $B_{00}(r,\theta)$, $A_{01}(r,\theta)$ and $B_{01}(r,\theta)$ can not be determined. It is thus necessary to compute the far-field limit of the electric and magnetic fields given by Eqs. (4.39) and (4.40). Again it is possible to factorise these functions into

$$\mathbf{E}_{00}(r,\theta,\phi)=E_0A_{00}(r,\theta)\left(\mathbf{m}_{00}^{1(1)}(r,\theta,\phi)+\frac{ih_2^{(1)}(kR_{sp})}{kR_{sp}h_1^{(1)}(kR_{sp})}\mathbf{n}_{00}^{2(1)}(r,\theta,\phi)\right)=E_0A_{00}(r,\theta)\mathbf{E}_{f,00}(r,\theta,\phi) \tag{4.41}$$

and

$$\mathbf{H}_{00}(r,\theta,\phi)=-iE_0\sqrt{\frac{\varepsilon}{\mu_0}}A_{00}(r,\theta)\left(i\mathbf{m}_{00}^{2(1)}(r,\theta,\phi)+\frac{h_2^{(1)}(kR_{sp})}{kR_{sp}h_1^{(1)}(kR_{sp})}\mathbf{n}_{00}^{1(1)}(r,\theta,\phi)\right)=-iE_0\sqrt{\frac{\varepsilon}{\mu_0}}A_{00}(r,\theta)\mathbf{H}_{f,00}(r,\theta,\phi). \tag{4.42}$$

for the 00 order. In order to calculate the far-field limit of the electric and magnetic vector, only the sum inside the brackets, i.e. $\mathbf{E}_{f,00}(r,\theta,\phi)$ and $\mathbf{H}_{f,00}(r,\theta,\phi)$ needs to be considered, since the time averaged amplitude $A_{00}(r,\theta)$ in the far-field limit will not change, and is thus given by Eq. (4.24). The normalisation constants here are given by

$$NKE_{f,00}(r,0,\phi)=\sqrt{\mathbf{E}_{f,00,r}(r,0,\phi)\mathbf{E}_{f,00,r}^{*}(r,0,\phi)+\mathbf{E}_{f,00,\theta}(r,0,\phi)\mathbf{E}_{f,00,\theta}^{*}(r,0,\phi)+\mathbf{E}_{f,00,\phi}(r,0,\phi)\mathbf{E}_{f,00,\phi}^{*}(r,0,\phi)}$$

and

$$NKH_{f,00}(r,0,\phi)=\sqrt{\mathbf{H}_{f,00,r}(r,0,\phi)\mathbf{H}_{f,00,r}^{*}(r,0,\phi)+\mathbf{H}_{f,00,\theta}(r,0,\phi)\mathbf{H}_{f,00,\theta}^{*}(r,0,\phi)+\mathbf{H}_{f,00,\phi}(r,0,\phi)\mathbf{H}_{f,00,\phi}^{*}(r,0,\phi)},$$

with θ=0 substituted. Performing now the calculation of the limit of the normalised functions leads to

$$\lim_{r\to\infty}\left(\frac{\mathbf{E}_{f,00}(r,\theta,\phi)}{NKE_{f,00}(r,0,\phi)}\right)=-\frac{1}{2}(1+\cos\theta)\begin{pmatrix}0\\ \sin\phi\\ \cos\phi\end{pmatrix} \tag{4.43}$$

and

$$\lim_{r\to\infty}\left(\frac{\mathbf{H}_{f,00}(r,\theta,\phi)}{NKH_{f,00}(r,0,\phi)}\right)=\frac{i}{2}(1+\cos\theta)\begin{pmatrix}0\\ \cos\phi\\ -\sin\phi\end{pmatrix}. \qquad (4.44)$$

Repeating this procedure for order 01 with

$$\mathbf{E}_{01}(r,\theta,\phi)=E_0A_{01}(r,\theta)\left(\mathbf{m}_{01}^{1(1)}(r,\theta,\phi)+\frac{i}{kR_{sp}^2}\mathbf{n}_{01}^{2(1)}(r,\theta,\phi)\right)=E_0A_{01}(r,\theta)\mathbf{E}_{f,01}(r,\theta,\phi) \qquad (4.45)$$

and

$$\mathbf{H}_{01}(r,\theta,\phi)=-iE_0\sqrt{\frac{\varepsilon}{\mu_0}}A_{01}(r,\theta)\left(i\mathbf{m}_{01}^{2(1)}(r,\theta,\phi)+\frac{1}{kR_{sp}^2}\mathbf{n}_{01}^{1(1)}(r,\theta,\phi)\right)=-iE_0\sqrt{\frac{\varepsilon}{\mu_0}}A_{01}(r,\theta)\mathbf{H}_{f,01}(r,\theta,\phi). \qquad (4.46)$$

leads to

$$\lim_{r\to\infty}\left(\frac{\mathbf{E}_{f,01}(r,\theta,\phi)}{NKE_{f,01}(r,0,\phi)}\right)=-\frac{1}{2}(1+\cos\theta)\begin{pmatrix}0\\ \sin\phi\\ \cos\phi\end{pmatrix} \qquad (4.47)$$

and

$$\lim_{r\to\infty}\left(\frac{\mathbf{H}_{f,01}(r,\theta,\phi)}{NKH_{f,01}(r,0,\phi)}\right)=\frac{i}{2}(1+\cos\theta)\begin{pmatrix}0\\ \cos\phi\\ -\sin\phi\end{pmatrix}. \qquad (4.48)$$

It can be clearly seen by comparing Eqs.(4.43) and (4.44) with Eqs. (4.47) and (4.48) that in the far-field limit the electric and magnetic fields for order 00 and order 01 differ only in their time averaged amplitude functions. Field plots of the electric and magnetic field respectively on the surface of a Gaussian reference hemisphere mapped onto a circle of radius $\frac{\pi}{2}$ in the far-field limit are shown in Figs. 4.2. and Figs. 4.3. respectively for values of kd=1, 10.

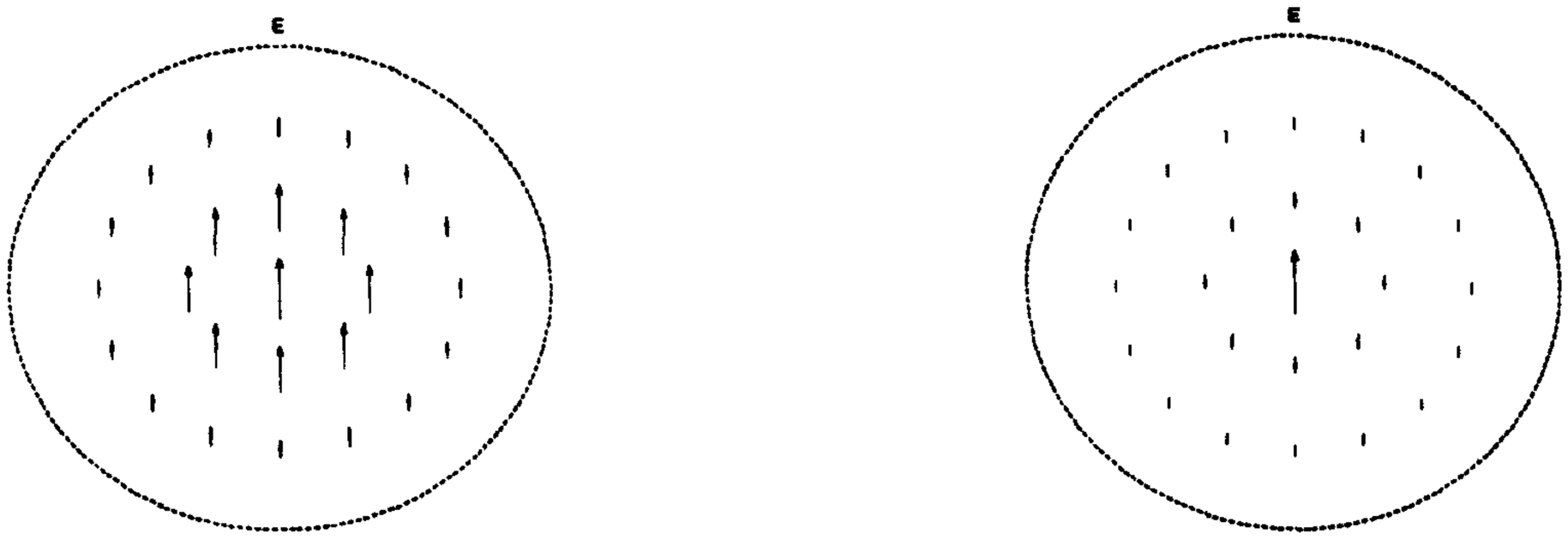

Fig. 4.2. **E** field obtained for $kd = 1$ and $kd = 10$ from Eq. (4.47), plotted as in Fig. 4.1.

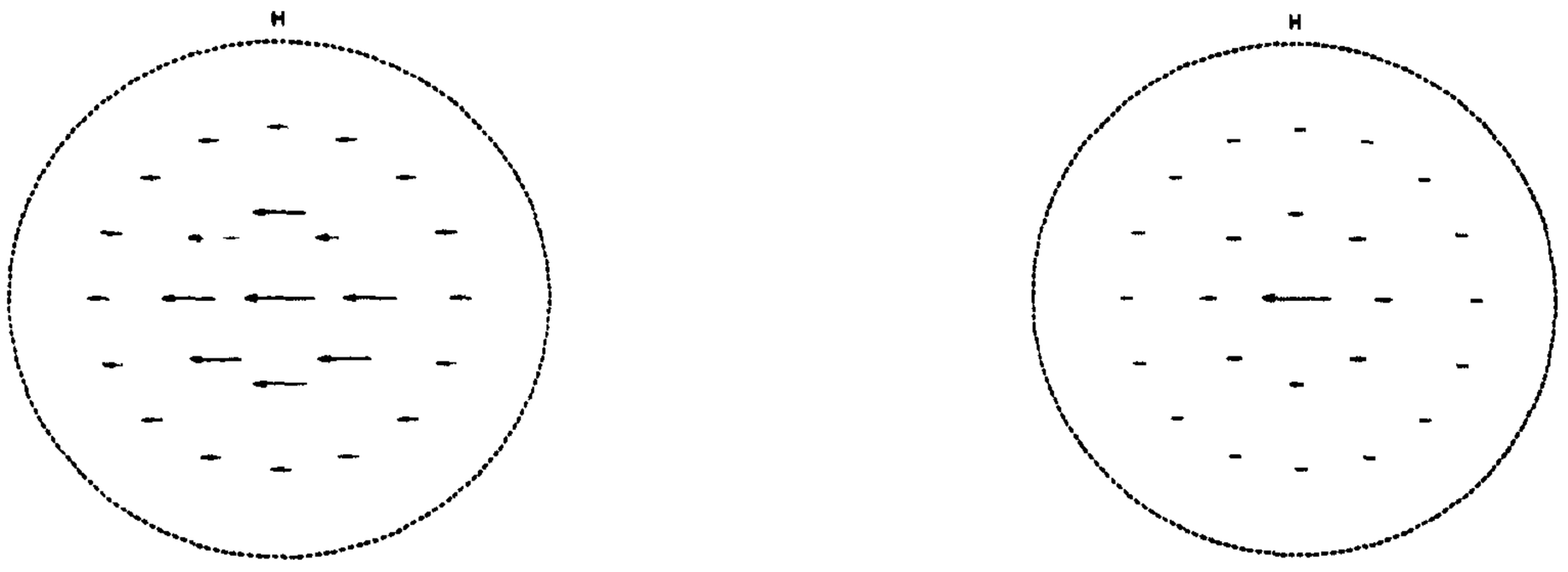

Fig. 4.3. **H** field obtained for $kd = 1$ and $kd = 10$ from Eq. (4.48), plotted as in Fig. 4.1.

Since these functions are expressed in spherical polar coordinates and the functions in Eqs. (4.2) are expressed in Cartesian coordinates, it is necessary to transform them back into Cartesian coordinates. This transformation is achieved by using the transformation matrix given in Eq. (4.5). Performing this calculation it is found that the normalised on-axis, time-averaged electric and magnetic fields of order 00 are given by

$$\mathbf{E}_{00}(x,y,z) = -\frac{1}{2}E_0 e^{-kd(1-\cos\theta)}(1+\cos\theta)\begin{pmatrix}(\cos\theta - 1)\cos\phi\sin\phi\\ 1-\sin^2\phi(1-\cos\theta)\\ -\sin\theta\sin\phi\end{pmatrix} \tag{4.49}$$

and

$$\mathbf{H}_{00}(x,y,z)=\frac{1}{2}E_0\sqrt{\frac{\varepsilon}{\mu_0}}e^{-kd(1-\cos\theta)}(1+\cos\theta)\begin{pmatrix}\cos\theta+\sin^2\phi(1-\cos\theta)\\(\cos\theta-1)\cos\phi\sin\phi\\-\sin\theta\cos\phi\end{pmatrix}, \quad (4.50)$$

where θ and ϕ are given by Eqs. (2.7). Similarly it is found that the normalised on-axis, time-averaged electric and magnetic fields of order 01 are given by

$$\mathbf{E}_{01}(x,y,z)=-\frac{1}{2}E_0e^{-kd(1-\cos\theta)}\cos\theta(1+\cos\theta)\begin{pmatrix}(\cos\theta-1)\cos\phi\sin\phi\\1-\sin^2\phi(1-\cos\theta)\\-\sin\theta\sin\phi\end{pmatrix} \quad (4.51)$$

and

$$\mathbf{H}_{01}(x,y,z)=\frac{1}{2}E_0\sqrt{\frac{\varepsilon}{\mu_0}}e^{-kd(1-\cos\theta)}\cos\theta(1+\cos\theta)\begin{pmatrix}\cos\theta+\sin^2\phi(1-\cos\theta)\\(\cos\theta-1)\cos\phi\sin\phi\\-\sin\theta\cos\phi\end{pmatrix}. \quad (4.52)$$

By comparing Eqs. (4.49), (4.50), (4.51) and (4.52) with Eqs. (4.2) it is found that they are identical with respect to their polarisation patterns. Since the fact that the electric field in Eqs. (4.2) is proportional to the magnetic field given in Eqs. (4.50) and (4.52) respectively and the magnetic field in Eqs. (4.2) is proportional to the electric field given in Eqs. (4.49) and (4.51) respectively is of no significance, as this only implies that the fields are rotated with respect to each other. Hence this section can be concluded by stating that indeed the superposition chosen leads to an E.M. field which satisfies Maxwell's equations and in the far-field limit satisfies the Richards and Wolf [1] polarisation conditions. Additionally the problem which was present in the scalar case that $Q_{00}(\alpha)$ did not go to zero at $\alpha=\pm\frac{\pi}{2}$ is still present in the vector case, (see Eqs. (4.49) and (4.50), replacing α with θ). It can be seen, like in the scalar case, from Eqs. (4.51) and (4.52), that the E.M. field of order 01 goes to zero at $\theta=\pm\frac{\pi}{2}$. However, the common factor in the order 00 case, (see Eqs. (4.49) and (4.50)),

$$e^{-kd(1-\cos\theta)}(1+\cos\theta) \quad (4.53)$$

and the common factor in the order 01 case, (see Eqs. (4.51) and (4.52)),

$$e^{-kd(1-\cos\theta)}\cos\theta(1+\cos\theta) \quad (4.54)$$

are not identical to the ones of Richards and Wolf [1]. Sheppard and Saghafi [5] have pointed out, that the factor $(1+\cos\theta)$ corresponds to the E.M. field amplitude of an electric and magnetic mixed dipole pair. Additionally it is mentioned in [5] that the Gaussian function $e^{1-\cos\theta}$ is of the form produced by focusing by a system satisfying the Herschel condition. The combination of these factors is rather interesting, since according to Sheppard and Gu [6] the Abbe sine and Herschel condition cannot hold simultaneously. However the common factors in Eqs. (4.53) and (4.54) are for a Gaussian beam which satisfies Maxwell's equations. Thus it is expected that the far-field amplitude profile is slightly different from the one produced by focusing of a plane wave with an aberration free lens satisfying the Abbe sine or the Herschel condition. The amplitude profile given by Eq. (4.54) corresponds to a hemisphere of incoming radiation, as expected, where the amplitude profile given by Eq. (4.53) corresponds to an entire sphere of incoming radiation. However, as mentioned in chapter 2, there was concern with reference to the order 00 case, as the amplitude does not go to zero at $\theta = \pm\frac{\pi}{2}$. Sheppard and Saghafi [5] have introduced an additional common factor for this case in their scalar treatment, namely

$$\frac{1+\cos\theta}{2}.$$

By introducing this factor, their solution is not an exact solution to the Helmholtz equation any more, even though, as they pointed out, the function still has the correct form in the paraxial limit. However, if Sheppard and Saghafi [5] would have considered the vector case instead, they would have found that this factor is not needed, as can be seen from Eq. (4.53).

4.2.3. The derived E.M. field

By substituting $\alpha_1=1$, $\alpha_2=\alpha_3=0$, $\beta_2=i$ $\beta_1=\beta_3=0$, $m=0$ and $n=0,1$ in Eqs. (4.1.a) and (4.1.b) it can be seen from Eqs. (4.49) - (4.52) that the criteria b), c) and f) are satisfied. Thus the E.M. field due to order 00 can be written in Cartesian coordinates as

$$\mathbf{E}_{00}(x,y,z)=\frac{E_0 e^{-kd}}{R^2}\begin{pmatrix} ixyj_2(kR) \\ -R(z-id)j_1(kR)+ij_2(kR)\left(2\frac{Rj_1(kR)}{kj_2(kR)}-R^2+y^2\right) \\ y(Rj_1(kR)+i(z-id)j_2(kR)) \end{pmatrix} \tag{4.55}$$

and

$$\mathbf{H}_{00}(x,y,z)=\frac{-iE_0e^{-kd}}{R^2}\sqrt{\frac{\varepsilon}{\mu_0}}\begin{pmatrix} iR(z-id)j_1(kR)+j_2(kR)\left(2\dfrac{Rj_1(kR)}{kj_2(kR)}-R^2+x^2\right)\\ xyj_2(kR)\\ x\left(-iRj_1(kR)+(z-id)j_2(kR)\right)\end{pmatrix} \tag{4.56}$$

and the E.M. field due to order 01 as

$$\mathbf{E}_{01}(x,y,z)=\frac{E_0(z-id)e^{-kd}j_2(kR)}{kR^4}\begin{pmatrix} kR^2\left(\dfrac{Rj_1(kR)}{k(z-id)j_2(kR)}-(z-id)\right)+i\left(4R^2-\left(R^2-y^2\right)\left(5-\dfrac{kRj_1(kR)}{j_2(kR)}\right)\right)\\ y\left(kR^2-i\left(\dfrac{R^2}{z-id}-(z-id)\left(5-\dfrac{kRj_1(kR)}{j_2(kR)}\right)\right)\right)\end{pmatrix}$$

$$ixy\left(5-\frac{kRj_1(kR)}{j_2(kR)}\right) \tag{4.57}$$

and

$$\mathbf{H}_{01}(x,y,z)=\frac{-iE_0e^{-kd}j_2(kR)(z-id)}{kR^4}\sqrt{\frac{\varepsilon}{\mu_0}}\begin{pmatrix} -ikR^2\left(\dfrac{Rj_1(kR)}{k(z-id)j_2(kR)}-(z-id)\right)+4R^2-\left(R^2-x^2\right)\left(5-\dfrac{kRj_1(kR)}{j_2(kR)}\right)\\ xy\left(5-\dfrac{kRj_1(kR)}{j_2(kR)}\right)\\ x\left(-ikR^2\dfrac{R^2}{z-id}+(z-id)\left(5-\dfrac{kRj_1(kR)}{j_2(kR)}\right)\right)\end{pmatrix}. \tag{4.58}$$

From the scalar treatment of the orders 00 and 01, it is expected that criteria a) and e) are satisfied by the electromagnetic field of both orders, however it is expected that criterion g) is only satisfied by the electromagnetic field of order 01. Thus in the remainder of this chapter, it will be investigated as if the remaining criteria are satisfied.

4.3. The polarisation

It is customary in discussion of polarisation to focus attention on the electric field $\mathbf{E}(\mathbf{r},t)$. It will be explained in detail in chapter 5 that the operational principle of laser tweezers is based on the reflectance and transmittance of the E.M. radiation by the trapped object. It will also be demonstrated in chapter 5 that the reflectance and transmittance of the incident E.M. radiation is polarisation dependent. It is therefore appropriate to investigate the polarisation property of the $\mathbf{E}_{mn}(x,y,z)$ fields given in Eqs. (4.55) and (4.57) for order 00 and order 01 next. An E.M. wave can be either linearly, circularly (left and right handed) or elliptically (left and right handed) polarised. Lekner [7] has described the different types of polarisation by determining the degree of linear and circular polarisation respectively. Since at any fixed plane in space, the tip of the electric vector describes an ellipse within one period of the field (i.e. in the time $\frac{2\pi}{\omega}$ [7]), it is possible to rewrite Eqs. (1.27) as

$$\mathbf{E}_R(\mathbf{r},0)+i\mathbf{E}_I(\mathbf{r},0)=\left(\mathbf{E}_1(\mathbf{r},0)+i\mathbf{E}_2(\mathbf{r},0)\right)e^{i\sigma}, \tag{4.59}$$

where

$$\mathbf{E}_1(\mathbf{r},0)=\mathbf{E}_R(\mathbf{r},0)\cos\sigma+\mathbf{E}_I(\mathbf{r},0)\sin\sigma$$

and

$$\mathbf{E}_2(\mathbf{r},0)=-\mathbf{E}_R(\mathbf{r},0)\sin\sigma+\mathbf{E}_I(\mathbf{r},0)\cos\sigma.$$

The advantage of Eq. (4.59) is that σ can be chosen so that the real vectors $\mathbf{E}_1(\mathbf{r},t)$ and $\mathbf{E}_2(\mathbf{r},t)$ are perpendicular. Thus the value of σ is given by

$$\tan 2\sigma=\frac{2\mathbf{E}_R(\mathbf{r},0)\bullet\mathbf{E}_I(\mathbf{r},0)}{E_R^2(\mathbf{r},0)-E_I^2(\mathbf{r},0)}. \tag{4.60}$$

In the plane of $(\mathbf{E}_R(\mathbf{r},0), \mathbf{E}_I(\mathbf{r},0))$ or $(\mathbf{E}_1(\mathbf{r},0), \mathbf{E}_2(\mathbf{r},0))$ the electric field

$$\mathbf{E}(\mathbf{r},t)=\mathrm{Re}\left(\left(\mathbf{E}_1(\mathbf{r},0)+i\mathbf{E}_2(\mathbf{r},0)\right)e^{i(\sigma-\omega t)}\right)=\mathbf{E}_1(\mathbf{r},0)\cos(\omega t-\sigma)+\mathbf{E}_2(\mathbf{r},0)\sin(\omega t-\sigma)$$

has orthogonal components $\mathbf{E}_1(\mathbf{r},0)$ and $\mathbf{E}_2(\mathbf{r},0)$ provided σ satisfies Eq. (4.60) with magnitudes given by

$$E_1^2(\mathbf{r},0)=\frac{1}{2}\left[E_R^2(\mathbf{r},0)+E_I^2(\mathbf{r},0)+\sqrt{\left(E_R^2(\mathbf{r},0)-E_I^2(\mathbf{r},0)\right)^2+4\left(\mathbf{E}_R(\mathbf{r},0)\bullet\mathbf{E}_I(\mathbf{r},0)\right)^2}\right]$$

and

$$E_2^2(\mathbf{r},0)=\frac{1}{2}\left[E_R^2(\mathbf{r},0)+E_I^2(\mathbf{r},0)-\sqrt{\left(E_R^2(\mathbf{r},0)-E_I^2(\mathbf{r},0)\right)^2+4\left(\mathbf{E}_R(\mathbf{r},0)\bullet\mathbf{E}_I(\mathbf{r},0)\right)^2}\right], \tag{4.61}$$

where the lengths of the semi-axes of the vibration ellipse can be identified with $E_1(\mathbf{r},0)$ and $E_2(\mathbf{r},0)$. The E.M. wave is linearly polarised if $E_2(\mathbf{r},0)=0$, which requires $\mathbf{E}_R(\mathbf{r},0)$ and $\mathbf{E}_I(\mathbf{r},0)$ to be collinear, or in mathematical terms

$$E_R^2(\mathbf{r},0)E_I^2(\mathbf{r},0)-\left(\mathbf{E}_R(\mathbf{r},0)\bullet\mathbf{E}_I(\mathbf{r},0)\right)^2=0 \tag{4.62}$$

The E.M. wave is circularly polarised if $E_1^2(\mathbf{r},0)=E_2^2(\mathbf{r},0)$, thus it is required that $\mathbf{E}_R(\mathbf{r},0)$ and $\mathbf{E}_I(\mathbf{r},0)$ are perpendicular to each other and have equal magnitude. In mathematical terms this condition can be written as

$$\mathbf{E}_R(\mathbf{r},0)\bullet\mathbf{E}_I(\mathbf{r},0)=0 \text{ and } E_R^2(\mathbf{r},0)=E_I^2(\mathbf{r},0) \tag{4.63}$$

The degree of linear polarisation, $\Lambda(\mathbf{r},0)$, of a coherent monochromatic electric wave is

$$\Lambda(\mathbf{r},0)=\frac{\sqrt{\left(E_R^2(\mathbf{r},0)-E_I^2(\mathbf{r},0)\right)^2+4\left(\mathbf{E}_R(\mathbf{r},0)\bullet\mathbf{E}_I(\mathbf{r},0)\right)^2}}{E_R^2(\mathbf{r},0)+E_I^2(\mathbf{r},0)}=\frac{\left|\mathbf{E}^2(\mathbf{r},0)\right|}{\left|\mathbf{E}(\mathbf{r},0)\right|^2}. \tag{4.64}$$

$\Lambda(\mathbf{r},0)=1$ implies that the electric field is linearly polarised, if $\Lambda(\mathbf{r},0)=0$, then the electric field is circularly polarised.

4.3.1. The polarisation of the electric field at the beam waist

In order to determine the polarisation of the electric field of order 00 and order 01 at the beam waist, it is necessary to first investigate the spherical Bessel functions of order 0, 1 and 2 at the beam waist. Again the region inside the focal circle is considered first. In this region the complex radius given by Eq. (2.39) can be rewritten as

$$R_{in} = i\sqrt{d^2 - \rho^2} \ . \tag{4.65}$$

It is found that in this region the spherical Bessel functions of order 0 and 2 are purely real and the spherical Bessel function of order 1 and the complex radius are purely imaginary. In the region outside the focal circle the complex radius given by Eq. (2.39) can be rewritten as

$$R_{out} = \sqrt{\rho^2 - d^2} \qquad . \tag{4.66}$$

It is found that in this region, the complex radius and the spherical Bessel functions of order 0, 1, 2 are real. From Eq. (4.39) it can be seen that in order to determine the polarisation of the electric field, it is easiest to evaluate the real and imaginary parts of the $\mathbf{M}^1_{mn}(x,y,z)$ and $\mathbf{N}^2_{mn}(x,y,z)$ functions first. At the beam waist, these functions for order 00 can be written, using Eqs. (3.22.a) and (3.23.b), as

$$\mathbf{M}^1_{00}(x,y,0) = \frac{e^{-kd} j_1(kR)}{R} \begin{pmatrix} 0 \\ id \\ y \end{pmatrix} \tag{4.67}$$

and

$$\mathbf{N}^2_{00}(x,y,0) = \frac{e^{-kd} j_2(kR)}{R^2} \begin{pmatrix} xy \\ 2R\dfrac{j_1(kR)}{kj_2(kR)} - x^2 + d^2 \\ -iyd \end{pmatrix}. \tag{4.68}$$

It then follows that inside the focal circle the real and imaginary parts of $\mathbf{M}^{1}_{00,inside}(x,y,0)$ are given by

$$\mathrm{Re}\left[\mathbf{M}^{1}_{00,inside}(x,y,0)\right]=\frac{e^{-kd}\,j_1(kR_{in})}{R_{in}}\begin{pmatrix}0\\0\\y\end{pmatrix} \tag{4.69}$$

and

$$\mathrm{Im}\left[\mathbf{M}^{1}_{00,inside}(x,y,0)\right]=\frac{e^{-kd}\,j_1(kR_{in})}{R_{in}}\begin{pmatrix}0\\d\\0\end{pmatrix} \quad . \tag{4.70}$$

The real and imaginary parts of $\mathbf{N}^{2}_{00,inside}(x,y,0)$ inside the focal circle are given by

$$\mathrm{Re}\left[\mathbf{N}^{2}_{00,inside}(x,y,0)\right]=\frac{e^{-kd}\,j_2(kR_{in})}{R_{in}^{2}}\begin{pmatrix}xy\\2R_{in}\dfrac{j_1(kR_{in})}{kj_2(kR_{in})}-x^2+d^2\\0\end{pmatrix} \tag{4.71}$$

and

$$\mathrm{Im}\left[\mathbf{N}^{2}_{00,inside}(x,y,0)\right]=\frac{e^{-kd}\,j_2(kR_{in})}{R_{in}^{2}}\begin{pmatrix}0\\0\\-dy\end{pmatrix} \quad . \tag{4.72}$$

Thus at the beam waist, inside the focal circle, the real and imaginary part of the electric field of order 00 are given, using Eq. (4.39) and Eqs. (4.69) – (4.72), by

$$\mathrm{Re}\left[\mathbf{E}_{00,inside}(x,y,0)\right]=E_0\left[\frac{e^{-kd}\,j_1(kR_{in})}{R_{in}}\begin{pmatrix}0\\0\\y\end{pmatrix}+\frac{e^{-kd}\,j_2(kR_{in})}{R_{in}^{2}}\begin{pmatrix}0\\0\\dy\end{pmatrix}\right] \tag{4.73}$$

and

$$\mathrm{Im}\left[\mathbf{E}_{00,inside}(x,y,0)\right]=E_0\left[\frac{e^{-kd}j_1(kR_{in})}{R_{in}}\begin{pmatrix}0\\d\\0\end{pmatrix}+\frac{e^{-kd}j_2(kR_{in})}{R_{in}^2}\begin{pmatrix}xy\\2R_{in}\dfrac{j_1(kR_{in})}{kj_2(kR_{in})}-x^2+d^2\\0\end{pmatrix}\right]. \quad (4.74)$$

It can be seen form Eq. (4.73) and Eq. (4.74) that the real and imaginary parts are not collinear. Additionally

$$\mathrm{Re}\left[\mathbf{E}_{00,inside}(x,y,0)\right]\bullet\mathrm{Im}\left[\mathbf{E}_{00,inside}(x,y,0)\right]=0 \text{ and } \left|\mathrm{Re}\left[\mathbf{E}_{00,inside}(x,y,0)\right]\right|\neq\left|\mathrm{Im}\left[\mathbf{E}_{00,inside}(x,y,0)\right]\right|.$$

Thus using the definitions for polarisation given in section 4.3. it can be concluded that the electric field at the beam waist inside the focal circle is elliptically polarised.

Outside the focal circle the real and imaginary parts of $\mathbf{M}^1_{00,outside}(x,y,0)$ are given by

$$\mathrm{Re}\left[\mathbf{M}^1_{00,outside}(x,y,0)\right]=\frac{e^{-kd}j_1(kR_{out})}{R_{out}}\begin{pmatrix}0\\0\\y\end{pmatrix} \quad (4.75)$$

and

$$\mathrm{Im}\left[\mathbf{M}^1_{00,outside}(x,y,0)\right]=\frac{e^{-kd}j_1(kR_{out})}{R_{out}}\begin{pmatrix}0\\d\\0\end{pmatrix}. \quad (4.76)$$

The real and imaginary parts outside the focal circle of $\mathbf{N}^2_{00,outside}(x,y,0)$ are given by

$$\mathrm{Re}\left[\mathbf{N}^2_{00,outside}(x,y,0)\right]=\frac{e^{-kd}j_2(kR_{out})}{R_{out}^2}\begin{pmatrix}xy\\2R_{out}\dfrac{j_1(kR_{out})}{kj_2(kR_{out})}-x^2+d^2\\0\end{pmatrix} \quad (4.77)$$

and

$$\mathrm{Im}\left[\mathbf{N}^{2}_{00,outside}(x,y,0)\right]=\frac{e^{-kd}\,j_2(kR_{out})}{R^2_{out}}\begin{pmatrix}0\\0\\-dy\end{pmatrix}\quad . \tag{4.78}$$

Thus the real and imaginary part of the electric field outside the focal circle of order 00 at the beam waist, using Eq. (4.39) and Eqs. (4.75) – (4.78), are given by

$$\mathrm{Re}\left[\mathbf{E}_{00,outside}(x,y,0)\right]=E_0\left[\frac{e^{-kd}\,j_1(kR_{out})}{R_{out}}\begin{pmatrix}0\\0\\y\end{pmatrix}+\frac{e^{-kd}\,j_2(kR_{out})}{R^2_{out}}\begin{pmatrix}0\\0\\dy\end{pmatrix}\right] \tag{4.79}$$

and

$$\mathrm{Im}\left[\mathbf{E}_{00,outside}(x,y,0)\right]=E_0\left[\frac{e^{-kd}\,j_1(kR_{out})}{R_{out}}\begin{pmatrix}0\\d\\0\end{pmatrix}+\frac{e^{-kd}\,j_2(kR_{out})}{R^2_{out}}\begin{pmatrix}xy\\2R_{out}\dfrac{j_1(kR_{out})}{kj_2(kR_{out})}-x^2+d^2\\0\end{pmatrix}\right]. \tag{4.80}$$

It can be seen form Eq. (4.79) and Eq. (4.80) that the real and imaginary parts are not collinear. Additionally

$$\mathrm{Re}\left[\mathbf{E}_{00,outside}(x,y,0)\right]\bullet\mathrm{Im}\left[\mathbf{E}_{00,outside}(x,y,0)\right]=0 \text{ and } \left|\mathrm{Re}\left[\mathbf{E}_{00,outside}(x,y,0)\right]\right|\neq\left|\mathrm{Im}\left[\mathbf{E}_{00,outside}(x,y,0)\right]\right|.$$

Thus using the definitions for polarisation given in section 4.3. it can be concluded that the electric field at the beam waist outside the focal circle is also elliptically polarised. Hence at the beam waist the electric field of order 00 is everywhere elliptically polarised. The same process can now be repeated for order 01. It is found, using Eqs. (3.25.a) and (3.26.b) that the $\mathbf{M}^{1}_{01}(x,y,z)$ and $\mathbf{N}^{2}_{01}(x,y,z)$ functions at the beam waist can be written as

$$\mathbf{M}^{1}_{01}(x,y,0)=\frac{e^{-kd}\,j_2(kR)}{R^2}\begin{pmatrix}0\\\dfrac{Rj_1(kR)}{kj_2(kR)}+d^2\\-iyd\end{pmatrix} \tag{4.81}$$

and

$$\mathbf{N}_{01}^{2}(x,y,0)=\frac{e^{-kd}\,j_2(kR)}{kR^4}\begin{pmatrix} -idxy\left(5-\dfrac{kRj_1(kR)}{j_2(kR)}\right) \\ -id\left(4R^2-\left(x^2-d^2\right)\left(5-\dfrac{kRj_1(kR)}{j_2(kR)}\right)\right) \\ -y\left(R^2+d^2\left(5-\dfrac{kRj_1(kR)}{j_2(kR)}\right)\right)\end{pmatrix} \quad . \tag{4.82}$$

It then follows that inside the focal circle the real and imaginary parts of $\mathbf{M}_{01,inside}^{1}(x,y,0)$ are given by

$$\mathrm{Re}\left[\mathbf{M}_{01,inside}^{1}(x,y,0)\right]=\frac{e^{-kd}\,j_2(kR_{in})}{R_{in}^2}\begin{pmatrix}0\\ \dfrac{R_{in}j_1(kR_{in})}{kj_2(kR_{in})}+d^2\\ 0\end{pmatrix} \tag{4.83}$$

and

$$\mathrm{Im}\left[\mathbf{M}_{01,inside}^{1}(x,y,0)\right]=\frac{e^{-kd}\,j_2(kR_{in})}{R_{in}^2}\begin{pmatrix}0\\ 0\\ -yd\end{pmatrix} \quad . \tag{4.84}$$

The real and imaginary parts of $\mathbf{N}_{01,inside}^{2}(x,y,0)$ inside the focal circle are given by

$$\mathrm{Re}\left[\mathbf{N}_{01,inside}^{2}(x,y,0)\right]=\frac{e^{-kd}\,j_2(kR_{in})}{kR_{in}^4}\begin{pmatrix}0\\ 0\\ -y\left(R_{in}^2+d^2\left(5-\dfrac{kR_{in}j_1(kR_{in})}{j_2(kR_{in})}\right)\right)\end{pmatrix} \tag{4.85}$$

and

$$\mathrm{Im}\left[\mathbf{N}^2_{01,inside}(x,y,0)\right]=\frac{e^{-kd}\,j_2(kR_{in})}{kR_{in}^4}\begin{pmatrix} -dxy\left(5-\dfrac{kR_{in}\,j_1(kR_{in})}{j_2(kR_{in})}\right) \\ -d\left(4R_{in}^2-\left(x^2-d^2\right)\left(5-\dfrac{kR_{in}\,j_1(kR_{in})}{j_2(kR_{in})}\right)\right) \\ 0 \end{pmatrix}. \quad (4.86)$$

Thus the real and imaginary parts of the electric field inside the focal circle of order 01 at the beam waist, using Eq. (4.39) and Eqs. (4.83) – (4.86), are given by

$$\mathrm{Re}\left[\mathbf{E}_{01,inside}(x,y,0)\right]=E_0\left[\frac{e^{-kd}\,j_2(kR_{in})}{R_{in}^2}\begin{pmatrix}0\\ \dfrac{R_{in}\,j_1(kR_{in})}{kj_2(kR_{in})}+d^2\\ 0\end{pmatrix}+\frac{e^{-kd}\,j_2(kR_{in})}{kR_{in}^4}\begin{pmatrix} dxy\left(5-\dfrac{kR_{in}\,j_1(kR_{in})}{j_2(kR_{in})}\right) \\ d\left(4R_{in}^2-\left(x^2-d^2\right)\left(5-\dfrac{kR_{in}\,j_1(kR_{in})}{j_2(kR_{in})}\right)\right) \\ 0\end{pmatrix}\right] \quad (4.87)$$

and

$$\mathrm{Im}\left[\mathbf{E}_{01,inside}(x,y,0)\right]=E_0\left[\frac{e^{-kd}\,j_2(kR_{in})}{R_{in}^2}\begin{pmatrix}0\\0\\-yd\end{pmatrix}+\frac{e^{-kd}\,j_2(kR_{in})}{kR_{in}^4}\begin{pmatrix}0\\0\\-y\left(R_{in}^2+d^2\left(5-\dfrac{kR_{in}\,j_1(kR_{in})}{j_2(kR_{in})}\right)\right)\end{pmatrix}\right]. \quad (4.88)$$

It can be seen form Eq. (4.87) and Eq. (4.88) that the real and imaginary parts are not collinear. Additionally

$$\mathrm{Re}\left[\mathbf{E}_{01,inside}(x,y,0)\right]\bullet \mathrm{Im}\left[\mathbf{E}_{01,inside}(x,y,0)\right]=0 \text{ and } \left|\mathrm{Re}\left[\mathbf{E}_{01,inside}(x,y,0)\right]\right| \neq \left|\mathrm{Im}\left[\mathbf{E}_{01,inside}(x,y,0)\right]\right|.$$

Thus using the definitions for polarisation given in section 4.3. it can be concluded that the electric field at the beam waist inside the focal circle is elliptically polarised.

The real and imaginary parts of $\mathbf{M}^{1}_{01,outside}(x,y,0)$ outside the focal circle are given by

$$\mathrm{Re}\left[\mathbf{M}^{1}_{01,outside}(x,y,0)\right]=\frac{e^{-kd}\,j_2(kR_{out})}{R_{out}^2}\begin{pmatrix}0\\ \dfrac{R_{out}\,j_1(kR_{out})}{kj_2(kR_{out})}+d^2\\ 0\end{pmatrix} \tag{4.89}$$

and

$$\mathrm{Im}\left[\mathbf{M}^{1}_{01,outside}(x,y,0)\right]=\frac{e^{-kd}\,j_2(kR_{out})}{R_{out}^2}\begin{pmatrix}0\\ 0\\ -yd\end{pmatrix}. \tag{4.90}$$

The real and imaginary parts of $\mathbf{N}^{2}_{01,outside}(x,y,0)$ outside the focal circle are given by

$$\mathrm{Re}\left[\mathbf{N}^{2}_{01,outside}(x,y,0)\right]=\frac{e^{-kd}\,j_2(kR_{out})}{kR_{out}^4}\begin{pmatrix}0\\ 0\\ -y\left(R_{out}^2+d^2\left(5-\dfrac{kR_{out}\,j_1(kR_{out})}{j_2(kR_{out})}\right)\right)\end{pmatrix} \tag{4.91}$$

and

$$\mathrm{Im}\left[\mathbf{N}^{2}_{01,outside}(x,y,0)\right]=\frac{e^{-kd}\,j_2(kR_{out})}{kR_{out}^4}\begin{pmatrix}-dxy\left(5-\dfrac{kR_{in}\,j_1(kR_{out})}{j_2(kR_{out})}\right)\\ -d\left(4R_{out}^2-\left(x^2-d^2\right)\left(5-\dfrac{kR_{in}\,j_1(kR_{out})}{j_2(kR_{out})}\right)\right)\\ 0\end{pmatrix}. \tag{4.92}$$

Thus the real and imaginary parts of the electric field outside the focal circle of order 01 at the beam waist, using Eq. (4.39) and Eqs. (4.89) – (4.92), are given by

$$\mathrm{Re}\left[\mathbf{E}_{01,outside}(x,y,0)\right] = E_0\left[\begin{array}{l}\dfrac{e^{-kd}\,j_2(kR_{out})}{R_{out}^2}\begin{pmatrix}0\\ R_{out}\,j_1(kR_{out})\\ kj_2(kR_{out})\\ 0\end{pmatrix}+d^2+\\ \dfrac{e^{-kd}\,j_2(kR_{out})}{kR_{out}^4}\begin{pmatrix}dxy\left(5-\dfrac{kR_{out}\,j_1(kR_{out})}{j_2(kR_{out})}\right)\\ d\left(4R_{out}^2-(x^2-d^2)\left(5-\dfrac{kR_{out}\,j_1(kR_{out})}{j_2(kR_{out})}\right)\right)\\ 0\end{pmatrix}\end{array}\right] \tag{4.93}$$

and

$$\mathrm{Im}\left[\mathbf{E}_{01,outside}(x,y,0)\right] = E_0\left[\begin{array}{l}\dfrac{e^{-kd}\,j_2(kR_{out})}{R_{out}^2}\begin{pmatrix}0\\ 0\\ -yd\end{pmatrix}+\\ \dfrac{e^{-kd}\,j_2(kR_{out})}{kR_{out}^4}\begin{pmatrix}0\\ 0\\ -y\left(R_{out}^2+d^2\left(5-\dfrac{kR_{out}\,j_1(kR_{out})}{j_2(kR_{out})}\right)\right)\end{pmatrix}\end{array}\right] \tag{4.94}$$

It can be seen form Eq. (4.93) and Eq. (4.94) that the real and imaginary parts are not collinear. Additionally

$$\mathrm{Re}\left[\mathbf{E}_{01,outside}(x,y,0)\right]\bullet\mathrm{Im}\left[\mathbf{E}_{01,outside}(x,y,0)\right]=0 \text{ and } \left|\mathrm{Re}\left[\mathbf{E}_{01,outside}(x,y,0)\right]\right| \neq \left|\mathrm{Im}\left[\mathbf{E}_{01,outside}(x,y,0)\right]\right|.$$

Thus using the definitions for polarisation given in section 4.3. it can be concluded that the electric field at the beam waist outside the focal circle is elliptically polarised. Hence at the beam waist the electric field of order 01 is, like of order 00, everywhere elliptically

polarised. Another interesting aspect worth considering is the polarisation of the electric fields of order 00 and 01 at the beam waist in the paraxial limit. In order to determine the polarisation at the beam waist in the paraxial limit, it is necessary to normalise the electric field at the beam waist. The normalisation constant for order 00 and order 01, $E_{0,00}$ and $E_{0,01}$ respectively are calculated using the formulae

$$E_{0,00} = \sqrt{E_{00,x}(0,0,0)E^*_{00,x}(0,0,0) + E_{00,y}(0,0,0)E^*_{00,y}(0,0,0) + E_{00,z}(0,0,0)E^*_{00,z}(0,0,0)}. \quad (4.95.a)$$

$$E_{0,01} = \sqrt{E_{01,x}(0,0,0)E^*_{01,x}(0,0,0) + E_{01,y}(0,0,0)E^*_{01,y}(0,0,0) + E_{01,z}(0,0,0)E^*_{01,z}(0,0,0)}. \quad (4.95.b)$$

It is found that in the paraxial limit

$$\lim_{kd\to\infty}\left(\frac{\mathbf{E}_{00}(x,y,0)}{E_{0,00}}\right) = e^{\frac{k\left(x^2+y^2\right)}{2d}}\begin{pmatrix}0\\ i\\ 0\end{pmatrix} \quad (4.96)$$

and

$$\lim_{kd\to\infty}\left(\frac{\mathbf{E}_{01}(x,y,0)}{E_{0,01}}\right) = e^{\frac{k\left(x^2+y^2\right)}{2d}}\begin{pmatrix}0\\ 1\\ 0\end{pmatrix}. \quad (4.97)$$

Thus

$$\mathbf{E}_{00}(x,y,0) = E_{0,00}e^{\frac{k\left(x^2+y^2\right)}{2d}}\begin{pmatrix}0\\ i\\ 0\end{pmatrix} \quad (4.98)$$

and

$$\mathbf{E}_{01}(x,y,0) = E_{0,01}e^{\frac{k\left(x^2+y^2\right)}{2d}}\begin{pmatrix}0\\ 1\\ 0\end{pmatrix}. \quad (4.99)$$

It can be seen from Eq. (4.98) that in the paraxial limit the electric field of order 00 is purely imaginary. Thus according to the definitions given in section 4.3. it can be concluded that this field is linearly polarised in the y direction. The electric field of order 01 in the paraxial limit is according to Eq. (4.99) purely real, and thus also linearly polarised in the y direction. According to Lekner [7], the polarisation properties of the electric field are identical to the polarisation properties of the magnetic field in the case of a plane E.M. wave propagating in vacuum. It is therefore convenient to determine the

magnetic field at the beam waist in the paraxial limit in order to test if the superposition chosen in Eqs. (4.39) and (4.40) satisfy the criteria a), d), e). By performing the same calculations as for the electric field, it is found that the magnetic fields at the beam waist, in the paraxial limit are given by

$$\mathbf{H}_{00}(x,y,0) = -iE_{0,00}\sqrt{\frac{\varepsilon}{\mu_0}}e^{-\frac{k\left(x^2+y^2\right)}{2d}}\begin{pmatrix}1\\0\\0\end{pmatrix} \tag{4.100}$$

and

$$\mathbf{H}_{01}(x,y,0) = -iE_{0,01}\sqrt{\frac{\varepsilon}{\mu_0}}e^{-\frac{k\left(x^2+y^2\right)}{2d}}\begin{pmatrix}-i\\0\\0\end{pmatrix} . \tag{4.101}$$

By substituting Eqs. (4.98) and (4.100) into Eq.(1.34) it is found that the time averaged pointing vector in the paraxial limit at the beam waist for order 00 is

$$\langle \mathbf{S}_{00}(\mathbf{r}) \rangle = \frac{1}{2}\sqrt{\frac{\varepsilon}{\mu_0}}E_{0,00}^2 e^{-\frac{k\left(x^2+y^2\right)}{d}}\begin{pmatrix}0\\0\\1\end{pmatrix} = \frac{1}{2}\sqrt{\frac{\varepsilon}{\mu_0}}E_{0,00}^2 e^{-\frac{k\left(x^2+y^2\right)}{d}}\hat{\mathbf{k}} . \tag{4.102}$$

Similarly by substituting Eqs.(4.99) and (4.101) into Eq.(1.34) it is found that the time averaged pointing vector in the paraxial limit at the beam waist for order 01 is

$$\langle \mathbf{S}_{01}(\mathbf{r}) \rangle = \frac{1}{2}\sqrt{\frac{\varepsilon}{\mu_0}}E_{0,01}^2 e^{-\frac{k\left(x^2+y^2\right)}{d}}\begin{pmatrix}0\\0\\1\end{pmatrix} = \frac{1}{2}\sqrt{\frac{\varepsilon}{\mu_0}}E_{0,01}^2 e^{-\frac{k\left(x^2+y^2\right)}{d}}\hat{\mathbf{k}} . \tag{4.103}$$

By comparing Eqs. (4.102) and (4.103) with Eqs.(2.60), it can be seen that Eqs. (4.102) and (4.103) have the same irradiance at the beam waist in the paraxial limit as a paraxial Gaussian beam. Furthermore the irradiance is along the positive *z* axis. Therefore it has been established that the solutions given by Eqs. (4.55) - (4.58) satisfies the criteria a), d), e). Finally in the literature, for example Sheppard and Saghafi [8], the electric field of order 00 is in general referred to as an almost linearly polarised field. The reason for this can be understood by investigating the degree of linear polarisation, using Eq. (4.64) for different values of *kd* at a given point in space. It can be seen from Fig. 4.4. that at the point x=2, y=3 and z=0, the curve representing the degree of linear polarisation of the electric field $\mathbf{E}_{00}(\mathbf{r},0)$ approaches 1 rapidly, even for small values of *kd*.

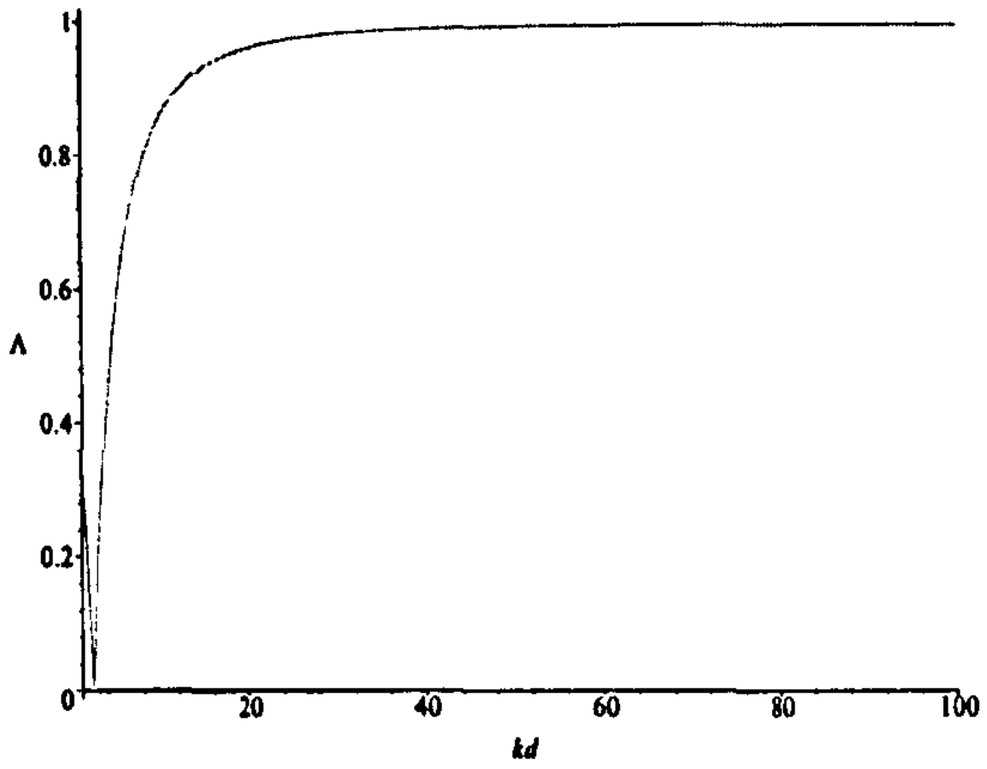

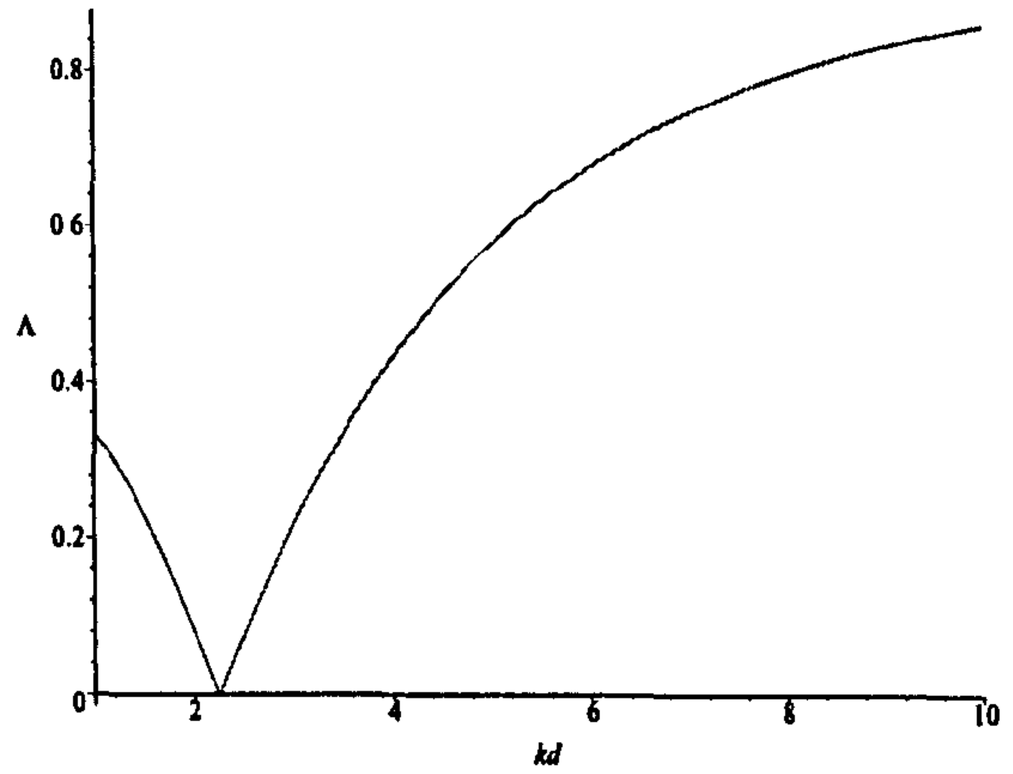

Fig. 4.4. Degree of linear polarisation of the electric field $\mathbf{E}_{00}(\mathbf{r},0)$ for different values of *kd*. $\Lambda(\mathbf{r},0)=1$ implies linearly polarisation and $\Lambda(\mathbf{r},0)=0$ implies circular polarisation.

At the same point in space also the electric field $\mathbf{E}_{01}(\mathbf{r},0)$ approaches 1 rapidly, even for small values of *kd* as can be seen from Fig. 4.5. The main difference between Fig. 4.4. and Fig. 4.5. is that in Fig. 4.5. the curve is smooth and does not drop to almost 0 for $kd\approx 2$ like it is seen in Fig. 4.4.

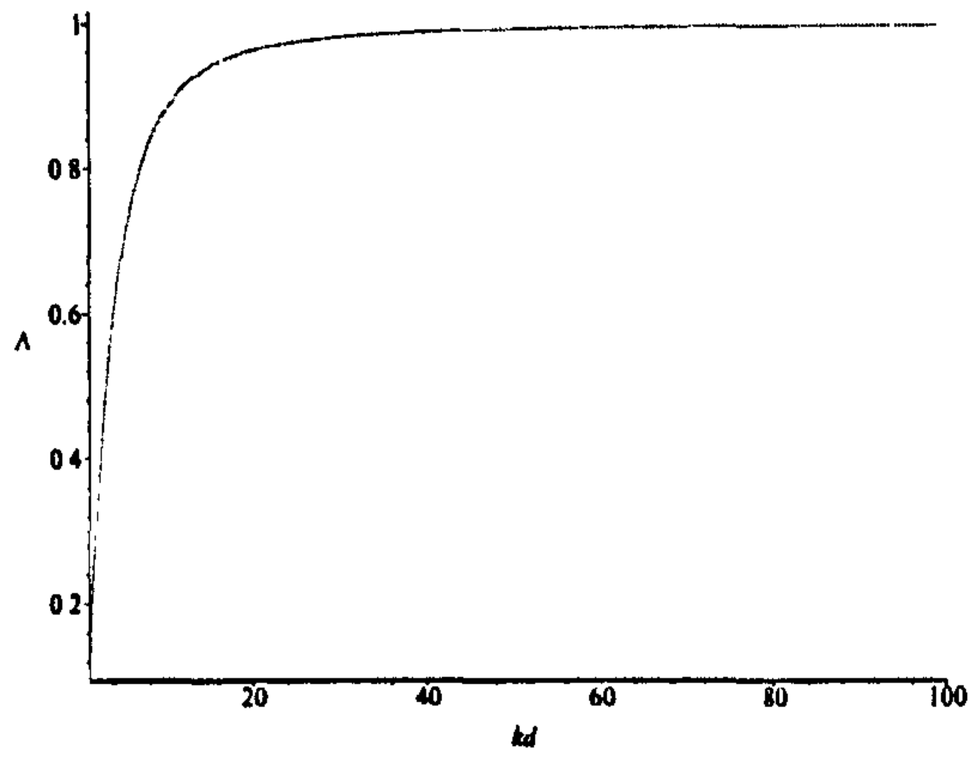

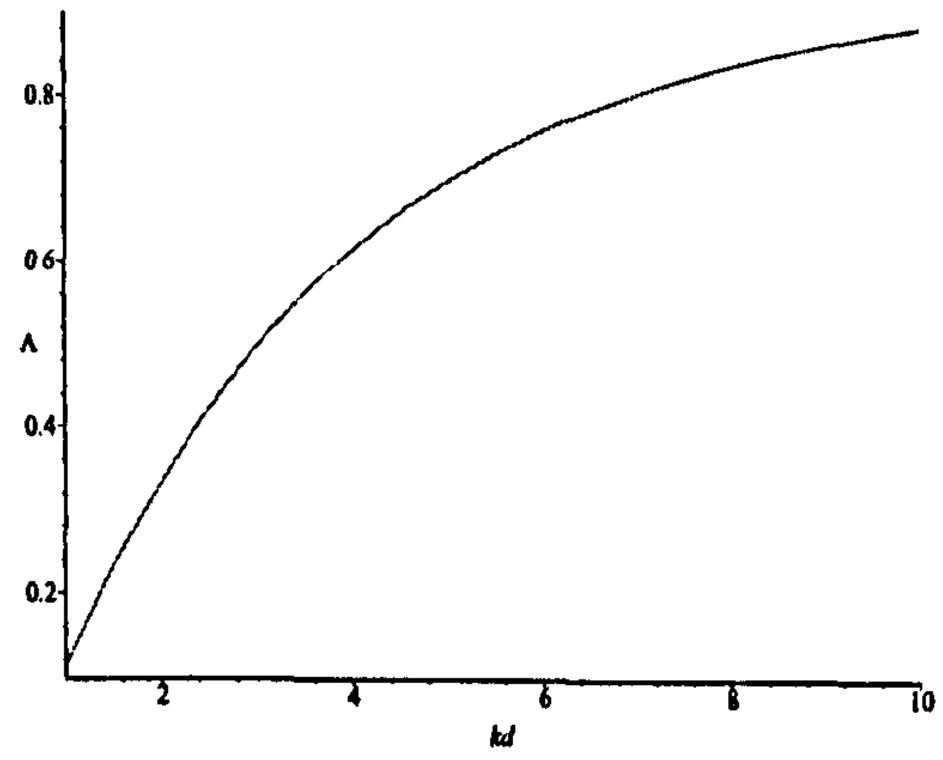

Fig. 4.5. Degree of linear polarisation of the electric field $\mathbf{E}_{01}(\mathbf{r},0)$ for different values of *kd*. $\Lambda(\mathbf{r},0)=1$ implies linearly polarisation and $\Lambda(\mathbf{r},0)=0$ implies circular polarisation.

Another way of demonstrating that at the beam waist the electric fields $\mathbf{E}_{00}(\mathbf{r},0)$ and $\mathbf{E}_{01}(\mathbf{r},0)$ are almost linearly polarised is to plot the field components separately. However, if the standard definition of the degree of linear polarisation would have been used, which only takes the transverse components of the E.M. field into account, the E.M. field would be linearly polarised for all values of *kd*. These components are plotted directly form Eqs. (4.55) and (4.57) in order to determine the relative strengths of the cross components. The electric field components of $\mathbf{E}_{00}(\mathbf{r},0)$ can be seen from Figs. 4.6. and the ones of $\mathbf{E}_{01}(\mathbf{r},0)$ from Figs. 4.7.

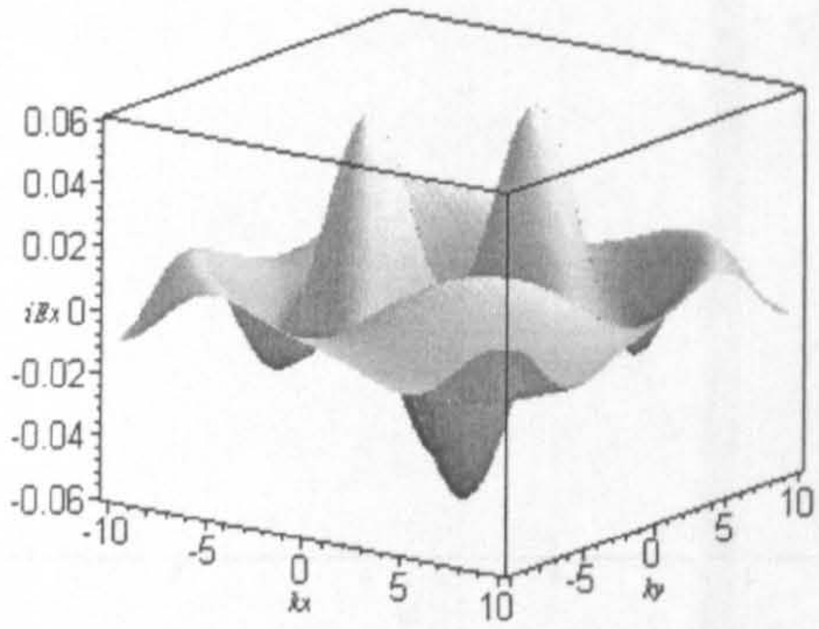

(a)

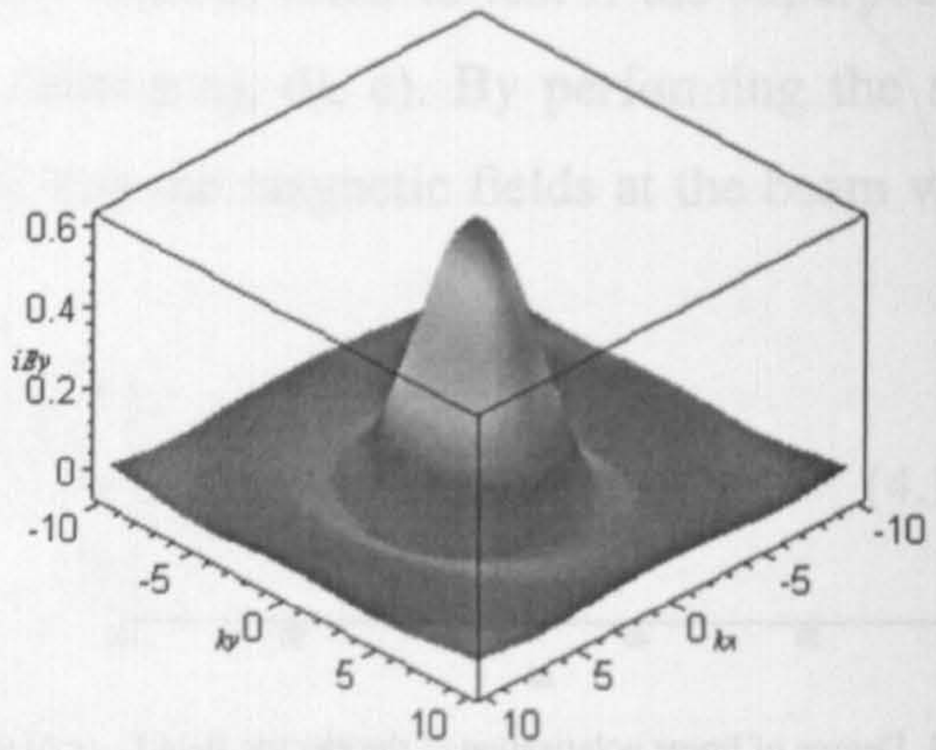

(b)

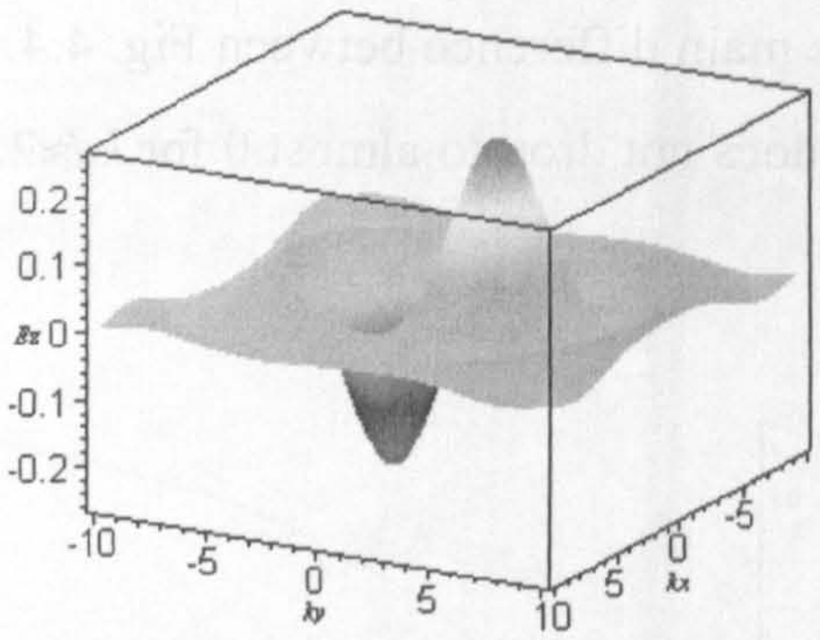

(c)

Fig. 4.6. Variation in the three components of the electric field strength at the beam waist for $\mathbf{E}_{00}(\mathbf{r},0)$ with kd=2: (a) iE_x, (b) iE_y, (c) E_z

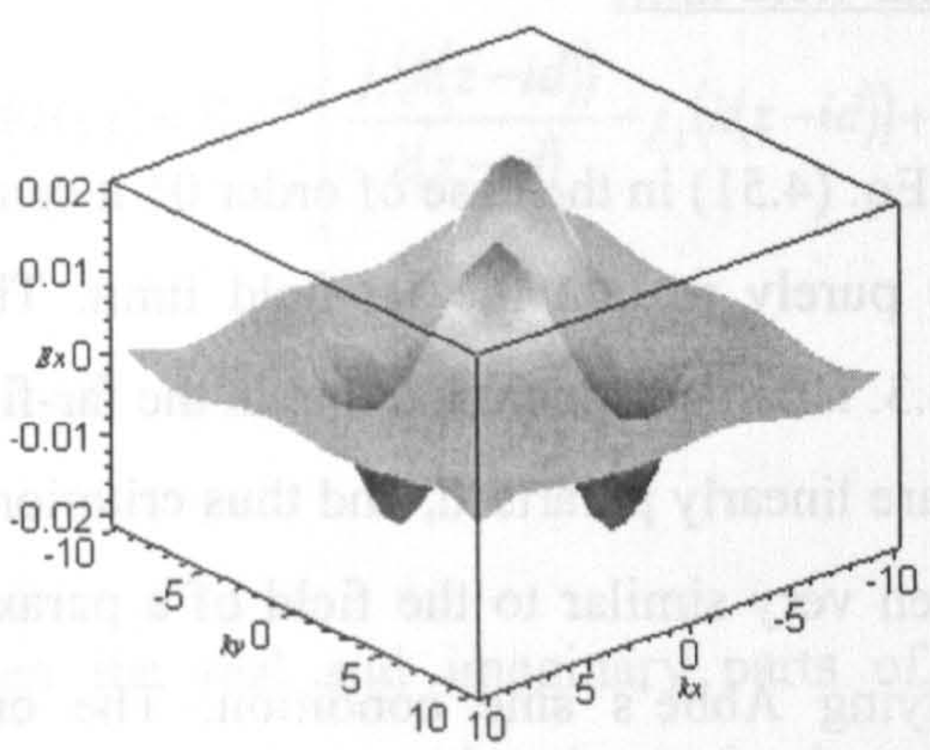

(a)

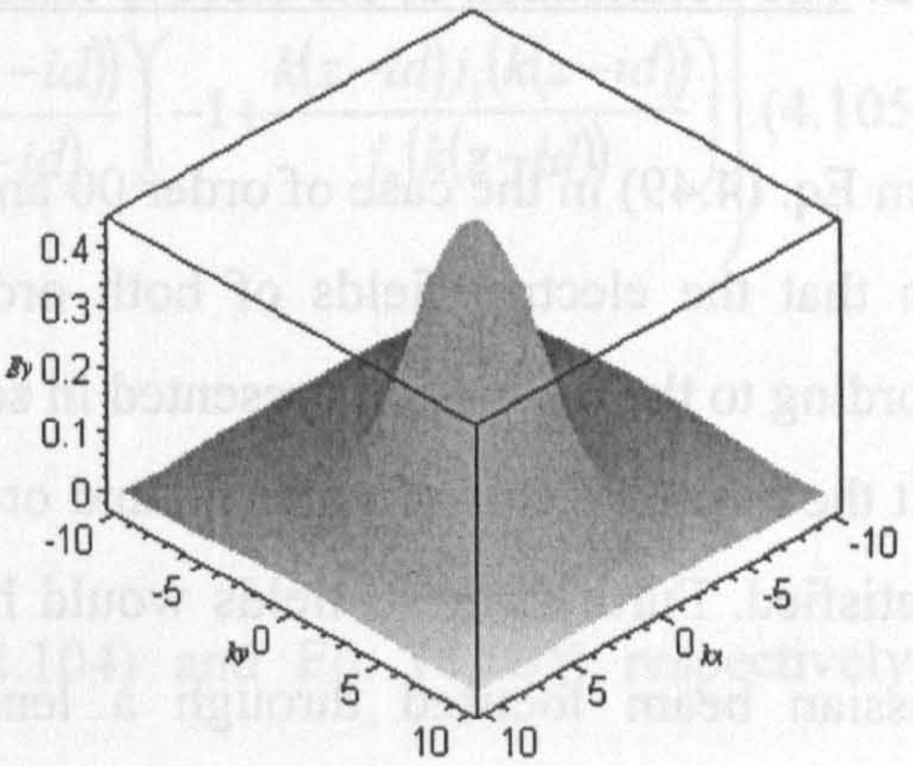

(b)

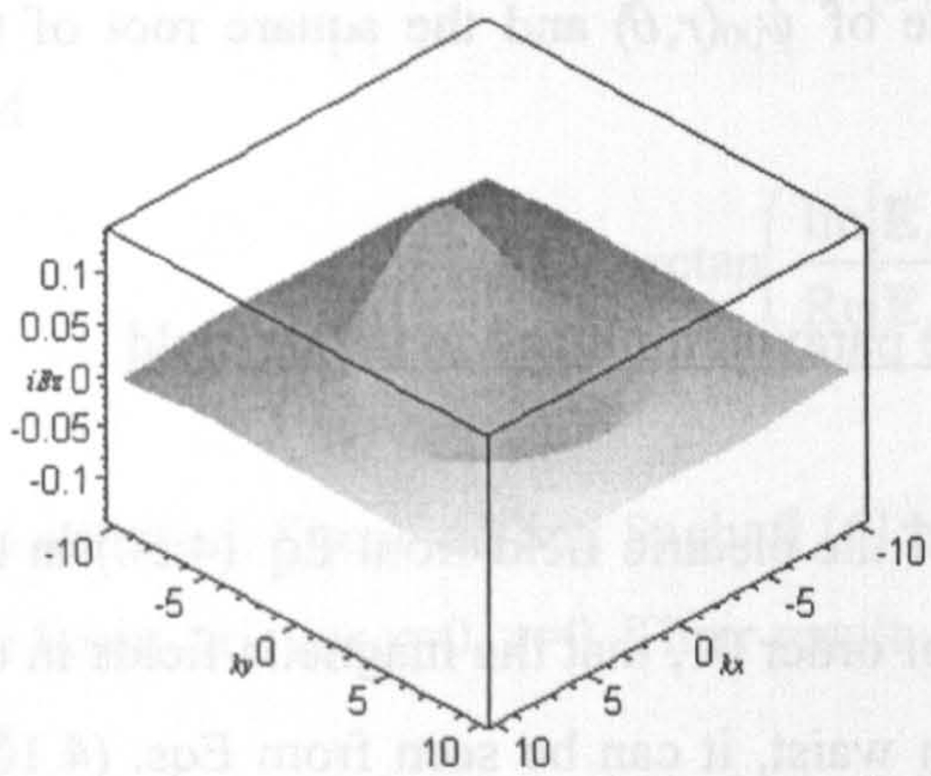

(c)

Fig. 4.7. Variation in the three components of the electric field strength at the beam waist for $\mathbf{E}_{01}(\mathbf{r},0)$ with kd=2: (a) E_x, (b) E_y, (c) iE_z

It can be seen from Fig. 4.6. that the z axial component of the electric field $\mathbf{E}_{00}(\mathbf{r},0)$ is approximately a factor of 2.5 smaller than the y component and that the x component is a factor of 10 smaller than the y component. Thus it can be concluded that the electric field $\mathbf{E}_{00}(\mathbf{r},0)$ is almost linearly polarised in the y direction, even for a strongly focused beam. From Fig. 4.7. it can be seen that the z component of the electric field $\mathbf{E}_{01}(\mathbf{r},0)$ is approximately a factor of 4 smaller than the y component and that the x component is a factor of 20 smaller than the y component. Thus it can be concluded that the electric field $\mathbf{E}_{01}(\mathbf{r},0)$ is almost linearly polarised in the y direction, even for a strongly focused beam. For both fields, these cross components become rapidly smaller as kd increases, as was predicted by Eq. (4.98) and Eq. (4.99) respectively. The absolute value of the z component in both cases exhibits twofold rotational symmetry and is zero for y=0. The x component in both cases exhibits fourfold symmetry and is zero for x=0 or y=0.

4.3.2. The polarisation of the electric field in the far-field limit

From Eq. (4.49) in the case of order 00 and from Eq. (4.51) in the case of order 01 it can be seen that the electric fields of both orders are purely real in the far-field limit. Thus according to the discussion presented in section 4.3. it can be concluded that in the far-field limit the electric fields of order 00 and order 01 are linearly polarised, and thus criterion f) is satisfied. Further, these fields would have been very similar to the field of a paraxial Gaussian beam focused through a lens satisfying Abbe's sine condition. The only difference is the time averaged amplitude function. For a paraxial Gaussian beam the time averaged amplitude function would be given by the square root of Eq. (2.61) and not by the square root of the first of Eqs.(2.72) in the case of $\psi_{00}(r,\theta)$ and the square root of the second of Eqs. (2.72) in the case of $\psi_{01}(r,\theta)$.

4.3.3. The polarisation of the magnetic field in the paraxial limit and in the far-field

It can be seen by analogy with the polarisation of the electric field from Eq. (4.50) in the case of order 00 and from Eq. (4.52) in the case of order 01, that the magnetic fields in the far-field limit are linearly polarised. At the beam waist, it can be seen from Eqs. (4.100) and (4.101) respectively, that the magnetic fields of order 00 and order 01 are linearly polarised in the x direction in the paraxial limit. Otherwise the magnetic fields, like the electric fields, are elliptically polarised at the beam waist.

4.4. The Guoy phase shift

It is well known that when an optical (or microwave) beam passes through a focal region, the phase of the beam is shifted. This phase shift is referred to as the Guoy phase shift and needs to be included in the present discussion in order to complete the analysis of the behaviour of the electric field at the beam waist. The Gouy phase shift along the beam axis is obtained by substituting x=y=0 into Eqs. (4.55) and (4.57) . Thus

$$\mathbf{E}_{00}(0,0,z)=E_0 e^{-ikd}\begin{pmatrix} 0 \\ -j_1(k(z-id))+\dfrac{2ij_1(k(z-id))}{k(z-id)}-ij_2(k(z-id)) \\ 0 \end{pmatrix} \tag{4.104}$$

and

$$\mathbf{E}_{01}(0,0,z)=E_0 e^{-ikd}\left(\begin{matrix}0\\ \frac{j_1(k(z-id))}{k(z-id)}-j_2(k(z-id))+i\left(\frac{j_2(k(z-id))}{k(z-id)}\right)\left(-1+\frac{k(z-id)j_1(k(z-id))}{j_2(k(z-id))}\right)\\ 0\end{matrix}\right). \quad (4.105)$$

Then the real and imaginary parts of Eq. (4.104) and Eq. (4.105) respectively are calculated and hence the phases for the two fields

$$\phi_{00}=\arctan\left(\frac{\mathrm{Im}[\mathbf{E}_{00}(0,0,z)]}{\mathrm{Re}[\mathbf{E}_{00}(0,0,z)]}\right) \quad (4.106)$$

and

$$\phi_{01}=\arctan\left(\frac{\mathrm{Im}[\mathbf{E}_{01}(0,0,z)]}{\mathrm{Re}[\mathbf{E}_{01}(0,0,z)]}\right), \quad (4.107)$$

are obtained. Sheppard and Saghafi [6] have calculated the phase shift for $\mathbf{E}_{00}(0,0,z)$ along the beam axis for x=0, y=0. Their result, with a phase kz suppressed, can be seen from Fig. 4.8..

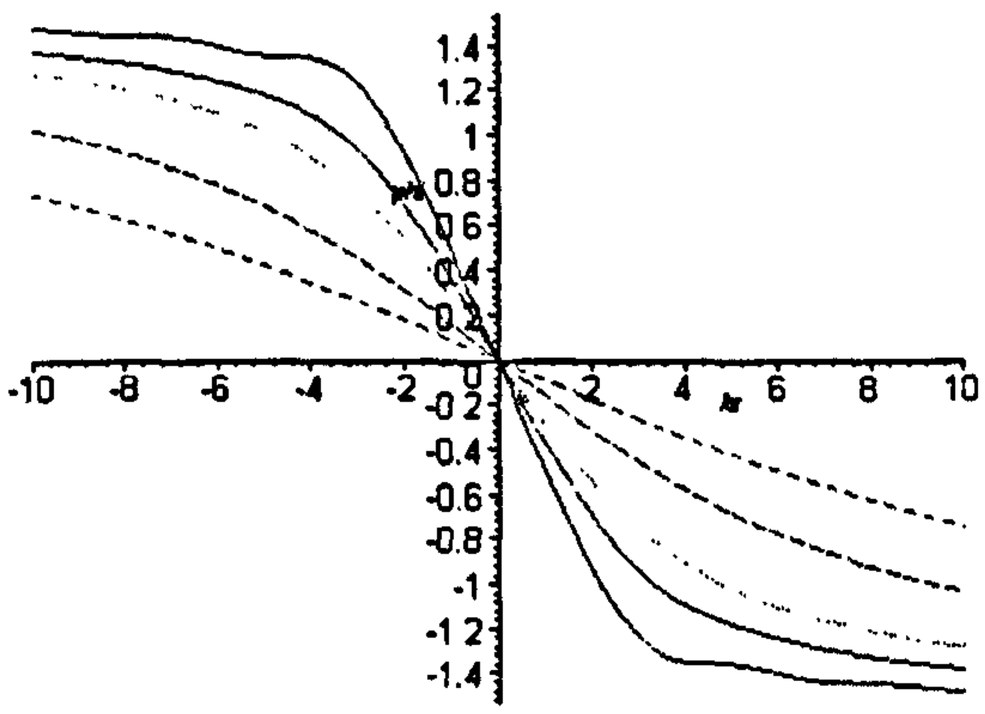

Fig. 4.8. Axial variation in phase for $\mathbf{E}_{00}(0,0,z)$ for values of kd=0, 1, 2, 5, 10. Showing the Gouy phase anomaly, which is greatest for kd=0 and smallest For kd=10.

The Gouy phase shift for $\mathbf{E}_{01}(0,0,z)$, with a phase kz suppressed, can be seen from Fig. 4.9..

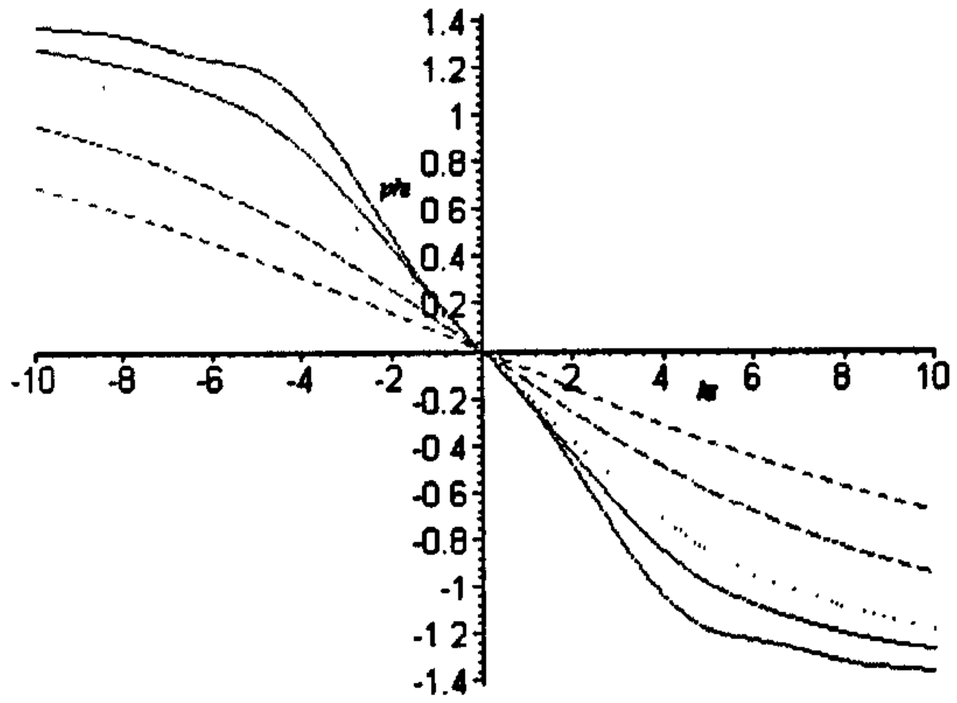

Fig. 4.9. Axial variation in phase for $\mathbf{E}_{01}(0,0,z)$ for values of kd=0, 1, 2, 5, 10.
Showing the Gouy phase anomaly, which is greatest for kd=0 and smallest
For kd=10.

By comparing Figs. 4.8. and 4.9. it can be seen that the Gouy phase shifts of $\mathbf{E}_{00}(0,0,z)$ and $\mathbf{E}_{01}(0,0,z)$ are similar, especially for large kd.

4.5. The approach of Sheppard and Saghafi

Sheppard's and Saghafi's approach [8] to calculate the E.M. field of a strongly focused Gaussian laser beam is based on the theory of a complex point source and sink. Cullen and Yu [9] extended the complex source point method introduced in section 1.11.3. for the lowest order mode to the E.M. case. They have shown that an almost plane polarised beam is produced by crossed electric and magnetic dipoles positioned at an imaginary distance. However this derivation suffers from the problem of singularities. Sheppard and Saghafi [10] introduced a modified theory, in which the source is accompanied by a sink. This can be recognised as a description of the Huygen's principle: The external focused radiation excites the source, which then reradiates. In this theory the singularities are replaced by phase singularities, which are according to Nye and Berry [11] physically realisable. The important distinction of the complex source-sink solution developed by Sheppard and Saghafi [8] is that it is a rigorous solution of Maxwell's equations in all space. Sheppard and Saghafi [8] further demonstrate that the combined incoming and outgoing wave is given by Eq. (2.43). The E.M. field presented by Sheppard and Saghafi [8] can be re-expressed in terms of the $\mathbf{M}_{00}^{1}(x,y,z)$, $\mathbf{M}_{00}^{2}(x,y,z)$, $\mathbf{N}_{00}^{1}(x,y,z)$ and $\mathbf{N}_{00}^{2}(x,y,z)$ functions as

$$\mathbf{E}_{00}(x,y,z)=\frac{3}{2e^{-kd}}E_0\left(i\mathbf{M}^2_{00}(x,y,z)+\mathbf{N}^1_{00}(x,y,z)\right)$$
$$\mathbf{H}_{00}(x,y,z)=\frac{3}{2e^{-kd}}E_0\sqrt{\frac{\varepsilon}{\mu_0}}\left(\mathbf{N}^2_{00}(x,y,z)-i\mathbf{M}^1_{00}(x,y,z)\right) \quad (4.108)$$

which implies that this field is identical to the field given in Eqs. (4.55) and (4.56). Thus the far-field limits of Eqs. (4.108) are proportional to Eqs. (4.49) and (4.50). Another approach in order to derive an E.M. field for a strongly focused Gaussian laser beam was used by Volyar *et al.* [12].

4.6. The approach of Volyar *et al.*

Volyar *et al.* [12] obtained vector solutions to the vector Helmholtz equation, based on the Whittaker potentials. Volyar *et al.* obtained transverse and longitudinal beams, which are denoted as e_t and h_t for the transverse components of the electric and magnetic field respectively and e_z and h_z denote the longitudinal components of the electric and magnetic field respectively. The notation LP(e_x), LP(e_y), LP(h_x) and LP(h_y) indicates the homogeneous linear polarization of the electric and magnetic field respectively along a preset direction (LP stands for linearly polarized). Furthermore these four modes exhibit no phase singularity on the transverse component on the optical axis (x=y=0) and convert for $kd \rightarrow\infty$ into a paraxial Gaussian beam. The other two modes TE and TM exhibit a polarization declination on the axis. For the axially symmetric beams, the fields LP(e_x) and LP(h_x) can be obtained from LP(e_y) and LP(h_y) through a rotation by $\frac{\pi}{2}$ and, hence, are degenerate. However any small deformation of the beam cross section would lift the degeneracy. It can be seen from table 4.1., that it is possible to represent the six beam modes presented by Volyar [12] in terms of the $\mathbf{M}^1_{00}(x,y,z)$, $\mathbf{M}^2_{00}(x,y,z)$, $\mathbf{M}^3_{00}(x,y,z)$, $\mathbf{N}^1_{00}(x,y,z)$, $\mathbf{N}^2_{00}(x,y,z)$ and $\mathbf{N}^3_{00}(x,y,z)$ functions of order 00 derived in this work.

Mode	e_t	e_z	$\sqrt{\frac{\mu_0}{\varepsilon_0}}h_t$	$\sqrt{\frac{\mu_0}{\varepsilon_0}}h_z$
LP(e_y)	$-i\mathbf{M}^1_{00}(x,y,z)$	$-i\mathbf{M}^1_{00}(x,y,z)$	$\mathbf{N}^1_{00}(x,y,z)$	$\mathbf{N}^1_{00}(x,y,z)$
LP(e_x)	$-i\mathbf{M}^2_{00}(x,y,z)$	$-i\mathbf{M}^2_{00}(x,y,z)$	$\mathbf{N}^2_{00}(x,y,z)$	$\mathbf{N}^2_{00}(x,y,z)$
LP(h_y)	$\mathbf{N}^1_{00}(x,y,z)$	$\mathbf{N}^1_{00}(x,y,z)$	$i\mathbf{M}^1_{00}(x,y,z)$	$i\mathbf{M}^1_{00}(x,y,z)$
LP(h_x)	$\mathbf{N}^2_{00}(x,y,z)$	$\mathbf{N}^2_{00}(x,y,z)$	$i\mathbf{M}^2_{00}(x,y,z)$	$i\mathbf{M}^2_{00}(x,y,z)$
TE	$-i\mathbf{M}^3_{00}(x,y,z)$	$-i\mathbf{M}^3_{00}(x,y,z)$	$\mathbf{N}^3_{00}(x,y,z)$	$\mathbf{N}^3_{00}(x,y,z)$
TM	$\mathbf{N}^3_{00}(x,y,z)$	$\mathbf{N}^3_{00}(x,y,z)$	$i\mathbf{M}^3_{00}(x,y,z)$	$i\mathbf{M}^3_{00}(x,y,z)$

Table 4.1. Volyar's functions expressed in terms of the $\mathbf{M}^1_{00}(x,y,z)$, $\mathbf{M}^2_{00}(x,y,z)$, $\mathbf{M}^3_{00}(x,y,z)$, $\mathbf{N}^1_{00}(x,y,z)$, $\mathbf{N}^2_{00}(x,y,z)$ and $\mathbf{N}^3_{00}(x,y,z)$ functions, derived in this work.

Volyar *et al.* [12] state, that a symmetry in representation of the electric and magnetic fields of a non-paraxial beam can be obtained by taking the superposition of modes

$$\mathrm{LP}(eh)_y = \mathrm{LP}(e_y) \pm \mathrm{LP}(h_y)$$

$$\mathrm{LP}(eh)_x = \mathrm{LP}(e_x) \pm \mathrm{LP}(h_x),$$

or in terms of our own $\mathbf{M}^1_{00}(x,y,z)$, $\mathbf{M}^2_{00}(x,y,z)$, $\mathbf{M}^3_{00}(x,y,z)$, $\mathbf{N}^1_{00}(x,y,z)$, $\mathbf{N}^2_{00}(x,y,z)$ and $\mathbf{N}^3_{00}(x,y,z)$ as

$$\mathbf{E}_{00}(x,y,z) \propto E_0\left(-i\mathbf{M}^1_{00}(x,y,z) \pm \mathbf{N}^1_{00}(x,y,z)\right) \tag{4.109}$$

$$\mathbf{H}_{00}(x,y,z) \propto E_0\sqrt{\frac{\varepsilon}{\mu_0}}\left(-\mathbf{N}^1_{00}(x,y,z) \mp i\mathbf{M}^1_{00}(x,y,z)\right), \tag{4.110}$$

By comparing Eqs. (4.109) and (4.110) with Eqs. (4.39) and (4.40) it can be clearly seen that the E.M. field derived by Volyar does not satisfy the Richards and Wolf boundary conditions [1] in the far-field limit.

4.7. The irradiance

It was mentioned in chapter 1 that in optics the irradiance at a particular location is of interest. Thus the next step is to give an expression for the time averaged Poynting vector of the solution for order 00 (Eqs. (4.55) and (4.56)). In accordance with Eq. (1.34) the time averaged Poynting vector for order 00 can be written as

$$\langle \mathbf{S}_{00}(x,y,z)\rangle = \frac{1}{2}\sqrt{\frac{\varepsilon}{\mu_0}}E_0^2\,\frac{e^{-2kd}}{(RR^*)^2}\,\mathrm{Re}\begin{bmatrix} S_x \\ S_y \\ S_z \end{bmatrix}, \tag{4.111}$$

where

$$S_x = x\begin{bmatrix}\left(-iRj_1(kR)(z-id)-j_2(kR)\left(2\frac{Rj_1(kR)}{kj_2(kR)}-R^2+y^2\right)\right)\left(iR^*j_1(kR^*)+(z+id)j_2(kR^*)\right)- \\ y^2 j_2(kR^*)\left[iRj_1(kR)-j_2(kR)(z-id)\right]\end{bmatrix}$$

$$S_y = y\begin{bmatrix}\left(iRj_1(kR)-j_2(kR)(z-id)\right)\left(-iR^*j_1(kR^*)(z+id)+j_2(kR^*)\left(2\frac{R^*j_1(kR^*)}{kj_2(kR^*)}-R^{*2}+x^2\right)\right)+ \\ x^2 j_2(kR)\left[iR^*j_1(kR^*)+j_2(kR^*)(z+id)\right]\end{bmatrix}$$

$$S_z = \left(-iRj_1(kR)(z-id)-j_2(kR)\left(2\frac{Rj_1(kR)}{kj_2(kR)}-R^2+y^2\right)\right)\times$$
$$\left(iR^*j_1(kR^*)(z+id)-j_2(kR^*)\left(2\frac{R^*j_1(kR^*)}{kj_2(kR^*)}-R^{*2}+x^2\right)\right)$$

with

$$R=\sqrt{x^2+y^2+(z-id)^2}$$
$$R^*=\sqrt{x^2+y^2+(z+id)^2}.$$

In accordance with Eq. (1.34) the irradiance is given by the modulus of Eq. (4.111). Figs. (4.10.) show the irradiance normalised to 1 at (x=y=z=0) of the solution for order 00, at the beam waist (z=0, plane) (Fig. 4.10.a), in the z=1 plane (Fig. 4.10.b), in the z=2.3 plane (Fig. 4.10.c) and in the z=100 plane (Fig. 4.10.d) for k=1, d=2.3.

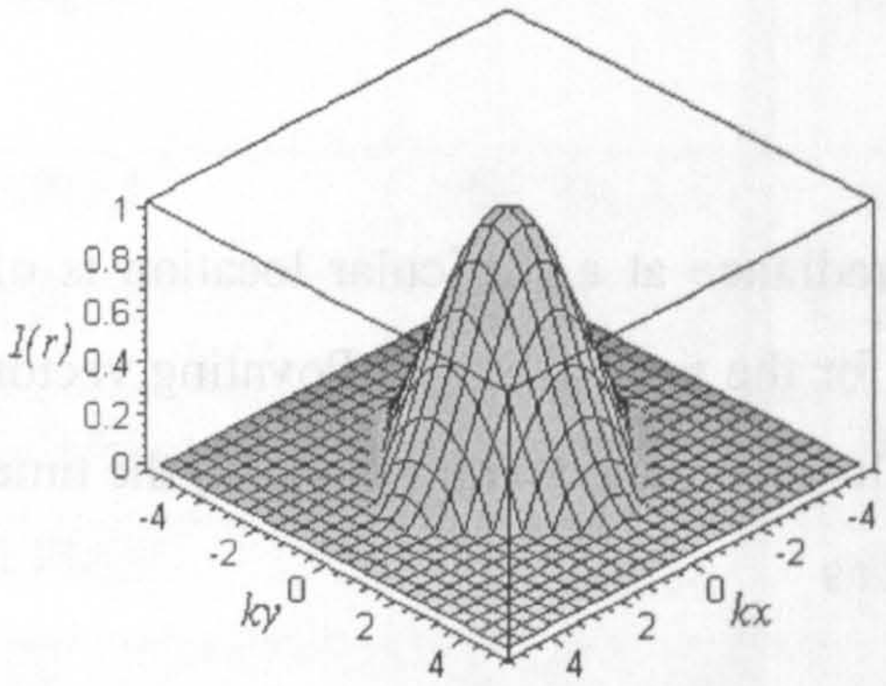

Fig, 4.10.a. Irradiance profile of order 00, normalised to 1 at , (x=y=z=0) at the beam waist z=0, for k=1, d=2.3.

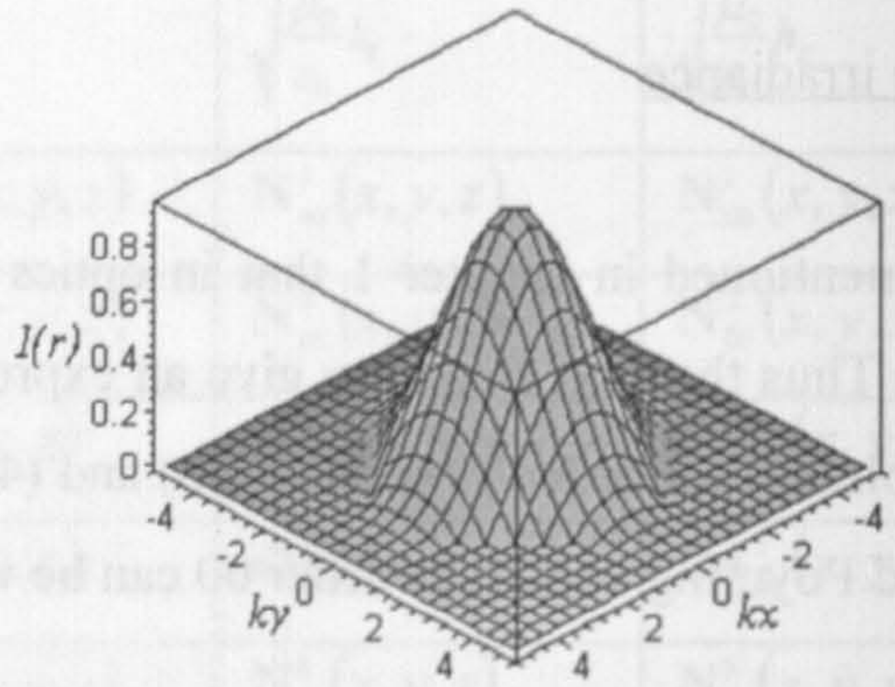

Fig. 4.10.b. Irradiance profile of order 00 normalised to 1 at (x=y=z=0) in the z=1 plane, for k=1, d=2.3.

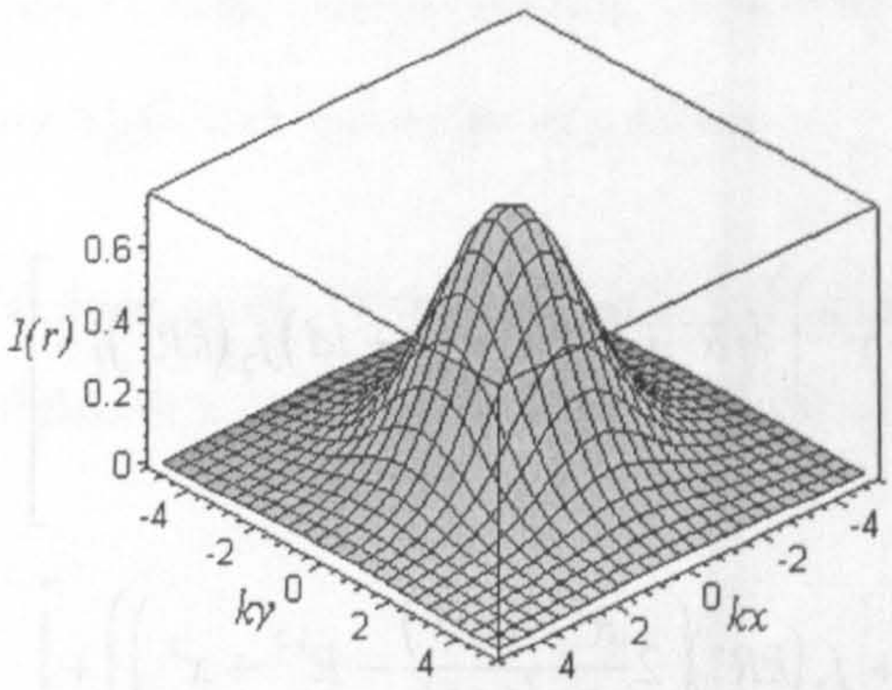

Fig, 4.10.c. Irradiance profile of order 00, normalised to 1 at , (x=y=z=0) in the z=2.3 plane, for k=1, d=2.3.

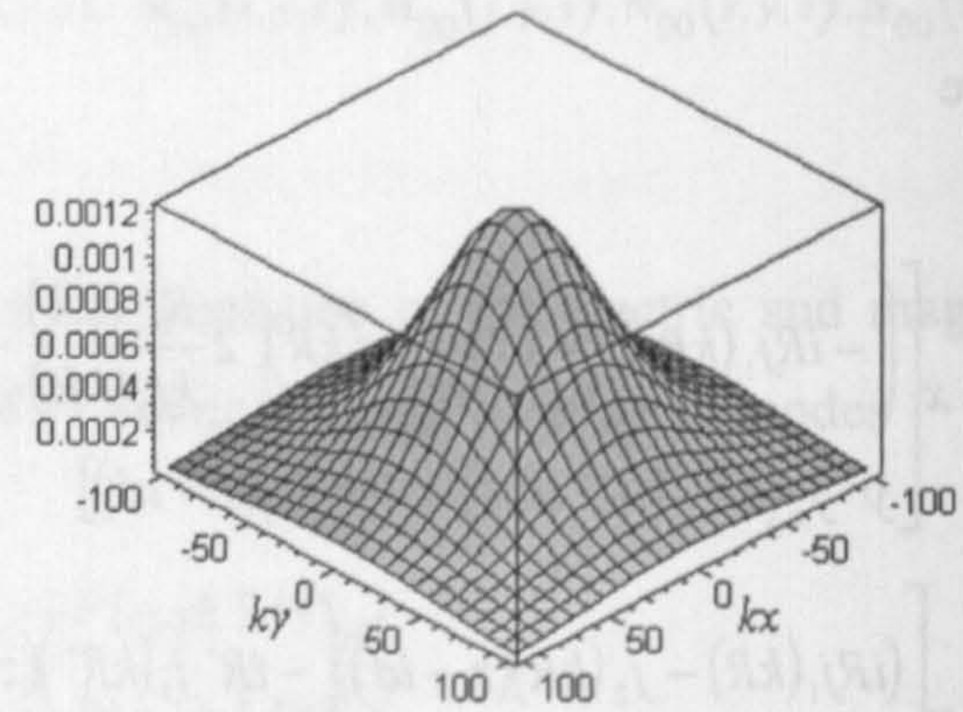

Fig. 4.10.d. Irradiance profile of order 00 normalised to 1 at (x=y=z=0) in the z=100 plane, for k=1, d=2.3.

Similarly, in accordance with Eq. (1.34) the time averaged Poynting vector for order 01 (Eqs. (4.57) and (4.58)) can be written as

$$\left\langle \mathbf{S}_{01}(x,y,z)\right\rangle = \frac{1}{2}\sqrt{\frac{\varepsilon}{\mu_0}}E_0^2\,\frac{e^{-2kd}\,j_2(kR)j_2(kR^*)(z^2+d^2)}{(kRR^*)^2}\,\mathrm{Re}\begin{bmatrix}S_x\\S_y\\S_z\end{bmatrix}, \tag{4.112}$$

where

$$S_x = x\left[\begin{array}{l}\left(\dfrac{iRj_1(kR)}{(z-id)j_2(kR)}-ik(z-id)-4+\dfrac{(R^2-y^2)\left(5-\dfrac{kRj_1(kR)}{j_2(kR)}\right)}{R^2}\right)\left(ik-\dfrac{1}{z+id}+\dfrac{(z+id)\left(5-\dfrac{kR^*j_1(kR^*)}{j_2(kR^*)}\right)}{R^{*2}}\right)- \\ \dfrac{y^2\left[iR^2\left(k-\dfrac{i}{z-id}\right)-(z-id)\left(5-\dfrac{kRj_1(kR)}{j_2(kR)}\right)\right]\left[5-\dfrac{kR^*j_1(kR^*)}{j_2(kR^*)}\right]}{(RR^*)^2}\end{array}\right]$$

$$S_y = y\left[\frac{\left(ik+\frac{1}{z-id}-\frac{(z-id)\left(5-\frac{kRj_1(kR)}{j_2(kR)}\right)}{R^2}\right)\left(\frac{iR^*j_1(kR^*)}{(z+id)j_2(kR^*)}-ik(z+id)+4-\frac{\left(R^{*2}-x^2\right)\left(5-\frac{kR^*j_1(kR^*)}{j_2(kR^*)}\right)}{R^{*2}}\right)+}{\frac{x^2\left(5-\frac{kRj_1(kR)}{j_2(kR)}\right)\left[R^{*2}\left(ik-\frac{1}{z+id}\right)+(z+id)\left(5-\frac{kR^*j_1(kR^*)}{j_2(kR^*)}\right)\right]}{(RR^*)^2}}\right]$$

$$S_z = \left(\frac{-iRj_1(kR)}{(z-id)j_2(kR)}+ik(z-id)+4-\frac{\left(R^2-y^2\right)\left(5-\frac{kRj_1(kR)}{j_2(kR)}\right)}{R^2}\right)\times$$

$$\left(\frac{iR^*j_1(kR^*)}{(z+id)j_2(kR^*)}-ik(z+id)+4-\frac{\left(R^{*2}-x^2\right)\left(5-\frac{kR^*j_1(kR^*)}{j_2(kR^*)}\right)}{R^{*2}}\right)$$

$$-\frac{x^2y^2\left(5-\frac{kRj_1(kR)}{j_2(kR)}\right)\left(5-\frac{kR^*j_1(kR^*)}{j_2(kR^*)}\right)}{(RR^*)^2}$$

In accordance with Eq. (1.34) the irradiance is given by the modulus of Eq. (4.112). Figs. (4.11.) show the irradiance normalised to 1 at (x=y=z=0) of the solution for order 01, at the beam waist (z=0, plane) (Fig. 4.11.a), in the z=1 plane (Fig. 4.11.b), in the z=2.3 plane (Fig. 4.11.c) and in the z=100 plane (Fig. 4.11.d) for k=1, d=2.3.

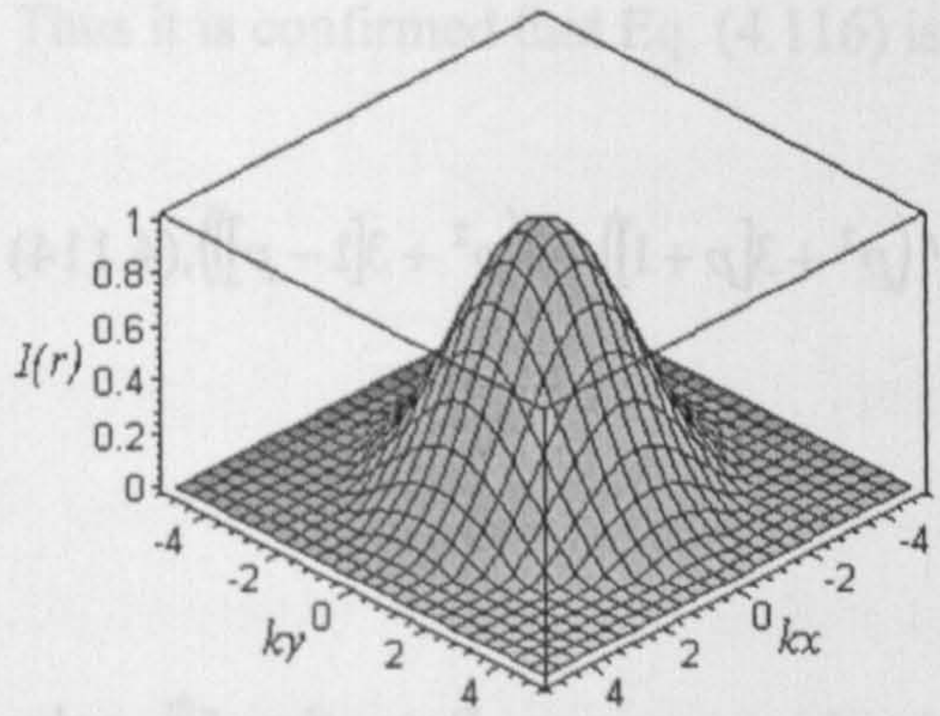

Fig, 4.11.a. Irradiance profile of order 01, normalised to 1 at , (x=y=z=0) at the beam waist z=0, for k=1, d=2.3.

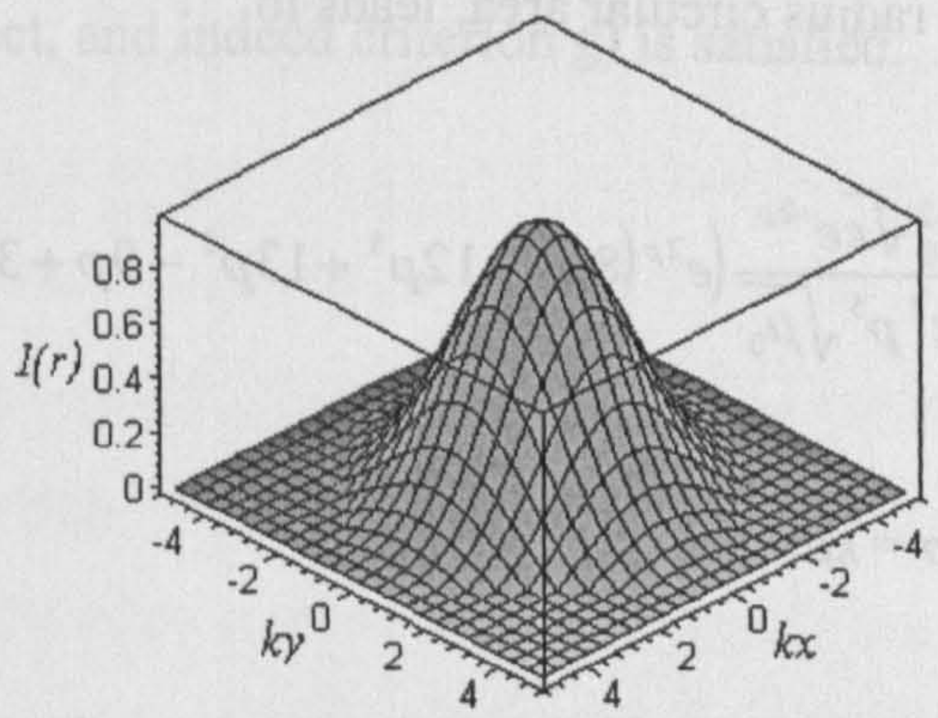

Fig. 4.11.b. Irradiance profile of order 01 normalised to 1 at (x=y=z=0) in the z=1 plane, for k=1, d=2.3.

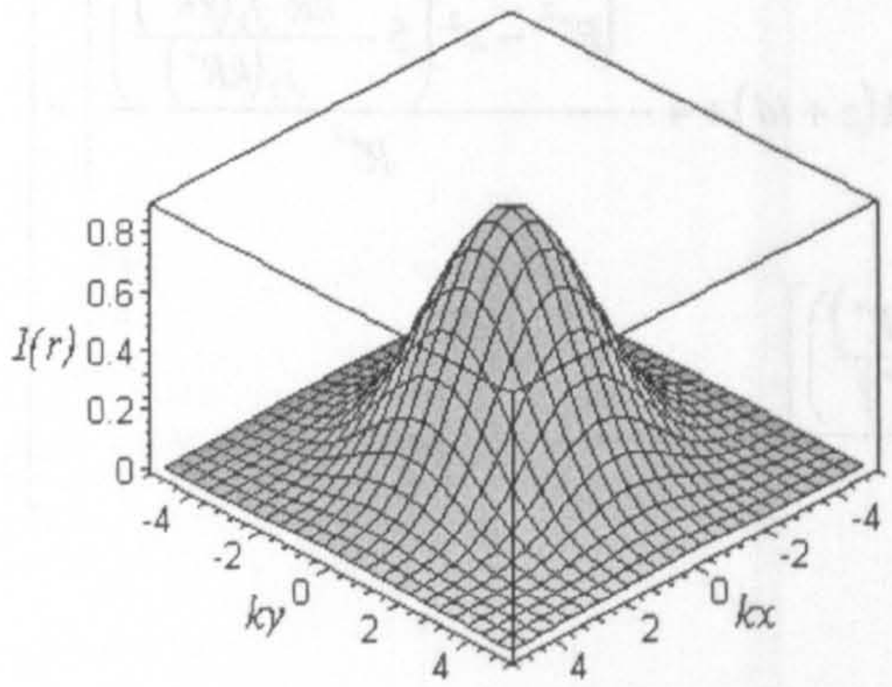

Fig, 4.11.c. Irradiance profile of order 01, normalised to 1 at , (x=y=z=0) in the z=2.3 plane, for k=1, d=2.3.

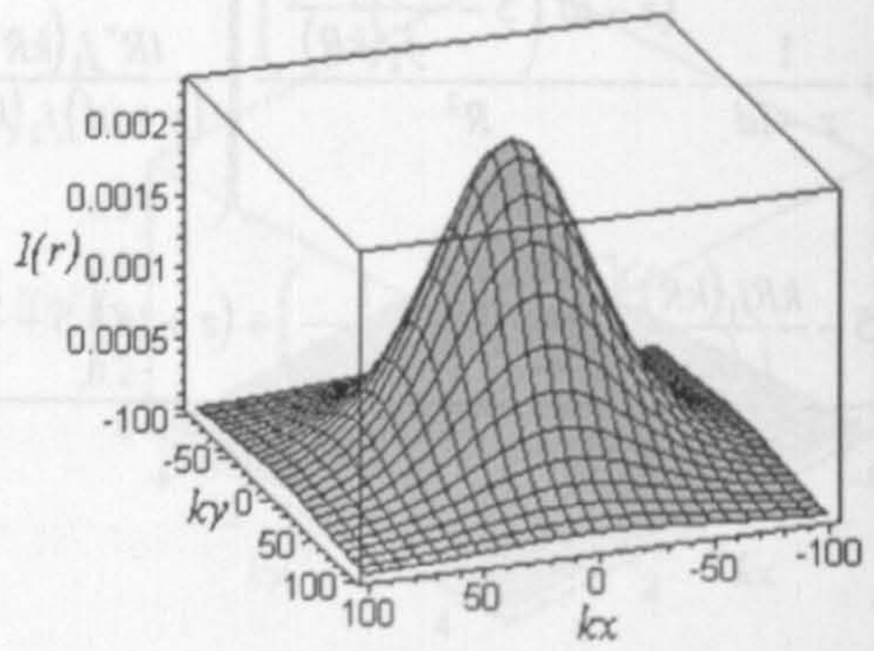

Fig. 4.11.d. Irradiance profile of order 01 normalised to 1 at (x=y=z=0) in the z=100 plane, for k=1, d=2.3.

4.8. The beam power

The last criterion which the solution of order 00 given by Eqs. (4.55) and (4.56) and the solution of order 01 given by Eqs. (4.57) and (4.58) have to satisfy is criterion g), which requires the beam power to be finite. In order to calculate the power of this Gaussian beam, the Poynting vector given by Eq. (1.34) needs to be calculated first. The power at the beam waist is dependent on the flux through the z=0 plane and thus is calculated by considering the z component of the Poynting vector. Thus the beam power is given by

$$P=\frac{1}{2}\int_0^{2\pi}\int_0^{\infty}\mathrm{Re}\left(\left[\mathbf{E}_{mn}(\mathbf{r},t)\times\mathbf{H}^{*}_{mn}(\mathbf{r},t)\right]_z\right)\rho d\rho d\phi\,. \tag{4.113}$$

As it has been demonstrated in the scalar case, the beam power of order 00 is infinite. Evaluating Eq. (4.113) for order 01, i.e. integrating the z component of Eq. (4.112) over an infinite radius circular area, leads to

$$P=\frac{\pi E_0^2\sqrt{\varepsilon}e^{-2p}}{16k^2p^5\sqrt{\mu_0}}\left(e^{2p}\left(8p^4-12p^3+13p^2-9p+3\right)+e^{-2p}\left(p^2+3[p+1]\right)-2\left(p^2+3[1-p]\right)\right), \tag{4.114}$$

where $p = kd$.

However, Barton [13] used an expression for the beam power P to the 5th order approximated Gaussian beam, which is based on the irradiance normalised to unity at (x=y=z=0). It will prove to be advantages in chapter 5 if this is done here for the beam power given in Eq. (4.114). Thus the normalised beam power is written as

$$P_{norm}=\frac{\pi E_0^2\sqrt{\varepsilon}}{4k^2\sqrt{\mu_0}}\frac{p^3\left(e^{2p}\left(8p^4-12p^3+13p^2-9p+3\right)+e^{-2p}\left(p^2+3[p+1]\right)-2\left(p^2+3[1-p]\right)\right)}{e^{2p}\left(4[p^6-4p^5+9p^4-13p^3]+49p^2-30p+9\right)+e^{-2p}\left(p^2+3[2p+3]\right)+4p[p^3+p^2+6]-14p^2-18}. \tag{4.115}$$

The square of the electric field amplitude at the focal point of the beam ($x=y=z=0$) can be related to the normalised beam power P_{norm} by

$$E_0^2=\frac{4P_{norm}k^2\sqrt{\mu_0}}{\pi\sqrt{\varepsilon}}\frac{e^{2p}\left(4[p^6-4p^5+9p^4-13p^3]+49p^2-30p+9\right)+e^{-2p}\left(p^2+3[2p+3]\right)+4p[p^3+p^2+6]-14p^2-18}{p^3\left(e^{2p}\left(8p^4-12p^3+13p^2-9p+3\right)+e^{-2p}\left(p^2+3[p+1]\right)-2\left(p^2+3[1-p]\right)\right)}. \tag{4.116}$$

A simple way to test if Eq. (4.116) is correct is to calculate E_0^2 in the paraxial limit. It is found that

$$\lim_{p\to\infty}\left(E_0^2\right)=\frac{2P_{norm}k\sqrt{\mu_0}}{\pi d\sqrt{\varepsilon}}.$$

Substituting Eq. (1.77) and remembering that in a dielectric medium $\varepsilon=\varepsilon_r\varepsilon_0$, $n=\sqrt{\varepsilon_r}$ and $c=\frac{1}{\sqrt{\varepsilon_0\mu_0}}$ leads to the following well known expression for E_0^2:

$$E_0^2=\frac{4P_{norm}}{\varepsilon_0 nc\pi w_0^2}. \tag{4.117}$$

Thus it is confirmed that Eq. (4.116) is correct, and indeed criterion g) is satisfied.

4.9. Conclusion

In this chapter it has been demonstrated that the E.M. fields

$$\mathbf{E}_{mn}(\mathbf{r},t) = E_0\left(\mathbf{M}^{(1)}_{mn}(\mathbf{r},t) + i\mathbf{N}^{(2)}_{mn}(\mathbf{r},t)\right)$$

$$H_{mn}(\mathbf{r},t) = -iE_0\sqrt{\frac{\varepsilon}{\mu}}\left(i\mathbf{M}^{(2)}_{mn}(\mathbf{r},t) + \mathbf{N}^{(1)}_{mn}(\mathbf{r},t)\right)$$

have the correct form in the paraxial limit for order 00 and 01 and also satisfies the far-field boundary conditions derived by Richards and Wolf [1] with respect to their polarisation pattern. It has been demonstrated, that due to a difference in the amplitude function, neither the radiation pattern due to $\psi_{00}(x,y,z)$ nor the one due to $\psi_{01}(x,y,z)$ is exactly identical to the one produced by a paraxial Gaussian beam focused by a lens satisfying Abbe's sine condition [1]. It is interesting to note that the only difference between the $\mathbf{M}^{1(1)}_{00}(x,y,z)$, $\mathbf{M}^{2(1)}_{00}(x,y,z)$, $\mathbf{N}^{1(1)}_{00}(x,y,z)$, $\mathbf{N}^{2(1)}_{00}(x,y,z)$ and the $\mathbf{M}^{1(1)}_{01}(x,y,z)$, $\mathbf{M}^{2(1)}_{01}(x,y,z)$, $\mathbf{N}^{1(1)}_{01}(x,y,z)$ and $\mathbf{N}^{2(1)}_{01}(x,y,z)$ functions in the far-field limit, is in their time averaged amplitude functions. These time averaged amplitude functions of the individual vector functions in the far-field limit are identical to the square root of their corresponding $Q_{00}(\alpha)$ and $Q_{01}(\alpha)$ function in the far-field limit due to their scalar functions. The derived E.M. field for order 00 and order 01 is in general elliptically polarised at the beam waist, but in the paraxial limit, these fields are linearly polarised. These fields have the correct far-field behaviour and they are linearly polarised in the far-field limit. It has additionally been demonstrated that $\psi_{01}(x,y,z)$ is a physically realizable solution to the scalar Helmholtz equation, since this function has a finite beam power, whereby $\psi_{00}(x,y,z)$ is physically not a possible solution, since this function has an infinite beam power, as pointed out already in the scalar treatment. Further it has been shown that the complex source point model of Sheppard and Saghafi [8] and the model based on Whittaker potentials [12] lead to the same, $\mathbf{M}^{1}_{00}(x,y,z)$, $\mathbf{M}^{2}_{00}(x,y,z)$, $\mathbf{M}^{3}_{00}(x,y,z)$, $\mathbf{N}^{1}_{00}(x,y,z)$, $\mathbf{N}^{2}_{00}(x,y,z)$ and $\mathbf{N}^{3}_{00}(x,y,z)$ functions for order 00.

In the next chapter the E.M. field of order 01, given explicitly by Eqs. (4.57) and (4.58), which satisfies all the criteria (a-g), will be used in order to calculate the optical trapping forces exerted on a spherical microparticle.

References

[1] Richards, B., Wolf, E., (1959) "Electromagnetic diffraction in optical systems, II. Structure of the image field in an aplanatic system," Proc. R. Soc. London, Ser. A **253**, 358-379

[2] Morse, P. M., Feshbach, H., (1953) Methods of Theoretical Physics, Part II, Mc Graw-Hill Book Company, Inc.

[3] Boas, M. L., (1983) Mathematical methods in the physical sciences, 2nd edition, John Wiley & Sons.

[4] Bohren, C. F., Huffman, D. R., (1983) Absorption and Scattering of Light by Small Particles, John Wiley & Sons.

[5] Sheppard, C. J. R., Saghafi, S. (1999) Electric and magnetic dipole beam modes beyond the paraxial approximation. *Optik,* **110,** *No.* **10** p.487-491

[6] Sheppard, C. J. R., Min Gu (1993) Imaging by a high aperture optical system. *J. mod. Opt.*, **40,** *No.* **8.** p.1631-1651.

[7] Lekner, J., (2003) Polarization of tightly focused laser beams. *J. Opt. A.: Pure Appl. Opt.* **5** p. 6-14.

[8] Sheppard, C. J. R., Saghafi, S. (1998) Electromagnetic Gaussian beams beyond the paraxial approximation. *J. Opt. Soc. Am.*, **16,** *No.* **6** p.1381-1386

[9] Cullen, A. L., Yu, P. K., (1979) Complex source point theory of the electro magnetic open resonator, Proc. R. Soc. London, Ser. A **366**, 155-171

[10] Sheppard, C. J. R., Saghafi, S. (1998) Beam modes beyond the paraxial approximation: a scalar treatment, Phys. Rev. A **57,** 2971-2979

[11] Nye, J. F., Berry, M., (1974) Dislocation in wave trains, Proc. R. Soc. London, Ser. A **336**, 165-190.

[12] Volyar, A. V., (2000) Nonparaxial Gaussian beams: 1 Vector Fields. *Technical Physics Letters* **26,** No. **7** p. 573-575

[13] Barton, J. P., Alexander, D. R., (1989), Fifth-order corrected electromagnetic field components for a fundamental Gaussian beam. *J. Appl. Phys.* **66,** No. **7** p. 2800-2802

5. Laser Tweezers

5.1. Introduction

Up to now, the discussions presented in this work were focused on the laser beam itself, but not on any applications for such a beam. In this chapter one application for a strongly focused beam, namely the laser tweezers, will be discussed. In 1873 Maxwell theoretically established that waves do indeed exert pressure. He wrote [1]: "*In a medium in which waves are propagated there is a pressure in the direction normal to the waves, and numerically equal to the energy in a unit of volume.*" In E.M. theory this pressure is referred to as radiation pressure. The same phenomena can be understood from the quantum mechanical view point, from which it is known that each photon carries momentum along the direction of propagation of the beam, which gives rise to radiation pressure as a result of photon collision with an object. The operational principle of laser tweezers is based on this radiation pressure, which pushes the to be trapped particle along the propagation direction of the beam. However due to refraction at the interface between the particle and the surounding medium the light rays are bent, giving rise to the so called gradient force. Pioneering work on laser tweezers started in 1970 by Ashkin [2], who succeeded in trapping and consequently moving micron-sized particles in liquids and gases by focused laser beams. Historically the main problem when studying radiation pressure in the laboratory was the obscuring effects of thermal forces, usually referred to as radiometric forces. These forces are caused by temperature gradients in the medium surrounding the object to be trapped. When the temperature gradients are caused by light and the particle moves, the effect is called photophoresis. These thermal forces are generally, even with lasers, orders of magnitude larger than the radiation pressure. Another well-known problem, which occurs when trapping living organisms, is damage induced to the organic object due to the absorption of the laser radiation by the organism, or in the worst case, the killing of the organism (optocution). Sterba and Sheetz [3] found that in order to trap biological materials the laser wavelength should be between 780 and 1100nm, since in general biological material is more transparent in the infrared spectrum at longer wavelength, and water is more transparent at shorter wavelengths. Ashkin [2, 4] avoided radiometric effects by suspending relatively transparent particles in relatively transparent media and by using a near infrared laser (Nd:YAG, λ=1064nm), whose wavelength was such that it was not absorbed by the organism, since heating of the organism is caused by absorption of the radiation. Due to Ashkin's discovery it became possible to trap a variety

of different particles, including living cells [5], organelles within cells [6] and even larger objects like giant amoeba [7]. There are various types of laser tweezers in use, including the single beam laser tweezers and the multi beam laser tweezers. It is the aim of this chapter to present a theoretical model of a single beam laser tweezers, which has been derived from the model presented in Barton *et al.* [8] and not to discuss all the different types of laser tweezers and their applications. Since the model presented in [8] is based on the E.M. field derived from the 5^{th} order Gaussian beam approximation [9], the accuracy of the results obtained using this model is compromised. Hence in order to improve the accuracy of the results, the 5^{th} order approximation is replaced by the E.M. fields derived in chapter 4. Very recently another model has been presented by Mazolli *et al.* [10], which is based on the Debye-type integral representation of the laser beam as a superposition of plane E.M. waves. The main difference is that Mazolli *et al.* take truncations of the beam by the focusing lens into account. This is not the case in Barton *et al.* [8] and the model presented here. Since Ashkin [11] has demonstrated that it is possible to explain the functional principle of laser tweezers using geometrical optics arguments, this approach will also be used here in order to discuss the results obtained from the E.M. theory treatment. Hence in the next section, the geometrical optics approach will be presented, and the important parameters for optical trapping determined.

5.2. The important parameters

Since optical trapping is dependent on the radiation pressure, it is implied that the beam power is important. Additionally the more the beam is focused, the smaller the area illuminated and thus the higher the radiation pressure at the focus. On the other hand optical trapping is also dependent on the physical properties and dimensions of the particle to be trapped. In order for a particle to be optically trappable, the particle must in general be transparent, even though it has been reported in [12, 13, 14] that metallic particles can also be trapped. If radiation is absorbed by the particle, then it will heat up, which is not desirable, as this can have destructive effects on the particle. These physical properties of the particle are determined by its refractive index. However it is known from Snell's law that the bending of the light rays at the interface between two media is dependent on the refractive index of both media. When referring to laser tweezers, the important parameter is called the complex relative index of refraction $\overline{n}$, defined as the ratio of the complex refractive index of the particle to the complex refractive index of the surrounding medium

[15]. In this work only the trapping of spherical, non-absorbing particles is considered. Thus the relative refractive index is real. The important parameter regarding the dimension of the particle is the so-called size parameter $\beta=ka$, a being the radius of the spherical particle and $k=\frac{2\pi n_1}{\lambda_0}$, with n_1 the refractive index of the surrounding medium and λ_0 the vacuum wavelength of the laser. A distinction has to be made between the two types of scattering, Mie scattering ($\beta>>1$), where the particle size is much larger than the laser wavelength and Rayleigh scattering ($\beta<<1$), where the particle size is approximately equal to or less than the laser wavelength. However this distinction is made for historical reasons. It has been demonstrated by Born and Wolf [16] that in the limit of small particle radius, Mie theory leads to the same result as Rayleigh theory. For values of $\bar{n}>1$, the spherical particle acts as a convex (focusing) lens. Ashkin [11] shows that a relative refractive index in the range $\bar{n}=1.05$ to $\bar{n}\cong 1.5$, which covers the regime of interest for most biological applications, leads to a good performance of the laser tweezers. At higher values of $\bar{n}$, the performance is reduced due to the increasing scattering force relative to the maximum gradient force. At values of $\bar{n}<1$, the spherical particle acts as a concave lens and hence the particle is pushed out of the beam. Finally the irradiance profile of the beam is important too, as the dielectric particle is pulled towards the region of higher light intensity. In the following sections, these parameters will be discussed in detail.

5.2.1. The refractive index

When light or any other E.M. wave travels through vacuum, it has a phase speed given by

$$v_0=\frac{1}{\sqrt{\varepsilon_0\mu_0}}=c\,. \tag{5.1}$$

The net effect of introducing a homogeneous, isotropic, dielectric, non magnetic medium into a region of free space is to change ε_0 into ε in Maxwell's equations. Hence the phase speed in the medium becomes

$$v=\frac{1}{\sqrt{\varepsilon\mu_0}}. \tag{5.2}$$

The absolute refractive index n is defined as the ratio of the speed of the E.M. wave in vacuum to the one in matter. I.e.

$$n\equiv\frac{c}{v}=\sqrt{\varepsilon_r}\,, \tag{5.3}$$

where $\varepsilon_r = \frac{\varepsilon}{\varepsilon_0}$.

However if the E.M. waves are propagating through conductive materials, then the refractive index is complex, and a certain amount of energy is absorbed by the particle in the form of heat.

5.2.2. The Fresnel reflection and transmission coefficients

At the interface between two media with different refractive indices, the E.M. wave, which travels from the first medium into the second medium will be partially transmitted into the second medium and partially reflected back into the first medium. The Fresnel refraction and transmission coefficients for a plane E.M. wave whose polarisation is perpendicular to the plane of incidence are given by Hecht [1] in the following form:

$$r_{\perp} = -\frac{\sin(\theta_i - \theta_t)}{\sin(\theta_i + \theta_t)} \tag{5.4}$$

and

$$t_{\perp} = \frac{2\sin\theta_t \cos\theta_i}{\sin(\theta_i + \theta_t)} \quad , \tag{5.5}$$

where θ_i is the incident angle and θ_t is the transmitted angle. The Fresnel refraction and transmission coefficients for an E.M. wave whose polarisation is parallel to the plane of incidence are

$$r_{\parallel} = \frac{\tan(\theta_i - \theta_t)}{\tan(\theta_i + \theta_t)} \tag{5.6}$$

and

$$t_{\parallel} = \frac{2\sin\theta_t \cos\theta_i}{\sin(\theta_i + \theta_t)\cos(\theta_i - \theta_t)} \quad . \tag{5.7}$$

A graphical representation of the magnitude of these coefficients can be seen from Figs. (5.1.) and (5.2.), where the first figure represents an argon laser beam (λ_0=514.5nm) traversing the interface between air (n_i=1) and water (n_t=1.334) and the second represents the same beam traversing the interface between water (n_i=1.334) and polystyrene (n_t=1.6).

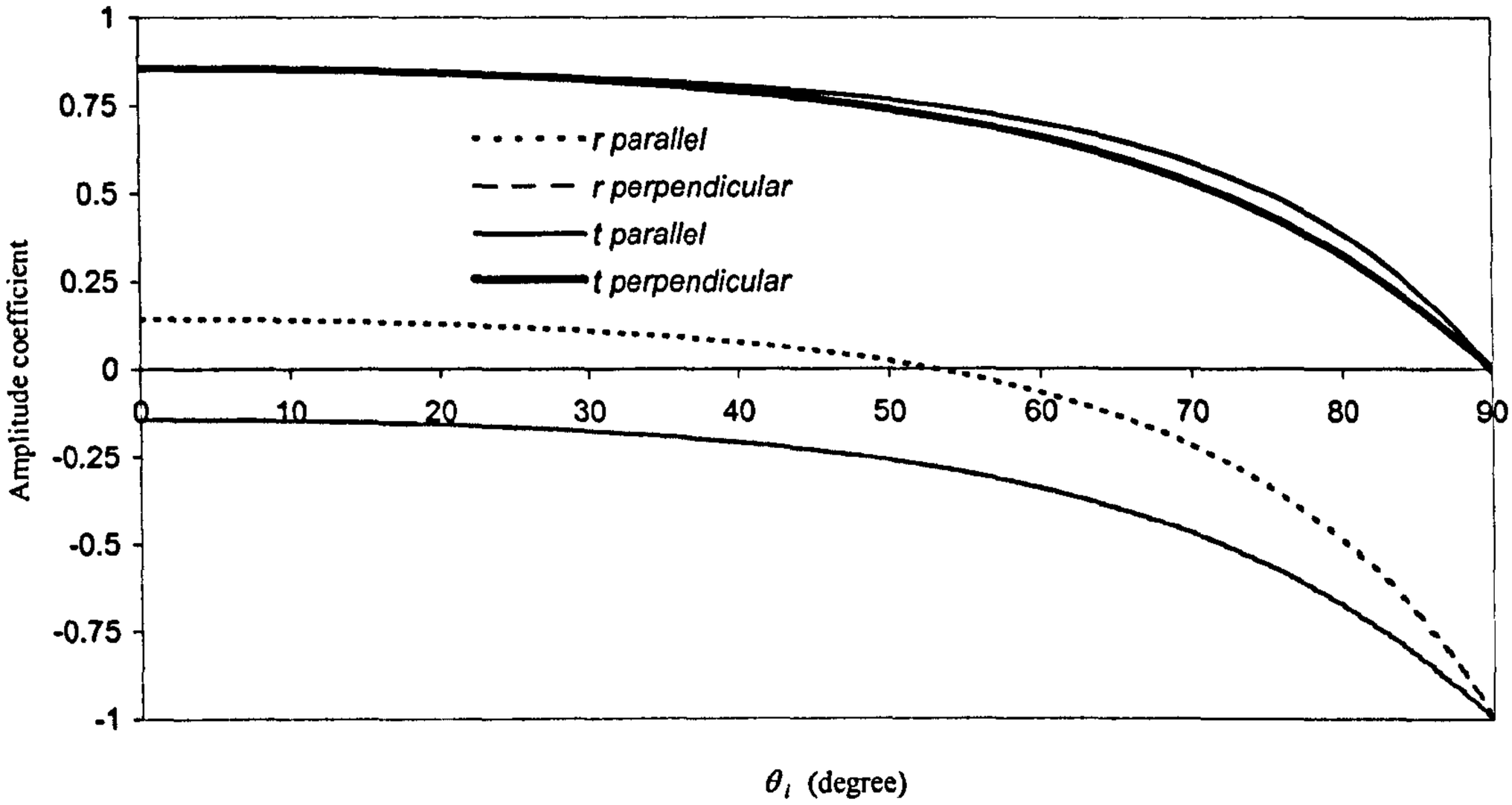

Fig. 5.1. The amplitude coefficients of reflection and transmission as a function of incident angle θ_i at an interface between air and water. The Brewster angle is 53.14^0.

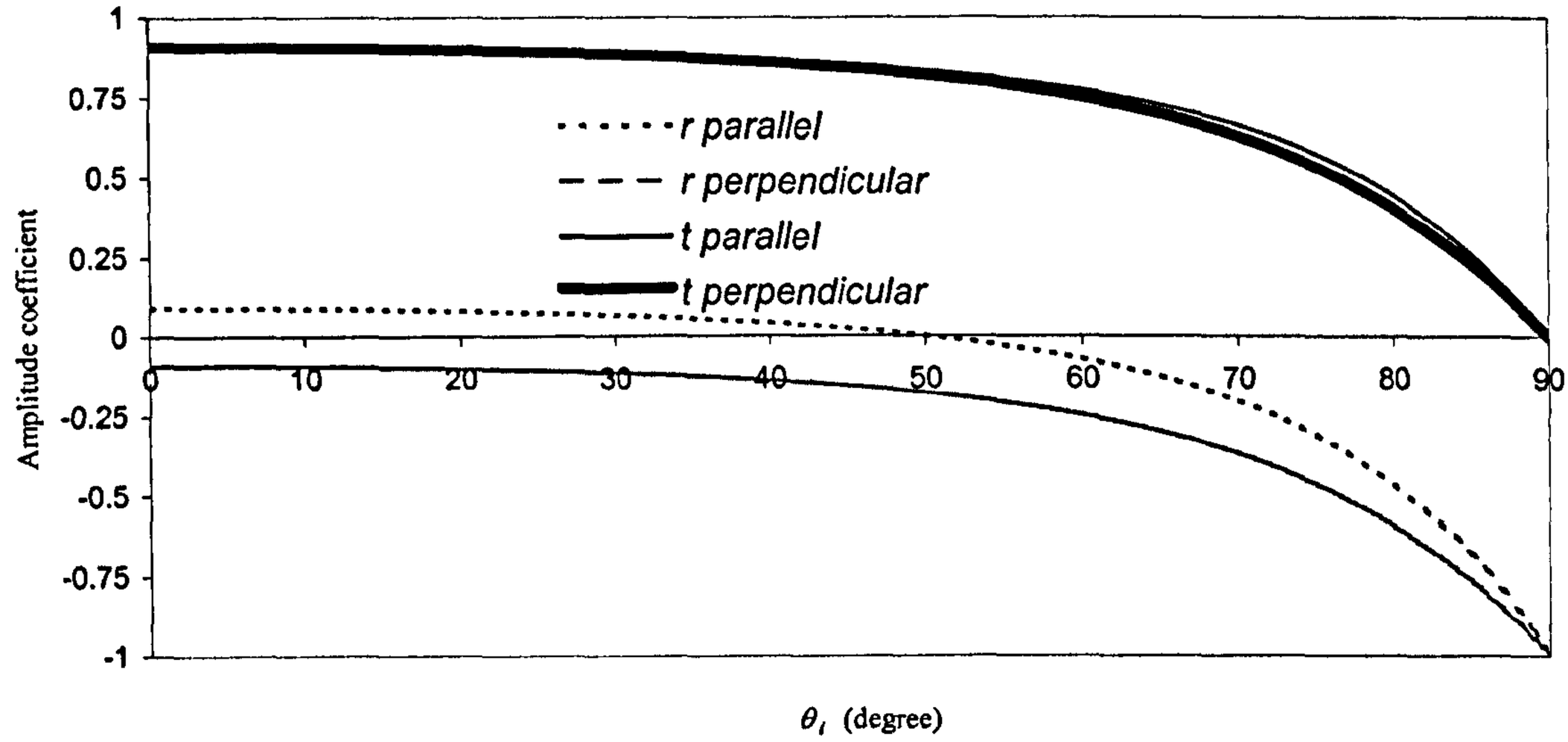

Fig. 5.2. The amplitude coefficients of reflection and transmission as a function of incident angle θ_i at an interface between water and polystyrene . The Brewster angle is 50.18^0.

It can also be seen from Figs. (5.1.) and (5.2.) that $r_{\parallel}$ starts off positive, then goes through zero and becomes negative. The incident angle θ_i at which $r_{\parallel} = 0$ is the angle for which $(\theta_i + \theta_t)=90^0$, is known as the Brewster angle or the angle of polarisation θ_p. Mathematically $\theta_p = \arctan\left(\frac{n_t}{n_i}\right)$. At θ_p all the incident light, which is polarised parallel to the incident plane is transmitted. In the case of a light beam traversing the interface between air and water, $\theta_p=53.14^0$ and for a light beam traversing the interface between

water and polystyrene, θ_p=50.18^0. So far only the cases where $n_i<n_t$ have been considered. The next step is to discuss the cases where $n_t<n_i$. This situation occurs when laser tweezers (λ_0=514.5nm) are used to trap a spherical water droplet in benzene (C_6H_6) (n_i=1.50). A graphical representation of the magnitudes of the reflection coefficients for this laser tweezers set up can be seen from Fig. (5.3.).

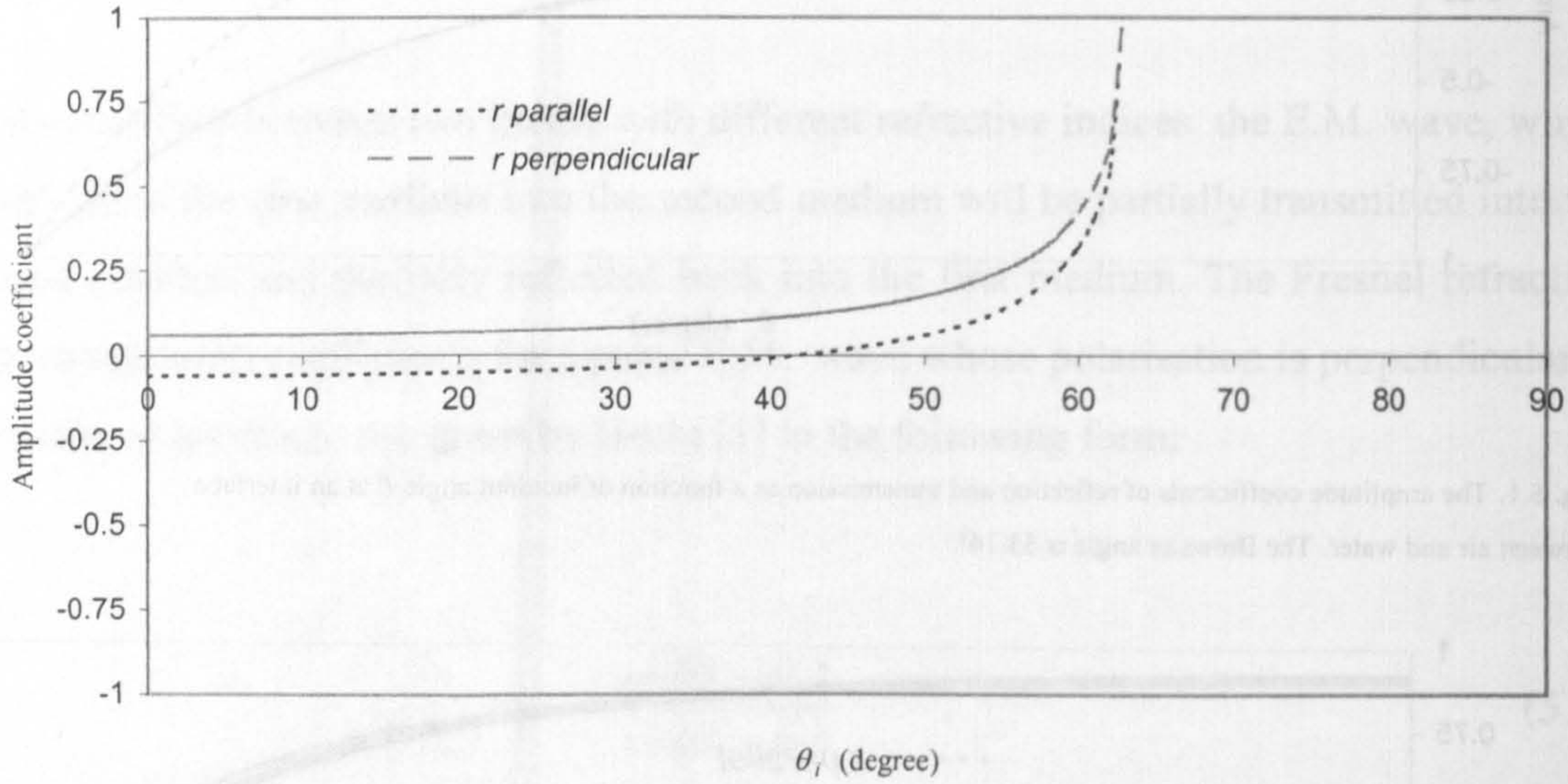

Fig. 5.3. The amplitude coefficients of reflection as a function of incident angle θ_i at an interface between benzene and water. The critical angle is 62.79^0 and the Brewster angle is 41.65^0.

It can be seen from Fig. (5.3.) that $r_{\parallel}$ starts of negative, then goes through zero and becomes positive. The Brewster angle in this case is θ_p=41.65^0 and the critical angle θ_c defined as $\theta_c = \arcsin\left(\frac{n_t}{n_i}\right)$ is 62.79^0 [1]. Thus at the critical angle all the light is internally reflected into the benzene.

5.2.3. The beam power

From Eq. (4.113) the relationship between the beam power and the E.M. field is known. Quantum theory considers the energy in an E.M. field to exist in discrete light quanta, referred to as photons. The relativistic relationship between total Energy E and momentum q of a particle of rest mass m_0 is given by

$$E^2 = c^2q^2 + m_0^2c^4 . \tag{5.8}$$

Since the photon's rest mass is zero, Eq. (5.8) reduces to

$$E = cq\,. \tag{5.9}$$

Thus each photon of energy E carries momentum

$$q = \frac{E}{c} = \frac{\hbar\omega}{c}. \tag{5.10}$$

If the energy in a wave is considered to be carried by photons, it can be seen that a plane wave incident on a metallic surface and reflected off it will exert a pressure on the surface. If the time averaged Poynting vector of the wave is $\langle \mathbf{S}(\mathbf{r}) \rangle$, then the average momentum crossing unit area per second, assuming the wave is propagating in vacuum, is in accordance with Eq. (5.10) $\frac{\langle \mathbf{S}(\mathbf{r}) \rangle}{c}$ [17]. If a plane incident wave is totally reflected at the surface of a perfect reflector, then the total change in momentum per unit area per second is $\frac{\langle 2\mathbf{S}(\mathbf{r}) \rangle}{c}$ and this is the pressure that the wave exerts on the reflecting surface. Thus the total force exerted by the beam on a perfectly reflecting infinite surface is given by

$$F_{tot} = \frac{2P}{c}, \tag{5.11}$$

assuming that the reflecting surface is perpendicular to the propagation axis of the beam. Thus for a general reflecting surface and a beam propagating in a medium with refractive index n_{ext}

$$F = \frac{Pn_{ext}}{c}\,. \tag{5.12}$$

Where P in Eqs. (5.11) and (5.12) is the beam power. Thus radiation pressure is linked to the beam power and hence the beam power is an important parameter for optical trapping.

In the previous section the Fresnel refraction and transmission coefficients were stated. These may now be linked to the reflectance and transmittance, which in turn are relevant

for optical trapping. The reflectance is defined as the ratio of the reflected amount of the radiant flux E_{0r}^2 over the incident amount of radiant flux E_{0i}^2. The transmittance is defined as the ratio of the transmitted amount of flux E_{0t}^2 over the incident amount of flux.

The reflectance of a plane E.M. wave is given by Hecht [1] as

$$R \equiv \left(\frac{E_{0r}}{E_{0i}} \right)^2 = r^2 , \tag{5.13}$$

where r^2 is either $r_\perp^2$ or $r_\parallel^2$

and the transmittance of a plane E.M. is given as

$$T \equiv \frac{n_t \cos\theta_t}{n_i \cos\theta_i} \left(\frac{E_{0t}}{E_{0i}} \right)^2 = \frac{n_t \cos\theta_t}{n_i \cos\theta_i} t^2 , \tag{5.14}$$

where t^2 is either $t_\perp^2$ or $t_\parallel^2$.

Due to conservation of energy

$$1 = \frac{E_{0r}^2}{E_{0i}^2} + \frac{n_t \cos\theta_t}{n_i \cos\theta_i} \frac{E_{0t}^2}{E_{0i}^2} = R + T . \tag{5.15}$$

A graphical representation of the magnitude of these coefficients can be seen from Figs.(5.4.) and (5.5.), where the first figure represents a beam traversing the interface between air and water and the second figure represents a beam traversing the interface between water and polystyrene.

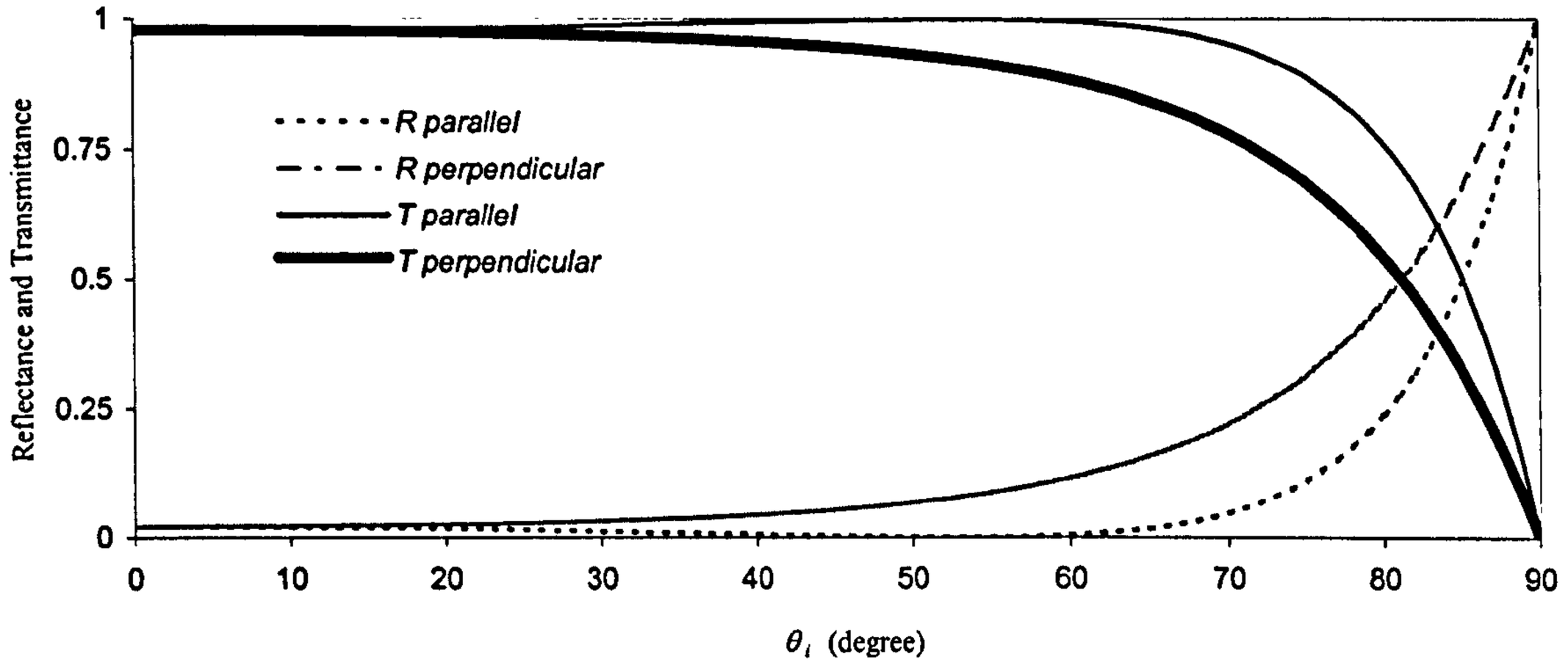

Fig. (5.4.) The reflectance and transmission as a function of incident angle θ_i at an interface between air and water. The Brewster angle is 53.14^0.

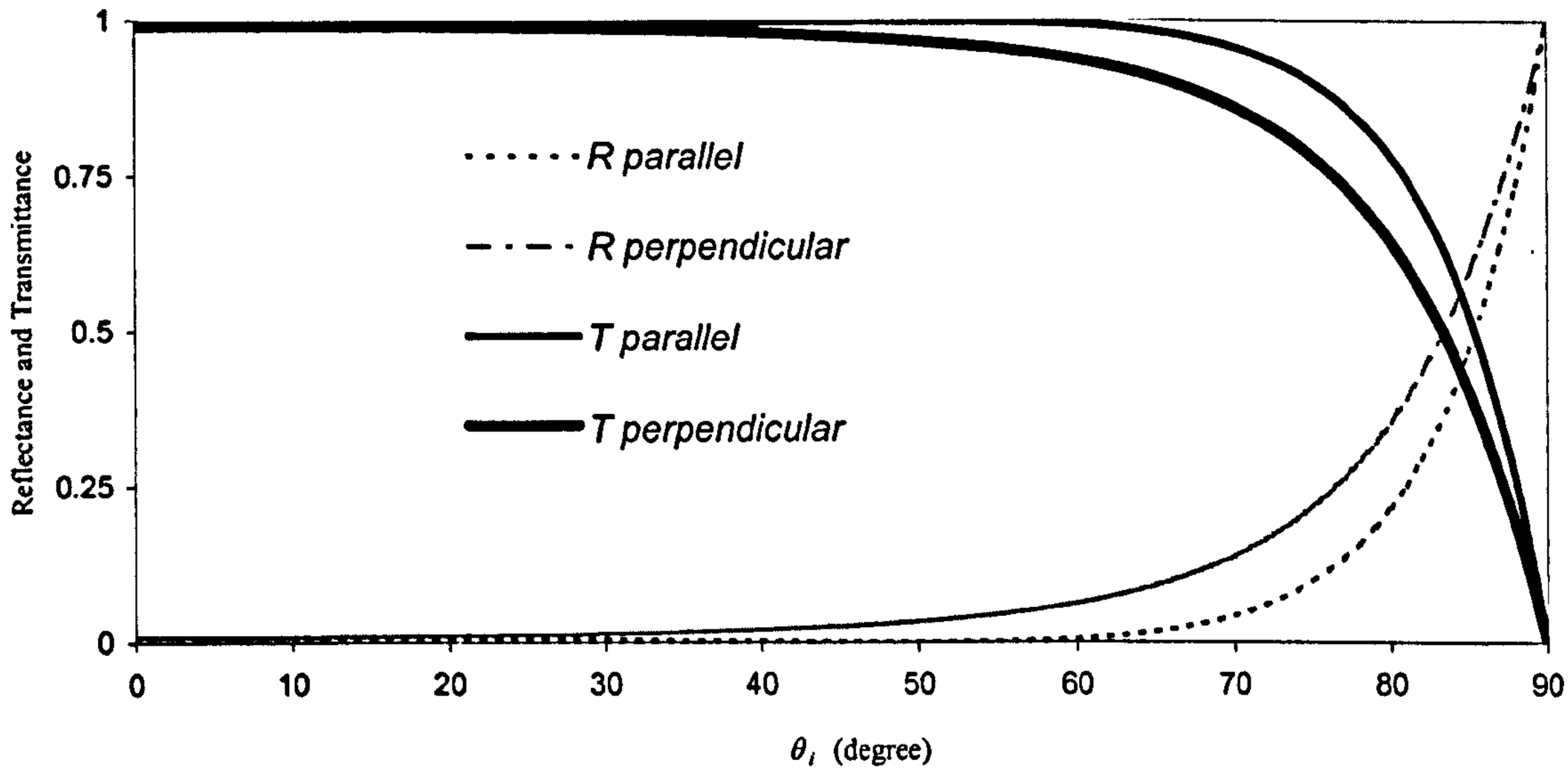

Fig. (5.5.) The reflectance and transmission as a function of incident angle θ_i at an interface between water and polystyrene . The Brewster angle is 50.18^0.

It can be seen from Figs. (5.4.) and (5.5.) that at θ_p, all the incident light, which is polarised parallel to the incident plane is transmitted. In the case of $n_t<n_i$ Fig. (5.6.) clearly shows that at the critical angle θ_c all the incident light is reflected.

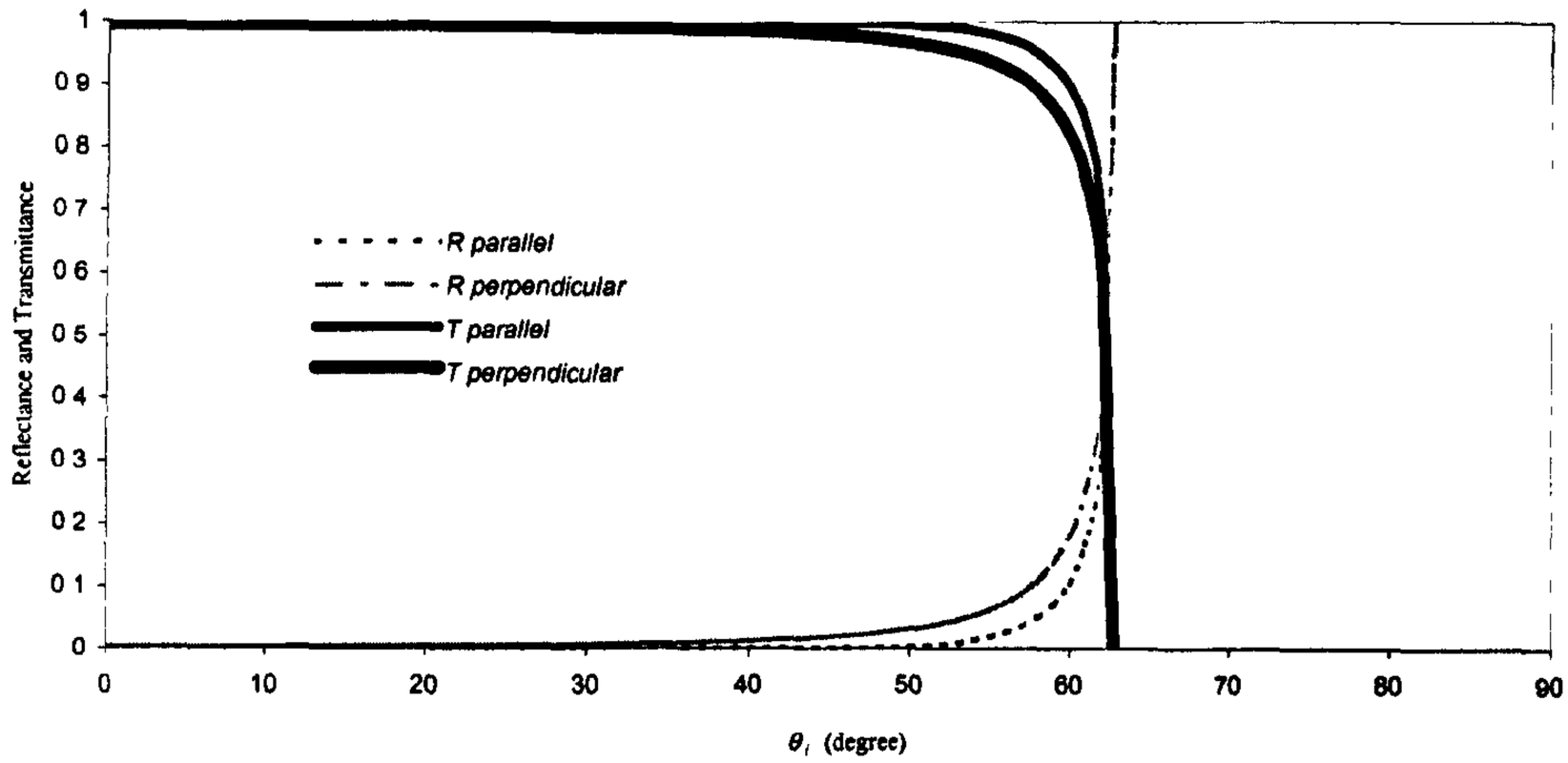

Fig. (5.6.) The reflectance and transmission as a function of incident angle θ_i at an interface between benzene and water. The critical angle is 62.79^0 and the Brewster angle is 41.65^0.

5.3. The geometrical optics representation

The geometrical optics description of the single beam laser tweezers, was first presented by Ashkin [2]. He states that in the geometrical optics representation: "*The total light beam is decomposed into individual rays, each with appropriate intensity, direction and state of polarisation, which propagate in straight lines in media of uniform refractive index. Each ray has the characteristic of a plane wave of zero wavelength that can change directions when it reflects, refracts and changes polarisation at dielectric interfaces according to the Fresnel formulae*". Ashkin pointed out that simple ray optics can only be used successfully for dielectric spheres which are large compared to the wavelength of the incident light in order to derive the radiation pressure force due to the scattering of the incident light momentum. For particles in the Rayleigh regime in which the size is much less than the wavelength of the incident light, the particle acts as a simple dipole. The force which acts on the dipole can be divided into two components, a scattering component which points in the direction of the incident light and the gradient component which points in the direction of the intensity gradient of the light beam. The same terminology is also used when discussing trapping forces in the geometrical optics regime. The stability of the optical trap results from the dominance of the gradient force pulling the particle in the direction of higher intensity, i.e. towards the focus, over the scattering force, which is trying to push the particle away from the focus in the propagation direction of the incident light. In order to get a good insight into the operational principle of single beam laser tweezers, it is useful to consider three locations of the spherical particle to be trapped. It is assumed that the

irradiance profile of the focused laser beam is Gaussian, and that the beam is propagating vertically downwards, i.e. along the positive z axis. The action of the trap on a dielectric sphere is described in terms of the total force due to a typical pair of rays A and B of the converging beam. Ashkin [2] made the simplifying assumption that the forces $\mathbf{F}_A$ and $\mathbf{F}_B$ are entirely due to refraction and are shown to point in the direction of the momentum change. The effect on the forces $\mathbf{F}_A$ and $\mathbf{F}_B$ due to the reflection of the rays at the surface of the dielectric sphere is not taken into account. For arbitrary displacements of the origin of the sphere O from the focal point u the vector sum of $\mathbf{F}_A$ and $\mathbf{F}_B$ gives the net restoring force $\mathbf{F}_{res}$, in the direction towards the focus. The ray optics figures are obtained by using the law of reflection and Snell's law, where $\hat{\mathbf{n}}$ in the following figures is the normal vector to the interface between the sphere and the surrounding medium, at the point where the rays A and B respectively reflect and refract. The refractive index of the dielectric sphere is assumed to be higher than the refractive index of the surrounding medium. Additionally these indices are assumed to be real, since the dielectric sphere and the surrounding medium are assumed to be non-absorbent. The first location to be considered is, the one where the centre of the spherical particle O is located on the z axis, after the focal point u. The geometrical illustration of this case is given in Fig. (5.7.a.).

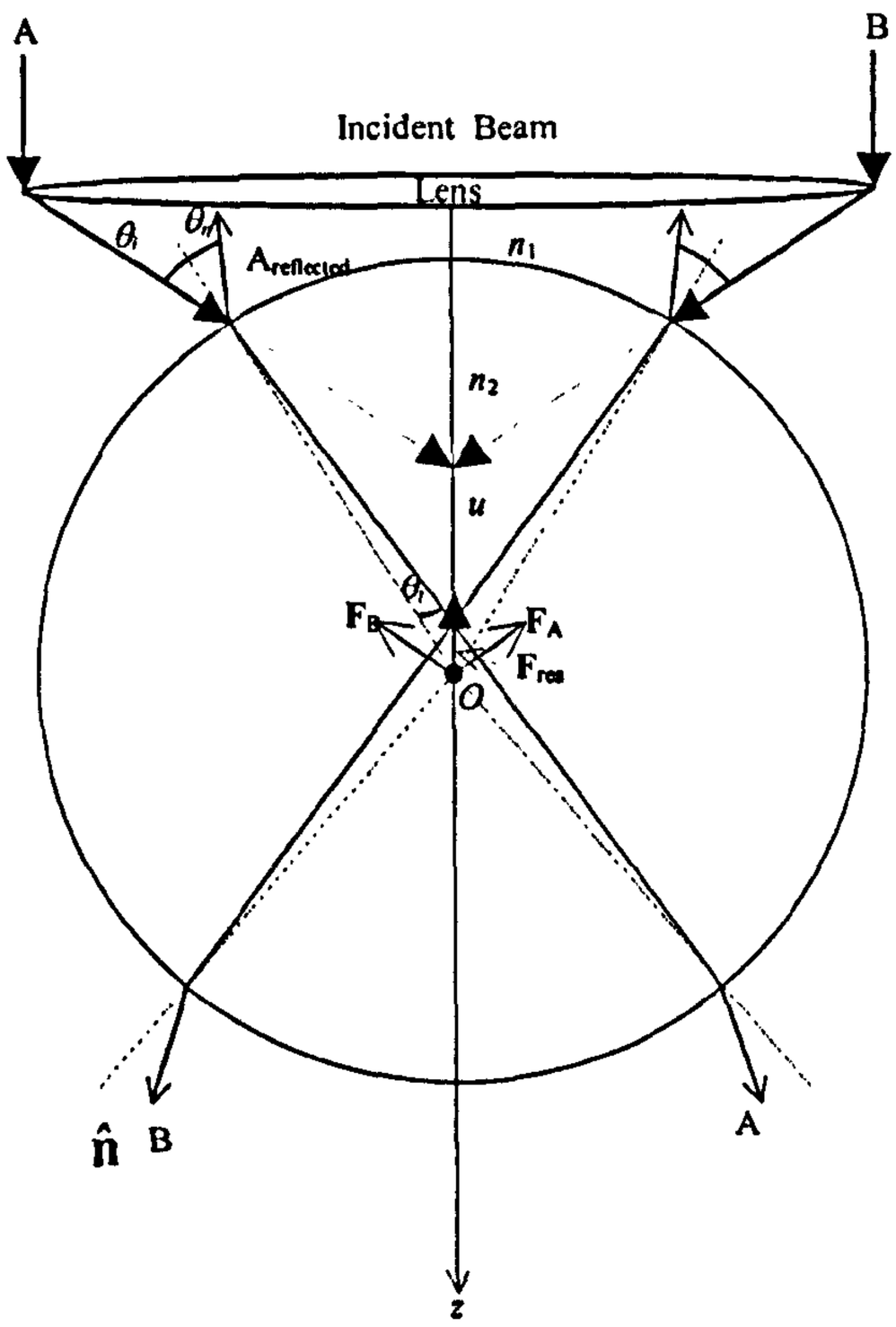

Fig. (5.7.a.) Geometrical optics representation of the trapping of a dielectric sphere, with its centre O located on the z axis after the focus. The refraction of a typical pair of rays A and B of the trapping beam gives forces $\mathbf{F}_A$ and $\mathbf{F}_B$ whose vector sum $\mathbf{F}_{res}$ is a restoring force directed towards the focal point u.

In Fig. (5.7.a.) it is implied that the photon travelling along A and the photon travelling along B carry the same momentum, since the origin of the dielectric sphere is located on the z axis, and the beam has a Gaussian irradiance profile, with its maximum on the axis. Thus the resultant trapping force has no transverse component due to conservation of momentum. Hence the resultant force is pulling the dielectric sphere towards the focal point u.

The second location to be considered is, the one where the centre of the spherical particle O is located on the z axis, before the focal point u. The geometrical illustration of this case is given in Fig. (5.7.b.).

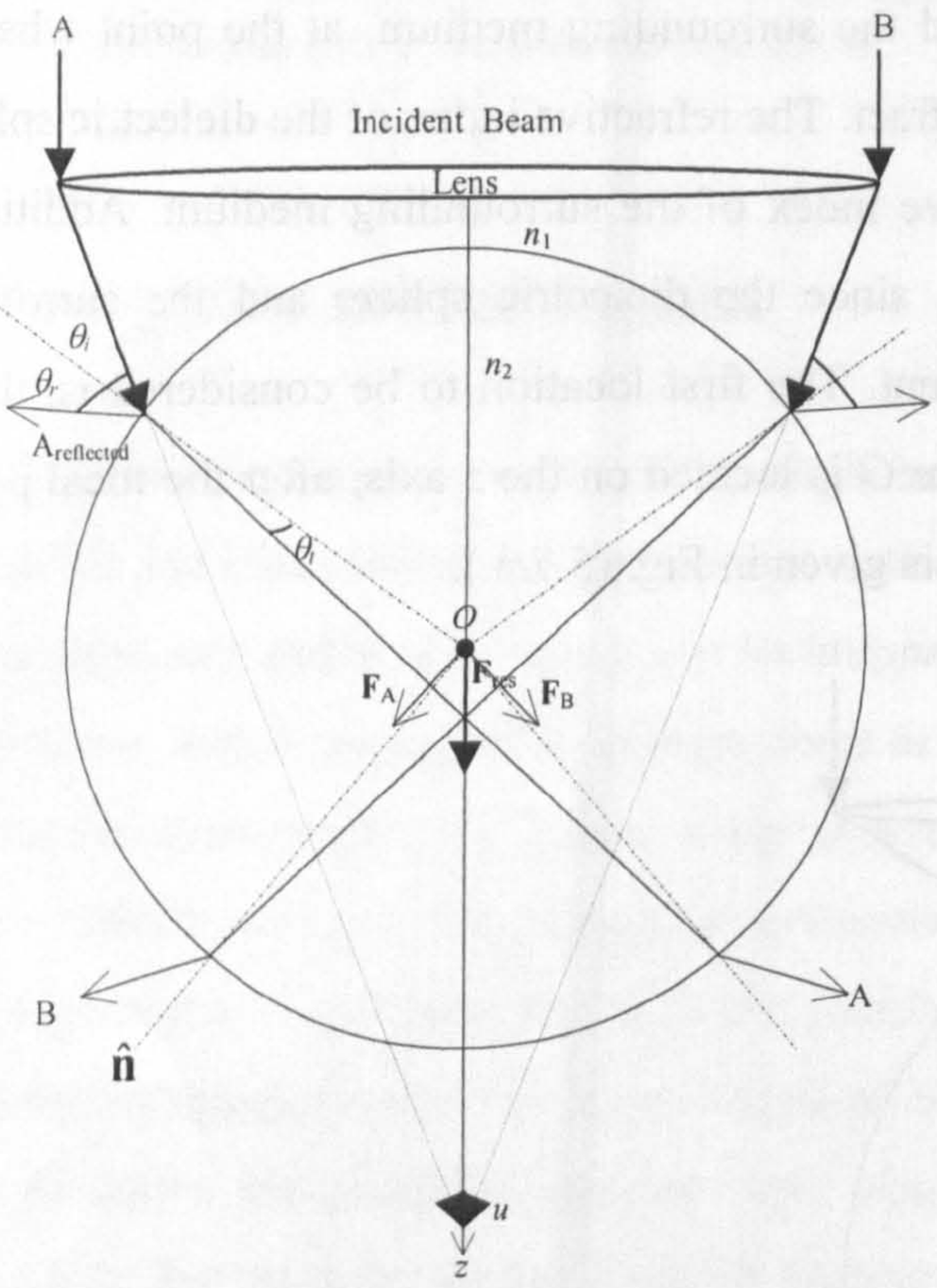

Fig. (5.7.b.) Geometrical optics representation of the trapping of a dielectric sphere, with its centre O located on the z axis before the focus. The refraction of a typical pair of rays A and B of the trapping beam gives forces $\mathbf{F}_A$ and $\mathbf{F}_B$ whose vector sum $\mathbf{F}_{res}$ is a restoring force directed towards the focal point u.

Again like in Fig. (5.7.a.) the resultant trapping force in Fig. (5.7.b.) has now transverse component, since the origin of the dielectric sphere is on the z axis and the resultant trapping force pushes the dielectric sphere towards the focal point u.

The third location to be considered is the one where the centre of the spherical particle O is located off the z axis, before the focal point u. The geometrical illustration of this case is given in Fig. (5.7.c.).

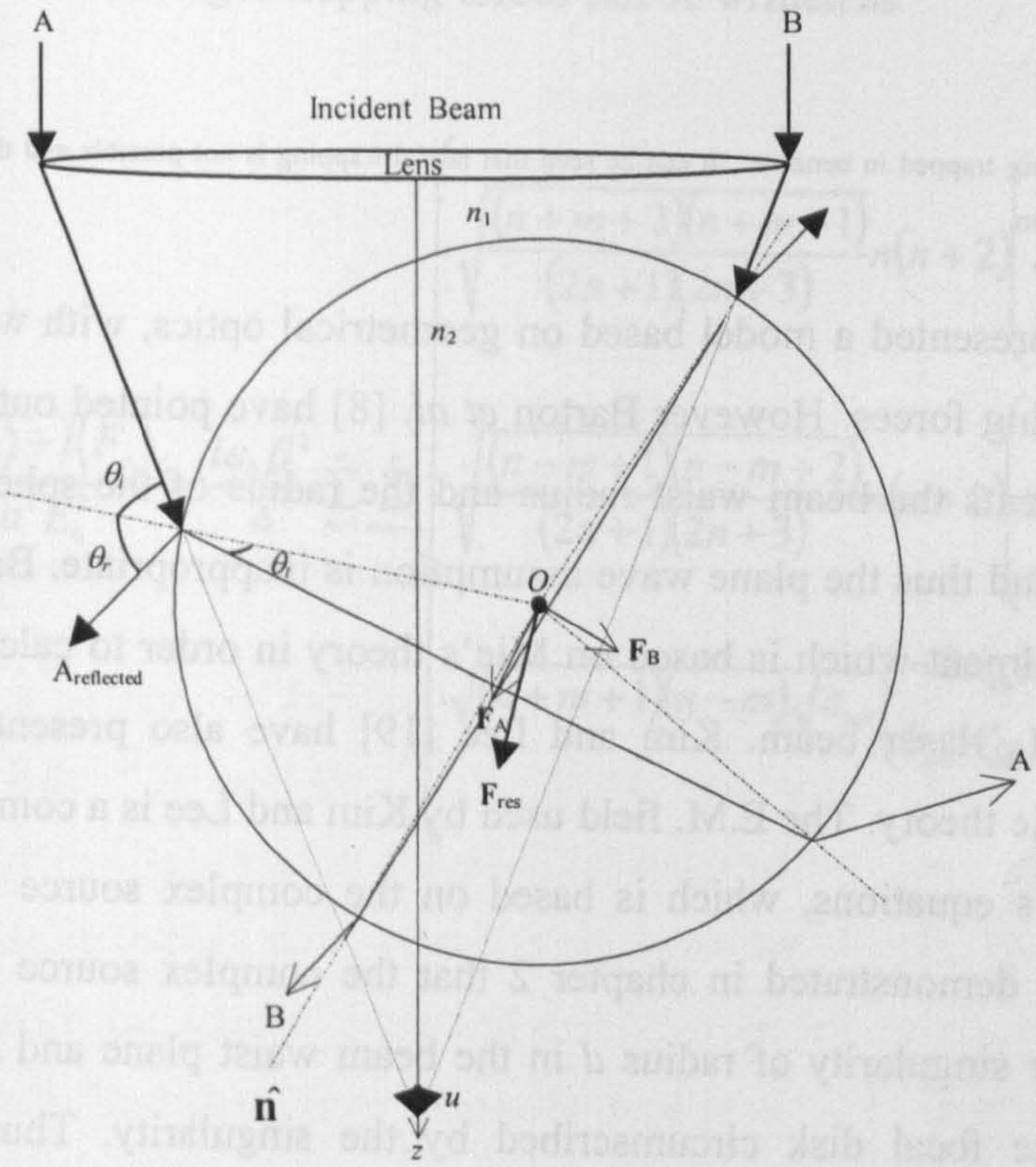

Fig. (5.7.c.) Geometrical optics representation of the trapping of a dielectric sphere, with its centre O located off the z axis before the focus. The refraction of a typical pair of rays A and B of the trapping beam gives forces $\mathbf{F}_A$ and $\mathbf{F}_B$ whose vector sum $\mathbf{F}_{res}$ is a restoring force directed towards the focal point u.

It can be seen from Fig. (5.7.c.) that the left half of the dielectric sphere is hit by a higher number of photons than the number of photons hitting the right half of the dielectric sphere. Thus the resultant trapping force has a longitudinal and a transverse component, pushing the dielectric sphere towards the focal point u. By considering a dielectric sphere whose refractive index is assumed to be lower than the refractive index of the surrounding medium, as is the case when laser tweezers are used to trap a water droplet in benzene, it can be seen from Fig. (5.7.d.), that in analogy with Fig. (5.7.c.) lateral trapping is not possible. The water droplet is pushed to the left out of the beam.

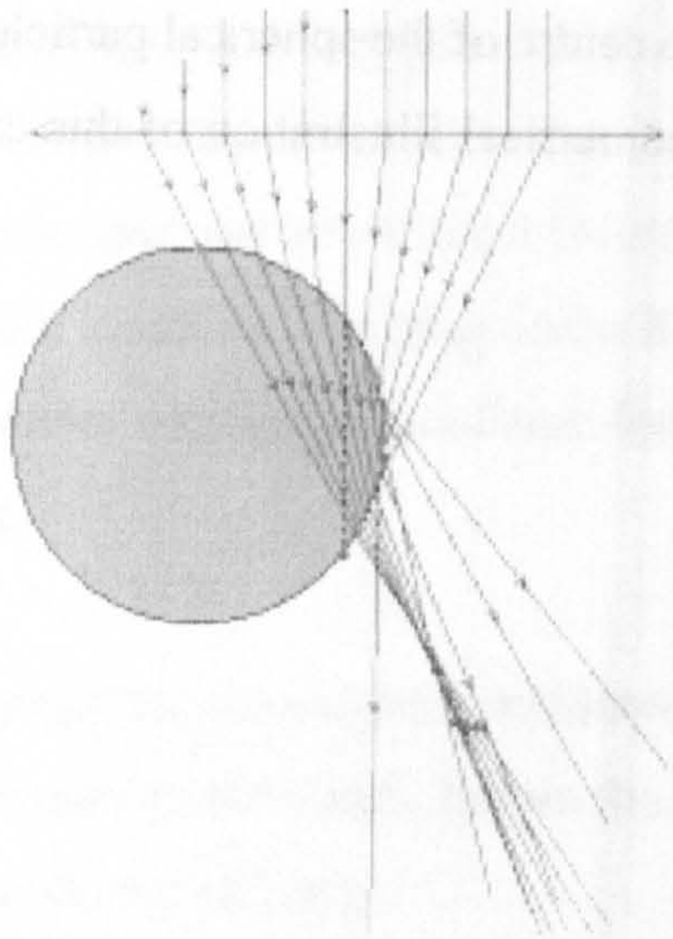

Fig. 5.7.d. Ray tracing for a water droplet being trapped in benzene. It can be seen that lateral trapping is not possible and that the particle will be pushed to the left out of the beam.

Roosen and Imbert [18] have presented a model based on geometrical optics, with which they calculate the optical trapping forces. However Barton *et al.* [8] have pointed out that for optical levitation arrangements the beam waist radius and the radius of the spherical particle are of the same order and thus the plane wave assumption is inappropriate. Barton *et al.* [8] have presented a treatment which is based on Mie's theory in order to calculate the trapping forces of a TEM_{00} laser beam. Kim and Lee [19] have also presented a treatment which is based on Mie theory. The E.M. field used by Kim and Lee is a complete rigorous solution to Maxwell's equations, which is based on the complex source point method. However it has been demonstrated in chapter 2 that the complex source point method gives rise to a circular singularity of radius d in the beam waist plane and has a discontinuity occurring on the focal disk circumscribed by the singularity. Thus the treatment of Kim and Lee [19] cannot be physically realisable. The complex source in the Kim and Lee [19] treatment would have to be accompanied by a complex sink. Thus the new Kim and Lee E.M. field would be similar to the E.M. field due to order 00 as presented in chapter 4, however not identical since Kim and Lee [19] have defined their electric field as

$$\mathbf{E}(x,y,z) = \mathbf{c}^1 \psi^{(1)}{}_{00}(x,y,z),$$

which is not identical to Eq.(4.55). In this research preference has been given to the Barton *et al.* [8] treatment for calculating the radiation force, since their treatment is valid for an arbitrary incident beam.

5.4. The Barton treatment

5.4.1. The theory

The Barton treatment is based on the light scattering theory derived by Lorenz [20] and Mie [21]. They formulated a theory with which the E.M. fields inside and outside a sphere can be calculated, when a plane incident wave is scattered by the sphere. Barton *et al.* [8] have used this theory, however generalised it for an arbitrary incident field and found that the time averaged trapping forces can be written as

$$\frac{\langle F_x\rangle + i\langle F_y\rangle}{a^2E_0^2} = \frac{i\varepsilon_0\beta^2}{4}\sum_{n=1}^{\infty}\sum_{m=-n}^{n}\left(\begin{array}{l}\sqrt{\frac{(n+m+2)(n+m+1)}{(2n+1)(2n+3)}}\,n(n+2)\left(\begin{array}{l}2\varepsilon_{ext}a_{nm}a^*_{n+1,m+1}+\varepsilon_{ext}a_{nm}A^*_{n+1,m+1}+\\ \varepsilon_{ext}A_{nm}a^*_{n+1,m+1}+2b_{nm}b^*_{n+1,m+1}+\\ b_{nm}B^*_{n+1,m+1}+B_{nm}b^*_{n+1,m+1}\end{array}\right)+\\ \sqrt{\frac{(n-m+1)(n-m+2)}{(2n+1)(2n+3)}}\,n(n+2)\left(\begin{array}{l}2\varepsilon_{ext}a_{n+1,m-1}a^*_{nm}+\varepsilon_{ext}a_{n+1,m-1}A^*_{nm}+\\ \varepsilon_{ext}A_{n+1,m-1}a^*_{nm}+2b_{n+1,m-1}b^*_{nm}+\\ b_{n+1,m-1}B^*_{nm}+B_{n+1,m-1}b^*_{nm}\end{array}\right)-\\ \sqrt{(n+m+1)(n-m)}\sqrt{\varepsilon_{ext}}\left(\begin{array}{l}-2a_{nm}b^*_{n,m+1}+2b_{nm}a^*_{n,m+1}-a_{nm}B^*_{n,m+1}+\\ b_{nm}A^*_{n,m+1}+B_{nm}a^*_{n,m+1}-A_{nm}b^*_{n,m+1}\end{array}\right)\end{array}\right) \tag{5.16}$$

and

$$\frac{\langle F_z\rangle}{a^2E_0^2} = -\frac{\varepsilon_0\beta^2}{2}\sum_{n=1}^{\infty}\sum_{m=-n}^{n}\mathrm{Im}\left(\begin{array}{l}n(n+2)\sqrt{\frac{(n-m+1)(n+m+1)}{(2n+3)(2n+1)}}\times\left(\begin{array}{l}2\varepsilon_{ext}a_{n+1,m}a^*_{nm}+\varepsilon_{ext}a_{n+1,m}A^*_{n,m}+\\ \varepsilon_{ext}A_{n+1,m}a^*_{nm}+2b_{n+1,m}b^*_{nm}+\\ b_{n+1,m}B^*_{nm}+B_{n+1,m}b^*_{nm}\end{array}\right)+\\ \sqrt{\varepsilon_{ext}}\,m\left(2a_{nm}b^*_{nm}+a_{nm}B^*_{nm}+A_{nm}b^*_{nm}\right)\end{array}\right), \tag{5.17}$$

where ε_{ext} is the permittivity of the surrounding material, β is the particle size parameter and a is the radius of the spherical dielectric particle as defined in section 5.2. The Mie scattering coefficients a_{nm} and b_{nm} are

$$a_{nm} = \frac{\psi_n'(\bar{n}\beta)\psi_n(\beta)-\bar{n}\psi_n(\bar{n}\beta)\psi_n'(\beta)}{\bar{n}\psi_n(\bar{n}\beta)\xi_n^{(1)\prime}(\beta)-\psi_n'(\bar{n}\beta)\xi_n^{(1)}(\beta)}A_{nm} \tag{5.18}$$

and

$$b_{nm} = \frac{\bar{n}\psi_n'(\bar{n}\beta)\psi_n(\beta) - \psi_n(\bar{n}\beta)\psi_n'(\beta)}{\psi_n(\bar{n}\beta)\xi_n^{(1)'}(\beta) - \bar{n}\psi_n'(\bar{n}\beta)\xi_n^{(1)}(\beta)} B_{nm} \quad , \tag{5.19}$$

where

$$A_{nm} = \frac{1}{n(n+1)\psi_n(\beta)} \int_0^{2\pi}\int_0^{\pi} \sin\theta E_r^i(a,\theta,\phi) Y_{nm}^*(\theta,\phi) d\theta d\phi \tag{5.20}$$

and

$$B_{nm} = \frac{1}{n(n+1)\psi_n(\beta)} \int_0^{2\pi}\int_0^{\pi} \sin\theta H_r^i(a,\theta,\phi) Y_{nm}^*(\theta,\phi) d\theta d\phi \,. \tag{5.21}$$

The function $\xi_n^{(1)}(\beta) = \psi_n(\beta) - i\chi_n(\beta)$, where here $\psi_n(\beta)$ and $\chi_n(\beta)$ are the Riccati-Bessel functions, defined as

$$\psi_n(\beta) = \beta j_n(\beta) \tag{5.22}$$

and

$$\chi_n(\beta) = \beta y_n(\beta) \quad , \tag{5.23}$$

where $j_n(\beta)$ and $y_n(\beta)$ are given by Eqs. (2.11.a) (exchanging x with β). $Y_{nm}(\theta,\phi)$ is the spherical harmonic function defined as [22]

$$Y_{nm}(\theta,\phi) \equiv \sqrt{\frac{2n+1}{4\pi}\frac{(n-m)!}{(n+m)!}} (-1)^m P_n^m(\cos\theta) e^{im\phi} \quad , \tag{5.24}$$

where the normalisation is chosen such that

$$\int_0^{2\pi}\int_0^{\pi} Y_n^m(\theta,\phi) Y_{n'}^{m'*}(\theta,\phi) \sin\theta d\theta d\phi = \int_0^{2\pi}\int_{-1}^{1} Y_n^m(\theta,\phi) Y_{n'}^{m'*}(\theta,\phi) d(\cos\theta) d\phi = \delta_{nn'}\delta_{mm'} \quad . \tag{5.25}$$

$P_n^m(\cos\theta)$ is given by Eq. (2.14), where $n = 0, \pm1, \pm2, \ldots$ and $m \le |n|$.

Ulanowski and Jones [23] have modelled the work of Barton *et al.* [8] and thus have calculated the radial part of the electric and magnetic fields, based on the 5th order Gaussian beam approximation given by Eqs. (1.136), as follows

$$\begin{aligned} E_r &= E_x \sin\theta\cos\phi + E_y \sin\theta\sin\phi + E_z \cos\theta \\ H_r &= H_x \sin\theta\cos\phi + H_y \sin\theta\sin\phi + H_z \cos\theta \end{aligned} \quad , \tag{5.26}$$

where the following substitutions were made

$$\begin{aligned} x &= a\sin\theta\cos\phi + x_0 \\ y &= a\sin\theta\sin\phi + y_0 \\ z &= a\cos\theta + z_0 \end{aligned} \quad , \tag{5.27}$$

With x_0, y_0 and z_0 representing the offsets from the focal point from the origin, which is at the centre of the sphere of radius a. The laser beam is assumed to propagate along the positive z axis direction, i.e. vertically upwards.

The radial parts of the electric and magnetic field components in Eqs. (5.26) are substituted into Eqs. (5.20) and (5.21) respectively and thus the Mie scattering coefficients calculated. However Ulanowski and Jones [23] have written the computer program for real relative refractive indices only, which is adequate for calculating the trapping forces for a water droplet being trapped in air and a polystyrene sphere being trapped in water, which are the particles considered here. The code developed by Ulanowski and Jones [23] is modified by replacing the electric and magnetic field given by Eqs. (1.136) with the electric and magnetic fields given by Eqs. (4.57) and (4.58) respectively and by replacing E_0^2 given by Eq. (1.137) with E_0^2 given by Eq. (4.116). This modification leads to more accurate results of the trapping forces, since the E.M. field is an exact solution to Maxwell's equations and not a to 5th order approximate solution. This new treatment is referred to as the "GB01" treatment and is used to calculate the trapping forces exerted by a focused order 01 laser beam on a spherical dielectric particle. In the next section the important parameters are determined.

5.4.2. The methodology

In general when designing an optical tweezers set up, the diameter of the focusing lens (D) and the beam diameter ($2w$) need to be chosen carefully in order to reduce F_z, which pushes the particle along the axis of propagation of the beam. Siegman [24] defines the speed (f-number) of the lens as

$$f^{\#}=\frac{f}{D}, \tag{5.28}$$

where f is the focal length of the lens. However, in the field of optical tweezers, the numerical aperture of a lens is normally considered. Hecht [1] defines the numerical aperture

$$\mathrm{NA}=\frac{1}{2f^{\#}}\ . \tag{5.29}$$

It was further mentioned in chapter 2 that

$$\frac{2f^2}{kw^2}=\frac{kw_0^2}{2}=d\ . \tag{5.30}$$

Hence

$$f=w\sqrt{\frac{kd}{2}}\ . \tag{5.31}$$

Wright *et al.* [25] have chosen for their laser tweezers set up, a beam waist radius w_0=0.39μm, a lens with NA=1.3 and a laser wavelength λ_0=1.06 μm. Thus using Eqs. (5.30) and (5.31) it is found that d=0.4508μm and kd=2.67. From Eq. (5.29) it follows that $f^{\#}$= 0.3846 and thus using Eqs. (5.28) and (5.31) it is found that Wright *et al.* [25] have chosen a lens diameter $D = 3w$. Using the formula for the transmitted power (Eq. (1.76)) it is found that 98.9% of the power is transmitted. However in the calculations 100% power transmission was assumed. Using the same lens diameter it is found that Barton *et al.*'s [8] calculations with a beam waist radius of 1 μm and a wavelength of λ_0=514.5nm lead to a numerical aperture of the focusing lens of NA=0.246, or kd=74.6. In the next section, the

results obtained by Barton *et al.* [8], based on the 5th order Gaussian beam approximation, are compared with the results based on the GB01 treatment.

5.5. The GB01 treatment versus the 5th order Gaussian beam approximation

In this section, the restoring accelerations exerted by a focused laser beam with kd=74.6, a beam power of 3.5mW, a beam waist radius of 1 μm and a wavelength of λ_0=514.5nm, on a spherical water droplet (n=1.334 [8]) of radius 2.48μm and mass $m_w=6.39\times10^{-14}$ kg suspended in air are calculated using the 5th order Gaussian beam approximation and the GB01 treatment. Fig. (5.8.) compares the restoring acceleration $a_z = \frac{F_z}{m_w}$ for sphere positions along the axis of propagation. However, the restoring acceleration is expressed in relation to the acceleration due to gravity g. Thus $[a_z/g]$ is calculated using both methods. The offset along the x and y axis is zero (x_0=y_0=0μm).

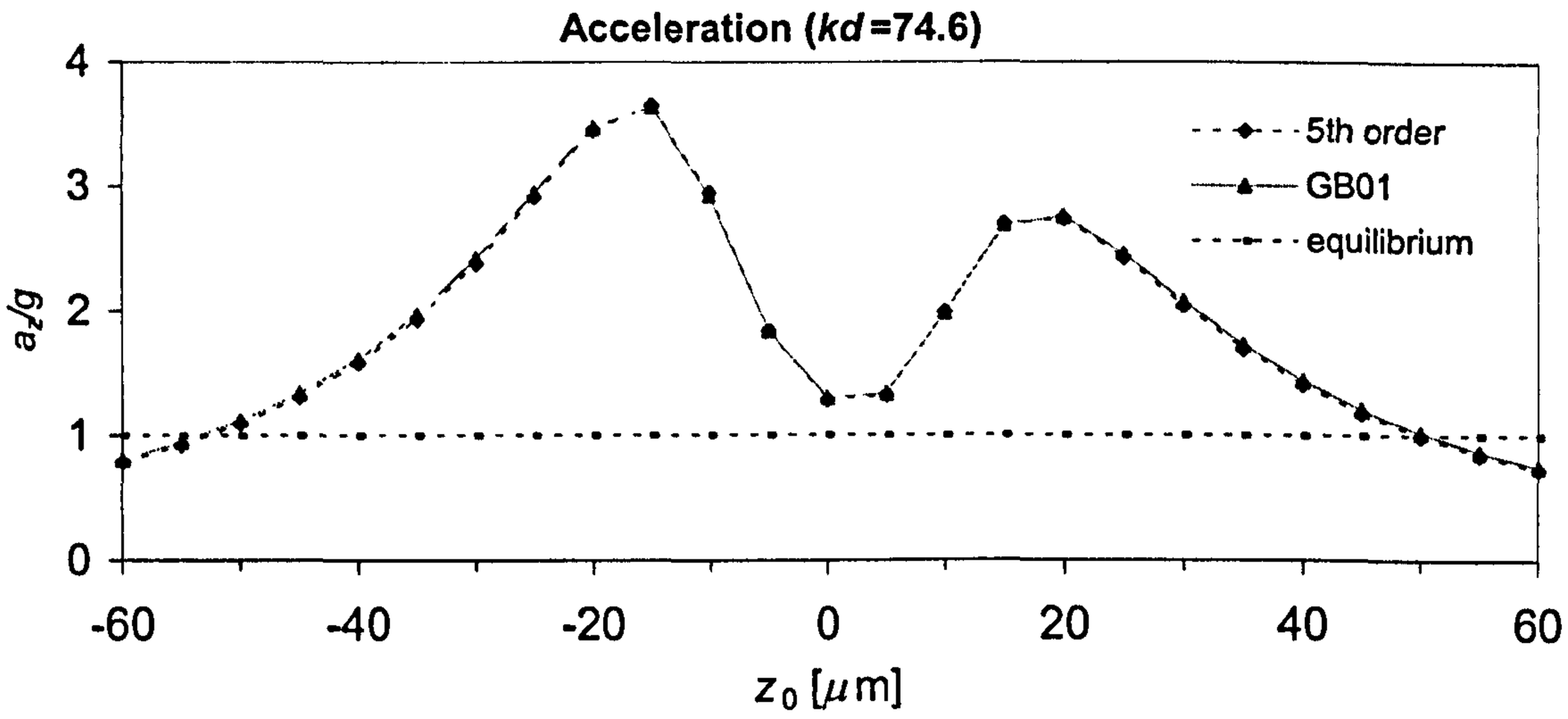

Fig. 5.8. Comparison of the restoring acceleration based on the 5th order Gaussian beam approximation (doted curve) and the GB01 treatment (solid curve), along the propagation axis for optical levitation of a water droplet in air, using a focused order 01 linearly polarised laser beam. (x_0=y_0=0, n=1.334 , diameter of water droplet = 4.96 μm, $\bar{n}$ = 1.334 , wavelength λ_0 = 0.5145 μm , w_0=1μm, kd=74.6 and a beam power of 3.5 mW.)

It can be seen that both curves cross the line, which represents the equilibrium, twice. Thus the next task is to establish if these equilibria are stable or unstable. By definition an equilibrium is stable in the z direction according to Ohanian [26] if

$$\frac{d(a_z/g)}{dz} < 0 \qquad (5.32)$$

and unstable if

$$\frac{d(a_z/g)}{dz} > 0 \quad . \tag{5.33}$$

Hence the equilibrium position near z_0=-50 μm is unstable and the equilibrium position near z_0=50 μm is stable. In table (5.1.) the numerical values for the restoring acceleration along the axis of propagation are given. The RMS error is calculated as follows:

$$\text{RMS error in \%} = \sqrt{\frac{(5^{\text{th}}\text{ order} - \text{GB01})^2}{(\text{GB01})^2}} * 100 \, . \tag{5.34}$$

z_0(μm)	a_z/g (5th order)	a_z/g (GB01)	RMS error in %
-60	0.7898	0.8085	2.32
-55	0.9233	0.9447	2.26
-50	1.0910	1.1154	2.19
-45	1.3043	1.3321	2.09
-40	1.5779	1.6094	1.95
-35	1.9301	1.9647	1.76
-30	2.3774	2.4134	1.49
-25	2.9151	2.9470	1.08
-20	3.4500	3.4665	0.47
-15	3.6460	3.6326	0.37
-10	2.9456	2.9183	0.94
-5	1.8327	1.8305	0.12
0	1.2801	1.2934	1.03
5	1.3198	1.3308	0.83
10	1.9837	1.9781	0.28
15	2.6929	2.6883	0.17
20	2.7370	2.7519	0.54
25	2.4214	2.4487	1.12
30	2.0371	2.0683	1.51
35	1.6909	1.7215	1.77
40	1.4056	1.4337	1.96
45	1.1770	1.2021	2.09
50	0.9948	1.0170	2.19
55	0.8489	0.8686	2.27
60	0.7313	0.7487	2.32
		average RMS error	**1.41**

Table 5.1. The numerical values of the restoring acceleration along the axis of propagation a_z/g calculated using the GB01 treatment and the 5th order Gaussian beam approximation model, for optical levitation of a water droplet in air, using a focused order 01 mode linearly polarised laser beam. (x_0=y_0=0, $\bar{n}$ = 1.334, diameter of spherical particle = 4.96 μm, wavelength λ_0 = 0.5145 μm, w_0=1μm, kd=74.6 and a beam power of 3.5 mW.)

It can be seen from Fig. (5.8.) and table (5.1.) that a good agreement is present with the results presented by Barton *et al.* [8]. The average RMS error is 1.41%. Since these restoring acceleration values are for an almost paraxial Gaussian beam (kd=74.6), they are

very useful to benchmark the restoring acceleration values based on the GB01 treatment. In the case where the restoring acceleration is calculated along the x axis in the 5th order Gaussian beam approximation (along the direction of polarisation), it has to be compared with the restoring acceleration along the y axis in the GB01 treatment, since the y axis is the direction of polarisation for this case (Eq.4.99). Barton *et al.* [8] chose the stable equilibrium position z_0=50μm above the focal point. The beam diameter is, in accordance with Eq. (1.80), $2w\approx16.5$ μm at this point, which is greater than the droplet diameter. In order to calculate the restoring accelerations along the x axis, y_0=0 μm. In the GB01 treatment, as the direction of polarisation is the y axis, the restoring acceleration along this axes is calculated with x_0=0 μm. Fig. (5.9.) compares the restoring acceleration for sphere positions along the direction of polarisation [a_x] and [a_y] respectively, calculated using both methods.

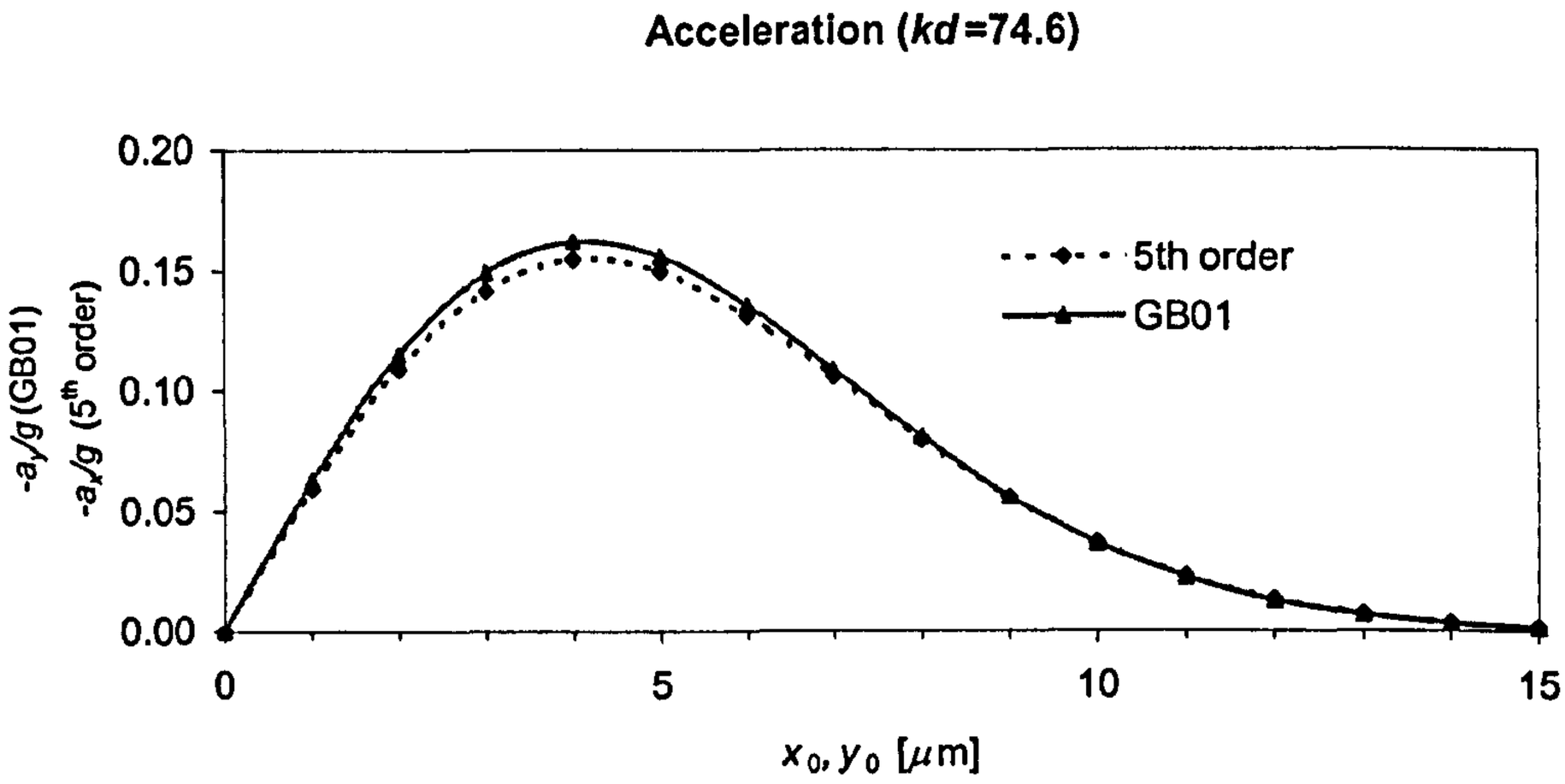

Fig. 5.9. Comparison of the restoring acceleration based on the 5th order Gaussian beam approximation (doted curve) and the GB01 treatment (solid curve), along the polarisation axis versus displacement along the polarisation axis for optical levitation of a water droplet in air, using a focused order 01 mode linearly polarised laser beam at a droplet propagation axis position of z_0 = 50 μm above the focal point. (x_0, y_0=0μm, z_0=50μm, $\overline{n}$ = 1.334 , diameter of spherical particle = 4.96 μm, wavelength λ_0 = 0.5145 μm, w_0=1μm, kd=74.6 and a beam power of 3.5 mW.)

In table (5.2.) the numerical values for the restoring acceleration along the axis of polarisation are given.

$x_0(\mu m)$, $y_0(\mu m)$	$-a_x/g$ (5th order)	$-a_y/g$ (GB01)	RMS error in %
0	0.0000	0.0000	0.00
1	0.0595	0.0630	5.46
2	0.1092	0.1153	5.27
3	0.1419	0.1493	4.96
4	0.1548	0.1621	4.52
5	0.1496	0.1558	3.96
6	0.1313	0.1357	3.26
7	0.1061	0.1087	2.43
8	0.0795	0.0807	1.47
9	0.0557	0.0559	0.37
10	0.0366	0.0363	0.86
11	0.0226	0.0221	2.19
12	0.0132	0.0127	3.58
13	0.0073	0.0069	4.94
14	0.0038	0.0036	6.13
15	0.0019	0.0018	7.01
		average RMS error	**3.53**

Table 5.2. The numerical values of the restoring acceleration along the axis of polarisation a_x/g and a_y/g respectively calculated using the GB01 treatment and the 5th order Gaussian beam approximation model, for optical levitation of a water droplet in air, using a focused order 01 mode linearly polarised laser beam. (x_0, y_0=0μm, z_0=50μm, $\overline{n}$ = 1.334 , diameter of spherical particle = 4.96 μm, wavelength λ_0 = 0.5145 μm, w_0=1μm, kd=74.6 and a beam power of 3.5 mW.)

Fig. (5.10.) compares the restoring acceleration for sphere positions along the axis perpendicular to the direction of polarisation [a_y] and [a_x] respectively, calculated using both models.

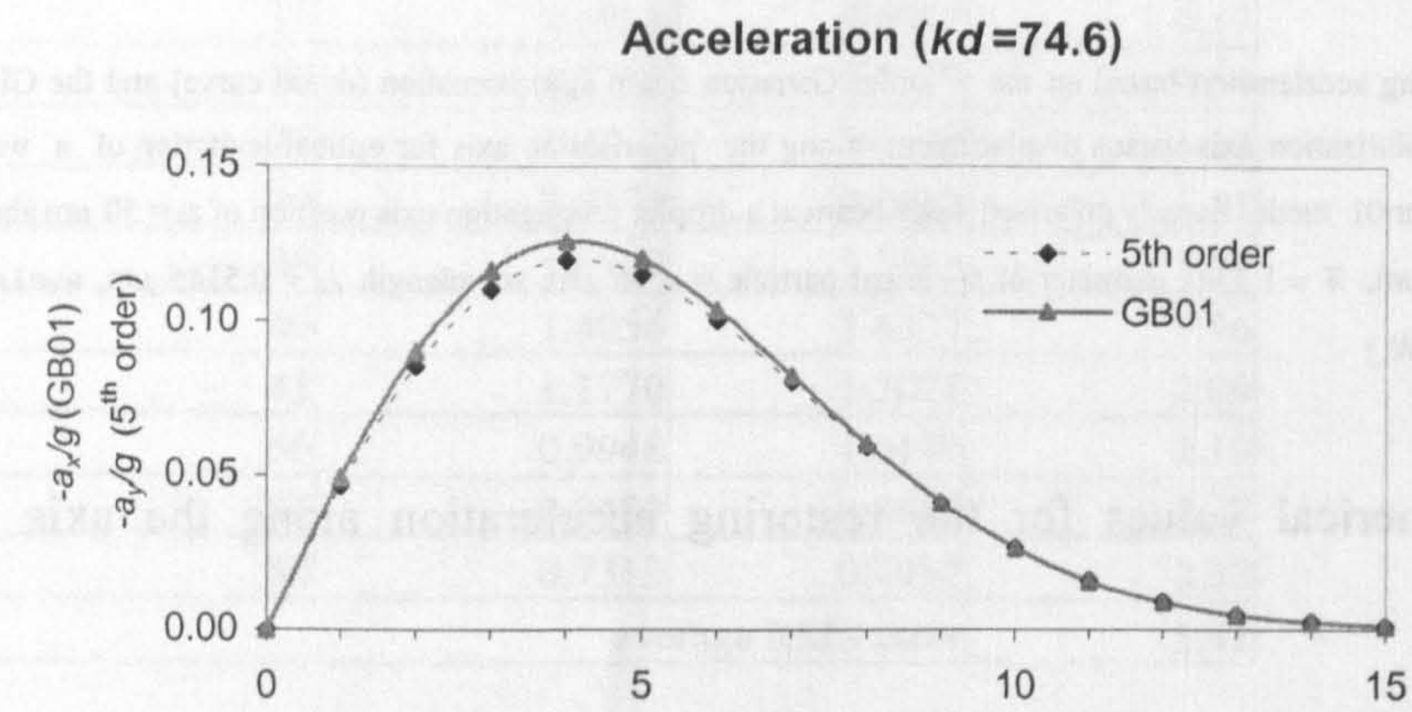

Fig. 5.10. Comparison of the restoring acceleration based on the 5th order Gaussian beam approximation (doted curve) and the GB01 treatment (solid curve), along the axis perpendicular to the direction of polarisation versus displacement along the axis perpendicular to the direction of polarisation axis for optical levitation of a water droplet in air, using a focused order 01 mode linearly polarised laser beam. (x_0, y_0=0μm, z_0=50μm, $\overline{n}$ = 1.334 , diameter of spherical particle = 4.96 μm, wavelength λ_0= 0.5145 μm, w_0=1μm, kd=74.6 and a beam power of 3.5 mW.)

By comparing Figs. (5.9.) and (5.10.) it can be seen, as expected, that the restoring acceleration along the polarisation axis of the beam is greater than the restoring acceleration along the axis perpendicular to the direction of polarisation. This is due to the fact that the Fresnel reflectance and transmittance coefficients are different for an incident E.M. wave being polarised parallel to the incident plane and perpendicular to the incident plane. It can be seen from Fig. (5.4.) that if the E.M. field is polarised parallel to the incident plane, more radiation is transmitted, than when the E.M. field is polarised perpendicular to the incident plane. It can thus be said, that even though the Fresnel coefficients are given for plane E.M. waves, they can be used for the E.M. fields of focused Gaussian beams, like the ones used here. Since optical trapping is dependent on the amount of radiation refracted, the trapping forces are larger for particle displacements parallel to the direction of polarisation of the E.M. field, compared to particle displacements perpendicular to the direction of polarisation of the E.M. field. It can also be seen from Figs. (5.9.) and (5.10.) that, in analogy with Eq. (5.32), the particle is in a stable equilibrium at $x_0=y_0=0$, and in analogy with Eq. (5.33) in an unstable equilibrium at $x_0=y_0\approx 15$.

In table (5.3.) the numerical values for the restoring acceleration along the axis perpendicular to the direction of polarisation are given.

$x_0(\mu m), y_0(\mu m)$	$-a_y/g$ (5th order)	$-a_x/g$ (GB01)	RMS error in %
0	0.0000	0.0000	0.00
1	0.0466	0.0494	5.7
2	0.0853	0.0903	5.51
3	0.1104	0.1164	5.19
4	0.1198	0.1258	4.74
5	0.1151	0.1201	4.17
6	0.1002	0.1038	3.46
7	0.0802	0.0823	2.62
8	0.0594	0.0604	1.64
9	0.0411	0.0413	0.53
10	0.0266	0.0264	0.71
11	0.0162	0.0159	2.06
12	0.0093	0.0090	3.44
13	0.0050	0.0048	4.71
14	0.0026	0.0024	5.63
15	0.0012	0.0012	0.00
	average RMS error		**3.13**

Table 5.3. The numerical values of the restoring acceleration along the axis perpendicular to the direction of polarisation a_x/g and a_y/g respectively calculated using the GB01 treatment and the 5th order Gaussian beam approximation model, for optical levitation of a water droplet in air, using a focused order 01 mode linearly polarised laser beam. ($x_0,y_0=0\mu m$, $z_0=50\mu m$, $\overline{n}=1.334$, diameter of spherical particle = 4.96 μm, wavelength $\lambda_0=0.5145$ μm, $w_0=1\mu m$, $kd=74.6$ and a beam power of 3.5 mW.)

It can be seen from table (5.1.) that the average RMS error of the 25 data points is 1.41%. From table (5.2.) it can be seen that the average RMS error of the 16 data points is 3.53% and from table (5. 3.) it can be seen that the average RMS of the 16 data points is 3.13%.

As these RMS errors are small, this section can be concluded by stating that there is a very good agreement between the two models for almost paraxial Gaussian beams. The likely reason why the average RMS errors in the transverse directions are larger than in the longitudinal direction is, that transverse forces are polarization dependent and the beam used in the 5^{th} order Gaussian beam approximation is linearly polarised everywhere and the beam used in the GB01 treatment is only linearly polarised in the beam waist in the paraxial limit and in the far-field. Otherwise the beam is elliptically polarised as discussed in chapter 4. The good agreement between the 5^{th} order Gaussian beam approximation and the GB01 treatment can also be seen from Fig. (5.11.), which represents a comparison of the normalised at the origin irradiance profile of the two beams.

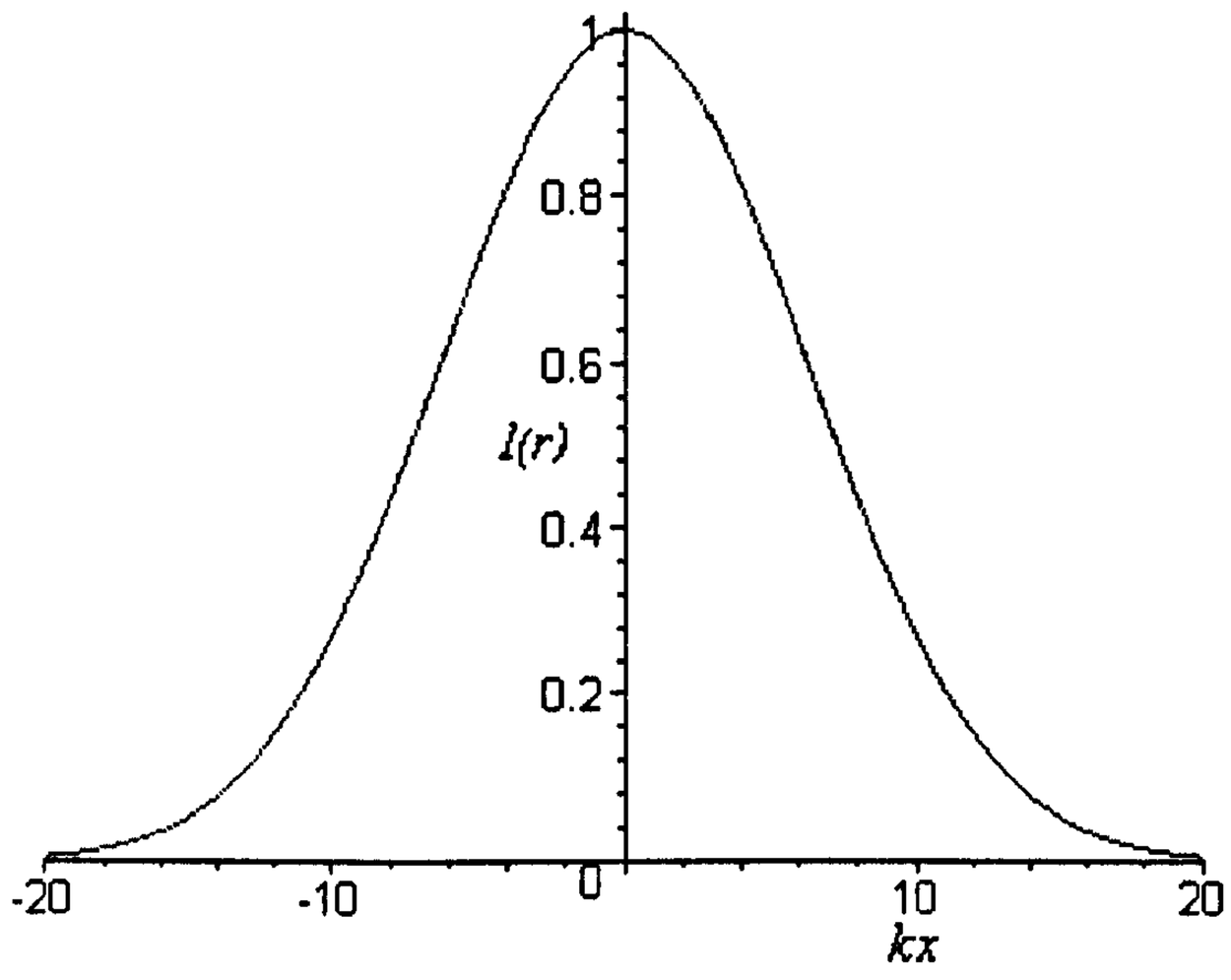

Fig. 5.11. Normalised irradiance profile at the beam waist for kd =74. 6. GB01 treatment (solid curve) versus 5^{th} order Gaussian beam approximation (doted curve).

However in a standard laser tweezers set up, the numerical aperture of the focusing lens is typically NA>1. As next the restoring acceleration exerted on a spherical water droplet of radius 1μm along the axis of propagation is calculated for an order 01 beam of wavelength (λ=0.5145μm) focused by NA≈1 lens, which corresponds to a value of kd=4. The beam spot size in this case is w_0=0.231 μm and the beam power is 3.5mW. The offset along the x and y axis is zero (x_0=y_0=0μm). As Barton *et al.* [8] have not presented these results, the results for the 5^{th} order Gaussian beam approximation are calculated using the code of Ulanowski and Jones [23]. Fig. (5.12.) compares the restoring acceleration for sphere positions along the axis of propagation [a_z/g].

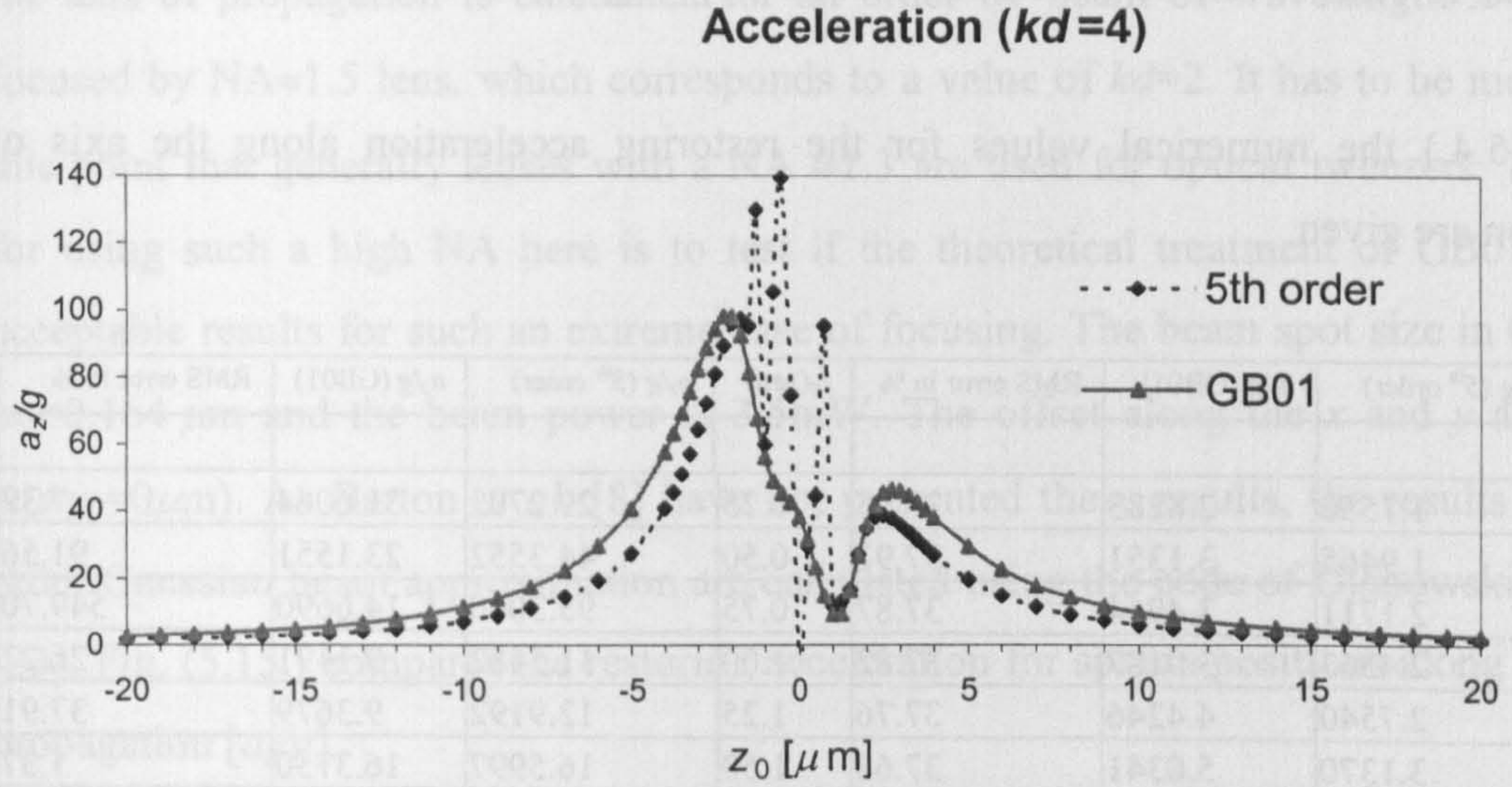

Fig. 5.12. Comparison of the restoring acceleration based on the 5th order Gaussian beam approximation (doted curve) and the GB01 treatment (solid curve), along the propagation axis for optical levitation of a water droplet in air, using a focused order 01 mode linearly polarised laser beam. (x_0=y_0=0, $\overline{n}$ = 1.334 , diameter of spherical particle = 2.0 μm, wavelength λ_0 = 0.5145 μm , w_0=0.231μm, *kd*=4and a beam power of 3.5 mW.)

It can be seen from Fig. (5.12.) that the results calculated using the 5th order Gaussian beam approximation (doted curve), are highly inaccurate in the range from z_0=[-1.25..0.75]. This is a clear indication that the 5th order Gaussian beam approximation breaks down for strongly focused beams, as was predicted in chapter 1. Figs. (5.13.) and (5.14.) show a comparison of the normalised at the origin irradiance profiles of the GB01 treatment versus the 5th order Gaussian beam approximation for *kd*=4 at the beam waist and at z_0=0.75μm respectively. The breakdown of the 5th order Gaussian beam approximation for *kd*=4 can be clearly seen from the difference in the irradiance profiles of the two beams at z_0=0.75 μm. Since the sphere has a diameter of 2 μm it is apparent that even though the irradiance profiles are almost identical at the beam waist, the contributions from the differences at z_0=0.75 μm will have an effect on the trapping forces at z_0=0μm.

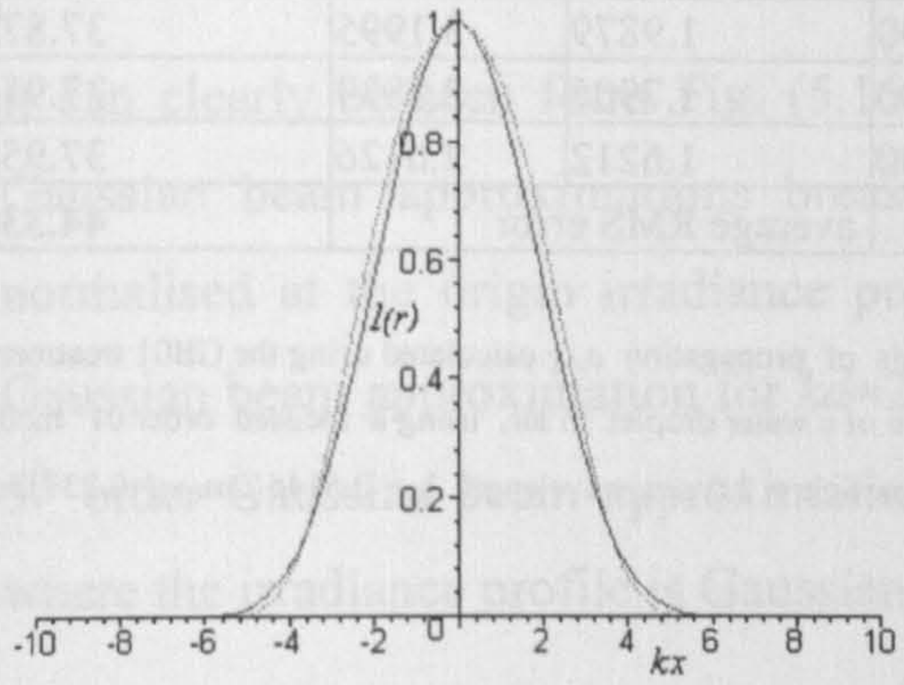

Fig. 5.13. Normalised irradiance profile at the beam waist for *kd*=4. GB01 treatment (solid curve) versus 5th order Gaussian approximation (doted curve)

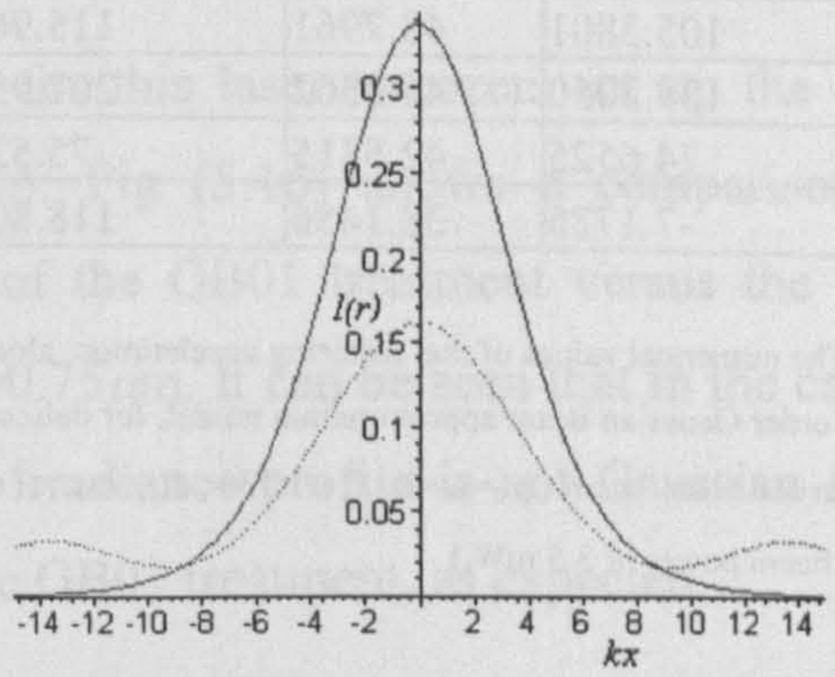

Fig. 5.14. Normalised irradiance profile at z_0=0.75μm for *kd*=4. GB01 treatment (solid curve) versus 5th order Gaussian beam approximation (doted curve).

Additionally it can be seen from Fig. (5.12.) that the restoring acceleration [a_z/g] is always greater than 1. Thus it can be concluded that no trapping occurs in this laser tweezers set up.

In table (5.4.) the numerical values for the restoring acceleration along the axis of propagation are given.

$z_0(\mu m)$	a_z/g (5th order)	a_z/g (GB01)	RMS error in %	$z_0(\mu m)$	a_z/g (5th order)	a_z/g (GB01)	RMS error in %
-20.00	1.7550	2.8283	37.95	0.25	29.2702	31.6064	7.39
-19.00	1.9465	3.1351	37.91	0.50	44.3552	23.1551	91.56
-18.00	2.1711	3.4944	37.87	0.75	95.3040	14.6690	549.70
-17.00	2.4367	3.9187	37.82	1.00	11.5482	9.1491	26.22
-16.00	2.7540	4.4246	37.76	1.25	12.9192	9.3679	37.91
-15.00	3.1370	5.0341	37.68	1.50	16.5997	16.3750	1.37
-14.00	3.6054	5.7773	37.59	1.75	26.8588	26.6225	0.89
-13.00	4.1860	6.6959	37.48	2.00	34.6757	35.7523	3.01
-12.00	4.9177	7.8486	37.34	2.25	38.2040	41.9660	8.96
-11.00	5.8570	9.3209	37.16	2.50	38.7950	45.2797	14.32
-10.00	7.0894	11.2396	36.92	2.75	37.7406	46.3527	18.58
-9.00	8.7484	13.7991	36.60	3.00	35.8561	45.8965	21.88
-8.00	11.0512	17.3075	36.15	3.25	33.6127	44.4830	24.44
-7.00	14.3678	22.2693	35.48	3.50	31.2737	42.5204	26.45
-6.00	19.3633	29.5371	34.44	3.75	28.9810	40.2830	28.06
-5.00	27.3026	40.5654	32.69	4.00	26.8072	37.9470	29.36
-4.00	40.6998	57.6383	29.39	5.00	19.6785	29.2312	32.68
-3.75	45.4009	63.1394	28.09	6.00	14.7813	22.5447	34.44
-3.50	50.8270	69.1488	26.50	7.00	11.4157	17.6923	35.48
-3.25	57.0760	75.5890	24.49	8.00	9.0439	14.1632	36.14
-3.00	64.2197	82.2673	21.94	9.00	7.3242	11.5523	36.60
-2.75	72.2474	88.7943	18.64	10.00	6.0436	9.5813	36.92
-2.50	80.9352	94.4653	14.32	11.00	5.0670	8.0635	37.16
-2.25	89.5475	98.1216	8.74	12.00	4.3067	6.8734	37.34
-2.00	96.2100	98.0970	1.92	13.00	3.7039	5.9247	37.48
-1.75	97.3779	92.5996	5.16	14.00	3.2184	5.1572	37.59
-1.50	95.1967	81.2363	17.19	15.00	2.8218	4.5281	37.68
-1.25	129.8709	67.4848	92.44	16.00	2.4938	4.0065	37.76
-1.00	59.7932	56.0694	6.64	17.00	2.2195	3.5693	37.82
-0.75	105.3801	48.7961	115.96	18.00	1.9879	3.1995	37.87
-0.50	139.3050	45.2362	207.95	19.00	1.7906	2.8839	37.91
-0.25	74.6525	42.5315	75.52	20.00	1.6212	2.6126	37.95
0.00	-7.1725	38.1456	118.80		average RMS error		**44.33**

Table 5.4. The numerical values of the restoring acceleration along the axis of propagation a_z/g calculated using the GB01 treatment and the 5th order Gaussian beam approximation model, for optical levitation of a water droplet in air, using a focused order 01 mode linearly polarised laser beam. ($x_0=y_0=0$, $\bar{n}$ = 1.334 , diameter of spherical particle = 2.0 μm, wavelength λ_0 = 0.5145 μm, w_0=0.231μm, kd=4 and a beam power of 3.5 mW.)

It can be seen from table (5.4.) that the average RMS error of the 65 data points is 44.33%. The largest RMS error is for a sphere location at z_0=0.75, where the RMS error is 549.7%.

Next, the restoring acceleration exerted on a spherical water droplet of radius 1μm along the axis of propagation is calculated for an order 01 beam of wavelength λ=0.5145μm focused by NA≈1.5 lens, which corresponds to a value of kd=2. It has to be mentioned at this point that generally lenses with a NA ≈1.3 are used for optical tweezers. The reason for using such a high NA here is to test if the theoretical treatment of GB01 produces acceptable results for such an extreme case of focusing. The beam spot size in this case is w_0=0.164 μm and the beam power is 3.5mW. The offset along the x and y axis is zero (x_0=y_0=0μm). As Barton *et al.* [8] have not presented these results, the results for the 5th order Gaussian beam approximation are calculated using the code of Ulanowski and Jones [23]. Fig. (5.15.) compares the restoring acceleration for sphere positions along the axis of propagation [a_z/g].

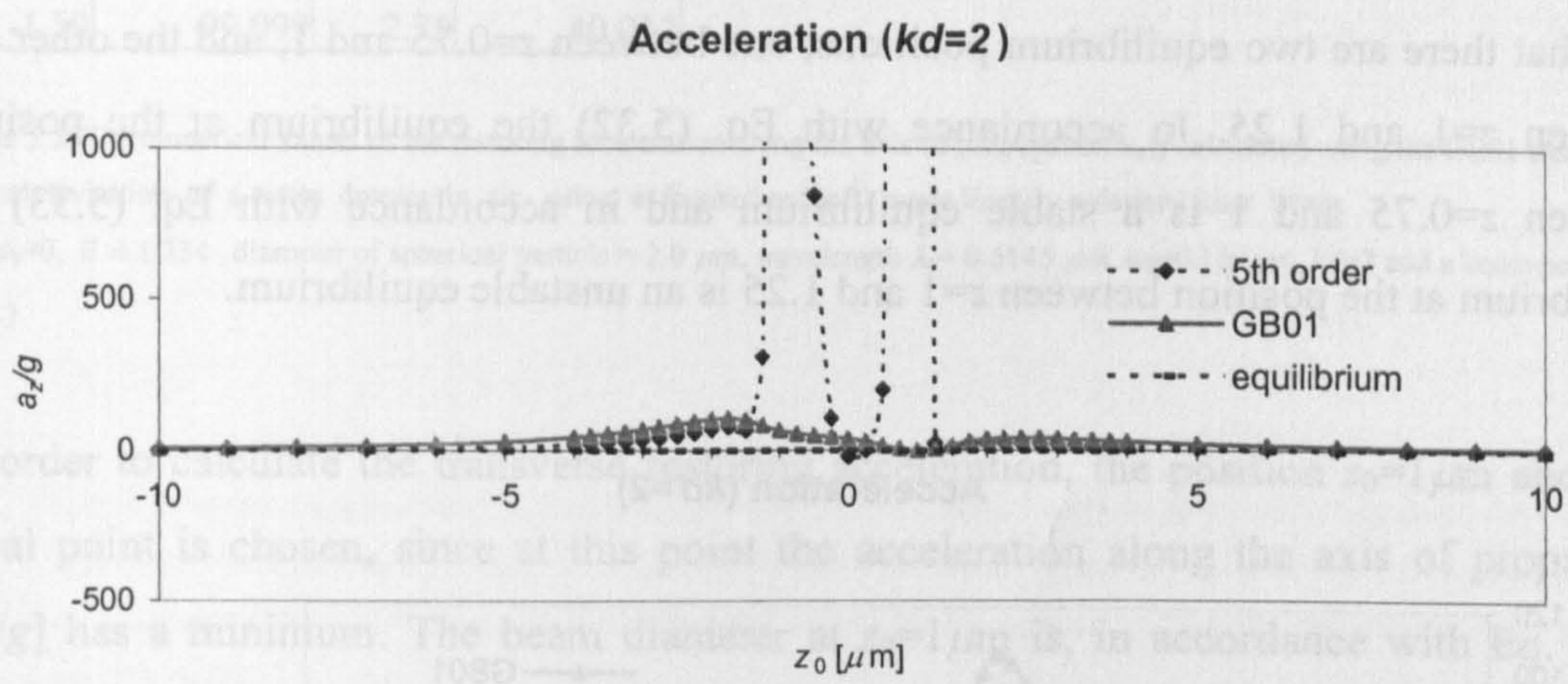

Fig. 5.15. Comparison of the restoring acceleration based on the 5th order Gaussian beam approximation (doted curve) and the GB01 treatment (solid curve), along the propagation axis for optical levitation of a water droplet in air, using a focused order 01 mode linearly polarised laser beam. (x_0=y_0=0, $\overline{n}$ = 1.334 , diameter of spherical particle = 2.0 μm, wavelength λ_0= 0.5145 μm , w_0=0.164μm, kd=2 and a beam power of 3.5 mW.)

It can clearly be seen form Fig. (5.15.) that for this laser tweezers set up the 5th order Gaussian beam approximations breaks down. Fig (5.16) shows a comparison of the normalised at the origin irradiance profiles of the GB01 treatment versus the 5th order Gaussian beam approximation for kd=2 at z_0=0.75μm. It can be seen that in the case of the 5th order Gaussian beam approximation, the irradiance profile is not Gaussian for kd=2, where the irradiance profile is Gaussian for the GB01 treatment, as expected.

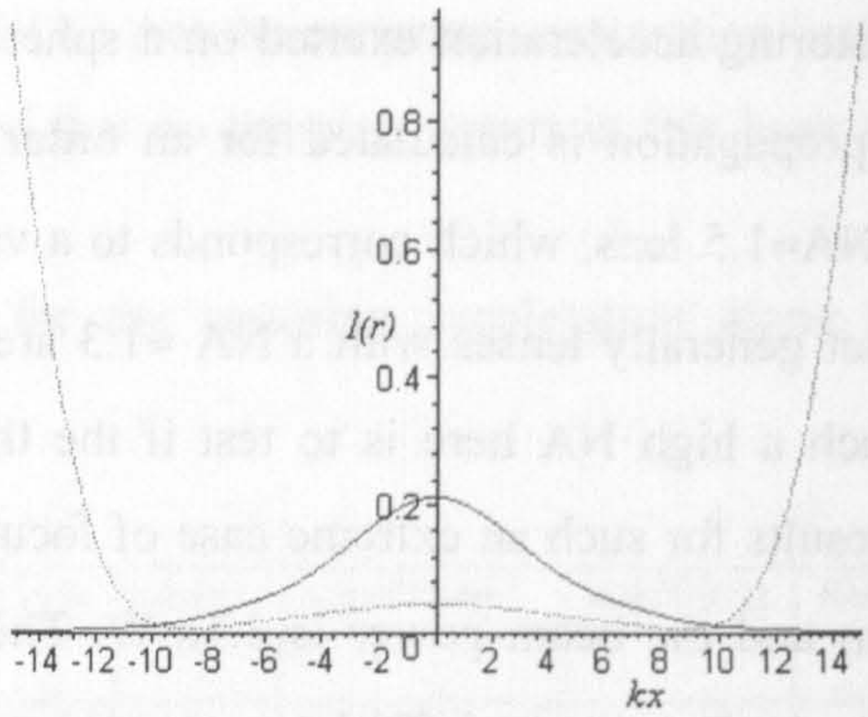

Fig. 5.16. Normalised irradiance profile at z_0=0.75μm for kd =2. GB01 treatment (solid curve) versus 5th order Gaussian beam approximation (doted curve).

Since according to Figs. (5.15) and (5.16) the 5th order Gaussian beam approximation breaks down for strongly focused beams, only the GB01 treatment is used to investigate the restoring acceleration [a_z/g] along the axis of propagation. From Fig. (5.17.) it can be seen that there are two equilibrium positions, one between z=0.75 and 1, and the other one between z=1 and 1.25. In accordance with Eq. (5.32) the equilibrium at the position between z=0.75 and 1 is a stable equilibrium and in accordance with Eq. (5.33) the equilibrium at the position between z=1 and 1.25 is an unstable equilibrium.

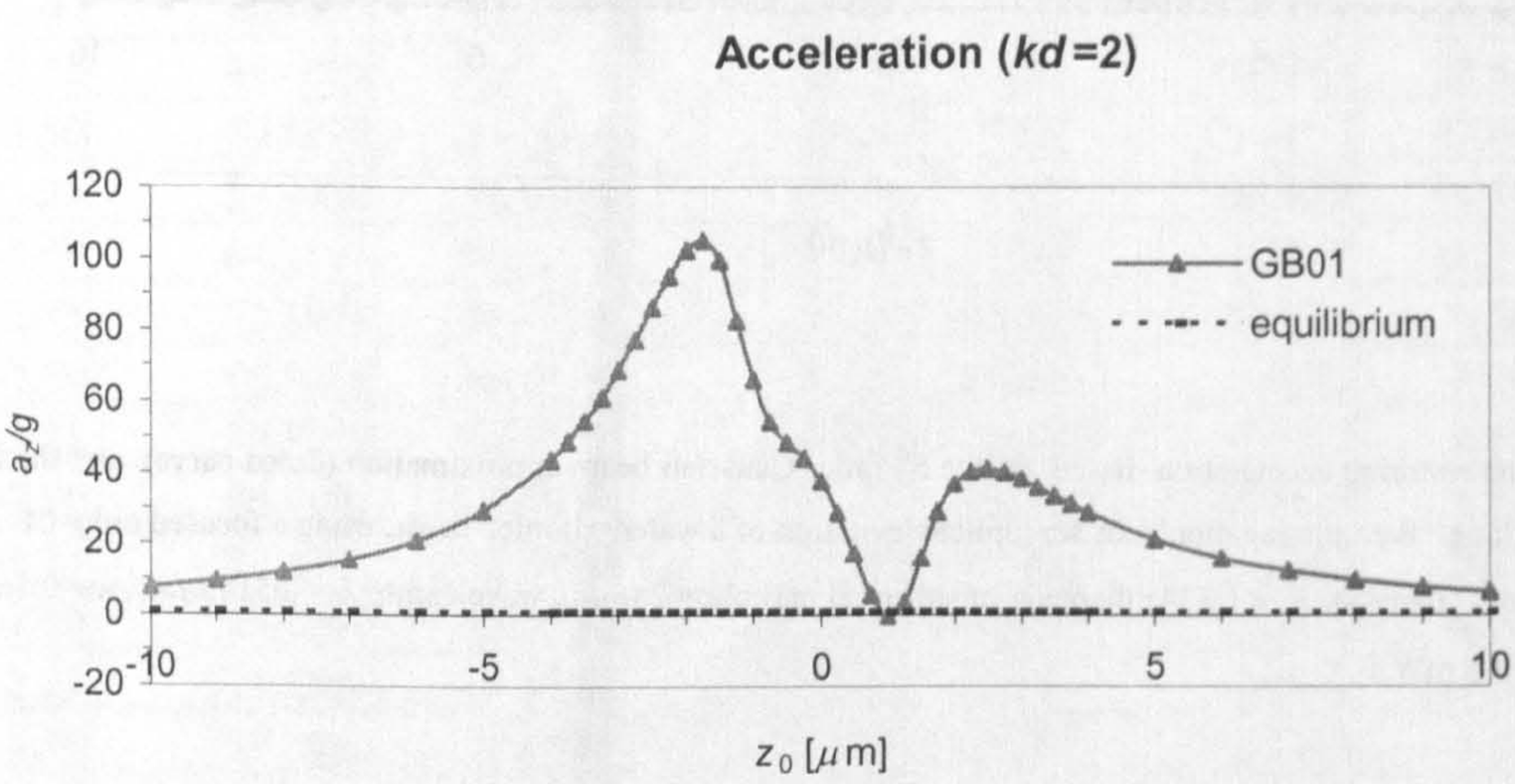

Fig. 5.17. Restoring acceleration based on the GB01 treatment (solid curve), along the propagation axis for optical levitation of a water droplet in air, using a focused order 01 mode linearly polarised laser beam. (x_0=y_0=0, $\overline{n}$ = 1.334 , diameter of spherical particle = 2.0 μm, wavelength λ_0 = 0.5145 μm , w_0=0.164μm, kd=2 and a beam power of 3.5 mW.)

In table (5.5.) the numerical values for the restoring acceleration along the axis of propagation are given.

$z_0(\mu m)$	a_z/g (GB01)	$z_0(\mu m)$	a_z/g (GB01)	$z_0(\mu m)$	a_z/g (GB01)
-10.00	7.602	-1.25	82.228	3.00	38.136
-9.00	9.380	-1.00	65.877	3.25	35.824
-8.00	11.849	-0.75	54.069	3.50	33.380
-7.00	15.403	-0.50	48.231	3.75	30.966
-6.00	20.755	-0.25	44.015	4.00	28.665
-5.00	29.249	0.00	37.504	5.00	21.074
-4.00	43.533	0.25	28.635	6.00	15.839
-3.75	48.527	0.50	17.110	7.00	12.237
-3.50	54.276	0.75	5.625	8.00	9.696
-3.25	60.874	1.00	-0.162	9.00	7.853
-3.00	68.384	1.25	3.528	10.00	6.480
-2.75	76.776	1.50	15.887		
-2.50	85.806	1.75	28.864		
-2.25	94.770	2.00	36.783		
-2.00	102.087	2.25	40.336		
-1.75	104.827	2.50	41.027		
-1.50	99.099	2.75	40.032		

Table 5.5. The numerical values of the restoring acceleration along the axis of propagation a_z/g calculated using the GB01 treatment, for optical levitation of a water droplet in air, using a focused order 01 mode linearly polarised laser beam. ($x_0=y_0=0$, $\overline{n}$ = 1.334 , diameter of spherical particle = 2.0 μm, wavelength λ_0= 0.5145 μm, w_0=0.164μm, kd=2 and a beam power of 3.5 mW.)

In order to calculate the transverse restoring acceleration, the position z_0=1μm above the focal point is chosen, since at this point the acceleration along the axis of propagation [a_z/g] has a minimum. The beam diameter at z_0=1μm is, in accordance with Eq. (1.80), $2w\approx2\mu$m, which is equal to the droplet diameter. Fig. (5.18.) shows the acceleration for sphere positions along the axes of polarisation [a_y].

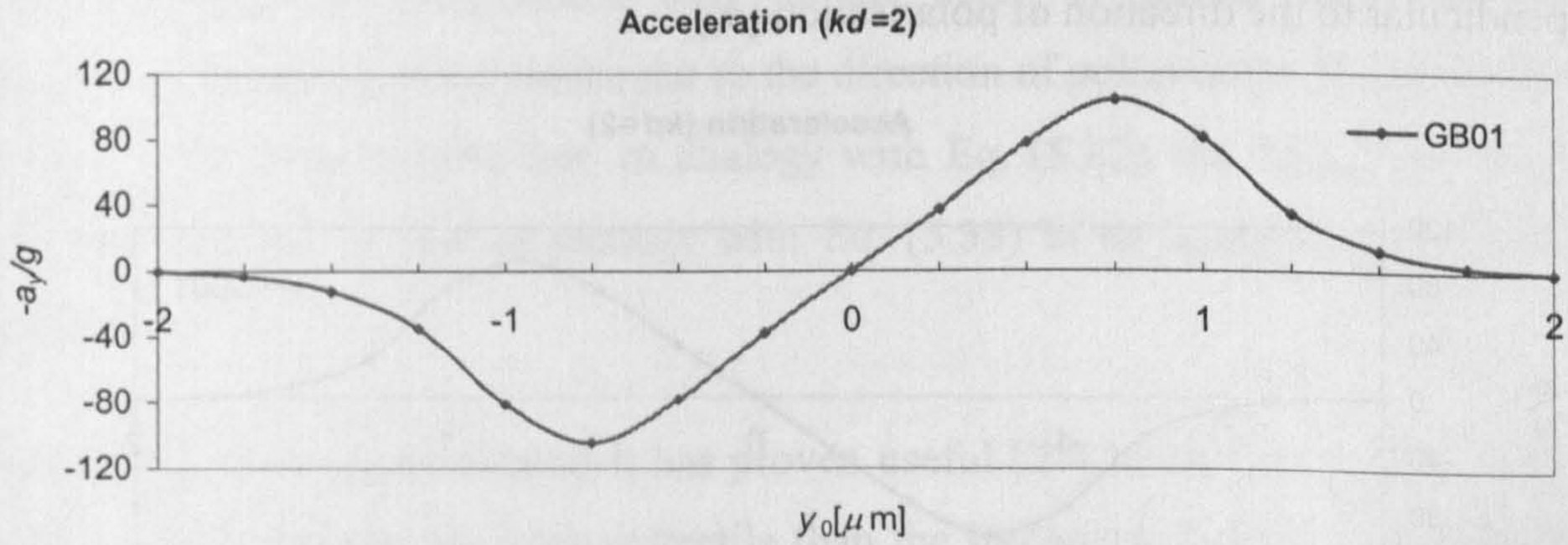

Fig. 5.18. The restoring acceleration based on the GB01 treatment, along the polarisation axis versus displacement along the polarisation axis for optical levitation of a water droplet in air, using a focused order 01 mode linearly polarised laser beam. (x_0=0μm, z_0=1μm, $\overline{n}$ = 1.334 , diameter of spherical particle = 2 μm, wavelength λ_0 = 0.5145 μm, w_0=0.164μm, kd=2 and a beam power of 3.5 mW.)

In table (5.6.) the numerical values for the restoring acceleration along the direction of polarisation are given.

$y_0(\mu m)$	$-a_y/g$ (GB01)
-2.00	-0.379
-1.75	-3.225
-1.50	-12.674
-1.25	-34.887
-1.00	-81.077
-0.75	-104.354
-0.50	-78.135
-0.25	-37.630
0.00	0.000
0.25	37.630
0.50	78.135
0.75	104.354
1.00	81.077
1.25	34.887
1.50	12.674
1.75	3.225
2.00	0.379

Table 5.6. The numerical values of the restoring acceleration along the direction of polarisation a_y/g calculated using the GB01 treatment, for optical levitation of a water droplet in air, using a focused order 01 mode linearly polarised laser beam. (x_0=0, $\overline{n}$ = 1.334 , z_0=1 μm, diameter of spherical particle = 2.0 μm, wavelength λ_0 = 0.5145 μm, w_0=0.164μm, kd=2 and a beam power of 3.5 mW.)

Fig. (5.19) shows the restoring acceleration for sphere positions along the axis perpendicular to the direction of polarisation [a_x].

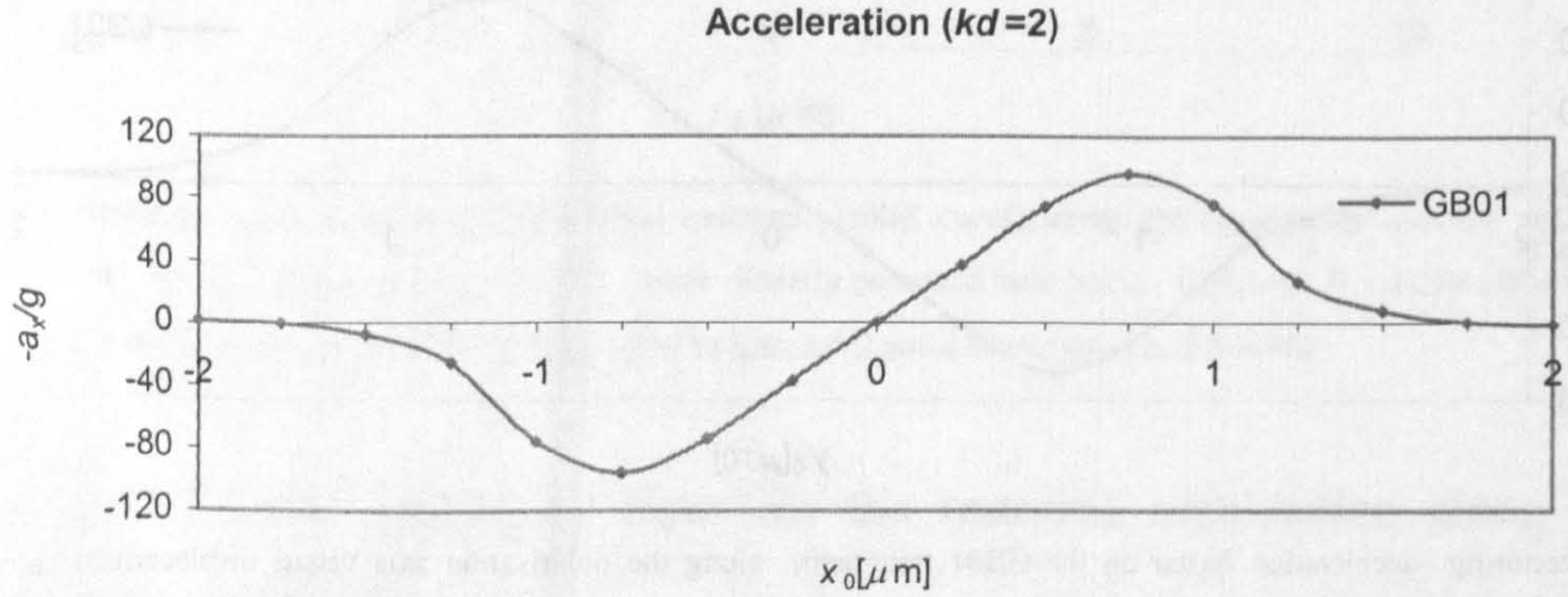

Fig. 5.19. The restoring acceleration based on the GB01 treatment, along the axis perpendicular to the direction of polarisation versus displacement along the axis perpendicular to the direction of polarisation for optical levitation of a water droplet in air, using a focused order 01 mode linearly polarised laser beam. (y_0=0μm, z_0=1μm, $\overline{n}$ = 1.334 , diameter of spherical particle = 2 μm, wavelength λ_0 = 0.5145 μm, w_0=0.164μm, kd=2 and a beam power of 3.5 mW.)

In table (5.7.), the numerical values for the restoring acceleration along the axis perpendicular to the direction of polarisation are given.

x_0 (μm)	$-a_x/g$ (GB01)
-2.00	1.439
-1.75	-0.304
-1.50	-7.924
-1.25	-25.942
-1.00	-75.666
-0.75	-95.996
-0.50	-74.083
-0.25	-36.910
0.00	0.000
0.25	36.910
0.50	74.083
0.75	95.996
1.00	75.666
1.25	25.942
1.50	7.924
1.75	0.304
2.00	-1.439

Table 5.7. The numerical values of the restoring acceleration along the axis perpendicular to the direction of polarisation a_x/g calculated using the GB01 treatment, for optical levitation of a water droplet in air, using a focused order 01 mode linearly polarised laser beam. (y_0=0, $\bar{n}$ = 1.334, z_0=1μm, diameter of spherical particle = 2.0 μm, wavelength λ_0= 0.5145 μm, w_0=0.164μm, kd=2 and a beam power of 3.5 mW.)

By comparing Figs. (5.18.) and (5.19.) it can be seen, as expected, that the restoring acceleration along the polarisation axis of the beam is greater than the restoring acceleration along the axis perpendicular to the direction of polarisation. It can also be seen from Figs. (5.18.) and (5.19.) that, in analogy with Eq. (5.32), the particle is in a stable equilibrium at x_0=y_0=0, and in analogy with Eq. (5.33) in an unstable equilibrium near x_0=y_0≈±2.

In order to trap biological material it has proven useful [27] to use polystyrene spheres as "handles", since they can be more refractile than the biological substance, thus supplying extra trapping forces. Furthermore the shape and the uniform size facilitates the calibration of the laser tweezers. For this reason, the restoring acceleration induced onto a polystyrene (n=1.6 [11]) sphere of radius 1μm suspended in water is calculated for kd=4, a beam power of 3.5mW, a beam waist radius of 0.231μm and a wavelength of λ_0=514.5nm. Polystyrene

has a density ρ=1.05×10^3 kgm^{-3} [28], thus the mass of the polystyrene sphere considered is m_p=4.4×10^{-15} kg. Fig. (5.20.) compares the restoring acceleration for sphere positions along the axis of propagation [a_z/g] calculated using the GB01 treatment and the 5th order Gaussian beam approximation model of Ulanowski and Jones [23]. The offset along the x and y axis is zero (x_0=y_0=0μm).

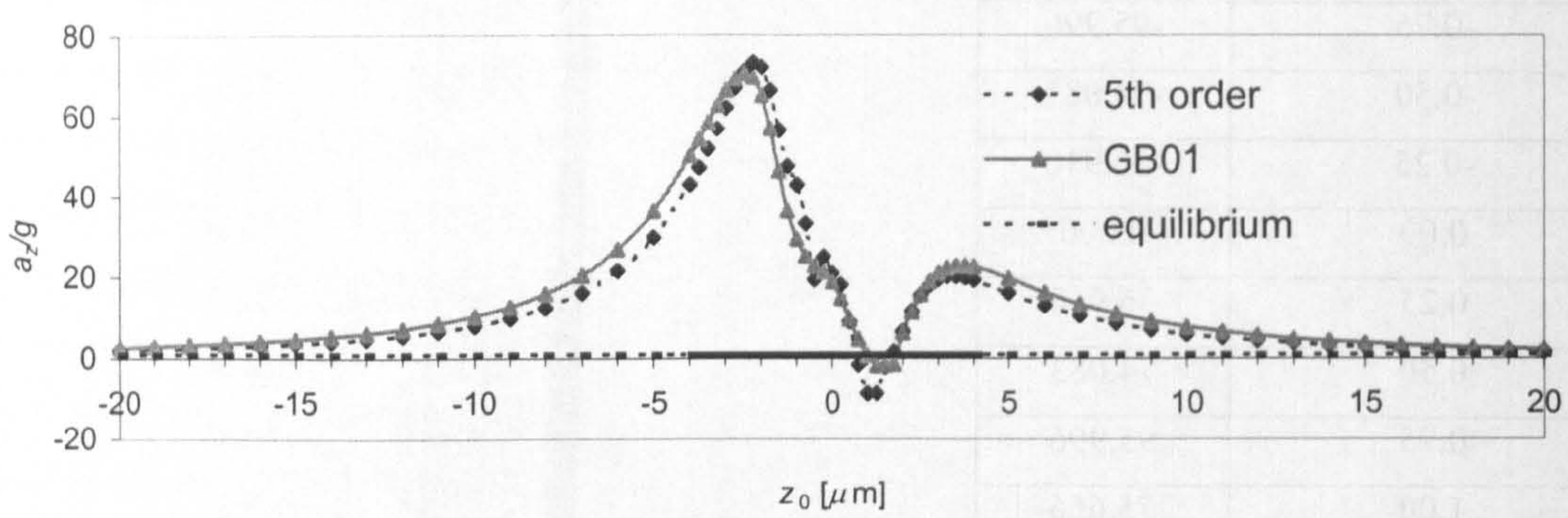

Fig. 5.20. Comparison of the restoring acceleration based on the 5th order Gaussian beam approximation (doted curve) and the GB01 treatment (solid curve), along the propagation axis for optical trapping of a polystyrene sphere in water, using a focused order 01 mode linearly polarised laser beam.
(x_0=y_0=0, $\overline{n}$ = 1.199 , diameter of spherical particle = 2.0 μm, wavelength λ_0 = 0.5145 μm , w_0=0.231μm, kd=4 and a beam power of 3.5 mW.)

In table (5.8.) the numerical values for the restoring acceleration along the axis of propagation are given.

$z_0(\mu m)$	a_z/g (5th order)	a_z/g (GB01)	RMS error in %	$z_0(\mu m)$	a_z/g (5th order)	a_z/g (GB01)	RMS error in %
-20.00	1.966	2.579	23.78	0.25	18.143	14.751	22.99
-19.00	2.182	2.861	23.74	0.50	9.016	9.619	6.27
-18.00	2.436	3.192	23.69	0.75	-1.531	4.732	132.35
-17.00	2.737	3.583	23.63	1.00	-8.637	0.752	1247.89
-16.00	3.096	4.050	23.57	1.25	-8.704	-1.769	392.08
-15.00	3.530	4.613	23.48	1.50	-2.067	-1.653	25.1
-14.00	4.061	5.300	23.38	1.75	1.670	-1.441	215.82
-13.00	4.719	6.149	23.26	2.00	6.575	6.292	4.5
-12.00	5.549	7.215	23.1	2.25	11.580	11.360	1.94
-11.00	6.613	8.576	22.89	2.50	15.486	15.686	1.28
-10.00	8.007	10.348	60.76	2.75	18.075	18.923	4.48
-9.00	9.877	12.705	22.26	3.00	19.549	21.086	7.29
-8.00	12.458	15.920	21.75	3.25	20.190	22.344	9.64
-7.00	16.136	20.426	21	3.50	20.248	22.899	11.58
-6.00	21.573	26.914	19.85	3.75	19.918	22.941	13.17
-5.00	29.910	36.436	17.91	4.00	19.341	22.620	14.5
-4.00	42.963	50.146	14.32	5.00	16.123	19.659	17.99
-3.75	47.195	54.214	12.95	6.00	13.002	16.228	19.88
-3.50	51.825	58.405	11.27	7.00	10.499	13.294	21.03
-3.25	56.788	62.538	9.19	8.00	8.573	10.958	21.77
-3.00	61.919	66.304	6.61	9.00	7.095	9.128	22.27
-2.75	66.876	69.218	3.38	10.00	5.950	7.691	22.63
-2.50	71.027	70.573	0.64	11.00	5.052	6.552	22.9
-2.25	73.301	69.458	5.53	12.00	4.337	5.640	23.1
-2.00	72.149	64.968	11.05	13.00	3.760	4.900	23.26
-1.75	66.201	56.813	16.52	14.00	3.289	4.293	23.38
-1.50	56.423	46.291	21.89	15.00	2.900	3.790	23.49
-1.25	47.473	36.446	30.26	16.00	2.575	3.369	23.57
-1.00	42.900	29.506	45.4	17.00	2.301	3.014	23.64
-0.75	33.273	25.198	32.04	18.00	2.069	2.711	23.69
-0.50	19.368	22.812	15.1	19.00	1.869	2.451	23.74
-0.25	25.107	21.268	18.05	20.00	1.697	2.226	23.78
0.00	20.921	18.836	11.07			average RMS error	**48.22**

Table 5.8. The numerical values of the restoring acceleration along the axis of propagation a_z/g calculated using the GB01 treatment and the 5th order Gaussian beam approximation model, for optical trapping of a polystyrene sphere in water, using a focused order 01 mode linearly polarised laser beam. (x_0=y_0=0, $\overline{n}$ = 1.199 , diameter of spherical particle = 2.0 μm, wavelength λ_0 = 0.5145 μm, w_0=0.231μm, kd=4 and a beam power of 3.5mW.)

It can be seen from table (5.8.) that the average RMS error of the 65 data points is 48.22%. The largest RMS error is for a sphere location at z_0=1.0, where the RMS error is 1247.89%.

It can be seen from Fig. (5.20) that in the case of trapping a polystyrene sphere suspended in water, the difference between the two models is not as big as in the case of water droplet suspended in air. It can further be seen by comparing Fig. (5.20) with Fig. (5.12), that a polystyrene sphere suspended in water is subjected to a smaller restoring acceleration, than a water droplet suspended in air. It can be seen from table (5.8.) that the polystyrene sphere in water is subjected to a maximum acceleration $a_z/g \approx 71$ at a sphere location $x_0=y_0=0$ μm and $z_0=-2.5\mu$m. From table (5.4) it can be seen that the water droplet in air is subjected to a maximum acceleration $a_z/g \approx 98$ at a sphere location $x_0=y_0=0$ μm and $z_0=-2.25\mu$m. Thus the polystyrene sphere in water is accelerated 1.4 times less than the water droplet in air. The reason for this can be understood from geometrical optics. The relative refractive index for the air water interface is $\bar{n}=1.334$ and the relative refractive index of the polystyrene water interface is $\bar{n}=1.199$. Thus the relative refractive index for the polystyrene water interface is lower than the relative refractive index for the air water interface. Thus a polystyrene sphere in water reflects less radiation than a water droplet in air, thus the magnitude of the forward directed force relative to the backward directed force is lower for a polystyrene sphere in water than for a water droplet in air. It can be seen from Fig. (5.21), which represents a comparison between the refracted angle θ_t at the air-water interface and the refracted angle at the water-polystyrene interface respectively versus the incident angle θ_i, that light rays are bent more strongly at the air-water interface then at the water-polystyrene interface.

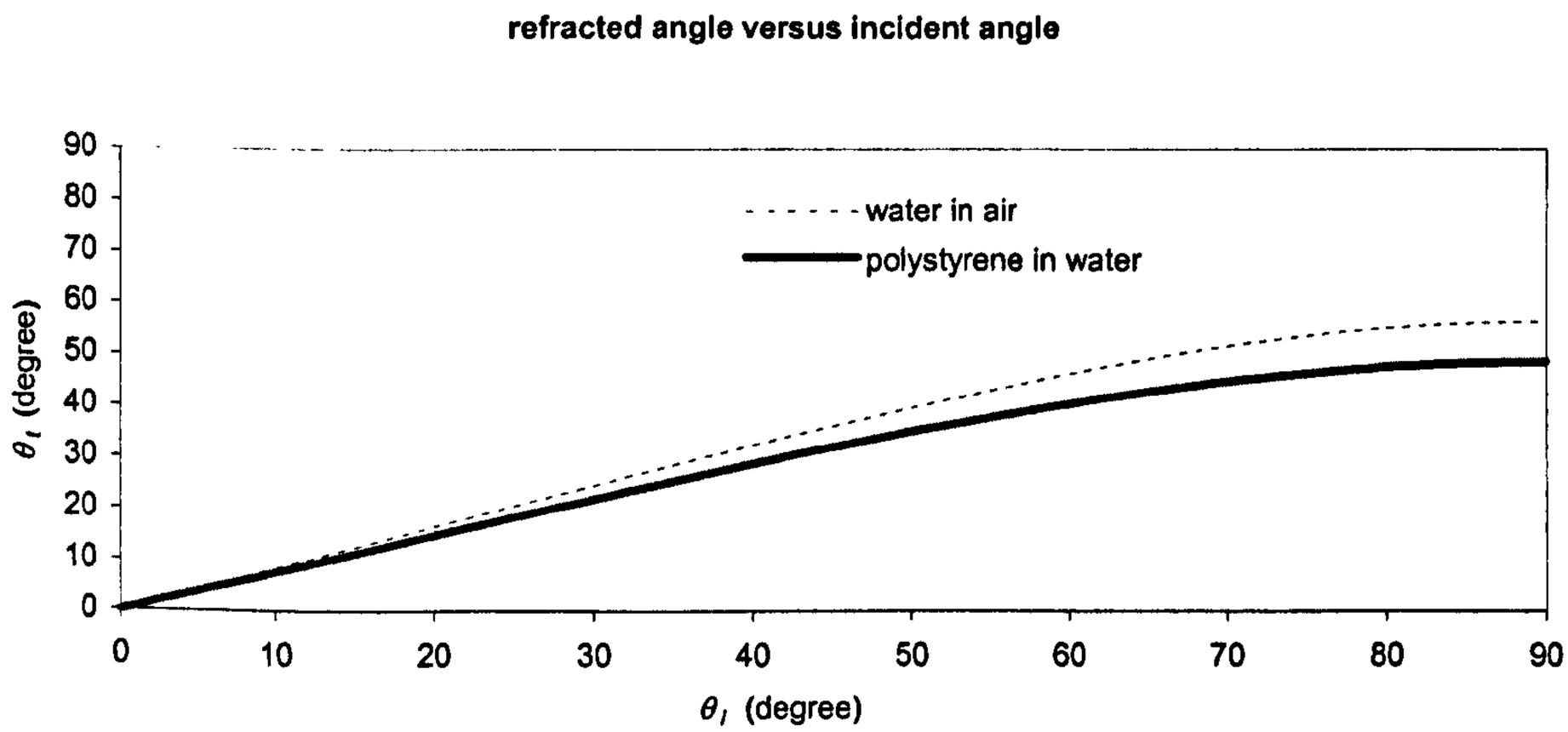

Fig. 5.21. Comparison between the refracted angle of the air-water interface and the refracted angle of the water-polystyrene interface versus incident angle θ_i.

This implies that the restoring acceleration is higher for the spherical water droplet being trapped in air, then for a polystyrene sphere being trapped in water. In general optical trapping experiments, the dimensionless trapping efficiency defined by Ashkin [11] as

$$Q = \left(\frac{Fc}{Pn_{ext}} \right), \tag{5.35}$$

is calculated, where in Eq. (5.35) F is the force, c=299792458ms^{-1} is the vacuum speed of light [26], P is the beam power and n_{ext} is the refractive index of the surrounding medium. The trapping efficiency is thus a measure of how much of the incident beam power is converted into trapping forces and what proportion of the beam does not reach the trapping particle. If all the radiation from the beam is reflected by the trapping particle than in accordance with Eq. (5.11) Q=2. If all the radiation is absorbed by the trapping particle then Q=1. If all the radiation is transmitted by the trapping particle then Q=0. However in general only a small proportion of the beam reaches the trapping particle and is reflected and refracted. Additionally as mentioned earlier, the two media are chosen in such a way as to reduce the relative refractive index, so less radiation is reflected. It can be clearly seen from Figs. (5.22.) and (5.23.), as expected, that the trapping efficiency is lower for a polystyrene sphere suspended in water than for a water droplet suspended in air. From Eqs. (5.16), (5.17) and (5.35) is can be seen that the mass of the trapped particle does not enter any of the formulae. Additionally it can be seen by substituting Eq. (5.12) into Eq. (5.35) that the trapping efficiency is independent of the beam power. In other words the trapping efficiency is a measure of how much of the incident momentum is converted into trapping forces. It can also be seen from Fig. (5.20.) that in accordance with Eq. (5.32) the polystyrene sphere is in a stable equilibrium position at $z_0 \approx 1$ and in accordance with Eq. (5.33) in an unstable equilibrium at $z_0 \approx 1.75$. The minimum value of the acceleration along the axis of propagation $[a_z/g]$ is according to Fig. (5.20.) at $z_0 = 1.25$. At this point, the beam diameter is, in accordance with Eq. (1.80) $2w \approx 1.77 \mu$m, which is less than the droplet diameter.

Fig. (5.22.) shows the trapping efficiency along the axis of propagation of the beam for a spherical water droplet of radius 1μm suspended in air by a beam of spot radius w_0=0.231 μm, a beam power of 3.5mW and a beam wavelength of 0.5145 μm, calculated using the 5th order Gaussian beam approximation and the GB01 treatment. Fig. (5.23) represents the trapping efficiency along the axis of propagation of the beam for a

polystyrene sphere of radius 1μm suspended in water by a beam of spot radius w_0=0.231 μm, a beam power of 3.5mW and a beam wavelength of 0.5145 μm, calculated using the 5th order Gaussian beam approximation and the GB01 treatment.

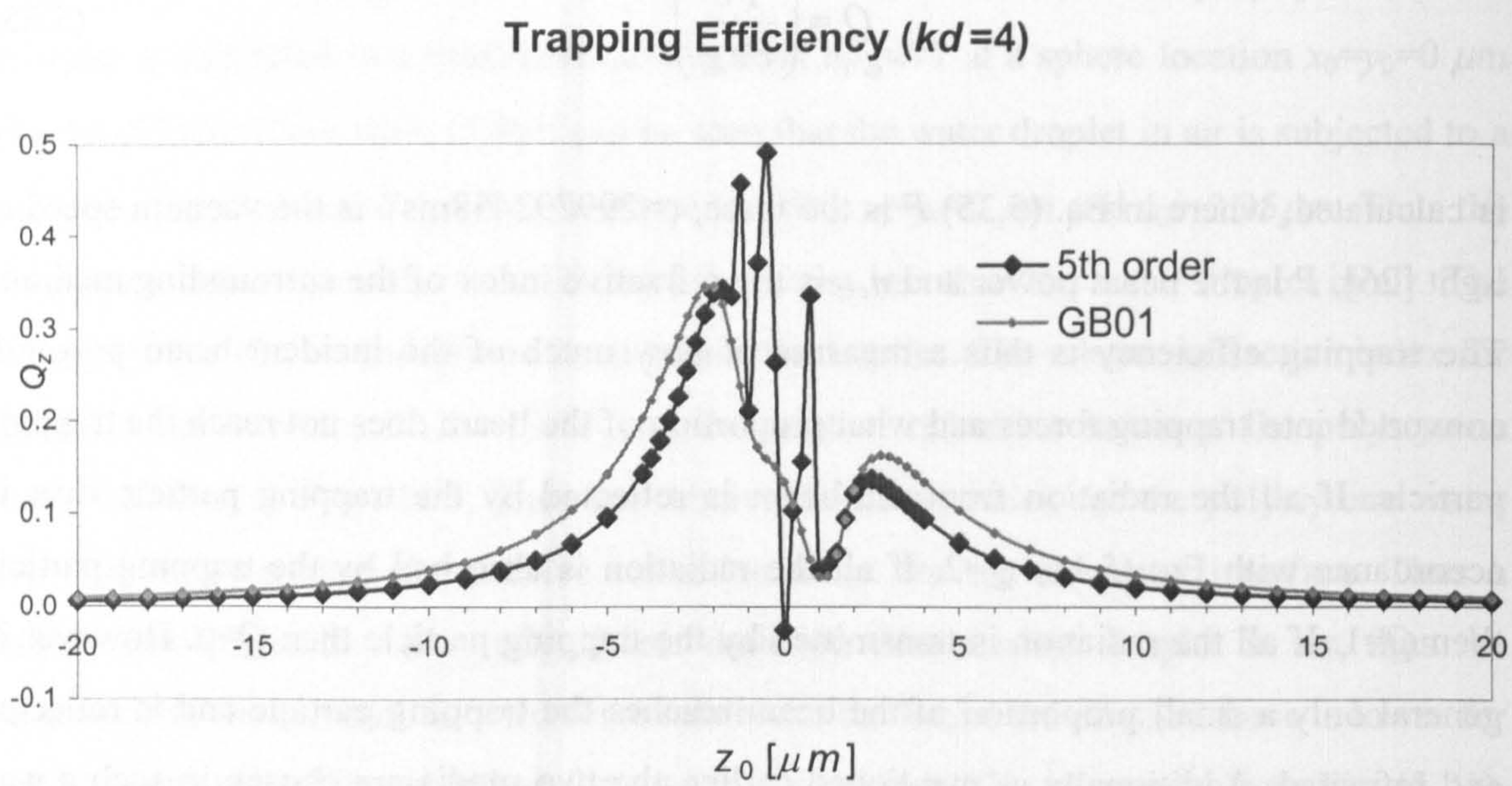

Fig. 5.22. Comparison of the trapping efficiency based on the 5th order Gaussian beam approximation (doted curve) and the GB01 treatment (solid curve), along the propagation axis for optical levitation of a water droplet in air, using a focused order 01 mode linearly polarised laser beam. (x_0=y_0=0, $\overline{n}$ = 1.334 , diameter of spherical particle = 2.0 μm, wavelength λ_0 = 0.5145 μm , w_0=0.231μm, kd=4 and a beam power of 3.5 mW.)

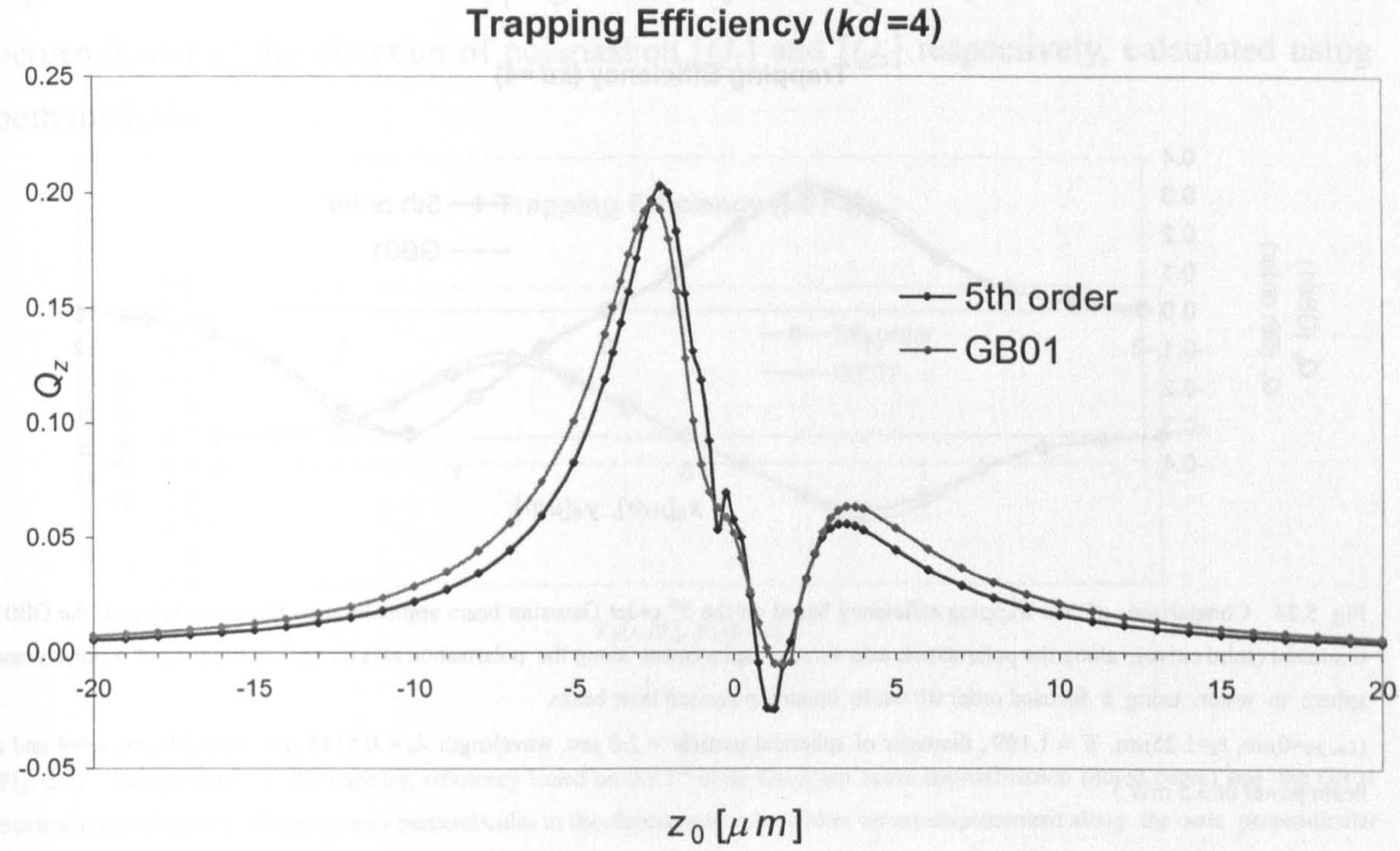

Fig. 5.23. Comparison of the trapping efficiency based on the 5th order Gaussian beam approximation (doted curve) and the GB01 treatment (solid curve), along the propagation axis for optical trapping of a polystyrene sphere in water, using a focused order 01 mode linearly polarised laser beam.

(x_0=y_0=0, $\overline{n}$ = 1.199 , diameter of spherical particle = 2.0 μm, wavelength λ_0 = 0.5145 μm , w_0=0.231μm, kd=4 and a beam power of 3.5 mW.)

By comparing Fig. (5.22) and (5.23) it can be seen that a polystyrene sphere can be much easier trap in water than a water droplet in air. The reason for this is that the reduction in relative refractive index assists the trapping process, as discussed earlier. It can also be seen from these figures, that the larger relative refractive index leads to a breakdown of the 5th order Gaussian beam approximation for kd=4. It can also be seen from Fig. (5.22) that the trapping efficiency is always positive in the GB01 treatment, which implies that the scattering force is always greater than the gradient force. This is not the case when trapping a polystyrene sphere in water. The polystyrene sphere is stabily trapped at z_0=1μm. In the rest of this chapter, the trapping efficiencies will be calculated for various trapping conditions. Next, the trapping efficiency along the axis of polarisation, y_0=0 μm is calculated using the 5th order Gaussian beam approximation. In the GB01 treatment, as the direction of polarisation is the y axis, the trapping efficiency along this axis is calculated with x_0=0 μm. Fig. (5.24.) compares the trapping efficiency for sphere positions along the direction of polarisation [Q_x] and [Q_y] respectively, calculated using both methods. The vertical position of the polystyrene sphere above the focus is z_0=1.25, since at this point the trapping efficiency along the axis of propagation [Q_z] has a minimum.

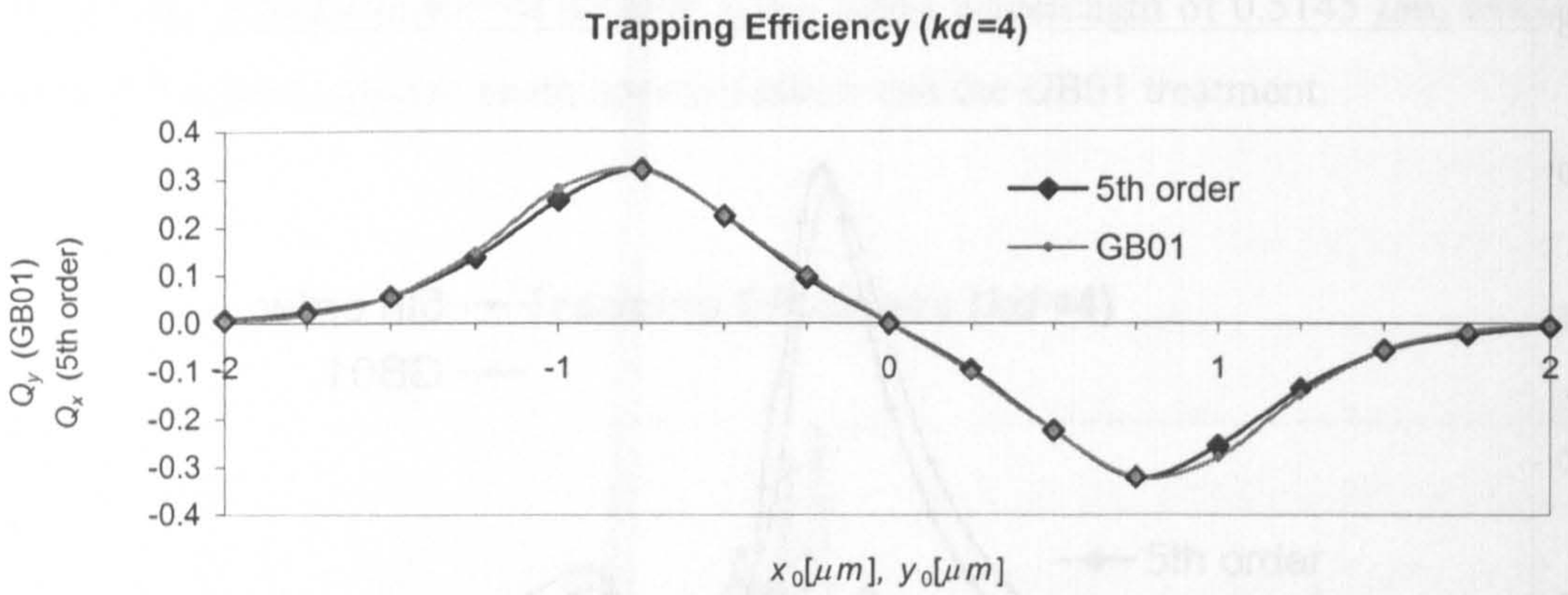

Fig. 5.24. Comparison of the trapping efficiency based on the 5th order Gaussian beam approximation (doted curve) and the GB01 treatment (solid curve), along the polarisation axis versus displacement along the polarisation axis for optical trapping of a polystyrene sphere in water, using a focused order 01 mode linearly polarised laser beam.
(x_0, y_0=0μm, z_0=1.25μm, $\overline{n}$ = 1.199, diameter of spherical particle = 2.0 μm, wavelength λ_0 = 0.5145 μm, w_0=0.231μm, kd=4 and a beam power of 3.5 mW.)

In table (5.9.) the numerical values for the trapping efficiency along the direction of polarisation are given.

x_0,y_0 (μm)	Q_x (5th order)	Q_y (GB01)	RMS error in %
-2.00	5.455E-03	4.600E-03	18.60
-1.75	2.212E-02	1.665E-02	32.83
-1.50	5.588E-02	5.527E-02	1.09
-1.25	1.367E-01	1.492E-01	8.38
-1.00	2.557E-01	2.800E-01	8.68
-0.75	3.207E-01	3.204E-01	0.10
-0.50	2.243E-01	2.245E-01	0.09
-0.25	9.522E-02	1.022E-01	6.87
0.00	2.831E-17	9.383E-17	69.83
0.25	-9.522E-02	-1.022E-01	6.87
0.50	-2.243E-01	-2.245E-01	0.09
0.75	-3.207E-01	-3.204E-01	0.10
1.00	-2.557E-01	-2.800E-01	8.68
1.25	-1.367E-01	-1.492E-01	8.38
1.50	-5.588E-02	-5.527E-02	1.09
1.75	-2.212E-02	-1.665E-02	32.83
2.00	-5.455E-03	-4.600E-03	18.60
		average RMS error	**13.12**

Table 5.9. The numerical values of the trapping efficiency along the direction of polarisation Q_x and Q_y respectively calculated using the GB01 treatment and the 5th order Gaussian beam approximation model, for optical trapping of a polystyrene sphere in water, using a focused order 01 mode linearly polarised laser beam.
(x_0,y_0=0μm, z_0=1.25μm, $\overline{n}$ = 1.199, diameter of spherical particle = 2.0 μm, wavelength λ_0 = 0.5145 μm, w_0=0.231μm, kd=4 and a beam power of 3.5 mW.)

Fig. (5.25.) compares the trapping efficiency for sphere positions along the axis perpendicular to the direction of polarisation [Q_y] and [Q_x] respectively, calculated using both methods.

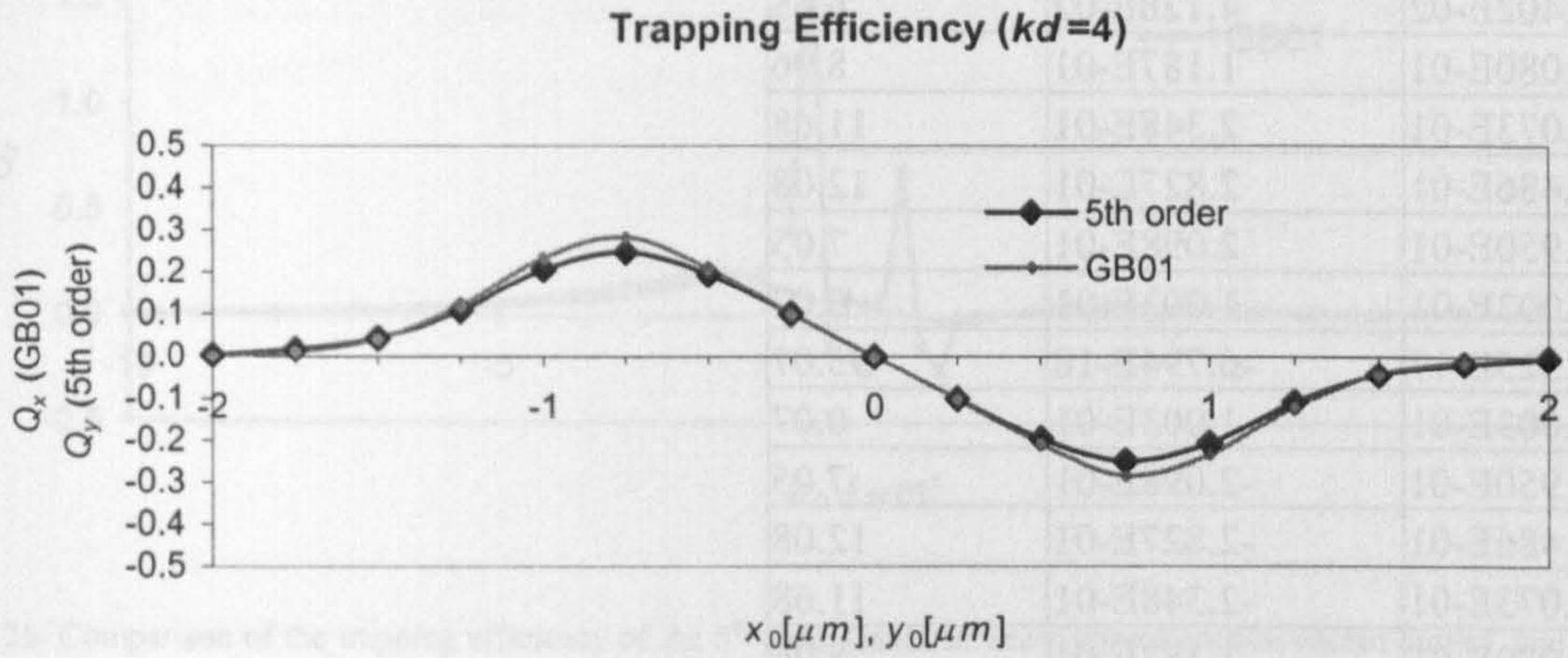

Fig. 5.25. Comparison of the trapping efficiency based on the 5th order Gaussian beam approximation (doted curve) and the GB01 treatment (solid curve), along the axis perpendicular to the direction of polarisation versus displacement along the axis perpendicular to the polarisation axis for optical trapping of a polystyrene sphere in water, using a focused order 01 mode linearly polarised laser beam.

(x_0, y_0=0μm, z_0=1.25μm, $\overline{n}$ = 1.199 , diameter of spherical particle = 2.0 μm, wavelength λ_0 = 0.5145 μm, w_0=0.231μm, kd=4 and a beam power of 3.5 mW.)

In table (5.10.) the numerical values for the trapping efficiency along the axis perpendicular to the direction of polarisation are given.

$x_0,y_0(\mu m)$	Q_y (5th order)	Q_x (GB01)	RMS error in %
-2.00	3.284E-03	2.859E-03	14.85
-1.75	1.753E-02	1.149E-02	52.57
-1.50	4.402E-02	4.128E-02	6.65
-1.25	1.080E-01	1.187E-01	8.96
-1.00	2.073E-01	2.348E-01	11.68
-0.75	2.486E-01	2.827E-01	12.08
-0.50	1.950E-01	2.098E-01	7.05
-0.25	1.003E-01	1.003E-01	0.07
0.00	-1.325E-17	-6.794E-18	95.07
0.25	-1.003E-01	-1.003E-01	0.07
0.50	-1.950E-01	-2.098E-01	7.05
0.75	-2.486E-01	-2.827E-01	12.08
1.00	-2.073E-01	-2.348E-01	11.68
1.25	-1.080E-01	-1.187E-01	8.96
1.50	-4.402E-02	-4.128E-02	6.65
1.75	-1.753E-02	-1.149E-02	52.57
2.00	-3.284E-03	-2.859E-03	14.85
		average RMS error	**18.99**

Table 5.10. The numerical values of the trapping efficiency along the axis perpendicular to the direction of polarisation Q_x and Q_y respectively, calculated using the GB01 treatment and the 5th order Gaussain beam approximation model, for optical trapping of a polystyrene sphere in water, using a focused order 01 mode linearly polarised laser beam.
(x_0, y_0=0μm, z_0=1.25μm, $\bar{n}$ = 1.199 , diameter of spherical particle = 2.0 μm, wavelength λ_0 = 0.5145 μm, w_0=0.231μm, kd=4 and a beam power of 3.5 mW.)

It can be seen from table (5.9.) that the average RMS error of the 17 data points is 13.12%. From table (5.10.) it can be seen that the average RMS error of the 17 data points is 18.99%. Again it can be seen by comparison of Fig. (5.24.) and Fig. (5.25.) that the trapping efficiency along the direction of polarisation is higher than the trapping efficiency along the axis perpendicular to the direction of polarisation. It can also be seen from Figs. (5.24) and (5.25), that in analogy with Eq. (5.32) the polystyrene sphere is in a stable equilibrium x_0=y_0=0 and in analogy with Eq. (5.33) in an unstable equilibrium at x_0=y_0=±2.

Next the trapping efficiency of a polystyrene sphere of radius 1μm positioned at various locations along the axis of propagation is calculated for an order 01 beam of wavelength λ_0=0.5145μm focused by NA≈1.5 lens, which corresponds to a value of kd=2. The beam spot size in this case is w_0=0.164 μm and the beam power is 3.5mW. The offset along the x and y axis is zero (x_0=y_0=0μm). Fig. (5.26.) compares the trapping efficiency for sphere positions along the axis of propagation [Q_z] calculated using the 5th order Gaussian beam approximation and the GB01 treatment.

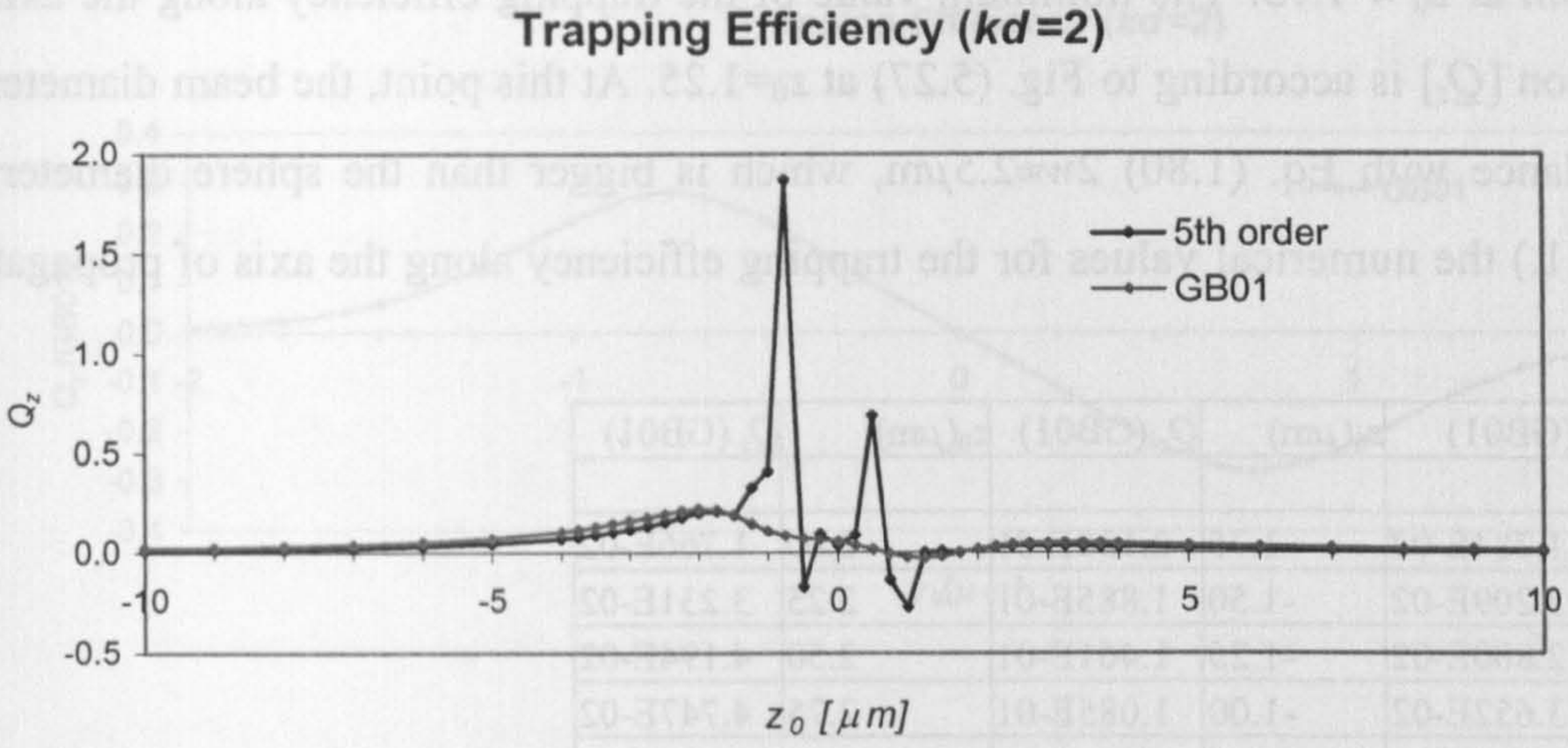

Fig. 5.26. Comparison of the trapping efficiency of the 5th order Gaussian beam approximation (doted curve) and the GB01 treatment (solid curve), along the propagation axis for optical trapping of a polystyrene sphere in water, using a focused order 01 mode linearly polarised laser beam.
(x_0=y_0=0, $\overline{n}$ = 1.199 , diameter of spherical particle = 2.0 μm, wavelength λ_0 = 0.5145 μm , w_0 = 0.1638 μm, kd=2 and a beam power of 3.5 mW.)

It is apparent from Fig. (5.26), that for a value of kd=2, as expected, the 5th order Gaussian beam approximations breaks down. In order to get accurate results for the trapping efficiency along the axis of propagation [Q_z], it is necessary to only plot the trapping efficiency values obtained from the GB01 treatment. Fig. (5.27) shows the trapping efficiency along the axis of propagation based on the GB01 treatment.

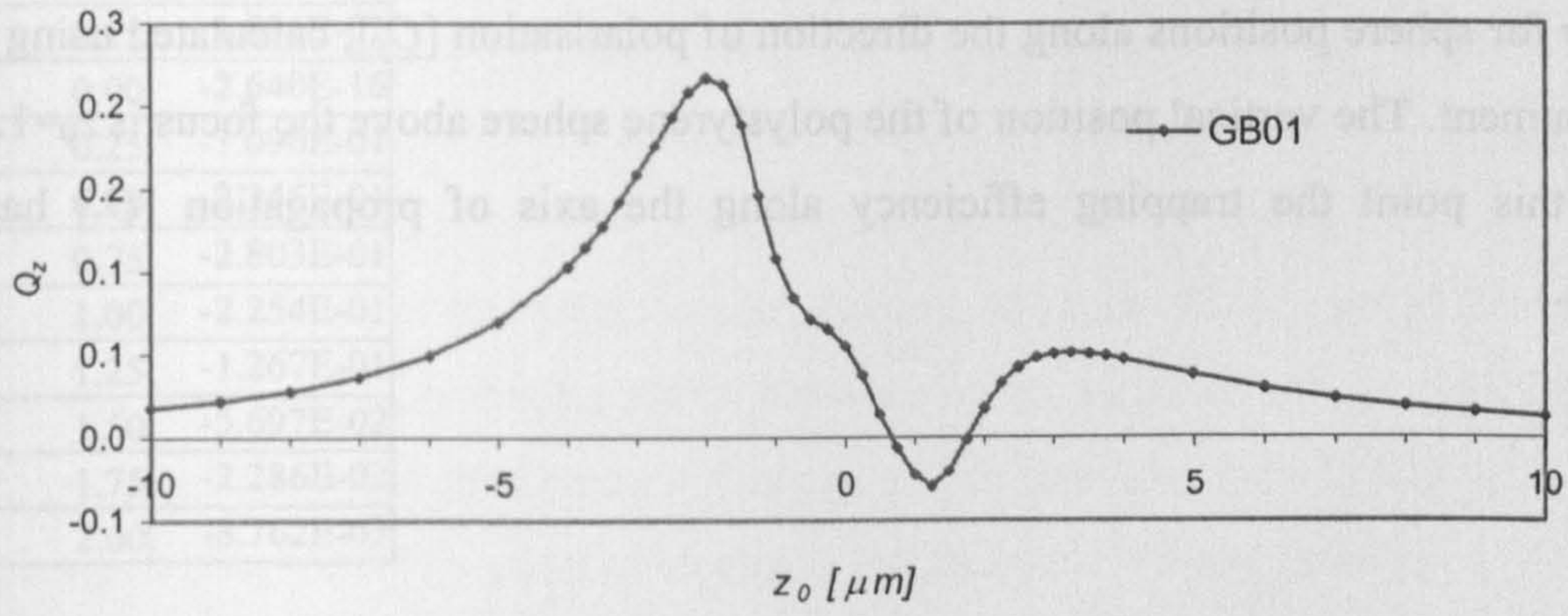

Fig. 5.27. Trapping efficiency based on the GB01 treatment, along the propagation axis for optical trapping of a polystyrene sphere in water, using a focused order 01 mode linearly polarised laser beam.
(x_0=y_0=0, $\overline{n}$ = 1.199 , diameter of spherical particle = 2.0 μm, wavelength λ_0 = 0.5145 μm , w_0 = 0.1638 μm, kd=2 and a beam power of 3.5 mW.)

It can be seen from Fig. (5.27) that the polystyrene sphere is in accordance with Eq. (5.32) in a stable equilibrium position at $z_0 \approx 0.75$ and in accordance with Eq. (5.33) in an unstable

equilibrium at $z_0 \approx 1.75$. The minimum value of the trapping efficiency along the axis of propagation [Q_z] is according to Fig. (5.27) at z_0=1.25. At this point, the beam diameter is, in accordance with Eq. (1.80) $2w \approx 2.5\mu$m, which is bigger than the sphere diameter. In table (5.11.) the numerical values for the trapping efficiency along the axis of propagation are given.

$z_0(\mu m)$	Q_z (GB01)	$z_0(\mu m)$	Q_z (GB01)	$z_0(\mu m)$	Q_z (GB01)
-10.00	1.784E-02	-1.75	2.130E-01	2.00	1.766E-02
-9.00	2.209E-02	-1.50	1.885E-01	2.25	3.231E-02
-8.00	2.800E-02	-1.25	1.461E-01	2.50	4.194E-02
-7.00	3.652E-02	-1.00	1.085E-01	2.75	4.747E-02
-6.00	4.937E-02	-0.75	8.455E-02	3.00	5.004E-02
-5.00	6.967E-02	-0.50	7.167E-02	3.25	5.061E-02
-4.00	1.033E-01	-0.25	6.550E-02	3.50	4.990E-02
-3.75	1.148E-01	0.00	5.514E-02	3.75	4.841E-02
-3.50	1.279E-01	0.25	3.712E-02	4.00	4.646E-02
-3.25	1.426E-01	0.50	1.419E-02	5.00	3.754E-02
-3.00	1.588E-01	0.75	-6.321E-03	6.00	2.974E-02
-2.75	1.761E-01	1.00	-2.244E-02	7.00	2.376E-02
-2.50	1.935E-01	1.25	-2.952E-02	8.00	1.926E-02
-2.25	2.086E-01	1.50	-2.067E-02	9.00	1.587E-02
-2.00	2.173E-01	1.75	-1.504E-03	10.00	1.326E-02

Table 5.11. The numerical values of the trapping efficiency along the axis of propagation Q_z calculated using the GB01 treatment for optical trapping of a polystyrene sphere in water, using a focused order 01 mode linearly polarised laser beam. (x_0=y_0=0, $\overline{n}$ = 1.199, diameter of spherical particle = 2.0 μm, wavelength λ_0 = 0.5145 μm, w_0=0.164μm, kd=2 and a beam power of 3.5 mW.)

Since the direction of polarisation in the GB01 treatment is the y axis, the trapping efficiency along this axis is calculated with x_0=0 μm. Fig. (5.28.) shows the trapping efficiency for sphere positions along the direction of polarisation [Q_y], calculated using the GB01 treatment. The vertical position of the polystyrene sphere above the focus is z_0=1.25, since at this point the trapping efficiency along the axis of propagation [Q_z] has a minimum.

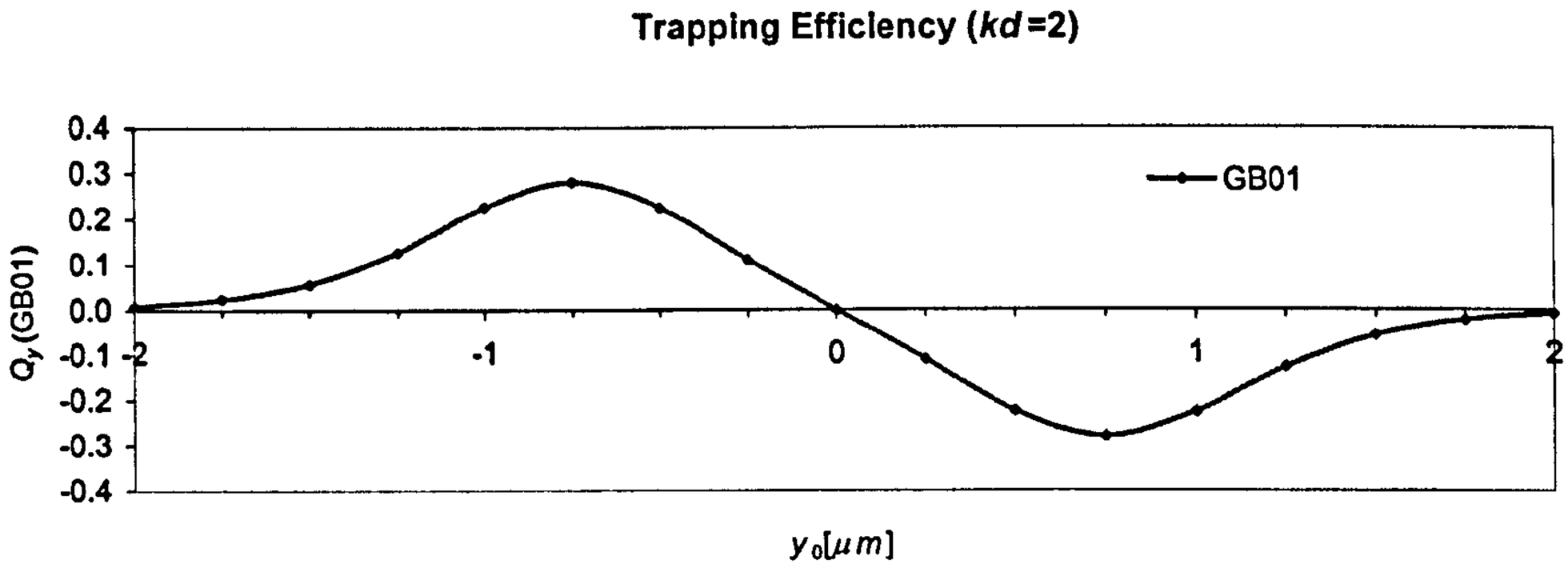

Fig. 5.28. The trapping efficiency based on the GB01 treatment, along the polarisation axis versus displacement along the polarisation axis for optical trapping of a polystyrene sphere in water, using a focused order 01 mode linearly polarised laser beam. (x_0=0μm, z_0=1.25μm, $\overline{n}$ = 1.199, diameter of spherical particle = 2 μm, wavelength λ_0 = 0.5145 μm, w_0=0.164μm, kd=2 and a beam power of 3.5 mW.)

In table (5.12.) the numerical values for the trapping efficiency along the direction of polarisation are given.

$y_0(\mu m)$	Q_y (GB01)
-2.00	8.762E-03
-1.75	2.286E-02
-1.50	5.697E-02
-1.25	1.267E-01
-1.00	2.254E-01
-0.75	2.803E-01
-0.50	2.245E-01
-0.25	1.096E-01
0.00	-2.640E-16
0.25	-1.096E-01
0.50	-2.245E-01
0.75	-2.803E-01
1.00	-2.254E-01
1.25	-1.267E-01
1.50	-5.697E-02
1.75	-2.286E-02
2.00	-8.762E-03

Table 5.12. The numerical values of the trapping efficiency along the direction of polarisation Q_y calculated using the GB01 treatment for optical trapping of a polystyrene sphere in water, using a focused order 01 mode linearly polarised laser beam. (x_0, y_0=0μm, z_0=1.25μm, $\overline{n}$ = 1.199, diameter of spherical particle = 2.0 μm, wavelength λ_0 = 0.5145 μm, w_0=0.164μm, kd=2 and a beam power of 3.5 mW.)

Fig. (5.29.) shows the trapping efficiency for sphere positions along the axis perpendicular to the direction of polarisation [Q_x], calculated using the GB01 treatment.

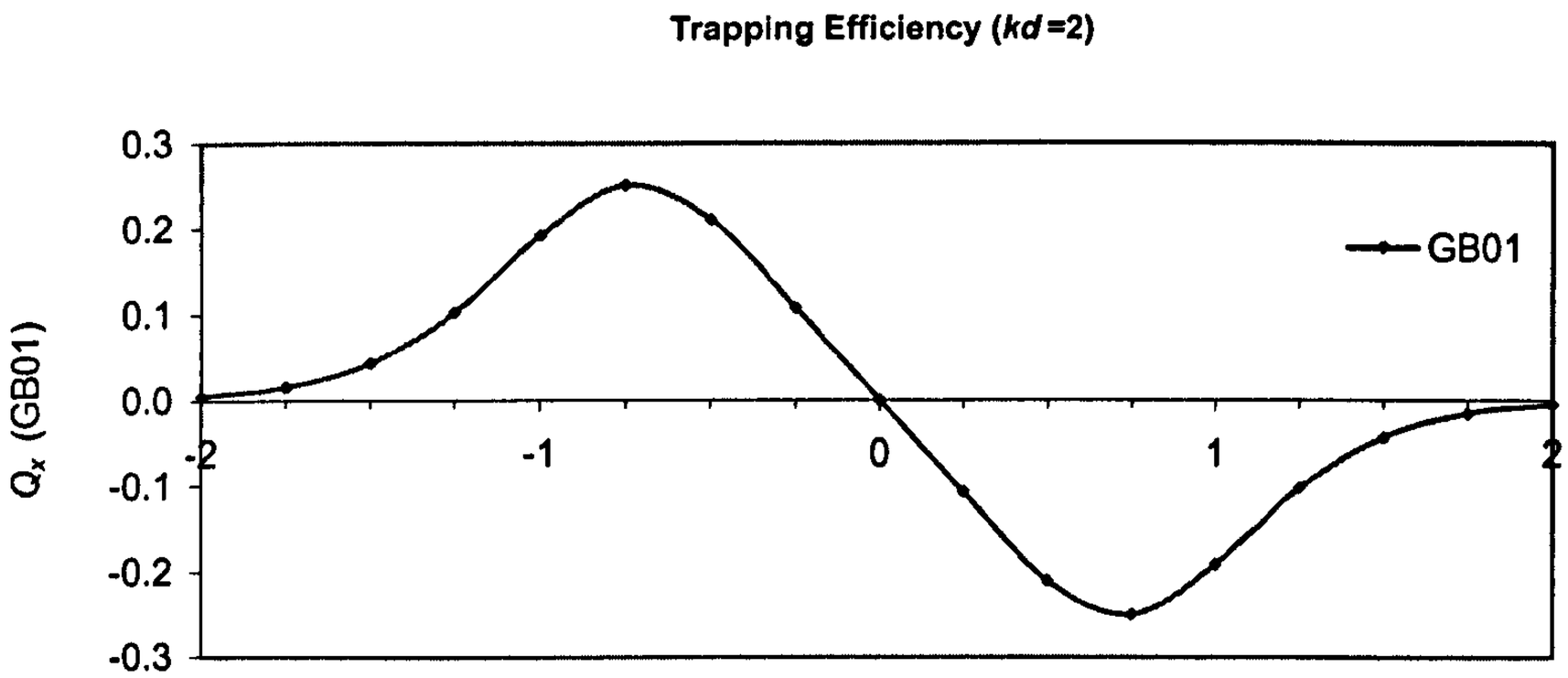

Fig. 5.29. The trapping efficiency based on the GB01 treatment, along the axis perpendicular to the polarisation axis versus displacement along the axis perpendicular to the polarisation axis for optical trapping of a polystyrene sphere in water, using a focused order 01 mode linearly polarised laser beam. (x_0=0μm, z_0=1.25μm, $\overline{n}$ = 1.199, diameter of spherical particle = 2 μm, wavelength λ_0 = 0.5145 μm, w_0=0.164μm, kd=2 and a beam power of 3.5 mW.)

In table (5.13.) the numerical values for the trapping efficiency along the axis perpendicular to the direction of polarisation are given.

$x_0(\mu m)$	Q_x (GB01)
-2.00	5.511E-03
-1.75	1.600E-02
-1.50	4.313E-02
-1.25	1.022E-01
-1.00	1.920E-01
-0.75	2.503E-01
-0.50	2.103E-01
-0.25	1.068E-01
0.00	2.497E-17
0.25	-1.068E-01
0.50	-2.103E-01
0.75	-2.503E-01
1.00	-1.920E-01
1.25	-1.022E-01
1.50	-4.313E-02
1.75	-1.600E-02
2.00	-5.511E-03

Table 5.13. The numerical values of the trapping efficiency along the axis perpendicular to the axis of polarisation Q_y calculated using the GB01 treatment for optical trapping of a polystyrene sphere in water, using a focused order 01 mode linearly polarised laser beam.
(x_0, y_0=0μm, z_0=1.25μm, $\overline{n}$ = 1.199, diameter of spherical particle = 2.0 μm, wavelength λ_0 = 0.5145 μm, w_0=0.164μm, kd=2 and a beam power of 3.5 mW.)

It can also be seen from Figs. (5.29) and (5.30), that in analogy with Eq. (5.32) the polystyrene sphere is in a stable equilibrium $x_0=y_0=0$ and in analogy with Eq. (5.33) in an unstable equilibrium at $x_0=y_0\approx\pm 2$.

5.6. Discussion

It has been demonstrated that for large values of *kd*, i.e. nearly paraxial Gaussian beams, the 5th order Gaussian beam approximation and the GB01 treatment are in good agreement. However, for small values of *kd* the 5th order Gaussian beam produces unreliable results. The relationship between the magnitude of the restoring acceleration, the beam diameter *w* and the radius of the spherical dielectric particle can be understood qualitatively from geometrical optics. Even though the Fresnel reflection and transmission coefficients were derived for plane incident waves, it has become apparent that these coefficients are also valid for strongly focused Gaussian beams such as the to 5th order approximated Gaussian beam and GB01. It can be seen by comparing Figs. (5.12.) and (5.17.) both representing the vertical restoring acceleration exerted by a focused beam on a water droplet of radius 1μm that no trapping is observed in the case of kd=4 and trapping is observed in the case of kd=2. Thus it can be concluded that the stronger the beam is focused, the stronger are the trapping forces. In the case of kd=4, the minimum vertical restoring acceleration $[a_z/g]$=9.15 (see table 5.4.) is observed at z_0=1μm, at this point the beam diameter $2w$=1.42μm, which is less than the diameter of the water droplet. Even though all the rays of the beam hit the hemispherical part of the droplet which faces the beam, only very few rays hit it at large incident angles, thus the resultant force in the vertical direction is reduced. In the case of kd=2, the minimum vertical restoring acceleration $[a_z/g]$=-0.16 (see table 5.5.) is observed at z_0=1μm, at this point the beam diameter $2w$=2.0μm, which is equal to the diameter of the water droplet. Also in this case all the rays of the beam hit the hemispherical part of the droplet which faces the beam, but here enough rays hit it at larger incident angles, so that the resultant force in the vertical direction is increased and hence trapping is observed. The same observation can be made for the trapping of a polystyrene sphere of radius 1 μm suspended in water by comparing Figs.(5.20.), (5.23.) and (5.27.) In the case of kd=4 a minimum vertical restoring acceleration $[a_z/g]$=-8.7 (see table 5.8.) is observed at z_0=1.25μm, which corresponds to a trapping efficiency of Q_z=-0.005. At this point the beam diameter $2w$=1.77μm, which is less than the diameter of the polystyrene sphere. However since the relative refractive index is lower for a polystyrene sphere suspended in water than for a water droplet in air, trapping was observed. However the

trapping efficiency is much lower for kd=4 than for kd=2. In the case of kd=2 the minimum vertical trapping efficiency Q_z=-0.03 (see table 5.11.) is observed again at z_0=1.25 μm. At this point the beam diameter is $2w$=2.5μm, i.e. greater than the diameter of the polystyrene sphere. It has to be mentioned that in this case not all the rays hit the hemispherical part of the polystyrene sphere which faces the beam. This does not have a big effect on the trapping of the sphere, since the photon density at the centre of the beam is much higher than on the outside of the beam and the number of photons which hit the hemisphere at large angles is higher than in the case of the water droplet suspended in air. The maximum vertical restoring acceleration in the case of a polystyrene sphere being trapped in water, using a value of kd=4 is $[a_z/g]$=70.6 (see table 5.8.), where the maximum vertical restoring acceleration for the same kd in the case of a water droplet being trapped in air is $[a_z/g]$=98.1 (see table 5.4.). Thus even though a polystyrene sphere can be trapped in water using a value of kd=4, where a water droplet in air could not be trapped using kd=4, the maximum vertical acceleration is lower in the case of the polystyrene sphere being trapped in water, then for the water droplet being trapped in air, due to the larger mass of the polystyrene sphere and due to the fact that the relative refractive index is lower for the polystyrene / water interface than for the air / water interface. Thus the scattering force is reduced. The trapping efficiencies along the horizontal directions, i.e. $[Q_x]$ and $[Q_y]$, are the highest when the beam diameter is slightly smaller than the diameter of the polystyrene sphere as is the case for a value of kd=4. This can be seen from Figs. (5.24.) and (5.25.), where z_0=1.25μm and hence $2w\approx$1.77μm, with a polystyrene sphere diameter of 2μm. The maximum values of the horizontal trapping efficiencies $[Q_x]$ and $[Q_y]$ in this case are ±0.28 and ±0.32 at x_0=y_0=±0.75μm respectively (see table 5.10. and 5.9. respectively). It is interesting to note, that even though the vertical trapping efficiencies are the highest for a value of kd=2, the horizontal trapping efficiencies are lower. This can be seen from Figs. (5.28) and (5.29), where z_0=1.25μm and hence $2w\approx$2.5 μm. The horizontal trapping efficiencies $[Q_x]$ and $[Q_y]$ in this case are ±0.25 and ±0.28 at x_0=y_0=±0.75μm respectively (see table 5.13. and 5.12. respectively). For a value of kd=2, the beam diameter is equal to the diameter of the water droplet, i.e. $2w\approx$2.0μm at a vertical location z_0=1μm. In the considered case the maximum horizontal restoring accelerations $[-a_x/g]$ and $[-a_y/g]$ are ±96 and ±104.35 at x_0=y_0=±0.75 respectively (see table 5.7. and 5.6. respectively). Nevertheless it can be concluded that the highest optical trap efficiencies occur when trapping a polystyrene sphere of radius 1μm suspended in water, with a laser beam of wavelength λ_0=0.5145 μm, with a beam waist radius of 0.164μm. However this case will rarely be examined experimentally, since it would require a lens with NA=1.5. It has also been

demonstrated, that it is easier to trap a polystyrene sphere in water, than a water droplet in air.

5.7. Conclusion

This piece of research can be concluded by stating that a set of solutions to Maxwell's equations has been found that describe strongly focused laser beams of arbitrary order *mn*, where *mn* are the orders of the associated Legendre functions, describing the polar angular dependence of the beam mode. The radial dependence of the beam mode is given by the spherical Bessel functions of order *n* and the azimuthal dependence is given additionally by a factor $e^{\pm im\phi}$ .It has further been demonstrated that the order 00 beam mode does not exist, as this beam mode has infinite energy, nor does any other order *mn* beam mode with even *n-m*. The order 01 beam mode has a Gaussian irradiance profile like the Hermite-Gaussian beam mode TEM_{00} or a Laguerre-Gaussian beam mode TEM^{*}_{00}. It satisfies the paraxial wave equation in the paraxial limit. In this limit, the E.M. field is linearly polarised. In the far-field limit the irradiance profile is slightly different from the one produced by focusing a Gaussian beam with an aberration free sine condition lens. The E.M. field in this limit is also linearly polarised. If the order 01 beam mode is focused by a high numerical aperture lens, i.e. the dimensionless beam parameter $1<kd<5$, then a standing wave is produced at the beam waist, which oscillates at right angle to the direction of propagation of the beam. Thus the physically realisable order 01 beam mode needs to be considered when referring to a Gaussian beam. The physically realisable order 12 beam mode has a similar irradiance profile to the one of the Lagurre-Gaussian beam mode TEM^{*}_{01}. Optical trapping forces have been calculated using the method presented by Barton *et al.* [8], which is valid for arbitrary E.M. fields. These calculations were performed for the E.M. field based on the 5th order Gaussian beam approximation and for the E.M. field of the order 01 beam mode. It has been demonstrated that the trapping forces calculated using the 5th order Gaussian beam approximation, presented by Barton *et al.* [8] are accurate for almost paraxial Gaussian beams (kd=74.6) when compared to the treatment based on the E.M. field of the order 01 beam mode. However for strongly focused beams like kd=4 or kd=2, the model presented by Barton *et al.* [8] is highly inaccurate and breaks down. It has been established that by focusing a Gaussian laser beam of wavelength λ_0=0.5145 μm and a beam power of 3.5mW with a NA=1.5 lens, which corresponds to a value of kd=2, a polystyrene sphere of radius 2 μm suspended in water can be strongly trapped. The location of the sphere along the axis of propagation at which

the highest restoring trapping efficiency was observed is z_0=1.25 μm above the focal point. At this point the beam diameter is $2w\approx$2.5 μm. However, in general the laser beams are focused by lenses with NA=1.3 and not NA=1.5. Additionally it has been demonstrated, that in order to trap a spherical dielectric particle such as a polystyrene sphere, it is advantageous to trap the sphere in a liquid, in order to reduce the relative refractive index. Further it has been highlighted that a laser beam propagating in the direction opposite to the direction of the force of gravity is necessary in order to achieve good levitation. The calculated trapping forces are in agreement with the predictions based on geometrical optics. It has been established in this research, that it is vital to have a description for a focused laser beam which satisfies Maxwell's equations, since in order to trap a particle most effectively the laser beam needs to be strongly focused (NA>1). Gaussian beam approximation models fail to predict the trapping efficiencies for very highly focused beams.

5.8. Future work

As first it would be interesting to compare the results produced by the GB01 treatment with the results presented by Kim and Lee [19]. This comparison will give a good insight in how important it is to introduce a complex sink in the complex source point method. It would also be interesting to calculate the optical trapping forces exerted on absorbing spheres and to compare the obtained results with the results presented by Huisken and Stelzer [14]. In order to perform these calculations, it will be necessary to use a complex refractive index. It would also be of interest to explore the oscillatory behaviour of the trapping forces as a function of the size parameter β as was shown by Mazolli et al. [10]. So far only trapping forces exerted on spherical dielectric particles have been calculated. In general metallic particles are trapped by a TEM^{*}_{01} Laguerre Gaussian beam. It would thus be interesting to calculate the trapping forces using the E.M. field based on order 12. However before these calculations can be performed it is necessary to test the polarisation properties of the E.M. field based on order 12. It might turn out to be necessary to derive a new E.M. field using a different linear super position of the **M** and **N** functions, since the donut mode has a minimum on axis and is in general thought to be a superposition of the Hermite Gaussian beam modes TEM_{10} and TEM_{01}. As there is great interest in Bessel Gaussian beams, which are a solution to the paraxial wave equation and not an exact solution to the wave equation, it would be interesting to investigate if Bessel Gaussian beams can be represented as a superposition of the beam modes derived in this research.

Having a description of a focused Gaussian beam which is an exact solution to Maxwell's equations should lead to new innovations in areas like biology, medicine, telecommunication and entertainment electronics. Overall it can be said that having such a description of a focused Gaussian beam opens potential opportunities for much research in many different areas of applications.

References

[1] Hecht, E., (2002), Optics, 4th edition, Addison Wesley.

[2] Ashkin, A., (1970), Acceleration and trapping of particles by radiation pressure, *Phys. Rev. Lett.* **24**, 4, p.156-159.

[3] Sterba, R. E. and Sheetz, M. P., (1998), Basic laser tweezers, Methods in Cell Biology, **55**, *Laser Tweezers in Cell Biology*, Academic press.

[4] Ashkin, A.,(2000), History of optical tapping and manipulation of small-neutral particles, atoms and molecules, *IEEE J. on selected topics in quantum electronics*, **6**, 6 . p. 841-856.

[5] Tadir, Y., Wright W. H., Vafa, O. et al., (1989), Micromanipulation of sperm by laser Generated optical trap. *Fertil. Steril..*, **52**, p. 870-873.

[6] Block, S. M., Blair, D. F., Berg, H. C., (1989), Compliance of bacterial flagella measured with optical tweezers, *Nature*, **338**, p.514-518.

[7] Ashkin, A., Schütze, K., Dziedzic, J. M., Euteneuer, U., Schliwa, M., (1990), Forces generated of organelle transport measured in vitro by an infrared laser trap., *Nature*, **348**, p.346-348.

[8] Barton, J. P, Alexander, D. R., Schaub, S. A., (1989), Theoretical determination of net radiation forces and torque for a spherical particle illuminated by a focused laser beam, , *J. Appl. Phys.* **66** 4594-4602.

[9] Barton, J. P, Alexander, (1989) Fifth-order corrected E.M. field components for a fundamental Gaussian beam, *J. Appl. Phys.* **66** 2800-2802.

[10] Mazolli, A., Maia Neto, P. A., Nussenzveig, H. M., (2003), Theory of trapping forces in optical tweezers. *Proc. R. Soc. Lond. A*, **459**, p. 3021-3041.

[11] Ashkin, A., (1992), Forces of a single-beam gradient laser trap on a dielectric sphere in the ray optics regime. *Biophys. J.* **61**, p. 569-582.

[12] Svoboda, K., Block, S. M., (1994), Optical trapping of metallic Rayleigh particles, *Opt. Lett.* **19**, 13. p. 930-932.

[13] Sasaki, K., Koshioka, M., Misawa, H., Kitamura, N., (1992), Optical trapping of a Metallic particle and a water droplet by scanning laser beam *Appl.Phys. Lett.* **60**, 7, p. 807-809.

[14] Huisken, J., Stelzer, E. H. K., (2002), Optical levitation of absorbing particles with a nominally Gaussian laser beam. *Optics Lett.* **27**, 14, p. 1223-1225.

[15] Bohren, C. F., Huffman, D. R., (1998), Absorption and scattering of light by small particles, John Wiley & Sons.

[16] Born, M. Wolf, E., (1999), Principle of optics, 7th (expanded edition), Cambridge University press.

[17] Grant, I. S., Phillips, W. R., (1990), Electromagnetism, 2nd edition, John Wiley & Sons.

[18] Roosen, G., Imbert, C., (1976), Optical levitation by means of two horizontal Laser beams: A theoretical and experimental study. *Phys. Lett.* **59A**, 1. p. 6-8.

[19] Kim, J. S., Lee, S. S., (1983), Scattering of laser beams and the optical potential well for a homogenous sphere. *J. Opt. Soc. Am.* **73**, 3, p. 303-312.

[20] Lorenz, L., (1898), Sur la lumière réfléchie et réfractée par une sphère transparente, in *Oeuvres Scientifiques de L. Lorenz, revues et annotées par H. Valentiner* (Librairie Lehmann et Stage, Copenhagen) p. 405-529.

[21] Mie, G., (1908), Beiträge zur Optik trüber Medien, speziell kolloidaler Metal-Lösungen, *Ann. Phys.* **25**. p. 377-445

[22] Irving, J., Mullineux, N., (1959), Mathematics in Physics and Engineering, Academic Press.

[23] Jones, N. T., (1994), Modelling laser entrapment forces on microspheres, MSc project report, University of Hertfordshire.

[24] Siegman, A. E., Lasers, (1986) University Science Books.

[25] Wright, W. H., Sonek, G. J., Berns, M. W., (1994), Parametric study of the forces on microspheres held by optical tweezers. *Appl. Opt.* **33**, 9, p. 1735-1748.

[26] Ohanian, H. C., (1989), Physics (2nd edition), W. W. Norton & Co.

[27] Svoboda, K., Block, S. M., (1994), Biological Applications of optical forces *Ann. Rev. Biophys. Biomol. Struct.* p. 247-285.

[28] Wright, W. H., Sonek, G. J., Berns, M. W., (1993), Radiation trapping forces on microspheres with optical tweezers . *Appl. Phys. Lett.* **63**, 6, p. 715-717.

Appendix

Exact Solutions of the Vector Wave Equation

For waves of a single frequency, the scalar and vector wave equations can be reduced to the scalar and vector Helmholtz equations :

$$\nabla \bullet \nabla f_{mn}(\mathbf{r}) + k^2 f_{mn}(\mathbf{r}) = 0 \tag{A.1}$$

$$\nabla \bullet \nabla \mathbf{G}_{mn}(\mathbf{r}) + k^2 \mathbf{G}_{mn}(\mathbf{r}) = 0 \tag{A.2}$$

by factoring out the time dependent function $e^{-i\omega t}$. The analysis will therefore investigate how the vector functions $\mathbf{G}_{mn}(\mathbf{r})$ can be generated from known solutions of the scalar functions $f_{mn}(\mathbf{r})$. But before proceeding, it should be pointed out that the scalar functions can be extended into a more general form by a change of the argument $\mathbf{r} \rightarrow \mathbf{r}' = \mathbf{r} + \mathbf{c}$, where $\mathbf{c}$ is a constant translation vector. This is possible due to the translational invariance of Eq.(A.1) which allows the origin of the co-ordinate system to be chosen arbitrarily. A displacement of particular interest is $\mathbf{c} = (\mathbf{a}, id)$.

Solutions of Eq.(A.2) are a longitudinal vector :

$$\mathbf{L}_{mn}(\mathbf{r}) = \frac{1}{k} \nabla f_{mn}(\mathbf{r}) \tag{A.3}$$

and two transverse vectors :

$$\mathbf{M}_{mn}(\mathbf{r}) = \nabla \times [\mathbf{A}(\mathbf{r}) f_{mn}(\mathbf{r})] \tag{A.4}$$

$$\mathbf{N}_{mn}(\mathbf{r}) = \frac{1}{k} \nabla \times \mathbf{M}_{mn}(\mathbf{r}) \tag{A.5}$$

where **A** (**r**) is an unknown vector function with the units of length so that $\mathbf{M}_{mn}$ (**r**) is dimensionless. The three types of vectors form a complete set over the vector space and hence are mutually orthogonal:

$$\int \mathbf{L}_{mn}(\mathbf{r}) \bullet \mathbf{M}^{*}_{mn}(\mathbf{r}) d\Omega = 0 \tag{A.6}$$

$$\int \mathbf{M}_{mn}(\mathbf{r}) \bullet \mathbf{N}^{*}_{mn}(\mathbf{r}) d\Omega = 0 \tag{A.7}$$

$$\int \mathbf{L}_{mn}(\mathbf{r}) \bullet \mathbf{N}^{*}_{mn}(\mathbf{r}) d\Omega = 0 \tag{A.8}$$

in which the integral is over the solid angle Ω.

Also,

$$\nabla[\nabla \bullet \mathbf{L}_{mn}(\mathbf{r})] = -k^2 \mathbf{L}_{mn}(\mathbf{r}) \tag{A.9}$$

$$\nabla \times \nabla \times \mathbf{M}_{mn}(\mathbf{r}) = k^2 \mathbf{M}_{mn}(\mathbf{r}) \tag{A.10}$$

$$\nabla \times \nabla \times \mathbf{N}_{mn}(\mathbf{r}) = k^2 \mathbf{N}_{mn}(\mathbf{r}) \tag{A.11}$$

From Eqs. (A.4) and (A.10), it follows that:

$$\nabla \times \mathbf{M}_{mn}(\mathbf{r}) = k^2 \mathbf{A}(\mathbf{r}) f_{mn}(\mathbf{r}) + \nabla U \tag{A.12}$$

or $$\nabla \times \nabla \times \mathbf{A}(\mathbf{r}) f_{mn}(\mathbf{r}) = k^2 \mathbf{A}(\mathbf{r}) f_{mn}(\mathbf{r}) + \nabla U \tag{A.13}$$

An informed trial expression for U is

$$U = \nabla \bullet [\mathbf{A}(\mathbf{r}) f_{mn}(\mathbf{r})] - 2a(\mathbf{r}) f_{mn}(\mathbf{r}) \tag{A.14}$$

where $a(\mathbf{r})$ is an unknown scalar function. The expansion of the l.h.s. of Eq.(A.13) by using the vector identity:

$$\nabla \times \nabla \times \_ \equiv \nabla(\nabla \bullet \_) - \nabla \bullet \nabla \_$$

and the substitution of U then leads to :

$$-\nabla \bullet \nabla(\mathbf{A}(\mathbf{r}) f_{mn}(\mathbf{r})) = k^2 \mathbf{A}(\mathbf{r}) f_{mn}(\mathbf{r}) - 2\nabla[a(\mathbf{r}) f_{mn}(\mathbf{r})] \tag{A.15}$$

However,

$$\begin{aligned} -\nabla \bullet \nabla(\mathbf{A}(\mathbf{r}) f_{mn}(\mathbf{r})) &= -\nabla \bullet [\mathbf{F}_{mn}(\mathbf{r}) \mathbf{A}(\mathbf{r}) + f_{mn}(\mathbf{r}) \nabla \mathbf{A}(\mathbf{r})] \\ &= -[\nabla \bullet \mathbf{F}_{mn}(\mathbf{r})] \mathbf{A}(\mathbf{r}) - 2\mathbf{F}_{mn}(\mathbf{r}) \bullet \nabla \mathbf{A}(\mathbf{r}) - f_{mn}(\mathbf{r}) \nabla \bullet \nabla \mathbf{A}(\mathbf{r}) \end{aligned} \tag{A.16}$$

where

$$\mathbf{F}_{mn}(\mathbf{r}) = \nabla f_{mn}(\mathbf{r}) \tag{A.17}$$

But by Eq.(A.1)

$$\nabla \bullet \mathbf{F}_{mn}(\mathbf{r}) = -k^2 f_{mn}(\mathbf{r}) \tag{A.18}$$

and so Eq.(A.15) reduces to

$$2\mathbf{F}_{mn}(\mathbf{r}) \bullet \nabla \mathbf{A}(\mathbf{r}) + f_{mn}(\mathbf{r}) \nabla \bullet \nabla \mathbf{A}(\mathbf{r}) = 2\mathbf{F}_{mn}(\mathbf{r}) a(\mathbf{r}) + 2 f_{mn}(\mathbf{r}) \nabla a(\mathbf{r}) \tag{A.19}$$

$$\nabla \mathbf{A}(\mathbf{r}) = \mathfrak{I} a(\mathbf{r}) \tag{A.20}$$

$$\nabla a(\mathbf{r}) = 0 \tag{A.21}$$

in which $\mathfrak{I}$ is the unity dyadic or idemfactor. Hence $a(\mathbf{r})$ is just a constant

$$a(\mathbf{r}) = a$$

and Eq.(A.20) can be written in cartesian co-ordinates as

$$\frac{\partial}{\partial x}A_x = a,\ \frac{\partial}{\partial y}A_y = a,\ \frac{\partial}{\partial z}A_z = a. \tag{A.22}$$

The solutions of the last set of equations are:

$$A_x = ax + b_x,\ A_y = ay + b_y,\ A_z = az + b_z$$

or

$$\mathbf{A}(\mathbf{r}) = a\mathbf{r} + \mathbf{b} \tag{A.23}$$

It should be noted that $\nabla \times \mathbf{A} = 0$ and $\nabla \bullet \mathbf{A} = 3a$ from which

$$\mathbf{M}_{mn}(\mathbf{r}) = \nabla f_{mn}(\mathbf{r}) \times \mathbf{A}(\mathbf{r}) \tag{A.24}$$

and

$$\mathbf{N}_{mn}(\mathbf{r}) = k\mathbf{A}(\mathbf{r}) f_{mn}(\mathbf{r}) + \frac{1}{k}\nabla\left[a f_{mn}(\mathbf{r}) + \mathbf{A}(\mathbf{r}) \bullet \nabla f_{mn}(\mathbf{r})\right] \tag{A.25}$$

can be obtained. These are completely general expressions.

Two particular solutions are:

(a) $\mathbf{A} = \mathbf{b}$, $a = 0$

$$\mathbf{M}_{mn}(\mathbf{r}) = \nabla f_{mn}(\mathbf{r}) \times \mathbf{b} \tag{A.26}$$

$$\mathbf{N}_{mn}(\mathbf{r}) = k\mathbf{b} f_{mn}(\mathbf{r}) + \frac{1}{k}\nabla\left[\mathbf{b} \bullet \nabla f_{mn}(\mathbf{r})\right] \tag{A.27}$$

An Example for $\mathbf{A} = \frac{1}{k}\mathbf{a}_x, a = 0, \mathbf{b} = \frac{1}{k}\mathbf{a}_x$:

$$\mathbf{M}_{mn}(\mathbf{r}) = \frac{1}{k}\nabla f_{mn}(\mathbf{r}) \times \mathbf{a}_x$$

$$\mathbf{N}_{mn}(\mathbf{r}) = \mathbf{a}_x f_{mn}(\mathbf{r}) + \frac{1}{k^2}\nabla\left[\frac{\partial}{\partial x} f_{mn}(\mathbf{r})\right]$$

and (b) $\mathbf{A} = \mathbf{r}$, $a = 1$, $\mathbf{b} = 0$

$$\mathbf{M}_{mn}(\mathbf{r}) = \nabla f_{mn}(\mathbf{r}) \times \mathbf{r} \tag{A.28}$$

$$\mathbf{N}_{mn}(\mathbf{r}) = k\mathbf{r} f_{mn}(\mathbf{r}) + \frac{1}{k}\nabla\left[f_{mn}(\mathbf{r}) + \mathbf{r} \bullet \nabla f_{mn}(\mathbf{r})\right] \tag{A.29}$$

$$= k\mathbf{r} f_{mn}(\mathbf{r}) + \frac{1}{k}\nabla\left[\frac{\partial}{\partial r}(r f_{mn}(\mathbf{r}))\right]$$